Spring 2021

Water-Oxidation Electrocatalysis and Concerted Proton-Electron Transfer by High-Valent Complexes of Copper and Nickel

Katherine Jennie Fisher
Yale University Graduate School of Arts and Sciences, katherinejfisher@gmail.com

Abstract

Water-Oxidation Electrocatalysis and Concerted Proton-Electron Transfer by High-Valent Complexes of Copper and Nickel

Katherine J. Fisher

2021

The development of renewable energy resources to replace traditional fossil fuels is among the major challenges facing the world today. One hurdle to fully transitioning to renewable energy sources to meet the world's energy demand is energy storage. A potential solution to this problem is to store energy generated from renewable resources in the form of chemical bonds, as plants do in the process of photosynthesis. Artificial photosynthetic systems could be used to split water into protons, electrons, and oxygen, and those components could then be used to generate fuel, such as H_2, that could be stored until needed. Water oxidation, however, is thermodynamically and kinetically challenging, often requiring large overpotentials in order to drive the reaction. Therefore, water oxidation catalysts must be developed to lower the energy barrier required for the reaction.

The first section of this thesis focuses on the development and study of water-oxidation electrocatalysts by Earth-abundant metal systems. Chapter 1 provides an introduction to water-oxidation catalysis and proton-coupled electron transfer. Chapter 2 describes the synthesis and characterization of a copper-based water-oxidation electrocatalyst, $Cu(pyalk)_2$ (pyalk = 2-(2′-pyridyl)-2-propanoate). This complex was shown to be a robust and active electrocatalyst for water oxidation under basic conditions. Further characterization of the complex demonstrated that the catalyst operates through a mononuclear mechanism, has a turnover frequency of ~0.7 s^{-1} at pH 12.5, and is active for over 12 hours and 30 catalytic turnovers. These results demonstrate the ability of the strongly donating pyalk ligand to stabilize Earth-abundant metal electrocatalysts for water oxidation. Chapter 3 presents a mechanistic study of water-oxidation electrocatalysis by $Cu(pyalk)_2$. It is proposed that the catalyst operates through a water-nucleophilic attack mechanism on a copper(III)-oxyl radical species. Experimental and theoretical analysis both support this proposed mechanism, and the measured kinetic isotope effect, turnover frequency, and rate of the

first chemical step all showed good agreement with the predicted theoretical values. This work provides one of the first mechanistic studies of a mononuclear copper-based water-oxidation electrocatalyst.

Many reactions relevant to energy production and storage include proton-coupled electron transfer steps, in which a proton and electron are transferred in either a stepwise or concerted fashion. The ability to understand and control how protons and electrons move in these systems could therefore prove valuable in designing more efficient catalysts for reactions such as water oxidation. The second section of this dissertation discusses the proton-coupled electron transfer reactivity of two high-valent systems related to the water-oxidation electrocatalyst $Cu(pyalk)_2$.

Chapter 4 describes the synthesis, characterization, and PCET reactivity of $Ni(pyalk)_2^+$, a square planar nickel(III) species structurally analogous to $Cu(pyalk)_2$. Multiple characterization methods, including X-ray photoelectron spectroscopy (XPS), electron paramagnetic resonance spectroscopy, and X-ray crystallography confirm the highly oxidized state of nickel, making it a rare example of nickel in the +3 oxidation state. $Ni(pyalk)_2^+$ was then shown to undergo proton-coupled electron transfer from a variety of phenolic and hydrocarbon substrates. Analysis of the kinetics of the reaction with various substrates indicates that $Ni(pyalk)_2^+$ reacts with these substrates through concerted proton-electron transfer. Further thermodynamic analysis showed that, during PCET, $Ni(pyalk)_2^+$ formed an O-H bond with a bond dissociation enthalpy of ~94 kcal/mol. The formation of this fairly strong bond may explain the fast reactivity of this system.

Chapter 5 describes the characterization and reactivity of a high-valent copper species, $Cu(pyalk)_2^+$, the one-electron oxidized form of $Cu(pyalk)_2$. XPS and X-ray crystallography measurements confirm the oxidation of the copper center, demonstrating that the copper of $Cu(pyalk)_2^+$ is in the +3 oxidation state, a rare oxidation state for copper. $Cu(pyalk)_2^+$ was shown to also react with phenolic and hydrocarbon substrates through a concerted proton-electron transfer mechanism in a similar manner to nickel. Thermodynamic analysis demonstrated that $Cu(pyalk)_2^+$ forms an O-H BDE of ~98 kcal/mol, significantly higher than its nickel counterpart, yet it was shown to only react 4-5 times faster than $Ni(pyalk)_2^+$ with the same substrates. Calculation of an asynchronicity factor for each compound demonstrated that $Ni(pyalk)_2^+$ may react through a more

asynchronous mechanism than $Cu(pyalk)_2^+$, which may explain the rather small difference in reactivity. These systems are two of only a handful of isolated Ni(III) and Cu(III) species that have been shown to undergo PCET reactivity. These results may provide valuable insight into PCET reactivity of electrocatalytic species, which could be used in designing the next generation of Earth-abundant water-oxidation electrocatalysts.

Water-Oxidation Electrocatalysis and Concerted Proton-Electron Transfer by High-Valent Complexes of Copper and Nickel

A Dissertation

Presented to the Faculty of the Graduate School

Of

Yale University

In Candidacy for the Degree of

Doctor of Philosophy

by

Katherine J. Fisher

Dissertation Directors: Gary W. Brudvig and Robert H. Crabtree

June 2021

Acknowledgments

I would first like to thank my advisers, Professor Gary Brudvig and Professor Robert Crabtree, for their support, advice, and ideas over the past five years. Both of you have been a constant source of encouragement and feedback over the course of my PhD, and under your guidance I have become a more thoughtful and independent scientist. Thank you for giving me the opportunity to pursue my own ideas, even if they didn't always go the ways I intended them to. Gary, thank you for your encouragement and direction and your big-picture perspective when I got too focused on the details. Bob, thank you for always having an open door to talk about research—I always left your office with so many more ideas than when I entered. I would also like to thank my committee member Nilay Hazari for his advice and feedback over the course of my PhD and for always having his door open to chat.

I undoubtedly owe thank-yous to my lab mates for many, many reasons. Kelly Materna served as a mentor to me when I first started in lab and helped design my first project, and Aaron Bloomfield provided me with invaluable advice and help with organic synthesis. Thoe Michaelos, Liam Sharninghausen, Shashi Sinha, and Dimitar Shopov helped me get started in the Crabtree lab and were a never-ending source of ideas, suggestions, and fun. Hannah Lant and Hao-Li Huang joined the lab at the same time as I did, and I couldn't have asked for a better cohort. I owe you both many thanks for your company over lunch and in the office for the past five years and for helping me flesh out (and discard) many ideas. Margo Feuer joined the group as an undergraduate student, and I had the opportunity to mentor her in lab. Margo, I'm excited to see all the amazing things you'll do in graduate school! And finally, a huge thank you to Claire Cody for cleaning out and shutting down the Crabtree lab with me. That was an experience that I will never forget. I'd also like to thank all the current and former members of the lab, including Daria Huang, David Vinyard, Shin Hee Lee, Jimmy Jiang, Jessie Wiwczar, Ipsita Ghosh, Gourab Banerjee, Gongfang Hu, Jen Troiano, Josie Jacob-Dolan, Arjun Jaini, Hanyu Liu, Chris Gisriel, Sarah Ostresh, Uriel Tayvah, Matt Capobianco, Jake Spies, Jens Neu, and Brian Pattengale.

I would also like to thank my scientific collaborators and the centers I have had the opportunity to be a part of. I would like to acknowledge the ANSER and LEAP EFRCs as well as

the ESI solar group. All of these groups gave me experience presenting my work to broad scientific audiences and gave me feedback from new perspectives that helped me improve my work and grow as a scientist. I'd also like to thank my computational collaborators Ben Rudshteyn and Ray Kelly, without whom some of this work would not have been possible.

In addition to my own labs, I owe a huge thank you to Jim Mayer and the Mayer lab for letting me invade their glove box space and use their instruments. In the last few years of my PhD, I did more work in your lab than in my own.

I owe a thank you to Daniel Martin for many reasons. Thank you for training me on about half the instruments in your lab, patiently re-training me when I forgot how to use them, and less patiently fixing the stopped flow all those times I clogged it. Thank you for being my TV binge-watching buddy, for going on many an adventure with me, and for your unwavering support. And thank you most of all for being a wonderful partner and friend over the past four years and in all the years to come.

Finally, I'd like to thank my parents, Renee Rendahl and Michael Fisher. Both of you have loved and supported me unconditionally my entire life, and without you I would not be the person I am today. Thank you for providing me with the opportunities to pursue my interests and passions, both academic and personal, and for always believing in me. This thesis could not have happened without you.

Table of Contents

Abstract 1
Acknowledgments 6
Table of Contents 8
List of Figures 8
List of Tables 16
List of Schemes 17
1 Introduction 18
Part One. Study of water oxidation-catalysis by first-row transition metal complexes. 45
2 Electrocatalytic water oxidation by a copper(II) complex of an oxidatively resistant ligand 45
3 The water-nucleophilic attack mechanism for the $Cu(pyalk)_2$ water-oxidation electrocatalyst 76
Part Two. Study of proton-coupled electron transfer by high-valent metal complexes. 105
4 Concerted Proton-Electron Transfer Oxidation of Phenols and Hydrocarbons by a High-Valent Nickel Complex 105
5 Concerted proton-electron transfer by a high-valent copper(III) complex and comparisons with an isostructural nickel(III) complex 155

List of Figures

Figure 1.1. Structure of pyalkH ligand 20

Figure 1.2. Catalytic "zone diagram" describing the relationship between catalytic wave shape and catalyst concentration C^0_p, substrate concentration C^0_A, scan rate υ, and rate constant for homogeneous electron transfer k_e 22

Figure 1.3. Transformation of the Cp*Ir(pyalk)(Cl) precatalyst to the proposed active catalyst of the "blue solution" 25

Figure 1.4. Structure of manganese-based water oxidation catalysts: the Mn-terpy dimer and the Mn-bipyalk dimer. 26

Figure 1.5. Proposed structures of $Cu(bpy)(OH)_2$ electrocatalyst and its derivatives discussed in this work 27

Figure 1.6. Structures of Cu-obpa catalysts and derivatives and structure of porphyrin catalyst. 28

Figure 1.7. Binuclear copper electrocatalysts discussed in this work, $[Cu_2(BPMAN)(\mu\text{-}OH)]^{3+}$ and $[[(Me_2TMPA)Cu(II)]_2\text{-}(\mu\text{-}OH)_2](OTf)_2$ 29

Figure 1.8. Stepwise and concerted mechanisms of proton-coupled electron transfer 33

Figure 1.9. Structure of [*cis*-$Ru^{IV}(bpy)_2(py)(O)]^{2+}$ and plot of ln(k) vs. substrate BDE for hydrocarbon substrates 34

Figure 1.10. Structures of Fe^{III}(Hbim), $RuCOO^-$, and $RuPhCOO^-$ 35

Figure 1.11. Structures of $([Mn(H_3buea)]^{2-}$ and $[Mn(H_3buea(O)]^-$ reported by Borovik and coworkers 36

Figure 1.12. Structure of the copper(III) complex reported by Tolman and coworkers, $Cu(pyN_2^{R2})$ 37

Figure 1.13. Structure of the Ni(III) complexes reported by McDonald and coworkers, $Ni(pyN_2^{Me2})(X)$ 38

Figure 2.1. Structures of pyalk ligand, $Cu(pyalkH)_2(Cl)^+$, and $Cu(pyalk)_2$ 46

Figure 2.2. Structures and UV-Visible spectra of **1** and **2** 47

Figure 2.3. Treatment of **2** with increasing equivalents of 1 M HCl to regenerate **1** 48

Figure 2.4. CV of **2** in 0.1 M KNO_3/0.1 M KOH at pH 8 and pH 13.3 49

Figure 2.5. Oxygen evolution by **2** at various pH values 50

Figure 2.6. Oxygen evolution and catalytic current by **2** over the course of 12 hours of controlled potential electrolysis 51

Figure 2.7. SEM and EDX analysis of working electrode following bulk electrolysis 52

Figure 2.8. Plot of O_2 produced vs. time for a 1 mM aqueous solution of **2** upon addition of 3% H_2O_2 solution 54

Figure 2.9. UV-Visible and molar absorptivity data for **2** 59

Figure 2.10. pH dependence of the peak of the catalytic wave 60

Figure 2.11. CV of 1 mM **2** in 0.1 M KNO_3 adjusted to pH 12.5 with 0.1 M KOH 60

Figure 2.12. Scan rate dependence of peak current of $Cu^{II/I}$ couple in water 61

Figure 2.13. Full oxygen evolution and chronoamperometry traces for water oxidation electrocatalysis by **2**, as measured by the Clark electrode 61

Figure 2.14. UV-visible measurement of **2** in 0.1 M KNO_3/0.1 M KOH at pH 12.5 before and after 12 h CPE 62

Figure 2.15. Rinse test of **2** 62

Figure 2.16. CV of 2 mM $Cu(SO_4)_2$ in 0.1 M KNO_3/KOH at pH 12.5 63

Figure 2.17. Original CV of $Cu(pic)_2$ and CV of the isolated solid in 0.1 M KNO_3 adjusted to pH 12.5 63

Figure 2.18. CV comparison of **2**, $Cu(pic)_2$, and homemade $Cu(OH)_2$ in 0.1 M KNO_3/KOH at pH 12.5 64

Figure 2.19. FTIR spectra of the precipitate collected from electrochemical studies on $Cu(picolinate)_2$ ("precipitate"), homemade $Cu(OH)_2$, and KNO_3 64

Figure 2.20. FTIR spectra of the precipitate collected from electrochemical studies on $Cu(picolinate)_2$ ("precipitate"), $Cu(picolinate)_2$, and picolinic acid 65

Figure 2.21. Concentration dependence of the catalytic wave at 1.1 V at pH 12.5 with an ITO working electrode in 0.1 M KNO_3/0.1 M KOH 65

Figure 2.22. Plot of the ratio of the catalytic current at 1.1 V to the peak current for the Cu(II/I) couple vs. $\nu^{-1/2}$ 66

Figure 2.23. Thermal ellipsoid diagram for **1** with complete numbering scheme 66

Figure 2.24. Hybrid diagram for **1** with thermal ellipsoid plot and contour electron density difference map 67

Figure 2.25. Thermal ellipsoid diagram of **2** with complete numbering scheme 69

Figure 2.26. Thermal ellipsoid diagram of **3** with complete numbering scheme 71

Figure 3.1. The structure of the proposed active water-oxidation electrocatalyst: *cis* $Cu^{II}(pyalk)_2$, **(2)** 77

Figure 3.2. Computed UV-Vis spectra for *trans* (**1**) and *cis* (**2**) as compared to the experimental spectrum of a 2 mM sample in water. 79

Figure 3.3. DFT optimized structures of **1** and **2** 81

Figure 3.4. DFT optimized structures of intermediates **3** and **4** as well as the ion pair and transition states 82

Figure 3.5. DFT optimized structures of intermediate **5**-**8** as well as transition state **5-TS** 83

Figure 3.6. Potential energy surface for the water-oxidation reaction catalyzed by (**2**) under E = 0 V vs. NHE and operating condition defined as E = 2.0 V vs. NHE 85

Figure 3.7. Structure of complex **9** Cu^{II}(bipydialk) 86

Figure 3.8. CV of **9** with and without KOH 87

Figure 3.9. Linear sweep voltammogram of 2 mM **1** in 0.1 M KNO_3 adjusted to pH 13 with 0.1 M KOH 87

Figure 3.10. Cyclic voltammograms of 0.5 mM **1** with [NaOH] = [NaOD] = 0.01 M 90

Figure 3.11. ^{1}H NMR spectrum of 2,2'-([2,2'-bipyridine]-6,6'-diyl)bis(propan-2-ol). 94

Figure 3.12. FTIR spectra of bipydialkH_2 and Cu(bipydialk) 95

Figure 3.13. Linear regression of foot-of-the-wave data used to determine k_1 96

Figure 3.14. Relaxed energy scan for triplet oxygen evolution from **7**. 96

Figure 3.15. Potential energy surface for the water-oxidation reaction catalyzed by (**2**) under E = 0 vs. NHE and operating condition defined by E = 1.8 V vs. NHE as computed with B3LYP..... 97

Figure 3.16. Structures of the additional intermediate (A) and transition state (A-TS) after the proton transfer..... 97

Figure 3.17. Thermal ellipsoid diagram for **9** with complete numbering scheme 100

Figure 4.1. X-ray crystal structure and cyclic voltammogram of $Ni(pyalk)_2$ (**1**)..... 106

Figure 4.2. Experimental and simulated EPR spectrum of **2** taken in CH_2Cl_2/toluene at 77 K and XPS spectrum of **2** and **1** 107

Figure 4.3. X-ray crystal structure of **3** and experimental and simulated EPR spectrum of **3** in CH_2Cl_2/pyridine at -80 °C. 109

Figure 4.4. UV-visible spectrum of **2** before and after addition of excess tri-tert-butylphenol 110

Figure 4.5. Representative UV-visible spectra as a function of time for the reaction of **2** with 4-X-2,6-DTBP in CH_2Cl_2 111

Figure 4.6. Hammett plot and plot of $\log(k_2)$ vs. BDE for the reaction of **2** with 4-X-2,6-DTBP substrates..... 112

Figure 4.7. Representative time trace of the absorbance at λ = 610 nm for the reaction of **2** with 2-6-DTBP-H, 2,6-DTBP-D, and plot of k_{obs} vs. concentration for 2,6-DTBP-H and 2,6-DTBP-D substrates..... 112

Figure 4.8. Plot of $\log(k_2)$ vs. bond dissociation enthalpy) for the reaction of **2** with hydrocarbon substrates..... 114

Figure 4.9. Structure of $[Ni(pyalkH)_2]^{2+}$ (**4**) and X-ray crystal structure of $Ni(pyalkH)_2(OAc)_2$ (**5**) 115

Figure 4.10. Cyclic voltammogram of **4** in MeCN..... 117

Figure 4.11. UV-visible spectrum of **3** in the absence and presence of excess pyridine 124

Figure 4.12 Actual and theoretical HRMS spectra of $Ni(pyalk)_2$ (**1**) and $[Ni(pyalk)_2]^+$ (**2**) in positive mode 125

Figure 4.13. ^1H NMR spectrum of a 5mM solution of **1** and **2** in CD_2Cl_2. 126

Figure 4.14. GC-MS spectrum of the products of the reaction between **2** and 2,6-DTBP. 127

Figure 4.15. Representative traces of the absorbance at λ = 610 nm as a function of time for four of the phenol substrates under pseudo-first order conditions. 127

Figure 4.16. Representative fits of the absorbance at λ = 610 nm of two of these phenol substrates: 4-Me-2,6-DTBP and 4-^{t}Bu-2,6-DTBP 128

Figure 4.17. Plot of k_{obs} vs. concentration the pseudo-first order reaction of **2** with 2,6-di-tert-butylphenol in CH_2Cl_2 at 25 °C..... 128

Figure 4.18. Plot of k_{obs} vs. concentration for the pseudo-first order reaction of **2** with 2,6-di-tert-butylphenol-D in CH_2Cl_2 at 25 °C 128

Figure 4.19. Plot of k_{obs} vs. concentration for the pseudo-first order reaction of **2** with 4-OMe-2,6-di-tert-butyl-phenol in CH_2Cl_2 at 25 °C 129

Figure 4.20. Plot of k_{obs} vs. concentration for the pseudo-first order reaction of **2** with 2,4,6-tri-tert-butylphenol in CH_2Cl_2 at 25 °C 129

Figure 4.21. Plot of k_{obs} vs. concentration for the pseudo-first order reaction of **2** with 4-methyl-2,6-di-tert-butylphenol in CH_2Cl_2 at 25 °C 130

Figure 4.22. Plot of k_{obs} vs. concentration for the pseudo-first order reaction of **2** with 4-Br-2,6-di-tert-butylphenol in CH_2Cl_2 at 25 °C 130

Figure 4.23. Plot of k_{obs} vs. concentration for the pseudo-first order reaction of **2** with 4-CN-2,6-di-tert-butylphenol in CH_2Cl_2 at 25 °C 131

Figure 4.24. Plots of log(k_2) vs. substrate pK_a and log(k_2) vs. substrate redox potential 131

Figure 4.25. Plot of log(k_2) vs. substrate BDFE in CH_2Cl_2 132

Figure 4.26. Plot of log$(k_2)_{DMSO}$ vs. substrate BDE and plot of log$(k_2)_{DMSO}$ vs. substrate BDFE. 133

Figure 4.27. ^{1}H NMR spectrum of the reaction of a 1 mM solution of dihydroanthracene with a 1 mM solution of **2** and proposed mechanism for the 2 H^+/2 e^- oxidation of 9,10-dihydroanthracene to anthracene by 2 equivalents of **2**. 134

Figure 4.28. Representative fits of the absorbance at λ = 610 nm as a function of time for two hydrocarbon substrates: dihydroanthracene and fluorene 135

Figure 4.29. Plot of k_{obs} vs. concentration for the reaction of **2** with 1,4-cyclohexadiene in CH_2Cl_2 at 25 °C 135

Figure 4.30. Plot of k_{obs} vs. concentration for the reaction of **2** with dihydroanthracene in CH_2Cl_2 at 25 °C 136

Figure 4.31. Plot of k_{obs} vs. concentration for the reaction of **2** with dihydroanthracene-d_4 in CH_2Cl_2 at 25 °C 136

Figure 4.32. Plot of k_{obs} vs. concentration for the reaction of **2** with fluorene in CH_2Cl_2 at 25 °C. 137

Figure 4.33. Plot of k_{obs} vs. concentration for the reaction of **2** with diphenylmethane in CH_2Cl_2 at 25 °C 137

Figure 4.34. Plot of k_{obs} vs. concentration for the reaction of **2** with tetrahydrofuran (THF) in CH_2Cl_2 at 25 °C 138

Figure 4.35. Representative fitting of pseudo-first order reaction between **2** and THF by method of initial rates 138

Figure 4.36. Plots of log(k_2) vs. substrate redox potential and log(k_2) vs. substrate pK_a 139

Figure 4.37. Representative time trace of the absorbance at λ = 600 nm for the reaction of **1** with dihydroanthracene (DHA) and DHA-d_4, and plot of k_{obs} vs. concentration for the reaction of **2** with DHA and DHA-d_4 139

Figure 4.38. ^{1}H NMR spectrum of **4**, [(Ni)(pyalkH)$_2$][2(BAr^F)] in CD_2Cl_2 140

Figure 4.39. Representative UV-visible spectra of a titration of **4** with DBU and linearized titration plot for the conversion of **4** to **1** 141

Figure 4.40. Thermal ellipsoid diagram for **1** with complete numbering scheme 145

Figure 4.41. Thermal ellipsoid diagram for **3** with complete numbering scheme 147

Figure 4.42. Thermal ellipsoid diagram for **5** with complete numbering scheme 149

Figure 5.1. XPS spectrum of **1** and **2**. 158

Figure 5.2. X-ray crystal structure of **2**. Atoms are displayed at the 50% probability level. 159

Figure 5.3. Representative UV-Visible spectra as a function of time, typical plot of absorbance at 430 nm vs. time, and plot of k_{obs} vs. substrate concentration for the reaction of **2** with 2,6-di-tert-butylphenol. 162

Figure 5.4. Plot of log(k) vs. hydrocarbon substrate bond dissociation enthalpy. 163

Figure 5.5. Thermochemical square scheme for stepwise vs. concerted proton-electron transfer for the copper compounds described in this work 164

Figure 5.6. UV-Visible spectrum of **1** and **2** in CH_2Cl_2. 173

Figure 5.7. High resolution mass spectrum of **2** and calculated spectrum 173

Figure 5.8. UV-Visible spectra of the reaction of **1** with tris(4-bromophenyl)ammoniumyl hexachloroantimonate to form **2** at 25 °C in CH_2Cl_2 over several minutes 174

Figure 5.9. Plot of the absorbance at 420 nm vs. time for the reaction of **1** with tris(4-bromophenyl)ammoniumyl hexachloroantimonate to form **2** at -40 °C in CH_2Cl_2 over the course of 1.5 hours 174

Figure 5.10. Representative fit of absorbance at λ = 420 nm vs. time for the reaction of **2** with 2,6-di-tert-butylphenol at -40 °C 175

Figure 5.11. Plot of k_{obs} vs. concentration for the reaction of **2** with 2,6-di-tert-butylphenol at -40 °C 175

Figure 5.12.^{1}H NMR spectrum of reaction of **2** with 2 equivalents 9,10-dihydroanthracene at -78 °C 176

Figure 5.13. Representative fit of absorbance at λ = 420 nm vs. time for the reaction of **2** with 9,10-dihydroanthracene at -40 °C 176

Figure 5.14. Plot of k_{obs} vs. concentration for the reaction of **2** with 9,10-dihydroanthracene at -40 °C 177

Figure 5.15. Representative fit of absorbance at λ = 420 nm vs. time for the reaction of **2** with 1,4-cyclohexadiene at -40 °C 177

Figure 5.16. Plot of k_{obs} vs. concentration for the reaction of **2** with 1,4-cyclohexadiene..... 178

Figure 5.17. Representative fit of absorbance at λ = 420 nm vs. time for the reaction of **2** with fluorene at -40 °C 178

Figure 5.18. Plot of k_{obs} vs. concentration for the reaction of **2** with fluorene at -40 °C 179

Figure 5.19. Representative fit of absorbance at λ = 420 nm vs. time for the reaction of **2** with diphenylmethane at -40 °C 179

Figure 5.20. Plot of k_{obs} vs. concentration for the reaction of **2** with diphenylmethane at -40 °C 180

Figure 5.21. Representative fit of absorbance at λ = 420 nm vs. time for the reaction of **2** with tetrahydrofuran (THF) at -40 °C 180

Figure 5.22. Plot of k_{obs} vs. concentration for the reaction of **2** with tetrahydrofuran (THF) at -40 °C 181

Figure 5.23. log(k) vs. $E_{1/2}$ data for the reaction of **2** hydrocarbon substrates 181

Figure 5.24. Plot of log(k) vs. pK_a for the reaction of **2** with hydrocarbon substrates..... 182

Figure 5.25. Plots of k_{obs} vs, concentration for the reaction of **2** with 9,10-dihydroanthracene and deuterated 9,10-dihydroanthracene 183

Figure 5.26. UV-Visible spectrum of copper-containing species after the reaction of **2** with 10 equivalents of 9,10-dihydroanthracene 183

Figure 5.27. CVs of **1** and **1H** in acetonitrile 184

Figure 5.28. Representative UV-Visible titration of **1** with acetic acid 184

Figure 5.29. Linearized titration plot for the conversion of **1** to **1H**..... 185

Figure 5.30. Representative fit of absorbance at λ = 600 nm vs. time for the reaction of **4** with 2,6-di-tert-butylphenol at -40 °C 185

Figure 5.31. Plot of k_{obs} vs. concentration for the reaction of **4** with 2,6-di-tert-butylphenol at -40 °C 186

Figure 5.32. Representative fit of absorbance at λ = 420 nm vs. time for the reaction of **2** with 9,10-diyhdroanthracene at -60 °C 186

Figure 5.33. Plot of k_{obs} vs. concentration for the reaction of **2** with 9,10-dihydroanthracene at -60 °C 187

Figure 5.34. Representative fit of absorbance at λ = 420 nm vs. time for the reaction of **2** with 9,10-diyhdroanthracene at -30 °C 187

Figure 5.35. Plot of k_{obs} vs. concentration for the reaction of **2** with 9,10-dihydroanthracene at -30 °C 188

Figure 5.36. Representative fit of absorbance at λ = 420 nm vs. time for the reaction of **2** with 9,10-diyhdroanthracene at -15 °C 188

Figure 5.37. Plot of k_{obs} vs. concentration for the reaction of **2** with 9,10-dihydroanthracene at -15 °C 189

Figure 5.38. Plot of ln(k/T) vs. 1/T for the reaction of **2** with 9,10-dihydroanthracene. 189

Figure 5.39. Representative fits of the decay of the absorbance at λ = 600 nm vs. time for the reaction of **4** with 9,10-diyhdroanthracene at various temperatures. 190

Figure 5.40. Plot of ln(k/T) vs. 1/T for the reaction of **4** with 9,10-dihydroanthracene 190

Figure 5.41. Representative fit of absorbance at λ = 420 nm vs. time for the reaction of **2** with 2,6-di-tert-butlyphenol (DTBP) at -30 °C 191

Figure 5.42. Plot of k_{obs} vs. concentration for the reaction of **2** with 2,6-di-tert-butlyphenol at -30 °C 191

Figure 5.43. Representative fit of absorbance at λ = 420 nm vs. time for the reaction of **2** with 2,6-di-tert-butlyphenol at -50 °C 192

Figure 5.44. Plot of k_{obs} vs. concentration for the reaction of **2** with 2,6-di-tert-butlyphenol at -50 °C 192

Figure 5.45. Representative fit of absorbance at λ = 420 nm vs. time for the reaction of **2** with 2,6-di-tert-butlyphenol at -60 °C 193

Figure 5.46. Plot of k_{obs} vs. concentration for the reaction of **2** with 2,6-di-tert-butlyphenol at -60 °C 193

Figure 5.47. Plot of ln(k/T) vs. 1/T for the reaction of **2** with 2,6-di-tert-butylphenol. Activation enthalpy and entropy parameters were extracted from the slope and y-intercept of the fit 194

Figure 5.48. Representative fit of absorbance at λ = 420 nm vs. time for the reaction of **4** with 2,6-di-tert-butlyphenol at 0 °C 194

Figure 5.49. Plot of k_{obs} vs. concentration for the reaction of **4** with 2,6-di-tert-butlyphenol at 0 °C 195

Figure 5.50. Representative fit of absorbance at λ = 420 nm vs. time for the reaction of **4** with 2,6-di-tert-butlyphenol at -20 °C 195

Figure 5.51. Plot of k_{obs} vs. concentration for the reaction of **4** with 2,6-di-tert-butlyphenol at -20 °C 196

Figure 5.52. Plot of ln(k/T) vs. 1/T for the reaction of **4** with 2,6-di-tert-butylphenol 196

Figure 5.53. Thermal ellipsoid diagram for **2** with complete numbering scheme 198

Figure 5.54. Thermal ellipsoid diagram for **1H$_2$** with complete numbering scheme 200

List of Tables

Table 2.1. Hydrogen bonds for **1** 67

Table 2.2. Crystal data and structure refinement for **1** 68

Table 2.3. Crystal data and structure refinement for **2** 70

Table 2.4. Crystal data and structure refinement for **3** 72

Table 3.1. Average theoretical bond lengths, bond angles, and dihedrals of **1** (without hydrogen-bonding waters) in the gas phase as compared to experimental values 78

Table 3.2 Literature values for H/D kinetic isotope effectsfor molecular copper water-oxidation catalysts. 89

Table 3.3. $<S^2>$ values for all doublet minima as well as Mulliken spin densities for the Cu center and the oxyl radical oxygen O1 or the nucleophilic water oxygen O2 98

Table 3.4. Crystal data and structure refinement for **9** 101

Table 4.1. Thermodynamic and kinetic parameters of high-valent metal compounds capable of performing CPET with hydrocarbon substrates 117

Table 4.2. Summary of kinetic and thermodynamic parameters used for analysis of the reaction of **2** with substituted phenols..... 132

Table 4.3. Summary of thermodynamic and kinetic parameters in our analysis of the reaction of **2** with hydrocarbon substrates 139

Table 4.4. Comparison of bond lengths between nickel in various oxidation states and the pyalk oxygen for several compounds discussed in this report 141

Table 4.5. Solvent parameters used in this analysis 142

Table 4.6. Crystal data and structure refinement for **1** 146

Table 4.7. Crystal data and structure refinement for **3** 148

Table 4.8. Crystal data and structure refinement for **5** 150

Table 5.1. Relevant bond lengths and angles from the X-ray crystal structures of **1**, **1H$_2$**, and **2** 159

Table 5.2. Thermodynamic and kinetic parameters of high-valent metal compounds capable of performing CPET with hydrocarbon substrates 165

Table 5.3. Comparison of rate constant (k) values, activation energy parameters, and bond strengths for **2** and **4** 166

Table 5.4. Summary of thermodynamic and kinetic parameters in our analysis of the reaction of **2** with hydrocarbon substrates at -40 °C..... 182

Table 5.5. Data used for asynchronicity factor (η) calculations in **Equation 5.3**..... 197

Table 5.6. Crystal data and structure refinement for **2** 199

Table 5.7. Crystal data and structure refinement for **1H$_2$** 201

List of Schemes

Scheme 3.1. Mechanism of water oxidation catalyzed by the complex Cu(pyalk)$_2$ **(1)** 80

Scheme 3.2. Water-nucleophilic attack (WNA) mechanism onto the oxyl radical of (**5**) to form (**6**) upon proton transfer to the pyalk ligand 84

Scheme 3.3. Mechanism of O_2 evolution by (**7**) to form (**8**) according to the reaction mechanism of Scheme 3.1 85

Scheme 3.4. Synthetic route for the preparation of the bipydialk ligand 93

Scheme 3.5. Synthetic route for the preparation of **9** 94

Scheme 4.1. Synthetic route for preparation of $Ni^{II}(pyalk)_2$ (**1**) and $Ni^{III}(pyalk)_2^+$ (**2**) 107

Scheme 4.2. Proposed PCET pathway for oxidation of phenols by **2** 109

Scheme 4.3. Thermochemical square scheme for stepwise vs. concerted proton and electron transfer to the complexes described in this work 116

Scheme 5.1. Metal pyalk compounds discussed in this work in their reduced and oxidized states 156

Scheme 5.2. Preparation of **2** by oxidation of **1** with tris(4-bromophenyl)ammoniumyl hexachloroantimonate at -40 °C in CH_2Cl_2 157

Scheme 5.3. Proposed PCET pathway for oxidation of phenols by $Cu(pyalk)_2^+$ 161

1 Chapter 1. Introduction

1.1 Energy Conversion and Storage

The recent sharp rise in atmospheric CO_2 levels has necessitated the development of carbon-neutral energy sources in order to meet the world's growing energy demand[1] without further impacting the Earth's climate and environment.[2] Over the past several decades, numerous methods of generating electricity from renewable, carbon-free resources have been developed, including wind and solar power. However, many such renewable energy sources provide energy only intermittently. Silicon-based photovoltaics, for instance, only produce electricity when they are directly illuminated by the sun, and wind energy is only generated when the wind is actively blowing. Therefore, to meet the global energy demand using exclusively renewable resources, the energy produced from these sources must be stored for use when it cannot be generated directly. One promising solution to this problem involves storing energy in the form of chemical bonds, which results in fuels that can be used on-demand.[3]

One approach to generating fuel from renewable resources is through "artificial photosynthesis,"[4-5] which utilizes sunlight to split water and generate O_2, protons, and electrons, as shown in **Equation 1.1**.

$$2H_2O \rightarrow O_2 + 4H^+ + 4e^- \qquad \textbf{(Equation 1.1)}$$

In an artificial photosynthetic system, a photosensitizer is used to harvest sunlight, resulting in photoexcitation followed by charge separation, at which point excited electrons are injected into a semiconductor material such as TiO_2 or SnO_2.[6-8] A neighboring water-oxidation catalyst then reduces the photosensitizer, resulting in oxidation of the catalyst by one electron. After four successive oxidation events, the catalyst can facilitate the oxidation of water. The protons and electrons generated in the water-oxidation process can then be used to form fuel in a fuel cell, allowing energy to be stored in the chemical bonds of the fuel until it is needed. Common fuels proposed for such fuel cells include hydrogen, methanol, and formic acid, although the formation of more complex hydrocarbon fuels, such as ethanol, is an area of active research.[9]

One major challenge in the development of artificial synthetic devices is efficiently and quickly oxidizing water. This thermodynamically and kinetically challenging reaction has a standard potential of 1.23 V at pH 0 but often requires additional potential beyond the thermodynamic requirements, also known as overpotential, to drive the reaction. One possible solution to this problem is the design of water-oxidation catalysts, which can lower this energy barrier.[10]

1.2 Molecular Water-Oxidation Catalysis

There has been considerable research into the design and study of water-oxidation catalysts that could be used in artificial photosynthetic systems.[11-13] Catalysts for the water-oxidation transformation generally fall into one of two categories: heterogeneous or homogeneous.[14] In heterogeneous catalysis, the reaction occurs at the interface of a solid material, while in a homogeneous system, the reaction is facilitated by molecules dissolved in solution. Heterogeneous catalysts are generally considered advantageous due to their ease of separation from reactants and products as well as their recyclability, but they often suffer from low tunability and selectivity. While less practical for use in solar fuels devices than their heterogeneous counterparts, homogeneous molecular water-oxidation catalysts are of particular interest in research because of their ease of study and tunability.[11] Molecular catalysts incorporate ligands that can be easily and precisely altered to modify their activity. These species can be readily studied by standard spectroscopic techniques, and study of individual reaction steps can provide information about the catalytic mechanism, allowing for a degree of understanding and control that is often not possible in heterogeneous species, which usually contain diverse types of surface sites. In addition, molecular catalysts can often be attached to surfaces through covalent bonds or electrostatic interactions, allowing them to be easily separated from reactants and products while still maintaining many of the advantages of homogeneous systems.[15-17]

1.2.1 Ligand design

An important consideration in the design of molecular catalysts is the design of the ligand itself. The chelating “pyalk” ligand (pyalk = 2-(2′-pyridyl)-2-propanoate) developed by our group

(**Figure 1.1**) possesses multiple features that are beneficial for catalysis, including the strongly donating alkoxide group formed upon deprotonation of the ligand, which can stabilize high-valent metal states. Additionally, the gem-dimethyl substitution at the benzylic position protects the vulnerable benzylic site from oxidation and degradation.[18] For these reasons, it is particularly suitable for water-oxidation catalysis and high-oxidation state chemistry. Pyalk and its derivatives have been used to stabilize a number of iridium- and manganese-based water-oxidation catalysts,[19-21] as described in the following sections, and it has also been used to stabilize highly oxidized rhodium(IV)[22] and iridium(V) species.[23-25]

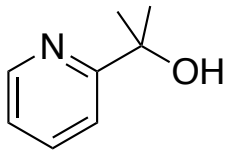

Figure 1.1. Structure of pyalkH ligand. When the alcohol group is deprotonated upon metalation or reaction with base, the strongly donating alkoxide unit is formed.

1.2.2 Understanding molecular electrocatalysis

Catalytic water-oxidation systems can be driven by a chemical oxidant or applied potential. Catalysts driven by applied potential, known as “electrocatalysts”, are oxidized at an electrode surface to generate a catalytically active species, which then performs the water-oxidation reaction in solution.[26] Driving catalytic reactions electrochemically is of particular interest as it avoids the use of harsh, stoichiometric oxidation reagents, which themselves may play a non-innocent role in catalysis.[27] Additionally, catalysts driven electrochemically are able to operate through single-electron steps, which is necessary for use in solar fuels devices.[15, 28]

1.2.2.1 Probing electrocatalysis through cyclic voltammetry

Electrocatalysis is most often probed through an electrochemical technique known as cyclic voltammetry (CV). In this technique, a working electrode is poised at an initial potential and sweeps out to more positive or negative potential at a given rate, called the scan rate (v). Once the electrode reaches the switching potential, it sweeps back in the reverse direction until reaching an end point. This technique can be used to investigate electron-transfer events by species in solution.

A brief description of the technique as it relates to electrocatalysis is provided, and more thorough treatments and theoretical background can be found in references 29-30.

In the absence of substrate, a molecular catalyst will generally undergo a one-electron redox event, which can be examined by CV. For the sake of example, consider a molecular species P that can be oxidized by one-electron to form species Q. At the beginning of the CV, the potential will be poised below the potential at which P can be oxidized, and only background capacitive current will be observed. As the potential becomes sufficiently positive to begin oxidizing P to Q, current will begin to flow, and the concentration P at the electrode will begin to be depleted as Q is formed. The amounts of species P and Q at the electrode surface at any given potential can be found from the Nernst equation (**Equation 1.2**), which relates the applied potential (E) to the formal potential for the oxidation of P to Q ($E^{o\prime}$) and the concentrations of the reduced and oxidized species P and Q.[31]

$$E = E^{o\prime} + 2.303\frac{RT}{F}\, log_{10}\frac{[Q]}{[P]} \qquad \textbf{(Equation 1.2)}$$

As the electrode scans to even more oxidizing potentials, the amount of P at the electrode is further depleted and the current begins to fall, resulting in a peaked wave. When the electrode reaches its switching potential, it begins scanning in the cathodic direction, and the Q present at the electrode surface is reduced by one electron back to P. Due to diffusion of the species to and from the electrode, the reverse cathodic peak will be slightly separated from the initial anodic peak. The halfway point between the anodic and cathodic peak is known as $E_{1/2}$, which is often estimated as the formal potential $E^{o\prime}$.

In the presence of substrate, the catalyst's CV response will look considerably different than the reversible one-electron event observed in the absence of substrate. Under these conditions, when P is oxidized by one electron, it can react with substrate in solution. Once the catalytic cycle is complete, P is regenerated and can be re-oxidized at the electrode. This cycle results in enhanced current relative to the reversible one-electron oxidation event, as well as a loss of reversibility of the observed wave in many cases. The catalytic wave may have different shapes depending on the catalyst and substrate concentrations, scan rate, and the intrinsic catalytic rate

constant. The shapes that may be observed and how they relate to these parameters are shown in **Figure 1.2**. For a more detailed explanation of this "zone diagram", see references 26 and 30.

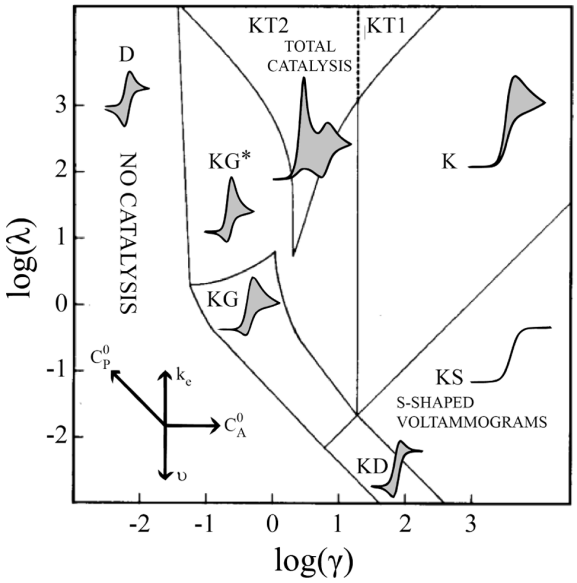

Figure 1.2. Catalytic "zone diagram" describing the relationship between catalytic wave shape and catalyst concentration C^0_P, substrate concentration C^0_A, scan rate υ, and rate constant for homogeneous electron transfer k_e Reprinted with permission from ref. 30. Copyright 2014 American Chemical Society.

1.2.2.2 Benchmarking molecular electrocatalysts

In both homogeneous and heterogeneous catalysis, it is important to understand catalyst parameters relating to efficiency and speed. These values can be used to compare catalysts. Described below are values commonly used to benchmark electrocatalysts for water oxidation.

Overpotential. The water-oxidation reaction has a thermodynamic potential of 1.23 V vs. NHE at pH 0 and shifts by -59 mV per additional pH unit. In addition to the thermodynamic potential, an overpotential (η) is required to overcome activation energy barriers and drive the kinetics of the reaction.

$$\eta = E_{app} - E_{O_2/H_2O} \qquad \textbf{(Equation 1.3)}$$

The overpotential required for catalysis is defined as the amount of potential in excess of the thermodynamic potential required for catalysis to occur, and the value of the overpotential can be found using **Equation 1.3** above. In this equation, E_{app} refers to the potential applied to drive

water oxidation, and E_{O_2/H_2O} is the thermodynamic potential for water oxidation under the catalytic conditions of interest. For a homogeneous molecular electrocatalyst, the potential at which half of the peak catalytic current is achieved is generally used for E_{app}.[32] This value, known as $E_{p/2}$, is generally considered the most precise value for determining overpotential from a catalytic CV. Overpotentials are sometimes instead reported based on onset potential at the base of the catalytic wave, which can be challenging to define, or peak potential, which can vary based on conditions such as scan rate.

Turnover frequency. Turnover frequency, also known as the catalytic rate, is the measure of how much product is formed per catalyst center per unit time. For an electrocatalytic species, the catalytic rate constant, k_{cat}, can be found from CV measurements using the following equation:[31]

$$i_c = n_{cat} FACD^{1/2} k_{cat}^{1/2} \quad \textbf{(Equation 1.4)}$$

In **Equation 1.4,** i_c refers to the catalytic current, n_{cat} is the number of electrons transferred in the catalytic reaction (4 for water oxidation), F is Faraday's constant, A is the surface area of the electrode, C is catalyst concentration, D is the diffusion coefficient for the catalyst, and k_{cat} is the observed rate constant, also known as the turnover frequency. In order to use this equation directly to find k_{cat}, however, it is necessary to know the electrode surface area, which may be greater than just the geometric surface area, and the diffusion coefficient for the molecule, which must be measured separately. By normalizing **Equation 1.4** to the peak current of a non-catalytic reversible couple (**Equation 1.5**), these variables can be removed, resulting in **Equation 1.6**:[31]

$$i_p = 0.4633 n_p FAC\left(\frac{n_p F \nu D}{RT}\right)^{1/2} \quad \textbf{(Equation 1.5)}$$

$$\frac{i_c}{i_p} = 0.359 \frac{n_{cat}}{(n_p)^{3/2}} \sqrt{k_{cat}/\nu} \quad \textbf{(Equation 1.6)}$$

In **Equations 1.5** and **1.6**, i_p refers to the peak current of the reversible, non-catalytic wave present in the absence of substrate, n_p refers to the number of electrons transferred in the reversible process, ν is the scan rate, R is the ideal gas constant, and T is the temperature.

It should be noted that these measurements must be made under conditions where the catalytic current is not limited by diffusion.[30, 33] In practical terms, the catalytic CV's should be S-shaped (Zone KS in **Figure 1.2**), and the plateau current should be independent of scan rate.

Faradaic efficiency. Faradaic efficiency compares the charged passed during electrocatalysis to the amount of substrate consumed or product formed, as shown in **Equation 1.7**.[34] In essence, it is a measure of the catalyst's selectivity under electrocatalytic conditions.

$$FE = \frac{F * n_{product} * z}{Q} \times 100\% \qquad \textbf{(Equation 1.7)}$$

In **Equation 1.7**, $n_{product}$ refers to the number of moles of products formed, Q is the total charged passed, z is the number of electrons required for the catalytic reaction (4 for water oxidation), and F is Faraday's constant.

High faradaic efficiency indicates that most or all of the charge passed is used to form the product of interest. A low faradaic efficiency is indicative of competing reactivity, either due to formation of another product (such as hydrogen peroxide in the case of water oxidation) or oxidation of other substrates, such as solvent or an organic ligand.

1.2.3 Water-oxidation catalysis with iridium and manganese

Many of the first reported molecular water-oxidation catalysts utilized precious metals, such as iridium and ruthenium. The first reported example of a molecular water-oxidation catalyst was the "blue dimer" from T. J. Meyer's group in 1982,[35-36] and following that report, numerous other precious metal water-oxidation catalysts were reported. Notably, iridium water-oxidation catalysts proved to be among the fastest and most robust.[37] In 2009, our group reported a number of Cp^*Ir^{III}(chelate) compounds that proved to be long-lived and active homogeneous water-oxidation catalysts.[38-39] Further work demonstrated these compounds were, in fact, *pre*catalysts for water oxidation and that the Cp* underwent oxidative degradation under reaction conditions (**Figure 1.3**).[21, 40-41] Of all the precatalysts studied, the species incorporating pyalk as the chelate ligand generated the most active homogeneous catalytic species, dubbed the "blue solution".[21, 42-43] The identity of the active catalyst in this "blue solution" has proved difficult to structurally characterize—

^{1}H NMR results indicate that multiple non-interconverting isomers are present.[23, 44] Spectroscopic studies and work with highly-oxidized model compounds suggest that the active species of the blue solution is most likely an iridium mono-μ-oxo dimer containing one pyalk ligand per metal center.[23-25, 45]

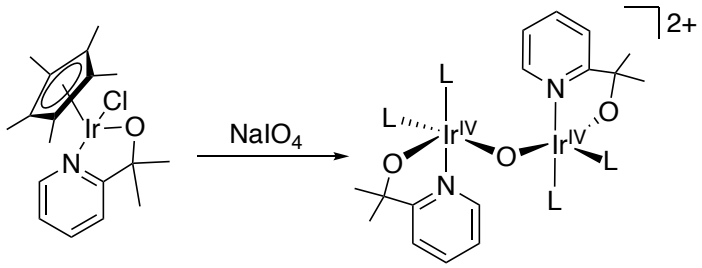

Figure 1.3. Transformation of the Cp*Ir(pyalk)(Cl) precatalyst to the proposed active catalyst of the "blue solution."

While precious metal catalysts have proven to be highly active for water oxidation, they require material that is both expensive and scarce—iridium, for example, comprises less than 0.001 parts per million of the Earth's crust and costs over $2500 per ounce as of December 2020.[46-47] As such, there is much interest in designing water-oxidation catalysts that incorporate Earth-abundant metals for use in commercial devices. Due to its relevance to the oxygen-evolving complex in Photosystem II, manganese was chosen by our group as the first-row transition metal of choice for the development of new water-oxidation catalysts. In 1999, our group reported water oxidation by the dimeric manganese compound $[Mn_2O_2(terpy)_2(H_2O)_2](NO_3)_3$ (terpy = 2,2′;6′,2″-terpyridine), also known as the Mn-terpy dimer (**Figure 1.4A**).[48] Water oxidation by this complex could be driven chemically by hypochlorite[48] or Oxone (potassium peroxymonosulfate).[49] The Mn-terpy dimer proved to be one the most active Mn-based water-oxidation catalysts reported in the literature, but it suffered from low stability due to degradation in its low-valent state. Further work resulted in the development of dinuclear manganese catalysts incorporating a pyalk derivative ligand, bipyalk (bipyalkH = 2-([2,2′-bipyridin]-6-yl)propan-2-ol).[20] While the Mn-bipyalk catalyst showed slower rates of O_2 evolution compared to the Mn-terpy dimer, it also proved to be much longer lived. Follow-up studies demonstrated that the catalytically active species was $[Mn_2O_2(bipyalk)_2(H_2O)_2][OTf]_2$ (**Figure 1.4B**).[19] Despite their activity for water oxidation using

chemical oxidants, neither the Mn-terpy dimer or the Mn-bipyalk dimer showed any activity for water oxidation under electrochemical conditions, and therefore they have not yet been incorporated into artificial photosynthetic systems.

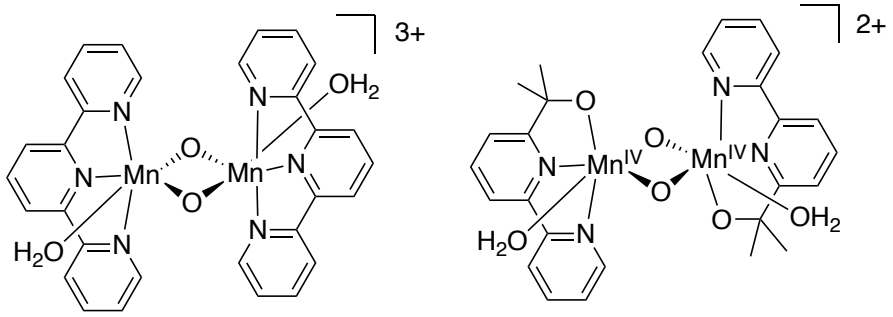

Mn-terpy dimer
(A)

Mn-bipyalk dimer
(B)

Figure 1.4. Structure of manganese-based water oxidation catalysts: the Mn-terpy dimer (A) and the Mn-bipyalk dimer (B).

1.2.4 Brief history of molecular copper-based electrocatalysts for water oxidation

Of the Earth-abundant transition metals, copper is an intriguing choice for water-oxidation catalysis due to its low cost and variety of available redox states. Copper also plays a key role in oxygen activation and transfer in several enzymatic systems.[50] The first copper-based water-oxidation electrocatalyst was reported in 2012 by Mayer and coworkers, who demonstrated that $Cu(bpy)(OH)_2$ (**Figure 1.5A**, bpy = 2,2'-bipyridine) was an active molecular electrocatalyst for water oxidation under basic conditions.[51] This catalyst operated at an overpotential of 750 mV at pH 12.8 with a turnover number of 100 s^{-1}. Follow-up work on related complexes demonstrated the influence of ligand design on catalytic performance. When one of the pyridine moieties in the bpy ligand was replaced with imidazole (**Figure 1.5C**), the overpotential was decreased to ~650 mV at pH 12, with a slightly lower turnover frequency of 35 s^{-1}.[52] This shift in overpotential was attributed to the more electron-donating nature of the imidazole ring. In another study, pendant hydroxyl groups were incorporated on to the bpy scaffold (**Figure 1.5B**), resulting in a decrease in overpotential to 510-560 mV in the pH range 12-14.[53] The decrease in overpotential was attributed

to involvement of the ligand in catalysis—by oxidizing the ligand in the second step rather than the metal, the potential required for catalysis was calculated to be lowered by ~300 mV.

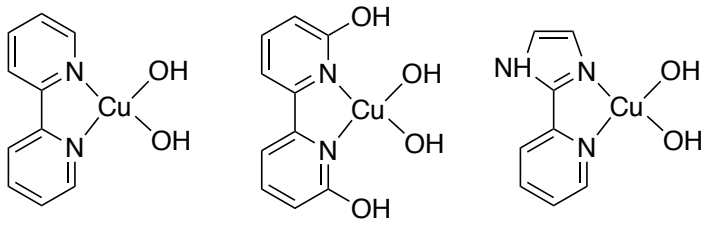

(A) **(B)** **(C)**

Figure 1.5. Proposed structures of $Cu(bpy)(OH)_2$ electrocatalyst and its derivatives discussed in this work.

Following the publication of the $Cu(bpy)(OH)_2$ catalyst, numerous other copper complexes were found to be water-oxidation electrocatalysts. While it is beyond the scope of this chapter to catalog every reported catalyst, a thorough review can be found in reference 54. Some notable examples with respect to benchmark values and mechanism are discussed in this section.

In 2014, Zhan's group reported $[Cu(obpa)]^{2-}$ (**Figure 1.6A,** obpa = o-phenylenebis(oxamato)) as an electrocatalyst for water oxidation, with an overpotential of 626 mV and turnover frequency of 1.13 s^{-1} at pH 10.8.[55] This work was later expanded by Llobet's group, who synthesized a family of modified ligands that could be used with copper to generate water-oxidation electrocatalysts (**Figure 1.6B**).[56] With these modifications to the ligands, the overpotential for catalysis could be considerably reduced to as low as 170 mV for the most electron-donating ligand (R_1=R_2=OMe). There was a noted tradeoff between catalytic rate and overpotential—the analogue that operated at the highest overpotential (700 mV) also displayed the fastest rate (3.56 s^{-1}), while the one operating at the lowest overpotential (170 mV) had the slowest rate (0.36 s^{-1}). These complexes were all proposed to operate through a single-electron transfer water-nucleophilic attack mechanism, in which the ligand played a redox non-innocent role.

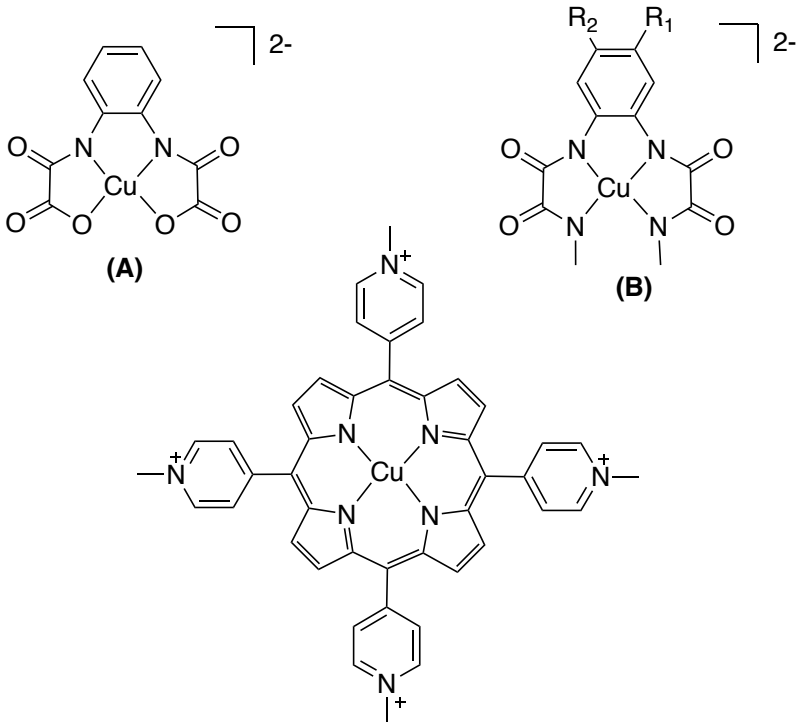

Figure 1.6. Structures of Cu-obpa catalysts and derivatives (top), and structure of porphyrin catalyst (bottom).

In 2019, Cao reported the water-soluble copper-based electrocatalyst utilizing the tetrakis(4-N-methylpyridyl)porphyrin ligand scaffold (**Figure 1.6C**). This electrocatalyst was reported to have an overpotential of 310 mV and turnover frequency of 30 s^{-1} in neutral pH solution (pH 7).[57] In addition to being one of only a handful of copper water-oxidation electrocatalysts to operate at neutral pH, this compound is proposed to operate through a mechanism involving the formation of a Cu-H_2O_2 species rather than the formation of a copper-oxyl radical, and it was postulated that this unique mechanism may be the reason the catalyst operates with such low overpotential under neutral pH conditions. Additionally, it was demonstrated that the catalyst could facilitate the $2e^-$ oxidation of water to H_2O_2 under acidic conditions.

The first dimeric copper water-oxidation electrocatalyst was $[Cu_2(BPMAN)(\mu\text{-}OH)]^{3+}$ (**Figure 1.7A**, BPMAN = 2,7-[bis(2-pyridylmethyl)aminomethyl]-1,8naphthyridine), reported by Zhang in 2015.[58] This catalyst operated at an overpotential of 780 mV with a turnover number of 0.6 s^{-1} and was also among first copper water-oxidation electrocatalysts to operate at neutral pH. Mechanistic

studies demonstrated that the complex likely generates O_2 through an intramolecular coupling mechanism. In a follow-up work, a mononuclear compound bearing the TPA ligand (TPA = tris-(pyridylmethyl)amine), the monodentate derivative of BPMAN, was tested for water-oxidation activity.[59] The authors found that the mononuclear species was competent for water-oxidation electrocatalysis, but it operated at significantly higher overpotentials and with much slower kinetics than its bimolecular counterpart. Based on DFT calculations, it was determined that the mononuclear and dinuclear catalyst operated through two different mechanisms: the single-site catalyst underwent water-nucleophilic attack, while the bimolecular species generated O_2 through an intramolecular coupling reaction. The authors hypothesized that the cooperative effects of having multiple copper centers resulted in the improved performance of the bimolecular species. In 2016, the Kieber-Emmons group also reported a dinuclear copper species capable of water-oxidation electrocatalysis, $[[(Me_2TMPA)Cu(II)]_2\text{-}(\mu\text{-}OH)_2](OTf)_2$., (**Figure 1.7B,** Me_2TMPA = bis((6-methyl-2-pyridyl)methyl)(2-pyridylmethyl)amine) and found that, regardless of whether the initial species was a mononuclear or dinuclear, catalysis proceeded through the same dinuclear species.[60]

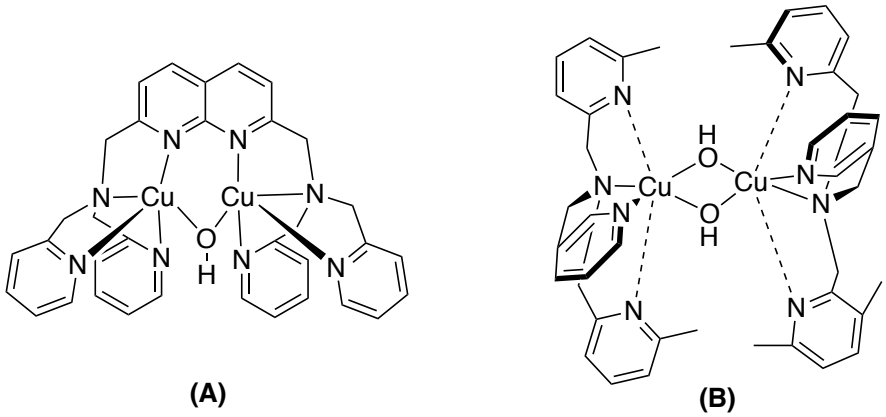

Figure 1.7. Binuclear copper electrocatalysts discussed in this work. (A) Structure of $[Cu_2(BPMAN)(\mu\text{-}OH)]^{3+}$. (B) Structure of $[[(Me_2TMPA)Cu(II)]_2\text{-}(\mu\text{-}OH)_2](OTf)_2$.

1.2.4.1 Important considerations for copper electrocatalysts

As copper is a labile metal in its low-valent states, it is important to ascertain the stability of molecular copper electrocatalysts under catalytic conditions. If a molecular complex loses its ligands in a low-valent state, or if the ligands are degraded under oxidizing conditions, copper salts

or heterogeneous copper oxides and copper hydroxide species may be formed, all of which have been shown to catalyze water oxidation electrochemically under basic conditions.[61-64] As many copper electrocatalysts for water oxidation operate at pH values above 8, such decomposition is of particular concern. Therefore, great care must be taken to ensure that the molecular species remains intact during catalysis. As only the molecules directly in contact with the electrode are active for electrocatalysis at any given time, it can be quite challenging to simply discern by eye whether or not an electrocatalyst is decomposing. The following techniques are often used to differentiate homogeneous species from heterogeneous ones.

Electrode surface analysis. The electrode surface can be probed using analytical methods to determine if heterogeneous species are present. Generally, bulk electrolysis under catalytic conditions is performed and subsequently the working electrode is gently rinsed or air-dried. The electrode surface can then be visually probed using microscopy methods such as scanning electrode microscopy (SEM). The surface composition can also be probed using energy dispersive X-ray spectroscopy (EDX), which can give insight into the elements present on the surface of the electrode, even if they cannot be observed visually.

Cyclic voltammetric methods. Cyclic voltammetry can provide insight into the nature of the active catalytic species. Common signs of decomposition of a molecular species include the presence of irreversible features directly prior to the onset of catalysis (also known as “pre-wave”) and curve-crossing on the return scan. The presence of a pre-wave is indicative of a transformation of the molecular species prior to catalysis,[65-67] while the presence of curve crossing indicates that the catalytic activity has increased over the course of the scan, suggesting a transformation to a more active species.[68] While neither feature is definitive proof of catalyst decomposition to a heterogeneous species, they do indicate that the active catalyst may not be the same as the species initially dissolved in solution, and further investigation as to the nature of the active catalyst is warranted.

Other important tests for heterogeneity that can be conducted using cyclic voltammetry include rinse tests and cycle tests. In a rinse test, CV or bulk electrolysis is performed with both the molecular catalyst and substrate in solution.[29, 67, 69-70] The working electrode is then removed from

solution, gently rinsed, and then placed into fresh solution containing only substrate, and a CV is taken. If a heterogeneous active species is present on the electrode, a catalytic wave will be observed. In a cycle test, a solution of catalyst and substrate undergoes dozens or hundreds of CV cycles and the peak current is monitored.[71] An increase in current over time may be suggestive of the formation of a heterogeneous species.

Chronoamperometry. While the formation of nanoparticles often cannot be observed directly on a CV timescale, longer time scale experiments can give insight as to whether a new species is being formed. In a typical chronoamperometry experiment, a constant potential is applied for a fixed duration of time, ranging from several minutes to several hours. During these experiments, physical decomposition of the catalyst, such as the formation of nanoparticles, may be observed. Additionally, the presence of an induction period in the current vs. time plots may also indicate the formation of a heterogeneous species.[67, 69] Such plots may show a marked increase in current with time due to the increased surface area of the heterogeneous species on the electrode. For water-oxidation catalysis, induction periods can additionally be probed using real-time gas analysis methods such as a Clark electrode. If a heterogeneous species needs to be formed before water oxidation can occur, a delay in product formation may be observed.[72-73]

Solution and in-situ methods for nanoparticle detection. In some instances, an electrocatalytically-active heterogeneous species may be formed during an experiment, but it does not adhere to the surface of the electrode and thus is not observed by SEM or other surface analysis methods. Therefore, to complement surface analysis, analysis of the catalytic solution should also be performed. Dynamic Light Scattering (DLS) is often used to probe for the presence of nanoparticles in solution.[44, 67]

Additionally, application of an oxidizing or reducing potential can generate an electrocatalytically active heterogeneous species that is unstable in the absence of applied potential. In some cases, the heterogeneous species formed under applied potential can even re-bind to the ligand framework once the applied potential is removed.[74] Therefore, it may be necessary to probe the solution for the presence of nanoparticles during electrocatalysis, not just after catalysis. In situ X-ray absorption and EXAFS measurements can be used to detect the

presence of nanoparticles or clusters under electrocatalytic conditions,[74-76] as can electrochemical quartz crystal microbalance measurements.[67, 77]

It is important to note that just one test is not sufficient for demonstrating the homogeneity of an electrocatalyst. For instance, if catalytically active nanoparticles are generated in solution but do not adhere to the electrode or decompose in the absence of applied potential, the system may pass a rinse test and SEM analysis even though the catalytically active species is not molecular. Therefore, numerous tests should be performed, and even one "failure" should be reason to suspect the formation of a heterogeneous species.

1.3 Proton-coupled electron transfer in energy conversion

Many reactions relevant to energy storage, including water oxidation, involve the transfer of both protons and electrons. The process of photosynthesis provides a quintessential example: 24 protons and 24 electrons are required to produce glucose from CO_2 and H_2O. In the case of most transformations relevant to energy storage, some steps involve the discrete transfer of an electron or proton, while other steps may involve a proton and electron traveling together in a concerted fashion. Understanding the factors that control proton-coupled electron transfer (PCET) reaction pathways is currently the subject of great interest, as such understanding could aid in the design of more efficient systems for energy-related transformations.

1.3.1 Mechanisms of proton-coupled electron transfer

Proton-coupled electron transfer can proceed through two types of pathways: stepwise or concerted, as shown in **Figure 1.8**.[78] The stepwise pathways consist of proton transfer followed by electron transfer (PT-ET) or electron transfer followed by proton transfer (ET-PT). In the concerted pathway, known as concerted proton-electron transfer (CPET) or hydrogen atom transfer (HAT),[79] the proton and electron travel simultaneously, although they may ultimately end up at different sites; for instance, a proton may travel to a ligand-based orbital of a molecule while the electron travels to the metal-based orbital. In a CPET/HAT mechanism, no discrete ET or PT intermediate is formed, and as such these mechanisms avoid the formation the high-energy intermediates that may be formed through stepwise pathways.

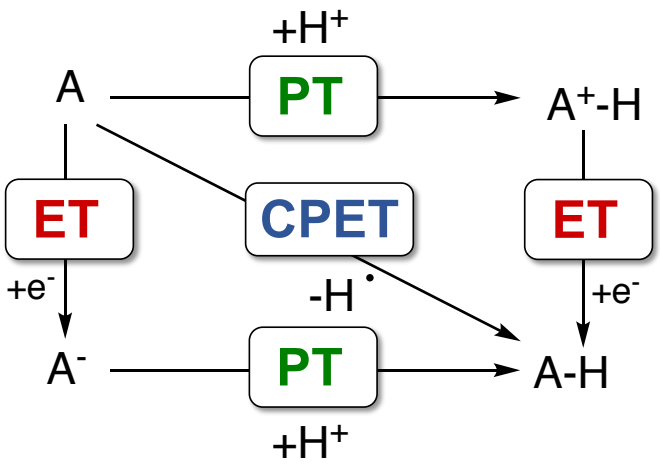

Figure 1.8. Stepwise and concerted mechanisms of proton-coupled electron transfer (PCET).

Reactions proceeding through concerted pathways can generally be distinguished from their stepwise counterparts through thermodynamic and kinetic measurements. For CPET/HAT reactions, the Evans-Polyani principle,[80-81] which relates the driving force for the reaction with the activation energy, is often invoked. This relationship can be demonstrated by plots of log(k), where k is the rate constant for the reaction, vs. substrate bond dissociation enthalpy (BDE) or bond dissociation free energy (BDFE). While BDE is often used due to the availability of BDE values for many compounds, Mayer and coworkers have demonstrated that the use of BDFE is more accurate, particularly for transition-metal based systems, as BDFEs take into account non-negligible entropic contributions.[81-83] In addition to plots of log(k) vs. BD(F)E, a plot of free energy barrier versus driving force can also be constructed, which should have a Brønsted slope of ½ for CPET/HAT, as predicted by Marcus theory.[84-85] Examples of such analyses are provided in the following section.

Recently, computational and experimental evidence has suggested that concerted proton-electron transfer can occur through “asynchronous” pathways, which lie between the two extremes of entirely stepwise and entirely concerted pathways.[86] In asynchronous CPET pathways, the transition state displays more PT- or ET-like character than for a purely concerted transition. Transition states that have significant PT character are referred to as “basic asynchronous,” while transition states that have significant ET character are referred to as “oxidative asynchronous”. It

has been proposed that asynchronous pathways may have lower activation energies than their synchronous counterparts.

1.3.2 Significant examples of PCET by high-valent metal species

Transition metal complexes have been extensively studied for their proton-coupled electron transfer reactivity. A thorough review of all high-valent metal species demonstrating PCET reactivity is outside of the scope of this Introduction, but thorough reviews can be found in references 78 and 87. Some notable examples of PCET mediated by high-valent metal species are discussed in this section.

One of the earliest and best characterized transition metal complexes that undergoes PCET from hydrocarbons is [*cis*-$Ru^{IV}(bpy)_2(py)(O)]^{2+}$ (bpy = 2,2'-bipyridine, py = pyridine, **Figure 1.9**).[87-88] In 2003, Mayer and coworkers demonstrated that this compound reacts with hydrocarbons through a hydrogen atom abstraction mechanism by showing that the rate of hydrogen atom abstraction varied linearly with substrate BDE, in accordance with the Evans-Polanyi relationship described earlier. It was also demonstrated that measured rate constants followed the Marcus cross relation.[89]

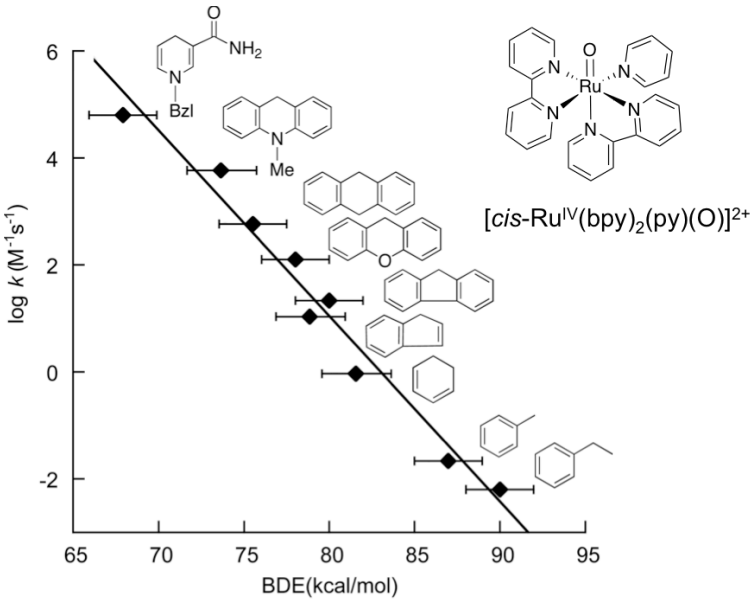

Figure 1.9. Structure of [*cis*-$Ru^{IV}(bpy)_2(py)(O)]^{2+}$ and plot of ln(k) vs. substrate BDE for hydrocarbon substrates. The linear correlation between log(k) and substrate BDE is consistent with a HAT mechanism. Reprinted with minor modifications with permission from ref. 81.

In addition to the [*cis*-$Ru^{IV}(bpy)_2(py)(O)]^{2+}$ system, a variety of high-valent metal-oxo and metal-hydroxo systems have been shown to mediate PCET processes. High-valent iron-oxo and manganese-oxo compounds are of particular interest due to their biological relevance for water and C-H oxidation. For example, both iron and manganese compounds incorporating PY5 ligands (PY5 = 2,6-(bis-(bis-2-pyridyl)methoxymethane)pyridine), synthesized as models of lipoxygenase, were shown to undergo hydrogen atom transfer from dihydroanthracene, as well as other organic substrates.[90] The iron complex was proposed to operate through an iron(IV)-oxo intermediate, while the manganese complex operated through manganese(III)-hydroxide. Both showed strong linear correlations between log(k) and substrate BDE.

Work from Mayer and coworkers further demonstrated that CPET can occur even when the proton-accepting or proton-donating site is not directly coordinated to the metal center. For example, in $Fe^{II}(H_2bim)$, the proton-donating site is located roughly ~4 Å away from the metal center, but proton and electron transfer from $Fe^{II}(H_2bim)$ are still coupled (**Figure 1.10A**).[91-92] This work was further expanded upon by Mayer through a series of ruthenium-carboxylate systems, in which the distance between the electron-accepting center and proton-accepting center was varied by up to 11 Å, but it was shown in all cases that the system still underwent concerted proton-electron transfer (**Figure 1.10B**).[93-94]

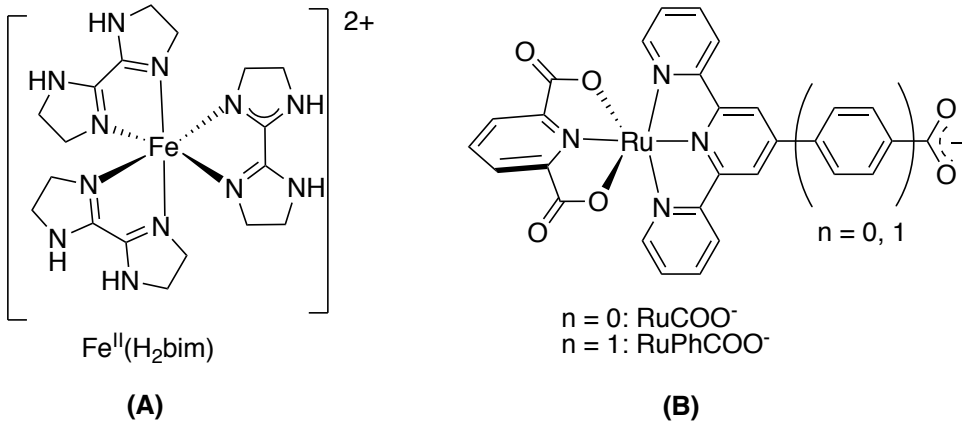

(A) **(B)**

Figure 1.10. Structures of $Fe^{II}(H_2bim)$ (A), $RuCOO^-$, and $RuPhCOO^-$ (B). These molecules react through concerted proton-electron transfer pathways despite the distance between electron and proton.

Not all metal-(hydr)oxo complexes that undergo PCET operate through CPET/HAT, however, and the electronics of the complex can drastically affect the mechanism by which PCET operates. For instance, when the central Mn atom is in its 4+ oxidation state in $[Mn(H_3buea)(O)]^-$ (**Figure 1.11B**, H_3buea = tris[(N)-*tert*-butylureaylato)-N-ethyl)]aminato), the complex undergoes PCET from hydrocarbons through a concerted mechanism. However, when Mn is reduced to the 3+ state in the same complex ($[Mn(H_3buea)(O)]^{2-}$, **Figure 1.11A**), it undergoes PCET through a stepwise PT-ET pathway, as evidenced by a faster rate constant for the reaction of Mn(III) with diyhdroanthracene despite a lower driving force.[95-96]

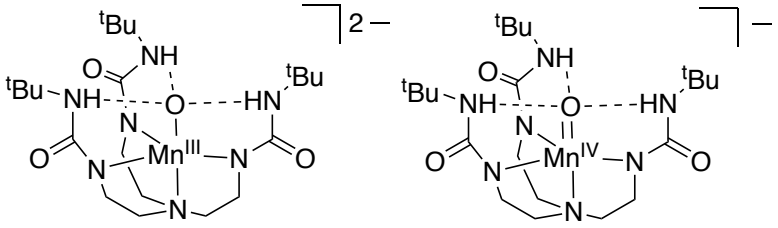

$[Mn^{III}H_3buea(O)]^{2-}$ **(A)**

$[Mn^{IV}H_3buea(O)]^-$ **(B)**

Figure 1.11. Structures of ($[Mn(H_3buea)(O)]^{2-}$ (A) and $[Mn(H_3buea(O)]^-$ (B), reported by Borovik and coworkers. (A) reacts with hydrocarbon substrates through a stepwise PT-ET mechanism, while (B) reacts through CPET/HAT.

Another mechanistic subtlety in CPET/HAT by high-valent metal complexes is asynchronicity. Recently, the Co(III)-oxo complex $PhB(^tBuIm)_3Co^{III}O$ ($PhB(^tBuIm)_3^-$ = tris(1-tert-butylimidazol-2-ylidene)phenylborate) was reported to react with hydrocarbons through a basic-asynchronous CPET mechanism.[97] The authors demonstrated that reaction rate correlated with substrate pK_a rather than BD(F)E, but DFT calculations and experimental evidence suggested that the reaction did not proceed through discrete stepwise intermediates. These findings led the authors to conclude that the reaction proceeded through a basic asynchronous pathway.

1.3.3 PCET reactivity of Cu(III) and Ni(III)

CPET from hydrocarbons and phenols by copper(III) complexes is relatively recent. Several notable early examples of copper(III) compounds showing hydrogen atom abstraction reactivity were di-μ-oxo copper dimers. One example was a bis(μ-oxo)copper(III) dimer which

demonstrated a wide range of reactivity with catechols and hydrocarbons. While PCET reactivity was observed, the exact mechanisms were not able to be determined due to complex reaction kinetics.[98]

In 2015, Tolman and coworkers reported the first mononuclear Cu(III) compound capable of hydrogen atom abstraction from hydrocarbons. The reported Cu^{III}-hydoxo complex $Cu(pyN_2^{iPr2})$ (pyN_2^{iPr2} = *N*,*N*′-bis(2,6-diisopropylphenyl)-2,6-pyridinedicarboxamide, **Figure 1.12**) showed fast reactivity with hydrocarbons, with a rate constant of k = ~186 M^{-1} s^{-1} at 25 °C for the reaction with dihydroanthracene, which rivals those of many high-valent Mn, Fe, and even Ru compounds. A plot of log(k) vs. BDE showed an excellent linear correlation, suggesting that the reaction proceed through CPET/HAT, and thermodynamic analysis gave a BDE of 90 ± 3 kcal mol^{-1} for the O-H bond formed in the Cu(II) product.[99] Structural variation of the complex through modification of the supporting ligand later demonstrated that the rate of reaction with dihydroanthracene corresponded with O-H BDE values of the products.[100] Further work on the reactivity of these complexes with phenols demonstrated some mechanistic dichotomy—PCET appeared to operate through a concerted pathway for most phenolic substrates tested, but reactions with the most acidic phenols appeared to operate through a stepwise PT-ET pathway.[101]

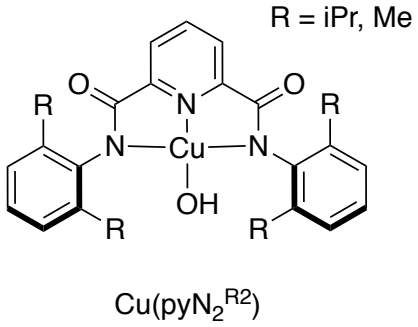

$Cu(pyN_2^{R2})$

Figure 1.12. Structure of the copper(III) complex reported by Tolman and coworkers, $Cu(pyN_2^{R2})$, which reacts with hydrocarbons and phenols through a hydrogen atom transfer mechanism.

Compared to copper, there are even fewer examples of PCET by Ni(III) complexes, and little thermodynamic data for the reported systems are available. One of the first reported examples of PCET by a Ni(III) complex was reported in 2012 by Ray and coworkers, who reported a putative nickel(III)-oxygen species generated from the reaction of $Ni(TMG_3tren)$ (TMG_3tren = 1,1,1-tris[2-[N_2-(1,1,3,3-tetramethylguanidino)]ethyl]amine) with *m*CPBA.[102] This species was reported to react with hydrocarbons through a CPET/HAT mechanism, but the exact identity of the reactive species could not be characterized. Similarly, Company and coworkers reported a potent

formally Ni(IV)-oxygen species capable of oxidizing C-H bonds through CPET/HAT,[103] but the transient nature of the species made it difficult to characterize thoroughly.

The first well-characterized mononuclear Ni(III) species to show oxidative CPET reactivity was reported by McDonald and coworkers in 2016 (**Figure 1.13**).[104] McDonald and coworkers prepared a series of Ni(III)-X species (X = ONO_2, OAc, OCO_2H) and tested their reactivity with phenols and hydrocarbons. The complexes all showed PCET reactivity with substrates, with X = ONO_2 being the fastest. A linear correlation between log(k) and BDE was demonstrated for the reaction with hydrocarbons, although the exact nickel-containing product of the reaction could not be directly observed. Furthermore, the pK_a values of these complexes could not be measured, and so thermodynamic measurements such as BDE/BDFE of the products could not be obtained.

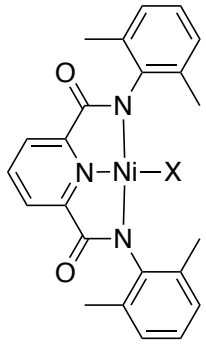

X = ONO_2, OAc, OCO_2H, Cl

Figure 1.13. Structure of the Ni(III) complexes reported by McDonald and coworkers, Ni(pyN_2^{Me2})(X), which reacts with hydrocarbons and phenols through a hydrogen atom transfer mechanism.

McDonald and coworkers soon after reported CPET/HAT by a Ni(III)-Cl species (X = Cl in **Figure 1.13**), which underwent a unique CPET mechanism to generate and release HCl.[105] This complex was mainly tested with substituted di-tert-butyl phenols, but also showed reactivity with hydrocarbons containing weak C-H bonds as well. Evans-Polanyi relationships as well as Hammett analysis demonstrated that this complex, too, operated through a concerted mechanism; however, complete thermodynamic measurements could not be made due to lack of pK_a data.

1.4 Outline of Dissertation

Over the course of my PhD, I have mainly worked on projects that fall into the two broad categories described in this chapter: water-oxidation electrocatalysis and proton-coupled electron transfer by high-valent molecules. As such, this thesis is broken into two sections. The first section (Chapters 2-3) describes work on the development and elucidation of the mechanism of a highly active copper electrocatalyst for water oxidation. Chapter 2 describes the synthesis and characterization of the water-oxidation electrocatalyst $Cu(pyalk)_2$. We found that this molecule oxidized water electrochemically under basic conditions and found it to be a robust system for water

oxidation. Chapter 3 describes the collaborative theoretical-experimental study of the mechanism of water oxidation by $Cu(pyalk)_2$. In this chapter, we provide theoretical and experimental support for a water-nucleophilic attack mechanism, including foot-of-the-wave analysis and kinetic isotope effects. The second section (Chapters 4-5) focuses on studies related to proton-coupled electron transfer by high-valent nickel- and copper-pyalk species. In Chapter 4, we describe synthesis and characterization of the Ni(III) species, $Ni(pyalk)_2^+$, and examine its activity for proton-coupled electron transfer with phenols and hydrocarbons. We found that this complex oxidizes C-H and O-H bonds through concerted proton-electron transfer and that the high BDE of the O-H bond formed likely explains its fast reactivity with substrates. Chapter 5 describes the synthesis and characterization of an analogous Cu(III) species, $Cu(pyalk)_2^+$, and addresses the PCET reactivity of this species compared to its isostructural nickel counterpart.

1.5 References

1. Newell, R.; Raimi, D.; Aldana, G. *Global Energy Outlook 2019: The Next Generation of Energy*; Resources for the Future: 2019; pp 3-5.
2. Council, N. R., *Hidden Costs of Energy: Unpriced Consequences of Energy Production and Use*. The National Academies Press: Washington, DC, 2010; p 506.
3. Lewis, N. S.; Nocera, D. G., Powering the Planet: Chemical Challenges in Solar Energy Utilization. *Proc. Natl. Acad. Sci.* **2006,** *103* (43), 15729-15735.
4. House, R. L.; Iha, N. Y. M.; Coppo, R. L.; Alibabaei, L.; Sherman, B. D.; Kang, P.; Brennaman, M. K.; Hoertz, P. G.; Meyer, T. J., Artificial Photosynthesis: Where Are We Now? Where Can We Go? *J. Photochem. Photobiol. C* **2015,** *25*, 32-45.
5. McConnell, I.; Li, G.; Brudvig, G. W., Energy Conversion in Natural and Artificial Photosynthesis. *Chemistry & Biology* **2010,** *17* (5), 434-447.
6. Berardi, S.; Drouet, S.; Francàs, L.; Gimbert-Suriñach, C.; Guttentag, M.; Richmond, C.; Stoll, T.; Llobet, A., Molecular Artificial Photosynthesis. *Chem. Soc. Rev.* **2014,** *43* (22), 7501-7519.
7. Concepcion, J. J.; House, R. L.; Papanikolas, J. M.; Meyer, T. J., Chemical Approaches to Artificial Photosynthesis. *Proc. Natl. Acad. Sci.* **2012,** *109* (39), 15560-15564.
8. Young, K. J.; Martini, L. A.; Milot, R. L.; Snoeberger III, R. C.; Batista, V. S.; Schmuttenmaer, C. A.; Crabtree, R. H.; Brudvig, G. W., Light-Driven Water Oxidation for Solar Fuels. *Coord. Chem. Rev.* **2012,** *256* (21–22), 2503-2520.
9. Fukuzumi, S., Production of Liquid Solar Fuels and Their Use in Fuel Cells. *Joule* **2017,** *1* (4), 689-738.
10. Dau, H.; Limberg, C.; Reier, T.; Risch, M.; Roggan, S.; Strasser, P., The Mechanism of Water Oxidation: From Electrolysis Via Homogeneous to Biological Catalysis. *ChemCatChem* **2010,** *2* (7), 724-761.
11. Blakemore, J. D.; Crabtree, R. H.; Brudvig, G. W., Molecular Catalysts for Water Oxidation. *Chem. Rev.* **2015,** *115* (23), 12974-13005.
12. Craig, M. J.; Coulter, G.; Dolan, E.; Soriano-López, J.; Mates-Torres, E.; Schmitt, W.; García-Melchor, M., Universal Scaling Relations for the Rational Design of Molecular Water Oxidation Catalysts with Near-Zero Overpotential. *Nat. Chem.* **2019,** *10* (1), 4993.

13. Song, J.; Wei, C.; Huang, Z.-F.; Liu, C.; Zeng, L.; Wang, X.; Xu, Z. J., A Review on Fundamentals for Designing Oxygen Evolution Electrocatalysts. *Chem. Soc. Rev.* **2020,** *49* (7), 2196-2214.
14. Crabtree, R. H., Resolving Heterogeneity Problems and Impurity Artifacts in Operationally Homogeneous Transition Metal Catalysts. *Chem. Rev.* **2011,** *112* (3), 1536-1554.
15. Young, K. J.; Martini, L. A.; Milot, R. L.; Snoeberger III, R. C.; Batista, V. S.; Schmuttenmaer, C. A.; Crabtree, R. H.; Brudvig, G. W., Light-Driven Water Oxidation for Solar Fuels. *Coord. Chem. Rev.* **2012,** *256* (21-22), 2503-2520.
16. Materna, K. L.; Rudshteyn, B.; Brennan, B. J.; Kane, M. H.; Bloomfield, A. J.; Huang, D. L.; Shopov, D. Y.; Batista, V. S.; Crabtree, R. H.; Brudvig, G. W., Heterogenized Iridium Water-Oxidation Catalyst from a Silatrane Precursor. *ACS Catal.* **2016,** *6* (8), 5371-5377.
17. Costentin, C.; Savéant, J.-M., Molecular Approach to Catalysis of Electrochemical Reaction in Porous Films. *Curr. Opin. Electrochem.* **2019,** *15*, 58-65.
18. Michaelos, T. K.; Shopov, D. Y.; Sinha, S. B.; Sharninghausen, L. S.; Fisher, K. J.; Lant, H. M. C.; Crabtree, R. H.; Brudvig, G. W., A Pyridine Alkoxide Chelate Ligand That Promotes Both Unusually High Oxidation States and Water-Oxidation Catalysis. *Acc. Chem. Res.* **2017,** *50* (4), 952-959.
19. Lant, H. M. C.; Michaelos, T. K.; Sharninghausen, L. S.; Mercado, B. Q.; Crabtree, R. H.; Brudvig, G. W., N,N,O Pincer Ligand with a Deprotonatable Site That Promotes Redox-Leveling, High Mn Oxidation States, and a Mn_2O_2 Dimer Competent for Catalytic Oxygen Evolution. *Eur. J. Inorg. Chem.* **2019,** *2019* (15), 2115-2123.
20. Michaelos, T. K.; Lant, H. M. C.; Sharninghausen, L. S.; Craig, S. M.; Menges, F. S.; Mercado, B. Q.; Brudvig, G. W.; Crabtree, R. H., Catalytic Oxygen Evolution from Manganese Complexes with an Oxidation-Resistant N,N,O-Donor Ligand. *ChemPlusChem* **2016,** *81* (10), 1129-1132.
21. Hintermair, U.; Sheehan, S. W.; Parent, A. R.; Ess, D. H.; Richens, D. T.; Vaccaro, P. H.; Brudvig, G. W.; Crabtree, R. H., Precursor Transformation During Molecular Oxidation Catalysis with Organometallic Iridium Complexes. *J. Am. Chem. Soc.* **2013,** *135* (29), 10837-10851.
22. Sinha, S. B.; Shopov, D. Y.; Sharninghausen, L. S.; Vinyard, D. J.; Mercado, B. Q.; Brudvig, G. W.; Crabtree, R. H., A Stable Coordination Complex of Rh(IV) in an N,O-Donor Environment. *J. Am. Chem. Soc.* **2015,** *137* (50), 15692-15695.
23. Sharninghausen, L. S.; Sinha, S. B.; Shopov, D. Y.; Choi, B.; Mercado, B. Q.; Roy, X.; Balcells, D.; Brudvig, G. W.; Crabtree, R. H., High Oxidation State Iridium Mono-Mu-Oxo Dimers Related to Water Oxidation Catalysis. *J. Am. Chem. Soc.* **2016,** *138* (49), 15917-15926.
24. Shopov, D. Y.; Sharninghausen, L. S.; Sinha, S. B.; Mercado, B. Q.; Balcells, D.; Brudvig, G. W.; Crabtree, R. H., A Dinuclear Iridium(V,V) Oxo-Bridged Complex Characterized Using a Bulk Electrolysis Technique for Crystallizing Highly Oxidizing Compounds. *Inorg. Chem.* **2018,** *57* (9), 5684-5691.
25. Sinha, S. B.; Shopov, D. Y.; Sharninghausen, L. S.; Stein, C. J.; Mercado, B. Q.; Balcells, D.; Pedersen, T. B.; Reiher, M.; Brudvig, G. W.; Crabtree, R. H., Redox Activity of Oxo-Bridged Iridium Dimers in an N,O-Donor Environment: Characterization of Remarkably Stable Ir(IV,V) Complexes. *J. Am. Chem. Soc.* **2017,** *139* (28), 9672-9683.
26. Savéant, J.-M., Molecular Catalysis of Electrochemical Reactions. Mechanistic Aspects. *Chem. Rev.* **2008,** *108* (7), 2348-2378.
27. Parent, A. R.; Crabtree, R. H.; Brudvig, G. W., Comparison of Primary Oxidants for Water-Oxidation Catalysis. *Chem. Soc. Rev.* **2013,** *42* (6), 2247-2252.
28. Thomsen, J. M.; Huang, D. L.; Crabtree, R. H.; Brudvig, G. W., Iridium-Based Complexes for Water Oxidation. *Dalton Trans.* **2015,** *44* (28), 12452-12472.
29. Elgrishi, N.; Rountree, K. J.; McCarthy, B. D.; Rountree, E. S.; Eisenhart, T. T.; Dempsey, J. L., A Practical Beginner's Guide to Cyclic Voltammetry. *J. Chem. Educ.* **2017,** *95* (2), 197-206.
30. Rountree, E. S.; McCarthy, B. D.; Eisenhart, T. T.; Dempsey, J. L., Evaluation of Homogeneous Electrocatalysts by Cyclic Voltammetry. *Inorg. Chem.* **2014,** *53* (19), 9983-10002.
31. Bard, A. J.; Faulkner, L. R., *Electrochemical Methods: Fundamentals and Applications*. 2nd ed.; Wiley: Hoboken, NJ, 2000.
32. Appel, A. M.; Helm, M. L., Determining the Overpotential for a Molecular Electrocatalyst. *ACS Catal.* **2014,** *4* (2), 630-633.

33. Costentin, C.; Drouet, S.; Robert, M.; Savéant, J.-M., Turnover Numbers, Turnover Frequencies, and Overpotential in Molecular Catalysis of Electrochemical Reactions. Cyclic Voltammetry and Preparative-Scale Electrolysis. *J. Am. Chem. Soc.* **2012,** *134* (27), 11235-11242.
34. Choi, J.; Kim, J.; Wagner, P.; Gambhir, S.; Jalili, R.; Byun, S.; Sayyar, S.; Lee, Y. M.; MacFarlane, D. R.; Wallace, G. G.; Officer, D. L., Energy Efficient Electrochemical Reduction of CO2 to Co Using a Three-Dimensional Porphyrin/Graphene Hydrogel. *Energy Environ. Sci.* **2019,** *12* (2), 747-755.
35. Gersten, S. W.; Samuels, G. J.; Meyer, T. J., Catalytic Oxidation of Water by an Oxo-Bridged Ruthenium Dimer. *J. Am. Chem. Soc.* **1982,** *104* (14), 4029-4030.
36. Concepcion, J. J.; Jurss, J. W.; Brennaman, M. K.; Hoertz, P. G.; Patrocinio, A. O.; Murakami Iha, N. Y.; Templeton, J. L.; Meyer, T. J., Making Oxygen with Ruthenium Complexes. *Acc. Chem. Res.* **2009,** *42* (12), 1954-65.
37. Limburg, B.; Bouwman, E.; Bonnet, S., Molecular Water Oxidation Catalysts Based on Transition Metals and Their Decomposition Pathways. *Coord. Chem. Rev.* **2012,** *256* (15-16), 1451-1467.
38. Hull, J. F.; Balcells, D.; Blakemore, J. D.; Incarvito, C. D.; Eisenstein, O.; Brudvig, G. W.; Crabtree, R. H., Highly Active and Robust Cp* Iridium Complexes for Catalytic Water Oxidation. *J. Am. Chem. Soc.* **2009,** *131* (25), 8730-8731.
39. Blakemore, J. D.; Schley, N. D.; Balcells, D.; Hull, J. F.; Olack, G. W.; Incarvito, C. D.; Eisenstein, O.; Brudvig, G. W.; Crabtree, R. H., Half-Sandwich Iridium Complexes for Homogeneous Water-Oxidation Catalysis. *J. Am. Chem. Soc.* **2010,** *132* (45), 16017-16029.
40. Savini, A.; Belanzoni, P.; Bellachioma, G.; Zuccaccia, C.; Zuccaccia, D.; Macchioni, A., Activity and Degradation Pathways of Pentamethyl-Cyclopentadienyl-Iridium Catalysts for Water Oxidation. *Green Chem.* **2011,** *13* (12), 3360-3374.
41. Zuccaccia, C.; Bellachioma, G.; Bolaño, S.; Rocchigiani, L.; Savini, A.; Macchioni, A., An Nmr Study of the Oxidative Degradation of Cp*Ir Catalysts for Water Oxidation: Evidence for a Preliminary Attack on the Quaternary Carbon Atom of the --C-CH_3 Moiety. *Eur. J. Inorg. Chem.* **2012,** *2012* (9), 1462-1468.
42. Hintermair, U.; Hashmi, S. M.; Elimelech, M.; Crabtree, R. H., Particle Formation During Oxidation Catalysis with Cp* Iridium Complexes. *J. Am. Chem. Soc.* **2012,** *134* (23), 9785-95.
43. Parent, A. R.; Brewster, T. P.; De Wolf, W.; Crabtree, R. H.; Brudvig, G. W., Sodium Periodate as a Primary Oxidant for Water-Oxidation Catalysts. *Inorg. Chem.* **2012,** *51* (11), 6147-52.
44. Huang, D. L.; Beltrán-Suito, R.; Thomsen, J. M.; Hashmi, S. M.; Materna, K. L.; Sheehan, S. W.; Mercado, B. Q.; Brudvig, G. W.; Crabtree, R. H., New Ir Bis-Carbonyl Precursor for Water Oxidation Catalysis. *Inorg. Chem.* **2016,** *55* (5), 2427-2435.
45. Yang, K. R.; Matula, A. J.; Kwon, G.; Hong, J.; Sheehan, S. W.; Thomsen, J. M.; Brudvig, G. W.; Crabtree, R. H.; Tiede, D. M.; Chen, L. X.; Batista, V. S., Solution Structures of Highly Active Molecular Ir Water-Oxidation Catalysts from Density Functional Theory Combined with High-Energy X-Ray Scattering and EXAFS Spectroscopy. *J. Am. Chem. Soc.* **2016,** *138* (17), 5511-5514.
46. Payne, D., Iridium's Impact. *Nat. Chem.* **2016,** *8* (4), 392.
47. Price Charts: Daily Prices of Platinum and Iridium. http://www.platinum.matthey.com/prices/price-charts# (accessed December 30).
48. Limburg, J.; Vrettos, J. S.; Liable-Sands, L. M.; Rheingold, A. L.; Crabtree, R. H.; Brudvig, G. W., A Functional Model for O-O Bond Formation by the O_2-Evolving Complex in Photosystem II. *Science* **1999,** *283* (5407), 1524-1527.
49. Limburg, J.; Vrettos, J. S.; Chen, H.; de Paula, J. C.; Crabtree, R. H.; Brudvig, G. W., Characterization of the O_2-Evolving Reaction Catalyzed by $[(terpy)(H_2O)Mn^{III}(O)_2Mn^{IV}(OH_2)(terpy)](NO_3)_3$ (terpy = 2,2':6,2"-terpyridine). *J. Am. Chem. Soc.* **2001,** *123* (3), 423-30.
50. Solomon, E. I.; Heppner, D. E.; Johnston, E. M.; Ginsbach, J. W.; Cirera, J.; Qayyum, M.; Kieber-Emmons, M. T.; Kjaergaard, C. H.; Hadt, R. G.; Tian, L., Copper Active Sites in Biology. *Chem. Rev.* **2014,** *114* (7), 3659-3853.
51. Barnett, S. M.; Goldberg, K. I.; Mayer, J. M., A Soluble Copper-Bipyridine Water-Oxidation Electrocatalyst. *Nat. Chem.* **2012,** *4* (6), 498-502.

52. Stott, L. A.; Prosser, K. E.; Berdichevsky, E. K.; Walsby, C. J.; Warren, J. J., Lowering Water Oxidation Overpotentials Using the Ionisable Imidazole of Copper(2-(2'-pyridyl)imidazole). *Chem. Commun.* **2017,** *53* (3), 651-654.
53. Zhang, T.; Wang, C.; Liu, S.; Wang, J. L.; Lin, W., A Biomimetic Copper Water Oxidation Catalyst with Low Overpotential. *J. Am. Chem. Soc.* **2014,** *136* (1), 273-81.
54. Lee, H.; Wu, X.; Sun, L., Copper-Based Homogeneous and Heterogeneous Catalysts for Electrochemical Water Oxidation. *Nanoscale* **2020,** *12* (7), 4187-4218.
55. Fu, L.-Z.; Fang, T.; Zhou, L.-L.; Zhan, S.-Z., A Mononuclear Copper Electrocatalyst for Both Water Reduction and Oxidation. *RSC Adv.* **2014,** *4* (96), 53674-53680.
56. Garrido-Barros, P.; Funes-Ardoiz, I.; Drouet, S.; Benet-Buchholz, J.; Maseras, F.; Llobet, A., Redox Non-Innocent Ligand Controls Water Oxidation Overpotential in a New Family of Mononuclear Cu-Based Efficient Catalysts. *J. Am. Chem. Soc.* **2015,** *137* (21), 6758-6761.
57. Liu, Y.; Han, Y.; Zhang, Z.; Zhang, W.; Lai, W.; Wang, Y.; Cao, R., Low Overpotential Water Oxidation at Neutral pH Catalyzed by a Copper(II) Porphyrin. *Chem. Sci.* **2019,** *10* (9), 2613-2622.
58. Su, X. J.; Gao, M.; Jiao, L.; Liao, R. Z.; Siegbahn, P. E.; Cheng, J. P.; Zhang, M. T., Electrocatalytic Water Oxidation by a Dinuclear Copper Complex in a Neutral Aqueous Solution. *Angew. Chem. Int. Ed.* **2015,** *54* (16), 4909-14.
59. Su, X.-J.; Zheng, C.; Hu, Q.-Q.; Du, H.-Y.; Liao, R.-Z.; Zhang, M.-T., Bimetallic Cooperative Effect on O–O Bond Formation: Copper Polypyridyl Complexes as Water Oxidation Catalyst. *Dalton Trans.* **2018,** *47* (26), 8670-8675.
60. Koepke, S. J.; Light, K. M.; VanNatta, P. E.; Wiley, K. M.; Kieber-Emmons, M. T., Electrocatalytic Water Oxidation by a Homogeneous Copper Catalyst Disfavors Single-Site Mechanisms. *J. Am. Chem. Soc.* **2017,** *139* (25), 8586-8600.
61. Chen, Z.; Meyer, T. J., Copper(II) Catalysis of Water Oxidation. *Angew. Chem. Int. Ed.* **2013,** *52* (2), 700-703.
62. Yu, F.; Li, F.; Zhang, B.; Li, H.; Sun, L., Efficient Electrocatalytic Water Oxidation by a Copper Oxide Thin Film in Borate Buffer. *ACS Catal.* **2015,** *5* (2), 627-630.
63. Liu, X.; Cui, S.; Sun, Z.; Du, P., Copper Oxide Nanomaterials Synthesized from Simple Copper Salts as Active Catalysts for Electrocatalytic Water Oxidation. *Electrochim. Acta* **2015,** *160*, 202-208.
64. Cui, S.; Liu, X.; Sun, Z.; Du, P., Noble Metal-Free Copper Hydroxide as an Active and Robust Electrocatalyst for Water Oxidation at Weakly Basic pH. *ACS Sustain. Chem. Eng.* **2016,** *4* (5), 2593-2600.
65. Anxolabéhère-Mallart, E.; Costentin, C.; Fournier, M.; Nowak, S.; Robert, M.; Savéant, J.-M., Boron-Capped Tris(glyoximato) Cobalt Clathrochelate as a Precursor for the Electrodeposition of Nanoparticles Catalyzing H_2 Evolution in Water. *J. Am. Chem. Soc.* **2012,** *134* (14), 6104-6107.
66. Klymenko, O. V.; Svir, I.; Amatore, C., Molecular Electrochemistry and Electrocatalysis: A Dynamic View. *Mol. Phys.* **2014,** *112* (9-10), 1273-1283.
67. Lee, K. J.; McCarthy, B. D.; Dempsey, J. L., On Decomposition, Degradation, and Voltammetric Deviation: The Electrochemist's Field Guide to Identifying Precatalyst Transformation. *Chem. Soc. Rev.* **2019,** *48* (11), 2927-2945.
68. Amatore, C.; Pinson, J.; Savéant, J. M.; Thiebault, A., Trace Crossings in Cyclic Voltammetry and Electrochemic Electrochemical Inducement of Chemical Reactions. *J. Electroanal. Chem.* **1980,** *107* (1), 59-74.
69. Artero, V.; Fontecave, M., Solar Fuels Generation and Molecular Systems: Is It Homogeneous or Heterogeneous Catalysis? *Chem. Soc. Rev.* **2013,** *42* (6), 2338-2356.
70. Crabtree, R. H., Deactivation in Homogeneous Transition Metal Catalysis: Causes, Avoidance, and Cure. *Chem. Rev.* **2014,** *115* (1), 127-150.
71. Fisher, K. J.; Materna, K. L.; Mercado, B. Q.; Crabtree, R. H.; Brudvig, G. W., Electrocatalytic Water Oxidation by a Copper(II) Complex of an Oxidation-Resistant Ligand. *ACS Catal.* **2017,** *7*, 3384-3387.
72. Schley, N. D.; Blakemore, J. D.; Subbaiyan, N. K.; Incarvito, C. D.; D'Souza, F.; Crabtree, R. H.; Brudvig, G. W., Distinguishing Homogeneous from Heterogeneous Catalysis in Electrode-Driven Water Oxidation with Molecular Iridium Complexes. *J. Am. Chem. Soc.* **2011,** *133* (27), 10473-10481.

73. Isaka, Y.; Kato, S.; Hong, D.; Suenobu, T.; Yamada, Y.; Fukuzumi, S., Bottom-up and Top-Down Methods to Improve Catalytic Reactivity for Photocatalytic Production of Hydrogen Peroxide Using a Ru-Complex and Water Oxidation Catalysts. *J. Mater. Chem. A* **2015,** *3* (23), 12404-12412.
74. Weng, Z.; Wu, Y.; Wang, M.; Jiang, J.; Yang, K.; Huo, S.; Wang, X. F.; Ma, Q.; Brudvig, G. W.; Batista, V. S.; Liang, Y.; Feng, Z.; Wang, H., Active Sites of Copper-Complex Catalytic Materials for Electrochemical Carbon Dioxide Reduction. *Nat. Chem.* **2018,** *9* (1), 415.
75. Feng, Z.; Ma, Q.; Lu, J.; Feng, H.; Elam, J. W.; Stair, P. C.; Bedzyk, M. J., Atomic-Scale Cation Dynamics in a Monolayer VOX/α-Fe_2O_3 Catalyst. *RSC Adv.* **2015,** *5* (126), 103834-103840.
76. Stoerzinger, K. A.; Hong, W. T.; Crumlin, E. J.; Bluhm, H.; Shao-Horn, Y., Insights into Electrochemical Reactions from Ambient Pressure Photoelectron Spectroscopy. *Acc. Chem. Res.* **2015,** *48* (11), 2976-83.
77. Sconyers, D. J.; Blakemore, J. D., Distinguishing between Homogeneous and Heterogeneous Hydrogen-Evolution Catalysis with Molecular Cobalt Complexes. *Chem. Commun.* **2017,** *53* (53), 7286-7289.
78. Warren, J. J.; Tronic, T. A.; Mayer, J. M., Thermochemistry of Proton-Coupled Electron Transfer Reagents and Its Implications. *Chem. Rev.* **2010,** *110* (12), 6961-7001.
79. The distinction between "CPET" and "HAT" is generally difficult to define, as many systems undergoing this type of reactivity fall somewhere in the middle. Therefore, we have either used the preferred nomenclature of the author whose work is being referenced or have referred to the mechanism as CPET/HAT in cases of ambiguity.
80. Evans, M. G.; Polanyi, M., Inertia and Driving Force of Chemical Reactions. *Trans. Faraday Soc.* **1938,** *34*.
81. Mayer, J. M., Understanding Hydrogen Atom Transfer: From Bond Strengths to Marcus Theory. *Acc. Chem. Res.* **2011,** *44* (1), 36-46.
82. Mader, E. A.; Davidson, E. R.; Mayer, J. M., Large Ground-State Entropy Changes for Hydrogen Atom Transfer Reactions of Iron Complexes. *J. Am. Chem. Soc.* **2007,** *129* (16), 5153-5166.
83. Mader, E. A.; Manner, V. W.; Markle, T. F.; Wu, A.; Franz, J. A.; Mayer, J. M., Trends in Ground-State Entropies for Transition Metal Based Hydrogen Atom Transfer Reactions. *J. Am. Chem. Soc.* **2009,** *131* (12), 4335-4345.
84. Darcy, J. W.; Koronkiewicz, B.; Parada, G. A.; Mayer, J. M., A Continuum of Proton-Coupled Electron Transfer Reactivity. *Acc. Chem. Res.* **2018,** *51* (10), 2391-2399.
85. Markle, T. F.; Rhile, I. J.; DiPasquale, A. G.; Mayer, J. M., Probing Concerted Proton-Electron Transfer in Phenol-Imidazoles. *Proc. Natl. Acad. Sci.* **2008,** *105* (24), 8185-8190.
86. Bim, D.; Maldonado-Dominguez, M.; Rulisek, L.; Srnec, M., Beyond the Classical Thermodynamic Contributions to Hydrogen Atom Abstraction Reactivity. *Proc. Natl. Acad. Sci.* **2018,** *115* (44), E10287-E10294.
87. Weinberg, D. R.; Gagliardi, C. J.; Hull, J. F.; Murphy, C. F.; Kent, C. A.; Westlake, B. C.; Paul, A.; Ess, D. H.; McCafferty, D. G.; Meyer, T. J., Proton-Coupled Electron Transfer. *Chem. Rev.* **2012,** *112* (7), 4016-4093.
88. Moyer, B. A.; Meyer, T. J., Oxobis(2,2'-bipyridine)pyridineruthenium(IV) Ion,$[(bpy)_2(py)Ru{=}O]^{2+}$. *J. Am. Chem. Soc.* **1978,** *100* (11), 3601-3603.
89. Bryant, J. R.; Mayer, J. M., Oxidation of C−H Bonds by $[(bpy)_2(py)Ru^{IV}O]^{2+}$ Occurs by Hydrogen Atom Abstraction. *J. Am. Chem. Soc.* **2003,** *125* (34), 10351-10361.
90. Goldsmith, C. R.; Stack, T. D. P., Hydrogen Atom Abstraction by a Mononuclear Ferric Hydroxide Complex: Insights into the Reactivity of Lipoxygenase. *Inorg. Chem.* **2006,** *45* (15), 6048-6055.
91. Roth, J. P.; Mayer, J. M., Hydrogen Transfer Reactivity of a Ferric Bi-Imidazoline Complex That Models the Activity of Lipoxygenase Enzymes. *Inorg. Chem.* **1999,** *38* (12), 2760-2761.
92. Roth, J. P.; Yoder, J. C.; Won, T.-J.; Mayer, J. M., Application of the Marcus Cross Relation to Hydrogen Atom Transfer Reactions. *Science* **2001,** *294* (5551), 2524.
93. Manner, V. W.; Mayer, J. M., Concerted Proton−Electron Transfer in a Ruthenium Terpyridyl-Benzoate System with a Large Separation between the Redox and Basic Sites. *J. Am. Chem. Soc.* **2009,** *131* (29), 9874-9875.

94. Manner, V. W.; DiPasquale, A. G.; Mayer, J. M., Facile Concerted Proton−Electron Transfers in a Ruthenium Terpyridine-4′-Carboxylate Complex with a Long Distance between the Redox and Basic Sites. *J. Am. Chem. Soc.* **2008,** *130* (23), 7210-7211.
95. Gupta, R.; Borovik, A. S., Monomeric MnIII/II and FeIII/II Complexes with Terminal Hydroxo and Oxo Ligands: Probing Reactivity Via O-H Bond Dissociation Energies. *J. Am. Chem. Soc.* **2003,** *125* (43), 13234-42.
96. Parsell, T. H.; Yang, M. Y.; Borovik, A. S., C-H Bond Cleavage with Reductants: Re-Investigating the Reactivity of Monomeric Mn(III/IV)-Oxo Complexes and the Role of Oxo Ligand Basicity. *J. Am. Chem. Soc.* **2009,** *131* (8), 2762-3.
97. Goetz, M. K.; Anderson, J. S., Experimental Evidence for pK_a-Driven Asynchronicity in C-H Activation by a Terminal Co(III)-Oxo Complex. *J. Am. Chem. Soc.* **2019,** *141* (9), 4051-4062.
98. Taki, M.; Itoh, S.; Fukuzumi, S., C−H Bond Activation of External Substrates with a Bis(μ-Oxo)Dicopper(III) Complex. *J. Am. Chem. Soc.* **2001,** *123* (25), 6203-6204.
99. Dhar, D.; Tolman, W. B., Hydrogen Atom Abstraction from Hydrocarbons by a Copper(III)-Hydroxide Complex. *J. Am. Chem. Soc.* **2015,** *137* (3), 1322-1329.
100. Dhar, D.; Yee, G. M.; Spaeth, A. D.; Boyce, D. W.; Zhang, H.; Dereli, B.; Cramer, C. J.; Tolman, W. B., Perturbing the Copper(III)–Hydroxide Unit through Ligand Structural Variation. *J. Am. Chem. Soc.* **2016,** *138* (1), 356-368.
101. Dhar, D.; Yee, G. M.; Markle, T. F.; Mayer, J. M.; Tolman, W. B., Reactivity of the Copper(III)-Hydroxide Unit with Phenols. *Chem. Sci.* **2017,** *8* (2), 1075-1085.
102. Pfaff, F. F.; Heims, F.; Kundu, S.; Mebs, S.; Ray, K., Spectroscopic Capture and Reactivity of S = 1/2 Nickel(III)–Oxygen Intermediates in the Reaction of a Ni^{II}-salt with mCPBA. *Chem. Commun.* **2012,** *48* (31), 3730.
103. Corona, T.; Pfaff, F. F.; Acuña-Parés, F.; Draksharapu, A.; Whiteoak, C. J.; Martin-Diaconescu, V.; Lloret-Fillol, J.; Browne, W. R.; Ray, K.; Company, A., Reactivity of a Nickel(II) Bis(amidate) Complex with meta-Chloroperbenzoic Acid: Formation of a Potent Oxidizing Species. *Chem. Eur. J.* **2015,** *21* (42), 15029-15038.
104. Pirovano, P.; Farquhar, E. R.; Swart, M.; McDonald, A. R., Tuning the Reactivity of Terminal Nickel(III)–Oxygen Adducts for C–H Bond Activation. *J. Am. Chem. Soc.* **2016,** *138* (43), 14362-14370.
105. Mondal, P.; Pirovano, P.; Das, A.; Farquhar, E. R.; McDonald, A. R., Hydrogen Atom Transfer by a High-Valent Nickel-Chloride Complex. *J. Am. Chem. Soc.* **2018,** *140* (5), 1834-1841.

Part One. Study of water oxidation-catalysis by first-row transition metal complexes.

2 Chapter 2. Electrocatalytic water oxidation by a copper(II) complex of an oxidatively resistant ligand

This work was adapted from Fisher, K. J.; Materna, K. L.; Mercado, B. Q.; Crabtree, R. H.; Brudvig, G. W. *ACS Catal.* **2017,** *7*, 3384-3387. KJF conducted experiments and wrote the manuscript. KLM assisted with Clark electrode and gas chromatography experiments as well as editing of the manuscript. BQM prepared X-ray crystal structures. Reprinted with minor modifications with permission from the American Chemical Society, 2017.

2.1 Introduction

Water oxidation (**Equation 1.1**) is a vital component of natural and artificial photosynthetic systems, which convert sunlight into storable chemical fuels.[1-2] As discussed in Chapter 1, a key challenge in developing artificial photosynthetic systems is designing stable, highly active water-oxidation catalysts (WOCs).[3-6] Early molecular WOCs primarily utilized precious metals, notably ruthenium[7-8] and iridium,[9-11] but in recent years, significant effort has gone toward the development of WOCs which incorporate inexpensive and abundant metals. Manganese was the first of these Earth-abundant metals to be utilized in a molecular WOC,[12-13] but recent research has expanded the WOC library to include iron,[14-15] cobalt,[16-17] nickel,[18-19] and copper.[20-21] Of these metals, copper is an attractive choice due to its Earth-abundance, biomimetic chemistry with oxygen,[22] and well-studied coordination chemistry.

$$H_2O \rightarrow O_2 + 4H^+ + 4e^- \qquad \textbf{(Equation 2.1)}$$

Since the 2012 report of the first molecular copper WOC, $Cu(bpy)(OH)_2$ (bpy = 2,2'-bipyridyl),[20] several other molecular copper WOCs have been developed.[21, 23-32] However, many of these catalysts operate at high overpotentials[20, 23] and have not been evaluated for stability during electrolysis over long periods of time. In this chapter, we report that the water-soluble and robust copper complex $Cu(pyalk)_2$ (**2, Figure 2.1C**) is an electrocatalyst for water oxidation at basic pH.

To retain the molecular nature of a catalyst under the harsh conditions necessary for water oxidation, oxidation resistant and tightly binding ligands are necessary. We have previously demonstrated the oxidation resistance of 2-pyridinyl-2-propanol (pyalkH, **Figure 2.1A**),[33-36] which

is an effective ligand for iridium WOCs.[37] As copper is more labile than iridium, we hoped to further demonstrate the ligand's resistance to dissociation. The bound ligand is easily deprotonated to form the strongly donating alkoxide form, which is known to stabilize high oxidation states such as Rh(IV)[34] and Ir(IV).[33]

2.2 Synthesis and characterization of $[Cu(pyalkH)_2Cl]^+$ and $Cu(pyalk)_2$

The pyalkH-containing catalyst precursor **1** (**Figure 2.1B**) was generated by treating copper(II) chloride with two equivalents of ligand in acetonitrile/methanol (1:10 v/v). The deprotonated form, **2 (Figure 2.1C)**, was prepared by the addition of 1 M potassium hydroxide to a solution of **1**.

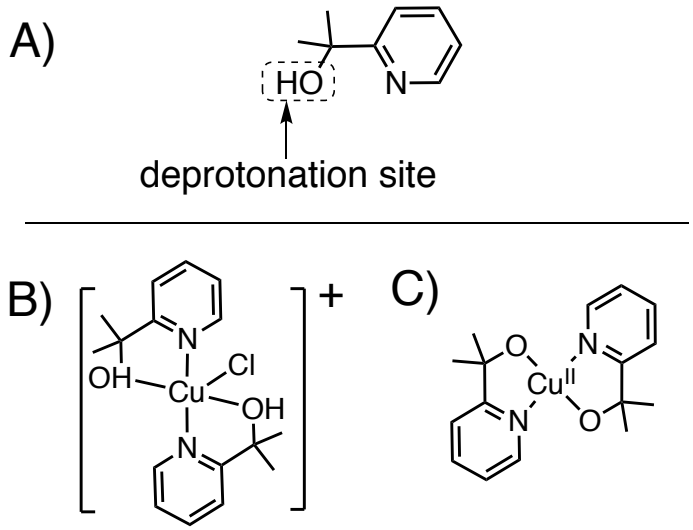

Figure 2.1. Structures of pyalk ligand, $Cu(pyalkH)_2(Cl)^+$, and $Cu(pyalk)_2$. A) Structure of 2-pyridinyl-2-propanol (pyalkH). The ligand can be deprotonated at the highlighted site to produce the highly-donating alkoxide form. B) Structure of $Cu(pyalkH)_2(Cl)^+$ (**1**). C) Structure of $Cu(pyalk)_2$ (**2**).

The X-ray crystal structures of copper-pyalk complexes **1** and **2** are shown in **Figure 2.2A-B**. **1** has a distorted trigonal bipyramidal structure (**Figure 2.2A**). Two pyalkH ligands are bound to the metal center with the fifth coordination site occupied by a chloride ligand. A second chloride serves as a counteranion. **1** has λ_{max} at 710 nm with ε = ~225 M^{-1} cm^{-1} (**Figure 2.2C**). An acetate analogue of **1**, $[Cu(Hpyalk)_2(OAc)](OAc)$ (**3**), was also synthesized (**Figure 2.26**).

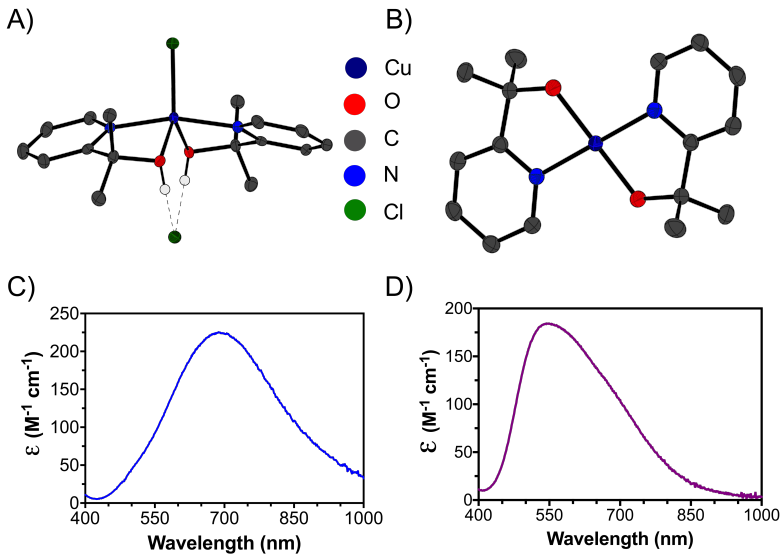

Figure 2.2. Structures and UV-Visible spectra of **1** and **2**. A) X-ray crystal structure of **1**, $[Cu^{II}(pyalkH)_2(Cl)]Cl$, with 50% thermal ellipsoid probability levels. Hydrogens, except those on heteroatoms, are omitted for clarity. B) X-ray crystal structure of **2**, $Cu(pyalk)_2$, with 50% thermal ellipsoid probability levels. Hydrogens are omitted for clarity. C) UV-visible spectrum of **1** in water. D) UV-visible spectrum of **2** in water.

Upon the addition of two equivalents of strong base to a solution of **1**, the pyalkH ligands are deprotonated, and the resulting Cu(II) complex **2** adopts a square planar structure with the pyalk O-donors mutually *trans* (**Figure 2.2B**). **2** displays λ_{max} at 575 nm with ε = ~175 M^{-1} cm^{-1} from pH 8 to 14 (**Figure 2.2D**). λ_{max} varies linearly with complex concentration, consistent with **2** being a single species in solution.[27] Upon the addition of two equivalents of hydrochloric acid, the pyalk ligands of **2** can be protonated to regenerate **1** (**Figure 2.3**). This reversible protonation of the ligand is an attractive feature for a water-oxidation catalyst, as it may allow for proton-coupled electron transfer (PCET), a common reaction step in water oxidation.

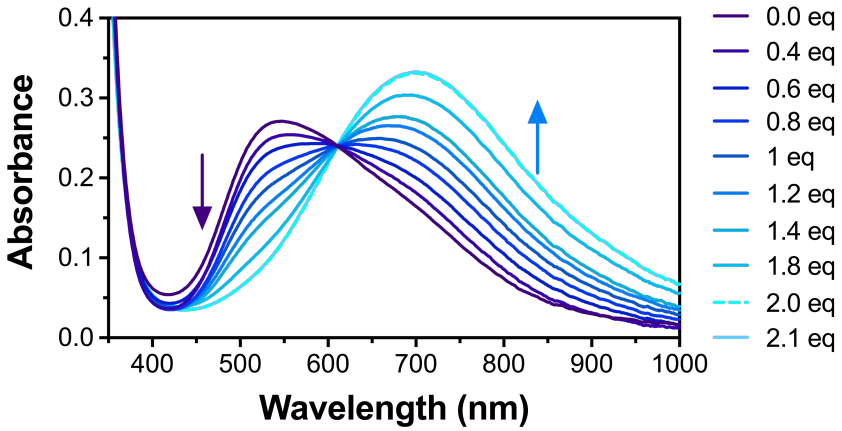

Figure 2.3. Treatment of **2** with increasing equivalents of 1 M HCl to regenerate **1** as monitored by UV-Visible spectroscopy.

2.3 Electrochemical characterization and water oxidation electrocatalysis of **2**

The electrochemical properties of **1** and **2** were probed by cyclic voltammetry (CV) using a boron-doped diamond (BDD) working electrode (**Figure 2.4**). All potentials are reported vs. NHE. Under neutral pH conditions in 0.1 M aqueous KNO_3, **1** displayed no significant redox features. **2** displayed a quasi-reversible couple with $E_{1/2}$ = 1.26 V. Prior work on $Rh^{IV}(pyalk)_3$ demonstrated that the ligand stabilizes high oxidation states without participating directly in housing the electron hole,[34] so this wave was assigned to a Cu(II/III) redox couple as opposed to ligand-centered oxidation. Upon the addition of 0.1 M KOH, a dramatic current enhancement relative to background was observed. Our data suggest that this current enhancement is a result of catalytic water oxidation. The catalytic wave is pH dependent, with the peak position varying by ~-40 mV/pH unit (**Figure 2.10**). The half-peak potential for catalysis between pH 10.4-13.3 ranges from 0.92-1.02 V, leading to an overpotential of 520-580 mV, a range comparable with those of other copper-based electrocatalysts.[31]

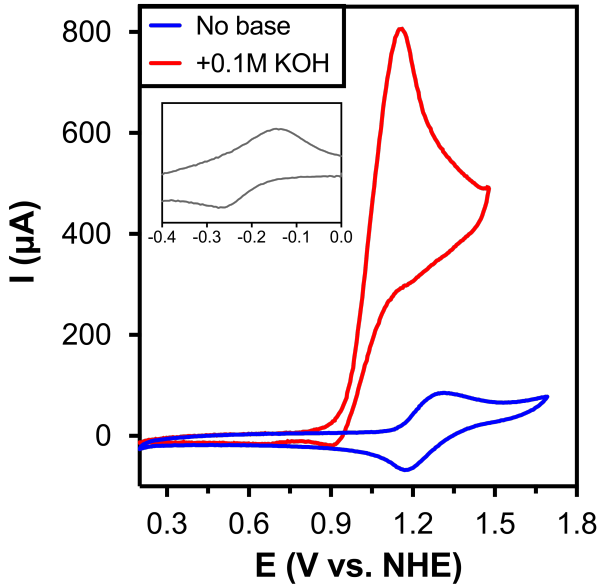

Figure 2.4. CV of **2** (5 mM) in 0.1 M KNO_3/0.1 M KOH at pH 8 *(blue)* and pH 13.3 *(red)*. Conditions: BDD working electrode, Pt wire auxiliary electrode, Ag/AgCl reference electrode, 100 mV/s scan rate. *Inset:* Enlarged view of the quasi-reversible Cu(II/I) couple.

While scanning cathodically under an N_2 atmosphere, **2** shows a quasireversible, scan-rate dependent wave with $E_{1/2}$ = -0.2 V (**Figure 2.4 inset, Figure 2.12**). This process was assigned to the Cu(II/I) couple. Both the catalytic wave and the Cu(II/I) couple are also present when glassy carbon is used as the working electrode (**Figure 2.11**).

Oxygen evolution by **2** was investigated using controlled potential electrolysis (CPE) at 1.1 V using a large surface area ITO working electrode (~1 cm^2). Oxygen evolution was detected using a Clark-type electrode and was monitored at four pH values for 250 s each (**Figure 2.5, Figure 2.13**). No significant oxygen evolution was observed below pH 10.4. The oxygen-evolution rate increased with pH, owing perhaps to the reduced thermodynamic barrier for water oxidation at higher pH values.

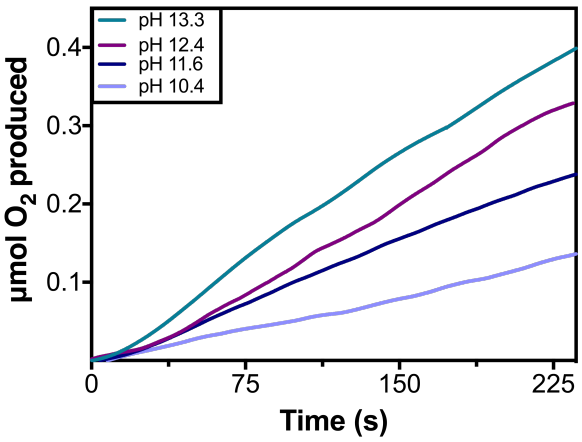

Figure 2.5. Oxygen evolution by **2** (1 mM) at various pH values in 0.1 M KNO_3/KOH. Oxygen evolution due to bare ITO at each pH is subtracted. Conditions: ITO working electrode, Pt wire auxiliary electrode, Ag/AgCl reference electrode, 1.1 V applied potential.

To evaluate the stability of the catalyst over longer periods of time, CPE was performed on a 2 mM solution of catalyst in 0.1 M KNO_3/KOH at pH 12.5. During CPE at 1.1 V for 12 h, current density was maintained at >1 mA/cm^2 (**Figure 2.6B**). The slight decay in current after several hours of electrolysis is attributed to the consumption of OH^- at the electrode, supported by the observed pH drift from 12.5 to ~10 over the course of CPE. The amount of O_2 produced was quantified by gas chromatography (**Figure 2.6A**). After accounting for the O_2 produced by bare ITO, the O_2 produced purely by the catalyst was found to be ~600 µmol, corresponding to >30 catalytic turnovers based on [**2**] in solution. This value is likely a substantial underestimate of the true turnover number, since at any time only a fraction of the catalyst in solution is near enough to the electrode surface to be active for electrocatalysis. Even so, this turnover number is fairly high when compared to similar data from other reported homogeneous copper catalysts;[31-32] thus, **2** can be considered a highly effective and robust catalyst for water oxidation.

Degradation of the catalyst during CPE was monitored by UV-visible spectroscopy. After 12 h of electrolysis, only ~20 % of the catalyst appeared to have degraded (**Figure 2.14**). This degradation is attributed to direct reduction of Cu(II) to Cu(0) on the counter electrode, a result of diffusion of some of the Cu(II) complex through the glass frit connecting the working and counter electrodes, and was visible as copper metal plated on the counter electrode. The Faradaic efficiency of water oxidation was calculated to be ~75% based on the charge passed during

electrolysis. The deviation from ideal efficiency may be explained by the presence of residual O_2 remaining dissolved in solution that would not be detected by headspace sampling.

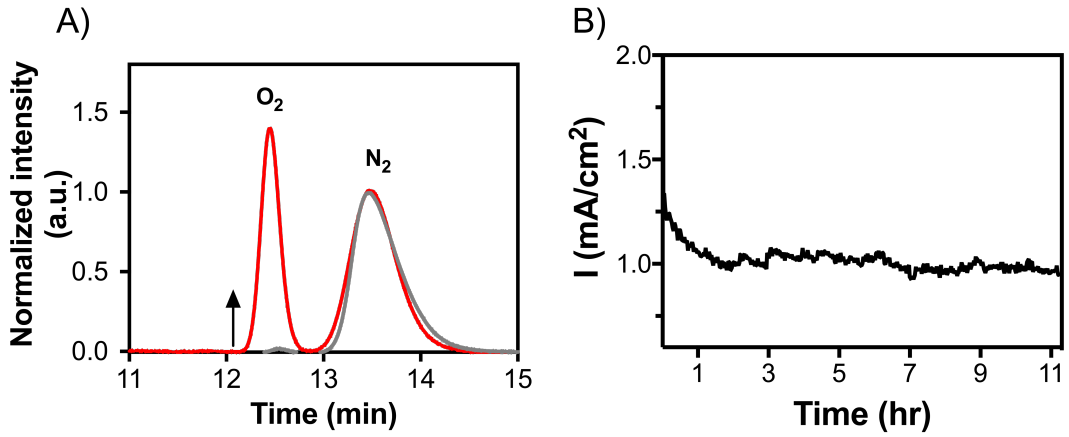

Figure 2.6. Oxygen evolution by **2** over the course of 12 hours. A) GC trace before CPE *(grey)* and after 12 hours of CPE at 1.1 V *(red). Conditions:* ITO working electrode, Pt wire auxiliary electrode, Ag/AgCl reference electrode. B) Catalytic current over 12 hours CPE.

We next wanted to determine if **2** remained homogeneous during catalysis. After 2 h of CPE at an ITO electrode, no particle or film formation was detectable on the surface of the working electrode by scanning electron microscopy (SEM), and no copper was detected by energy dispersive X-ray spectroscopy (EDX) over the surface (**Figure 2.7A-B**).

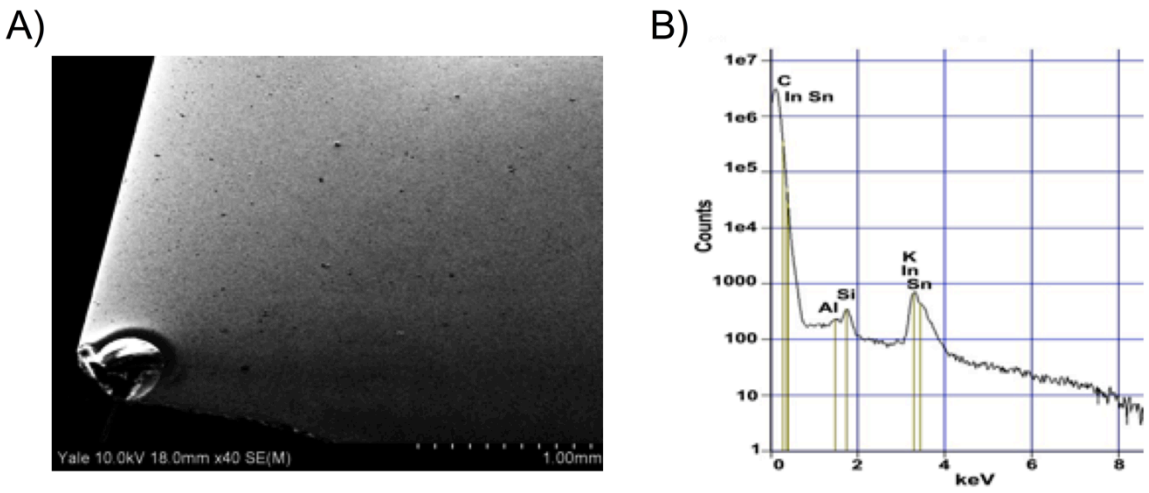

Figure 2.7. SEM and EDX analysis of working electrode following bulk electrolysis. A) SEM image of ITO electrode after 12 h CPE in 0.1 M KNO_3 adjusted to pH 12.5 at 1.2 V. B) EDX spectrum of ITO surface. No traces of Cu were found. The presence of Al and Si in the EDX spectrum is due to the glass substrate.

Additionally, when CPE was performed for 2 h with a BDD electrode on a 1 mM solution of **2** under catalytic conditions, no catalytic activity was observed when the electrode was rinsed and then placed into a fresh, catalyst-free solution (**Figure 2.15**). In addition, catalysis is not due to uncomplexed Cu(II) being formed in solution, as the addition of $Cu(SO_4)_2$ to electrolyte solution at pH 12.5 caused the immediate precipitation of $Cu(OH)_2$. While $Cu(OH)_2$ has some heterogeneous water oxidation activity, the half-peak potential is significantly higher than that of **2**, and the shape of the catalytic wave is significantly different (**Figure 2.16**).

No other homogeneous copper WOCs involving a bis-N,O ligand scaffold appear to be known. In order to compare the catalytic activity of **2** to that of a copper compound of similar geometry and donor types, the related copper(II) picolinate ($Cu(pic)_2$) was prepared. The CV of $Cu(pic)_2$ in 0.1 M KNO_3/KOH at pH 12.5 appeared to show activity for water-oxidation electrocatalysis; however, further inspection revealed the presence of a light blue precipitate in solution and on the electrode after repeated CV cycles. This solid was collected and resuspended in fresh electrolyte, and the resulting CV showed a catalytic wave almost identical to the first, demonstrating that this solid, identified as $Cu(OH)_2$ based on FTIR measurements (**Figure 2.19**, **Figure 2.20**),[38] was responsible for water oxidation (**Figure 2.17**, **Figure 2.18**). $Cu(pic)_2$ is, therefore, not competent for homogeneous water-oxidation catalysis under our conditions. This

result further demonstrates the effectiveness of pyalk as a ligand for homogeneous WOCs, notably in remaining bound under reaction conditions.

2.4 Kinetics and mechanistic insight on electrocatalysis by $Cu(pyalk)_2$

CV measurements of **2** show that the peak catalytic current varies linearly with [**2**] from 0-2 mM at pH 12.5 (**Figure 2.21**). This first order dependence is consistent with a single-site mechanism for water oxidation according to **Equation 2.2**.[39] In **Equation 2.2**, i_{cat} is the catalytic current, n_{cat} is the number of electrons transferred in the catalytic process (n_{cat} = 4 for water oxidation), F is Faraday's constant, A is the electrode surface area, D is the catalyst's diffusion coefficient, and k_{cat} is the pseudo-first order rate constant, often referred to as the turnover frequency (TOF).

$$i_{cat} = n_{cat}FA[Cu]D^{1/2}k_{cat}^{1/2} \qquad \textbf{(Equation 2.2)}$$

As discussed in Chapter 1, k_{cat} can be estimated by comparing the catalytic current to the diffusive current for a reversible process (**Equation 2.3**).[39] In **Equation 2.3**, n is the number of electrons transferred in the reversible process, ν is the scan rate, R is the universal gas constant, and T is the absolute temperature. All other constants are the same as in **Equation 2.2**.

$$i_p = 0.4633n_pFA[Cu]\left(\frac{nFvD}{RT}\right)^{1/2} \qquad \textbf{(Equation 2.3)}$$

Taking the ratio of **Equations 2.2** and **2.3**, substituting in the appropriate constants, and setting n_{cat} = 4 and n_p = 1, results in **Equation 2.4**, which gives a simple relationship between i_c/i_p and the TOF.

$$\frac{i_c}{i_p} = 1.38\sqrt{k_{cat}/_{v}} \qquad \textbf{(Equation 2.4)}$$

For **2**, i_c is the peak catalytic current and i_p is the peak current of the reversible couple. A plot of i_c/i_p vs. $\nu^{-1/2}$ (**Figure 2.22**) was constructed to estimate the TOF. From the slope of the graph, a TOF of ~0.7 s^{-1} at pH 12.5 was estimated, a result comparable to data reported for other copper-

based WOCs.[24, 27, 31] This value of k_{cat} is only an estimate, as the water-oxidation process is far more complicated than this simple model.

The partial water-oxidation product hydrogen peroxide was not observed during or after catalysis. When **2** is treated with hydrogen peroxide, H_2O_2 is rapidly converted to H_2O and O_2, as monitored by a Foxy OceanOptics fluorescence probe (**Figure 2.8**). If any H_2O_2 were formed, it would, therefore, not survive. We cannot exclude the intermediacy of a reactive CuOOH intermediate, as has been suggested for other copper WOCs.[21]

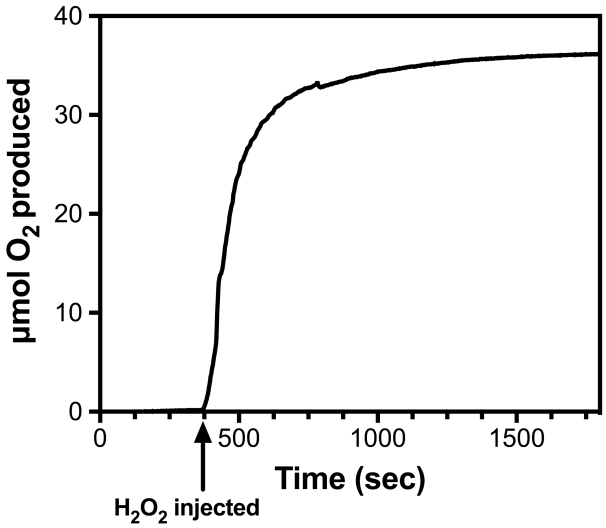

Figure 2.8. Plot of O_2 produced vs. time for a 1 mM aqueous solution of **2** upon addition of 3% H_2O_2 solution**.**

2.5 Conclusions and outlook

In summary, we have described a highly active and robust homogeneous copper water-oxidation electrocatalyst incorporating the oxidation- and dissociation-resistant pyalk ligand. The catalyst operates under basic conditions with an overpotential of 520-580 mV and can perform at least 30 catalytic turnovers with only ~20% catalyst degradation. Electrochemical and SEM/EDX analyses revealed no degradation to $Cu(OH)_2$ or CuO, indicating that **2** remains molecular under electrocatalytic conditions. Electrochemical mechanistic analysis indicates that the catalyst remains monomeric and has a turnover frequency of 0.7 s^{-1} at pH 12.5. **2** is also shown to be able to convert H_2O_2 to H_2O and O_2, suggesting that a copper-hydroperoxo intermediate is possible. Lastly, this study highlights the possibility of using the pyalk ligand to bind earth abundant metals for robust,

inexpensive water-oxidation catalysis. Copper compounds containing similar chelating ligands with weaker donor ability, such as picolinate, were shown to decompose under the same conditions where **2** is active. These results highlight the advantages of incorporating a strong donor ligand onto a first-row metal electrocatalyst for water oxidation.

2.6 Experimental

2.6.1 General

All materials were purchased from Aldrich or Alfa-Aesar and used without further purification unless otherwise noted. All solvents were purchased from commercial vendors. pyalkH was prepared according to literature procedures.[40]

2.6.2 Physical Methods

UV-visible Spectroscopy. Absorption spectra were collected using a Cary 50 spectrophotometer.

ATR-FTIR Spectroscopy. Attenuated total reflectance Fourier transform infrared (ATR-FTIR) spectroscopic measurements were performed using a PIKE technologies GladiATR.

SEM-EDX. A Hitachi SU-70 analytical scanning microscope was used for scanning electron microscopy-energy dispersive X-ray spectroscopy (SEM-EDX) measurements.

Electrochemistry and O_2 Evolution Measurements. Electrochemical measurements were performed using a Pine Wavenow Potentiostat. During cyclic voltammetry or controlled potential electrolysis, a BaSi Ag/AgCl (sat. KCl) or Hg/HgO (1 M NaOH) reference electrode and a Pt auxiliary electrode were used. To convert all measured potentials to the same NHE reference, 0.199 V was added to the Ag/AgCl (saturated KCl) values and 0.140 V was added to the Hg/HgO (1 M NaOH) values.[39]

Short-term O_2 evolution measurements were performed in an air-tight electrochemical cell containing 1 mM **2**, ITO as the working electrode, an Ag/AgCl (saturated with KCl) reference electrode, Pt counter electrode, a Clark-type electrode for O_2 detection, and a 0.1 M KNO3 electrolyte adjusted to the appropriate pH value with 0.1 M KOH. The air-saturated O_2 concentration in water was calculated prior to catalytic measurements and was used to calculate baseline readings. During electrochemical O_2 assays, no applied bias was taken during the first two minutes of each experiment to obtain a baseline reading. After the baseline reading, a bias of 1.10 V vs. NHE was applied to the electrochemical cell to initiate water-oxidation catalysis.

Long term O_2 measurements were performed in an air-tight electrochemical cell containing

ITO as the working electrode, an Ag/AgCl (saturated with NaCl) reference electrode, Pt counter electrode, and a 0.1 M KNO_3 electrolyte adjusted to pH 12.5 with 0.1 M KOH. The 2 mM solution of **2** was thoroughly sparged with N_2 before commencing controlled potential electrolysis (CPE). A bias of 1.10 V vs. NHE was applied to the electrochemical cell for 12 h. Analysis of the gas produced by CPE was done by gas chromatography (Varian-450 GC, He as a carrier gas).

O_2 measurement for the disproportionation of H_2O_2 by **2** was performed with an Ocean Optics MultiFrequency Phase Fluorometer (MFPF-100) outfitted with an Ocean Optics FOXY-R fluorescence probe. A 10 mL of a 1 mM solution of **2** was added to a water-jacketed cell at 25 °C equipped with stir bar. The probe was inserted into the headspace, and the solution was purged with N_2 for several minutes. N_2 was then turned off, and 1 mL of 3% H_2O_2 solution was injected into the cell through the septum. Data points were taken every second.

Single crystal X-ray diffraction. Low-temperature diffraction data (ω-scans) were collected on a Rigaku SCX Mini diffractometer coupled to a Rigaku Mercury275R CCD for the structures **1** and **3**. Similar data were collected on a Rigaku R-AXIS RAPID diffractometer coupled to an R-AXIS RAPID imaging plate detector for the structure of **2**. All sets of data were collected with Mo Kα radiation (λ = 0.71073 Å). The diffraction images were processed and scaled using Rigaku Oxford Diffraction software for **1** and **3** and Rigaku CrystalClear software for **2**.[41-42] The structures were solved with SHELXT and were refined against F^2 on all data by full-matrix least squares with SHELXL.[43] All non-hydrogen atoms were refined anisotropically. Unless stated otherwise, hydrogen atoms were included in the model at geometrically calculated positions and refined using a riding model. The isotropic displacement parameters of all hydrogen atoms were fixed to 1.2 times the U value of the atoms to which they are linked (1.5 times for methyl groups). The full numbering scheme of **1** - **3** can be found in the full details of the X-ray structure determination (CIF), which are included as Supporting Information. CCDC files 1527131 (**1**), 1527133 (**2**), and 1527132 (**3**) contain the supplementary crystallographic data for this paper. These data can be obtained free of charge from The Cambridge Crystallographic Data Center via www.ccdc.cam.ac.uk/data_request/cif.

2.6.3 Synthesis and characterization

Synthesis of $Cu(Hpyalk)_2Cl^+$ (1). The synthesis was adapted from a procedure reported for a similar compound.[44] To a 100 mL round-bottom flask equipped with a stir bar, 0.10 g $CuCl_2$ was added. The solid was dissolved in ~30 mL of MeOH/MeCN (1:10 v/v). To this solution, 0.15 g Hpyalk (2.1 eq) was added. The solution immediately became dark blue and was then allowed to stir at room temperature for 4 h. The solution was then taken to dryness by rotary evaporation, and the solid was redissolved in CH_2Cl_2. This solution was then filtered and crystals were grown from CH_2Cl_2/pentanes. Yield: 0.18 g (60%). Elemental analysis calculated for $CuC_{16}H_{22}N_2O_2Cl_2$: C, 57.20; H, 6.01; N, 8.34. Found: C, 56.90; H, 6.09; N, 8.24.

Synthesis of $Cu(pyalk)_2$ (2). The synthesis was adapted from a procedure reported for a similar compound.[44] To a 100 mL round-bottom flask equipped with a stir bar, 0.50 g $Cu(OAc)_2$ was added. The solid was dissolved in ~30 mL of MeOH/MeCN (1:10 v/v). To this solution, 0.80 g Hpyalk (2.1 eq) was added. The solution immediately became dark blue and was then allowed to stir at room temperature for 2 h, at which point 8 mL 1 M KOH in MeOH was added to the solution. The solution immediately turned purple and was allowed to stir for ~3 h at room temperature, at which point it was taken to dryness via rotary evaporation. The resulting solid was then redissolved in CH_2Cl_2 and filtered. Crystals were grown from CH_2Cl_2/pentane and appeared purple in color. Yield: 0.79 g (85%). Elemental analysis calculated for $CuC_{16}H_{20}N_2O_2$: C, 47.0; H, 5.43; N, 6.85. Found: C, 47.12; H, 5.49; N, 6.74

2 can also be prepared by treating a solution of **1** in MeOH/MeCN (1:10 v/v) with 1 M KOH and purifying as described above.

Synthesis of $Cu(Hpyalk)_2(OAc)^+$ (3). The synthesis was adapted from a procedure reported for a similar compound.[44] To a 100 mL round-bottom flask equipped with a stir bar, 0.15 g $Cu(OAc)_2$ was added. The solid was dissolved in ~30 mL of MeOH/MeCN (1:10 v/v). To this solution, 0.24 g Hpyalk (2.1 eq) was added. The solution immediately became dark blue and was then allowed to stir at room temperature for 4 h. The solution was then taken to dryness by rotary evaporation, and

the solid was then redissolved in CH_2Cl_2. This solution was then filtered and crystals were grown from CH_2Cl_2/pentanes. Yield: 0.25 g (65%).

Synthesis of Cu(picolinate)$_2$. Cu(picolinate)$_2$ was prepared according to a literature procedure.[45] 0.50 g of $CuCl_2$ was dissolved in 10 mL H_2O in a round bottom flask equipped with a stir bar. 0.92 g picolinic acid dissolved in ~10 mL H_2O was then added to this solution, followed by a solution of 0.13 g of NaOH in ~5 mL of water. Upon the addition of base, the solution turned cloudy blue, and this mixture was allowed to stir at room temperature for an additional two hours. The solution was then filtered to afford a bright blue solid. The solid was washed with diethyl ether and then dried under vacuum. Yield: 0.8 g (77%). IR: 3050-2980 (w), 1640 (s), 1600 (s), 1475 (m), 1450 (m), 1345 (s), 1284 (m), 1150 (w), 1045 (m), 848 (m), 771 (s), 690 (s), 555 (w), 460 (m).

Synthesis of Cu(OH)$_2$. 0.50 g $Cu(NO_3)_2 \cdot 3H_2O$ was dissolved in 10 mL deionized water. 2.0 mL 1 M NaOH was added, immediately yielding a blue precipitate. This precipitate was collected, washed with water (3 x 5 mL) and ether (3 x 5 mL), and dried under vacuum. Yield: 0.15 g (75%).

2.7 Supplementary Information

2.7.1 Supplementary Figures

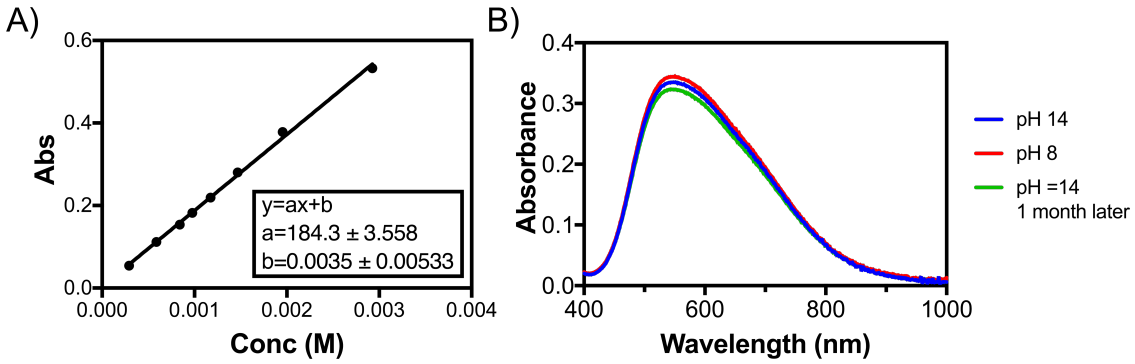

Figure 2.9. UV-Visible and molar absorptivity data for **2**. A) Molar absorptivity plot for absorbance at λ_{max} = 600 nm for **2**. B) UV-visible spectrum of **2** in water at pH 8 (red) and pH 14 (blue). The same sample at pH 14 was kept in aqueous solution for 1 month and its UV-visible spectrum was retaken at that time (green).

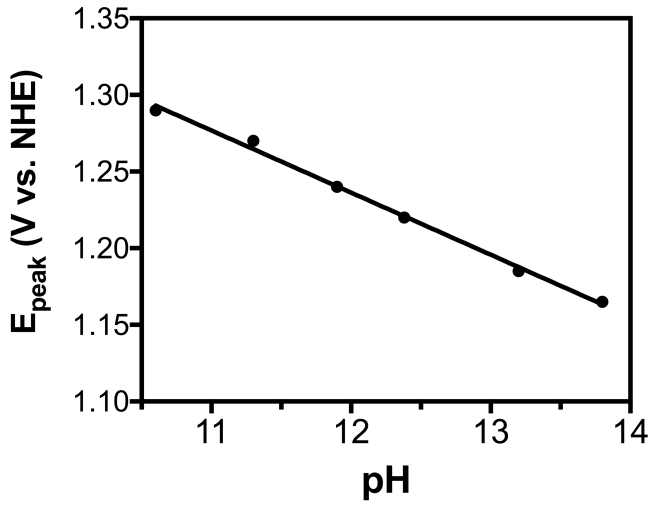

Figure 2.10. pH dependence of the peak of the catalytic wave in 0.1 M KNO_3 adjusted to the appropriate pH with 0.1 M KOH. Boron-doped diamond was used as the working electrode; Pt wire auxiliary electrode; Ag/AgCl (sat'd KCl) reference electrode; scan rate: 100 mV/s.

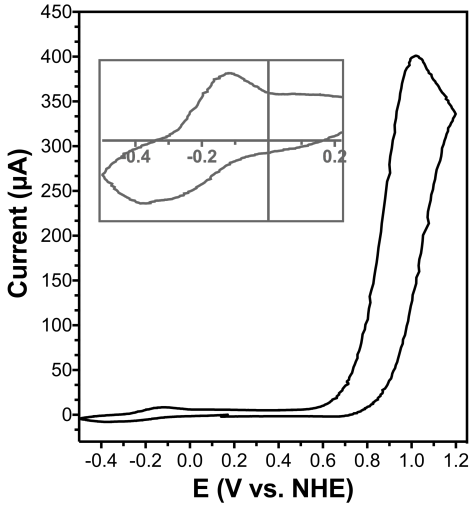

Figure 2.11. CV of 1 mM **2** in 0.1 M KNO_3 adjusted to pH 12.5 with 0.1 M KOH. Glassy carbon was used as the working electrode; Pt wire auxiliary electrode; Ag/AgCl (sat'd KCl) reference electrode; scan rate: 100 mV/s. *Inset*: magnified view of quasi-reversible $Cu^{II/I}$ wave.

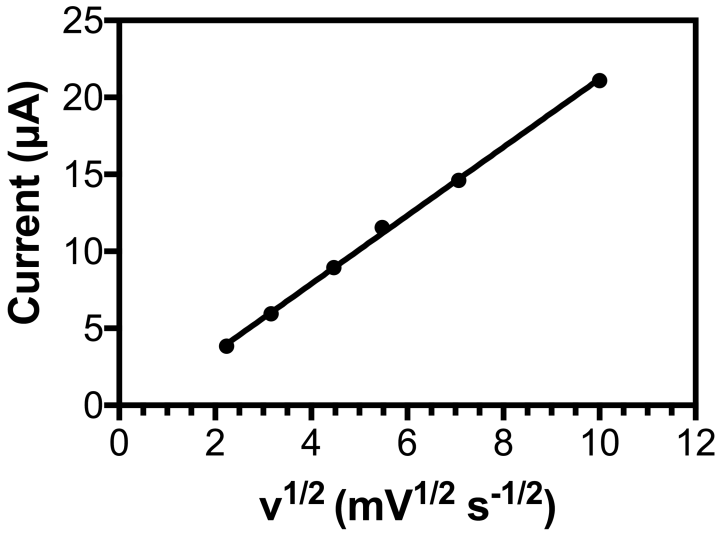

Figure 2.12. Scan rate dependence of peak current of $Cu^{II/I}$ couple in water. Boron-doped diamond was used as the working electrode; Pt wire auxiliary electrode; Ag/AgCl (sat'd KCl) reference electrode.

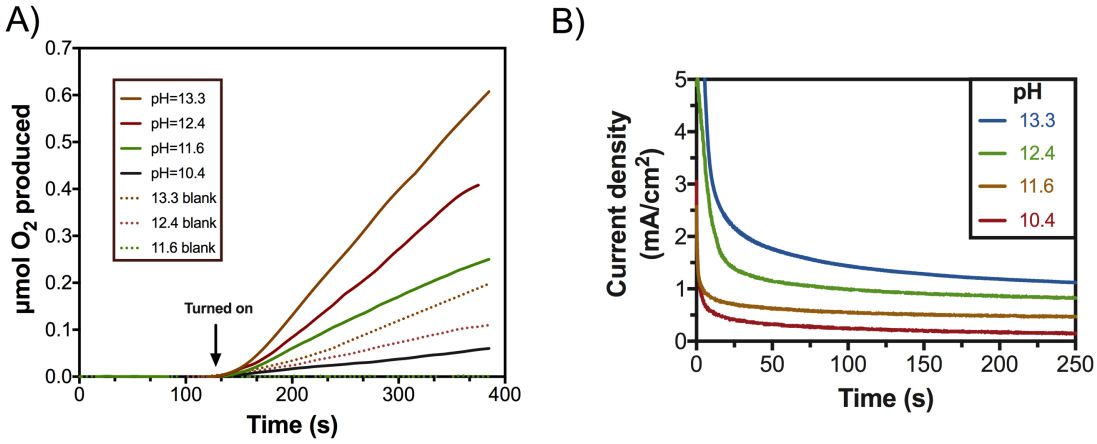

Figure 2.13. Full oxygen evolution and chronoamperometry traces for water oxidation electrocatalysis by **2**, as measured by the Clark electrode. A) Full time course of O_2 evolution from pH-dependent CPE experiments as measured by the Clark electrode. The ITO working electrode was held at 0 V for 120 s and then at 1.2 V for 250 s at each pH. Pt wire as used as the auxiliary electrode and Ag/AgCl (sat'd KCl) was used as the reference electrode. B) Catalytic current at each pH.

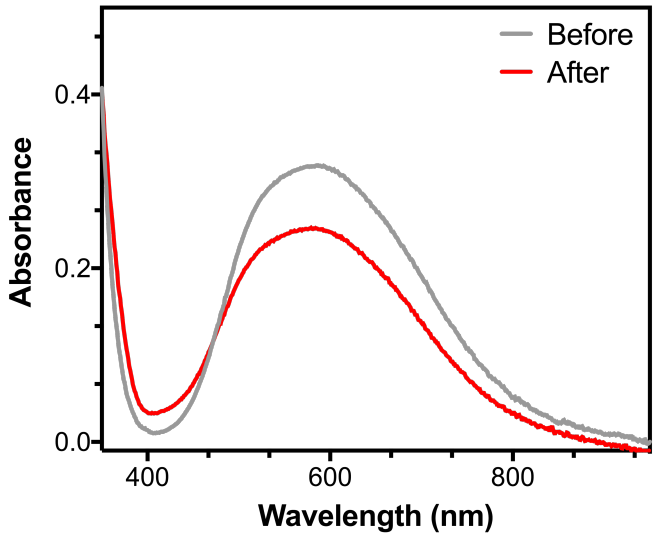

Figure 2.14. UV-visible measurement of **2** in 0.1 M KNO_3/0.1 M KOH at pH 12.5 before and after 12 h CPE. Initial [**2**] was 2 mM.

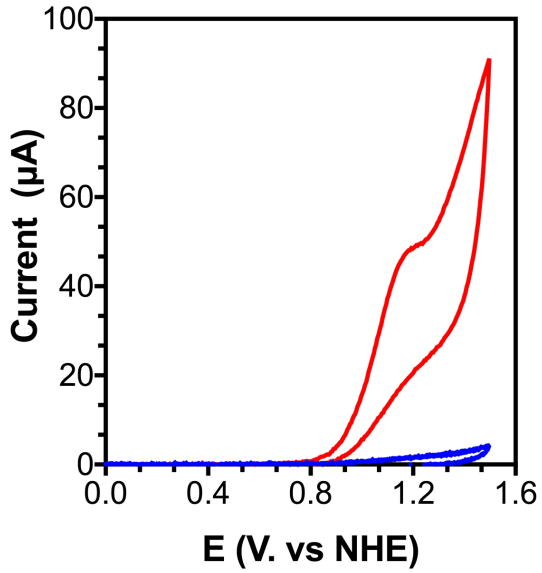

Figure 2.15. Rinse test of **2**. CV of 0.2 mM **2** after 2 h CPE at 1.2 V is shown in red. The electrode was then rinsed, but not polished, and placed in a fresh solution of 0.1 M KNO_3 adjusted to pH 12.5 (blue). Glassy carbon was used as the working electrode; Pt wire auxiliary electrode; Ag/AgCl (sat'd KCl) reference electrode; scan rate: 100 mV/s.

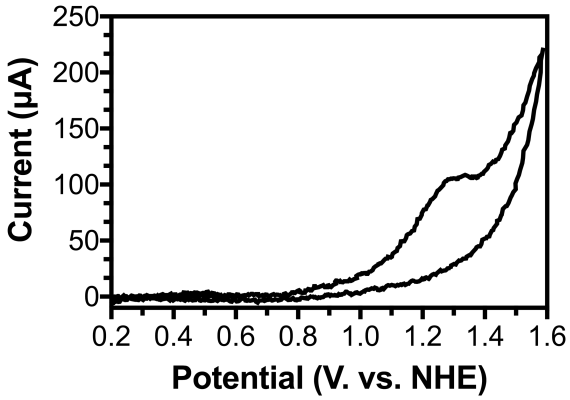

Figure 2.16. CV of 2 mM $Cu(SO_4)_2$ in 0.1 M KNO_3/KOH at pH 12.5. $Cu(OH)_2$ immediately precipitated out of solution upon addition to electrolyte. Boron-doped diamond was used as the working electrode; Pt wire auxiliary electrode; Hg/HgO (1 M NaOH) reference electrode; scan rate: 100 mV/s.

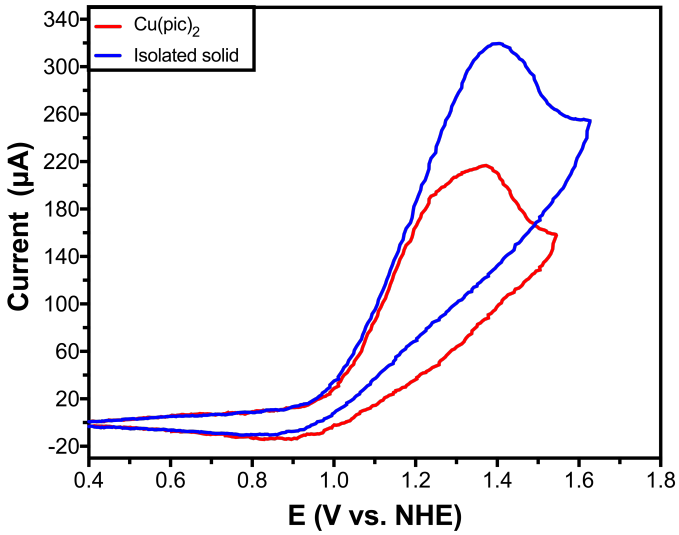

Figure 2.17. Original CV of $Cu(pic)_2$ (red) and CV of the isolated solid (blue) in 0.1 M KNO_3 adjusted to pH 12.5 with 0.1 M KOH. *Conditions:* Boron-doped diamond working electrode, Pt wire auxiliary electrode, Hg/HgO reference electrode (1 M NaOH), scan rate 100 mV/s.

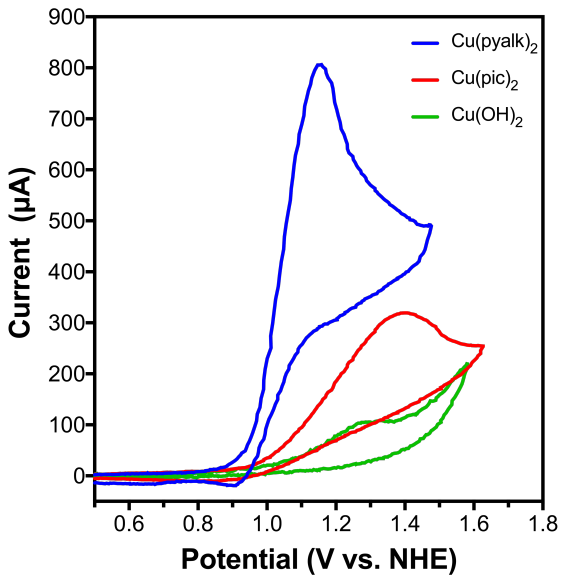

Figure 2.18. CV comparison of **2**, $Cu(pic)_2$, and homemade $Cu(OH)_2$ in 0.1 M KNO_3/KOH at pH 12.5. *Conditions:* Boron-doped diamond working electrode, Pt wire auxiliary electrode, Hg/HgO reference (1 M NaOH) electrode, scan rate 100 mV/s.

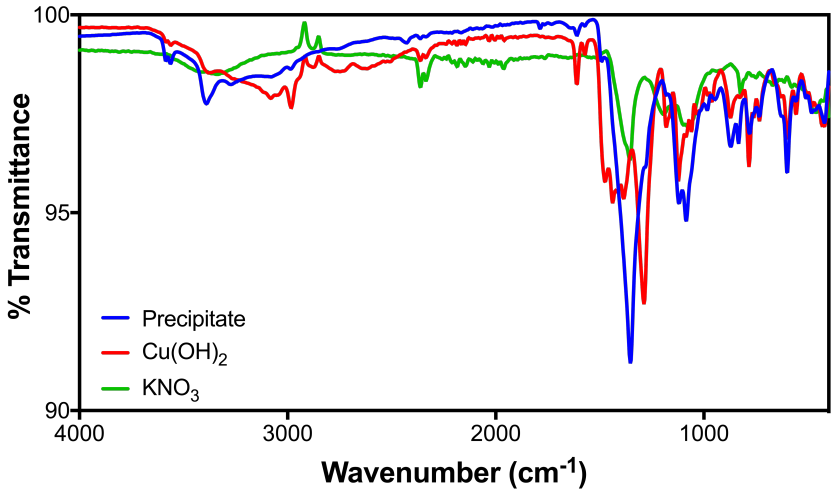

Figure 2.19. FTIR spectra of the precipitate collected from electrochemical studies on $Cu(picolinate)_2$ ("precipitate"), homemade $Cu(OH)_2$, and KNO_3. The peak at 1350 cm^{-1} in the precipitate spectrum is attributed to the NO_3^- anion, which was present in the electrolyte in electrochemical studies. This peak obscures several other peaks present in the $Cu(OH)_2$ spectrum; however, they can be observed as small shoulder peaks in the precipitate spectrum.

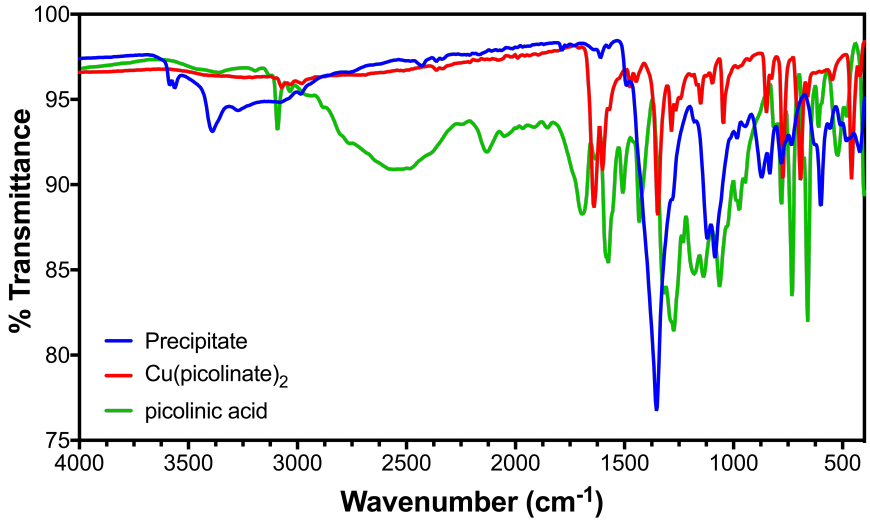

Figure 2.20. FTIR spectra of the precipitate collected from electrochemical studies on $Cu(picolinate)_2$ ("precipitate"), $Cu(picolinate)_2$, and picolinic acid. The lack of the carbonyl stretch at ~1650 cm^{-1} suggests that no ligand is present on the precipitate.

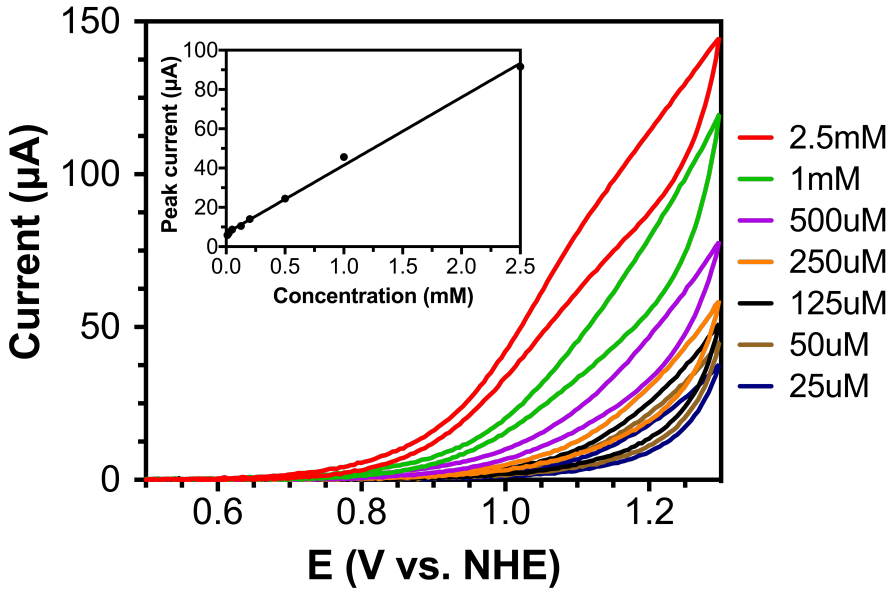

Figure 2.21. Concentration dependence of the catalytic wave at 1.1 V at pH 12.5 with an ITO working electrode in 0.1 M KNO_3/0.1 M KOH. Conditions: Pt wire auxiliary electrode; Ag/AgCl (sat'd KCl) reference electrode; scan rate: 100 mV/s. *Inset:* Plot of concentration vs. peak current.

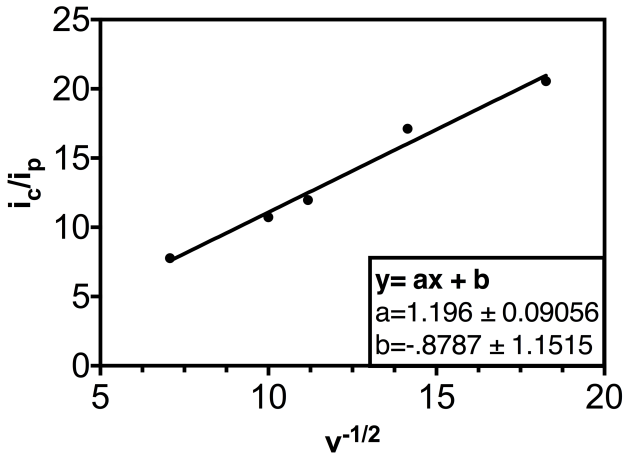

Figure 2.22. Plot of the ratio of the catalytic current at 1.1 V to the peak current for the Cu(II/I) couple vs. $\nu^{-1/2}$. Boron-doped diamond was used as the working electrode; Pt wire auxiliary electrode; Ag/AgCl (sat'd KCl) reference electrode.

2.7.2 Crystallographic details

Refinement details for 1

Hydrogen atoms H1 and H2 were found in the difference map and semi-freely refined with the aid of O-H distance restraints of 0.88(2) Å, as suggested by the difference map. Several low angle reflections were obscured by the beam stop and subsequently omitted.

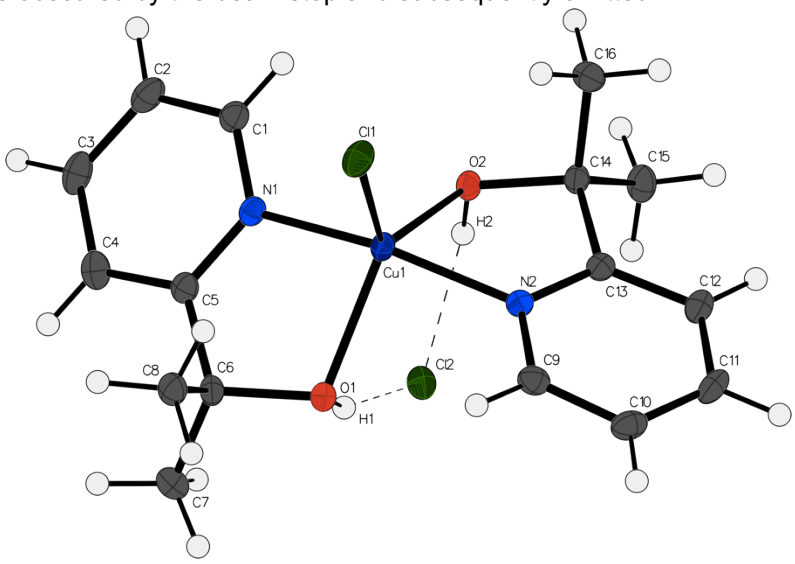

Figure 2.23. Thermal ellipsoid diagram for **1** with complete numbering scheme. Thermal ellipsoids are displayed at the 50% probability level. Hydrogen atoms are shown as circles for clarity.

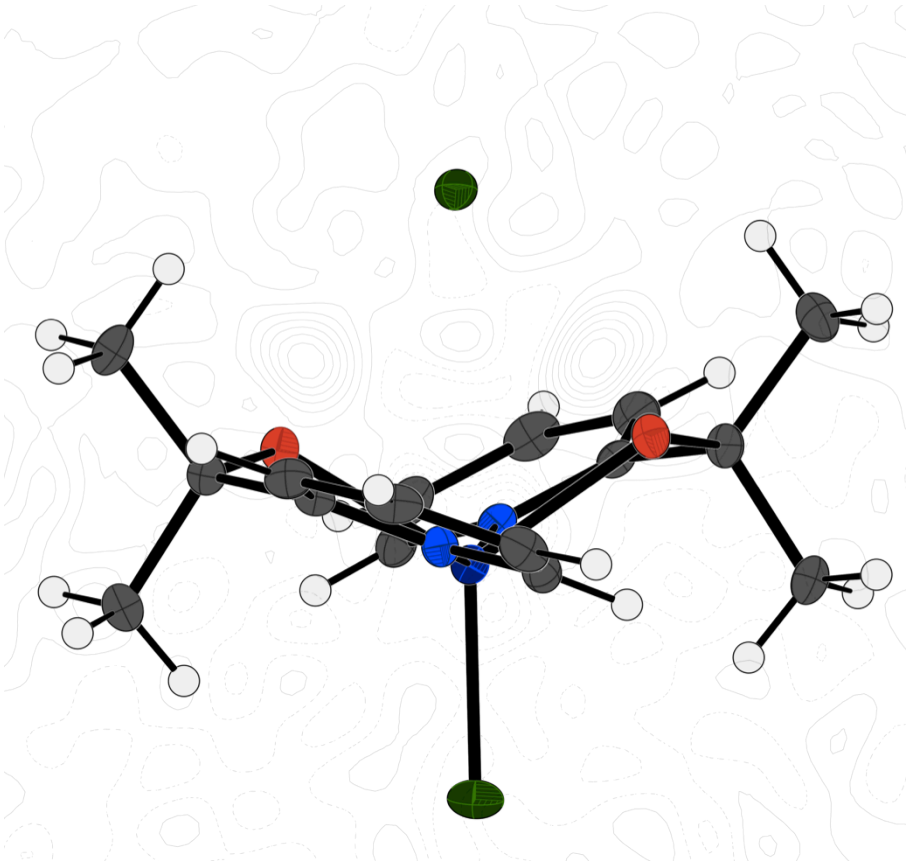

Figure 2.24. Hybrid diagram for **1** with thermal ellipsoid plot and contour electron density difference map. The contour map cross section contains the O1-Cl1-O2 plane. Each contour line corresponds to 0.1 electrons; solid lines represent positive density; dashed lines show negative. Note the density near the oxygen atoms.

Table 2.1. Hydrogen bonds for **1** [Å and °].

D-H...A	d(D-H)	d(H...A)	d(D...A)	<(DHA)
O(1)-H(1)...Cl(2)	0.839(16)	2.222(18)	3.0276(14)	161(2)
O(2)-H(2)...Cl(2)	0.845(17)	2.221(18)	3.0244(13)	159(2)

Table 2.2. Crystal data and structure refinement for **1**.

Identification code	mini-16100	
Empirical formula	$C_{16}H_{22}Cl_2CuN_2O_2$	
Formula weight	408.79	
Temperature	93(2) K	
Wavelength	0.71073 Å	
Crystal system	Triclinic	
Space group	P-1	
Unit cell dimensions	a = 8.1195(3) Å	α= 98.398(3)°.
	b = 10.0975(4) Å	β= 91.768(3)°.
	c = 11.3705(4) Å	γ = 91.545(3)°.
Volume	921.33(6) $Å^3$	
Z	2	
Density (calculated)	1.474 Mg/m^3	
Absorption coefficient	1.484 mm^{-1}	
F(000)	422	
Crystal size	0.300 x 0.080 x 0.010 mm^3	
Θ range for data collection	2.511 to 27.489°.	
Index ranges	-10<=h<=10, -13<=k<=13, -14<=l<=14	
Reflections collected	16202	
Independent reflections	4236 [R(int) = 0.0350]	
Completeness to θ = 25.242°	99.9 %	
Absorption correction	Semi-empirical from equivalents	
Max. and min. transmission	1.00000 and 0.94972	
Refinement method	Full-matrix least-squares on F^2	
Data / restraints / parameters	4236 / 2 / 220	
Goodness-of-fit on F^2	1.097	
Final R indices [I>2σ(I)]	R1 = 0.0294, wR2 = 0.0721	
R indices (all data)	R1 = 0.0351, wR2 = 0.0756	
Largest diff. peak and hole	0.404 and -0.480 e.$Å^{-3}$	

Refinement details for 2

One reflection was recorded improperly due to instrument artifacts and subsequently omitted.

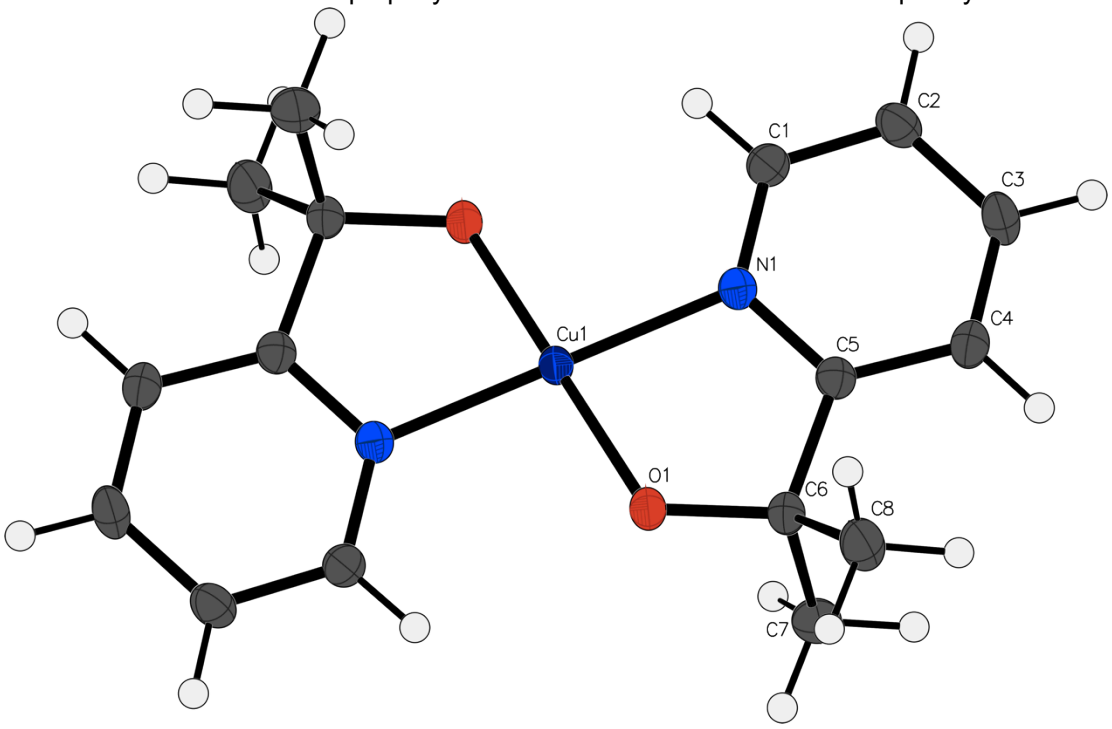

Figure 2.25. Thermal ellipsoid diagram of **2** with complete numbering scheme. Thermal ellipsoids are displayed at the 50% probability level. Hydrogen atoms are shown as circles for clarity. The model is on a special position; only the asymmetric unit is labeled.

Table 2.3. Crystal data and structure refinement for **2**.

Identification code	spider-16041	
Empirical formula	$C_{16}H_{20}CuN_2O_2$	
Formula weight	335.88	
Temperature	93(2) K	
Wavelength	0.71073 Å	
Crystal system	Monoclinic	
Space group	$P2_1/c$	
Unit cell dimensions	a = 8.2113(6) Å	α = 90°
	b = 10.0745(7) Å	β = 109.709(3)°.
	c = 9.9132(7) Å	γ = 90°
Volume	772.03(10) $Å^3$	
Z	2	
Density (calculated)	1.445 Mg/m^3	
Absorption coefficient	1.420 mm^{-1}	
F(000)	350	
Crystal size	0.200 x 0.100 x 0.100 mm^3	
Θ range for data collection	2.635 to 27.478°.	
Index ranges	-10<=h<=10, -13<=k<=13, -12<=l<=12	
Reflections collected	21367	
Independent reflections	1767 [R(int) = 0.0888]	
Completeness to θ = 25.242°	99.4 %	
Absorption correction	Semi-empirical from equivalents	
Max. and min. transmission	1.000 and 0.686	
Refinement method	Full-matrix least-squares on F^2	
Data / restraints / parameters	1767 / 0 / 99	
Goodness-of-fit on F^2	0.894	
Final R indices [I>2σ(I)]	R1 = 0.0239, wR2 = 0.0571	
R indices (all data)	R1 = 0.0304, wR2 = 0.0576	
Largest diff. peak and hole	0.611 and -0.274 e.$Å^{-3}$	

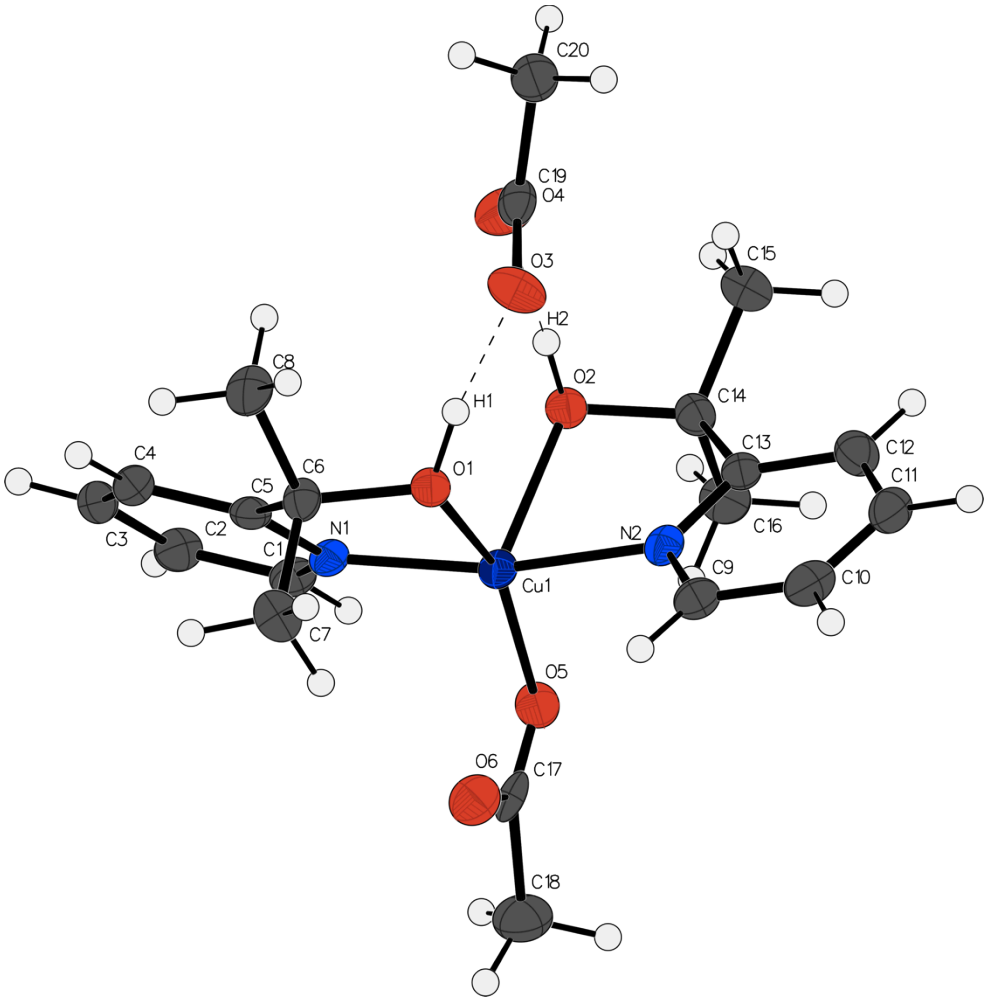

Figure 2.26. Thermal ellipsoid diagram of **3** with complete numbering scheme. Thermal ellipsoids are displayed at the 50% probability level. The hydrogen atoms are shown as circles for clarity.

Table 2.4. Crystal data and structure refinement for **3**.

Identification code	spider-16037	
Empirical formula	C20 H28 Cu N2 O6	
Formula weight	455.98	
Temperature	93(2) K	
Wavelength	0.71073 Å	
Crystal system	Monoclinic	
Space group	$P2_1/c$	
Unit cell dimensions	a = 9.1208(6) Å	α = 90°
	b = 8.2890(6) Å	β = 90.145(2)°
	c = 27.951(2) Å	γ = 90°
Volume	2113.2(3) $Å^3$	
Z	4	
Density (calculated)	1.433 Mg/m^3	
Absorption coefficient	1.072 mm^{-1}	
F(000)	956	
Crystal size	0.300 x 0.300 x 0.020 mm^3	
Theta range for data collection	2.563 to 25.025°.	
Index ranges	-10<=h<=10, -9<=k<=9, -33<=l<=33	
Reflections collected	41237	
Independent reflections	3720 [R(int) = 0.1207]	
Completeness to theta = 25.025°	99.7 %	
Absorption correction	Semi-empirical from equivalents	
Max. and min. transmission	1.000 and 0.551	
Refinement method	Full-matrix least-squares on F^2	
Data / restraints / parameters	3720 / 2 / 276	
Goodness-of-fit on F^2	0.816	
Final R indices [I>2sigma(I)]	R1 = 0.0276, wR2 = 0.0574	
R indices (all data)	R1 = 0.0408, wR2 = 0.0587	
Largest diff. peak and hole	0.458 and -0.509 $e.Å^{-3}$	

2.8 References

1. Bard, A. J.; Fox, M. A., Artificial Photosynthesis: Solar Splitting of Water to Hydrogen and Oxygen. *Acc. Chem. Res.* **1995,** *28* (3), 141-145.
2. Young, K. J.; Martini, L. A.; Milot, R. L.; Snoeberger III, R. C.; Batista, V. S.; Schmuttenmaer, C. A.; Crabtree, R. H.; Brudvig, G. W., Light-Driven Water Oxidation for Solar Fuels. *Coord. Chem. Rev.* **2012,** *256* (21–22), 2503-2520.
3. Eisenberg, R.; Gray, H. B., Preface on Making Oxygen. *Inorg. Chem.* **2008,** *47* (6), 1697-1699.
4. Kärkäs, M. D.; Johnston, E. V.; Verho, O.; Åkermark, B., Artificial Photosynthesis: From Nanosecond Electron Transfer to Catalytic Water Oxidation. *Acc. Chem. Res.* **2014,** *47* (1), 100-111.
5. Kärkäs, M. D.; Verho, O.; Johnston, E. V.; Åkermark, B., Artificial Photosynthesis: Molecular Systems for Catalytic Water Oxidation. *Chem. Rev.* **2014,** *114* (24), 11863-12001.
6. Blakemore, J. D.; Crabtree, R. H.; Brudvig, G. W., Molecular Catalysts for Water Oxidation. *Chem. Rev.* **2015,** *115* (23), 12974-13005.
7. Gersten, S. W.; Samuels, G. J.; Meyer, T. J., Catalytic Oxidation of Water by an Oxo-Bridged Ruthenium Dimer. *J. Am. Chem. Soc.* **1982,** *104* (14), 4029-4030.
8. Gilbert, J. A.; Eggleston, D. S.; Murphy, W. R.; Geselowitz, D. A.; Gersten, S. W.; Hodgson, D. J.; Meyer, T. J., Structure and Redox Properties of the Water-Oxidation Catalyst $[(bpy)_2(OH_2)RuORu(OH_2)(bpy)_2]^{4+}$. *J. Am. Chem. Soc.* **1985,** *107* (13), 3855-3864.
9. McDaniel, N. D.; Coughlin, F. J.; Tinker, L. L.; Bernhard, S., Cyclometalated Iridium(III) Aquo Complexes: Efficient and Tunable Catalysts for the Homogeneous Oxidation of Water. *J. Am. Chem. Soc.* **2008,** *130* (1), 210-217.
10. Hull, J. F.; Balcells, D.; Blakemore, J. D.; Incarvito, C. D.; Eisenstein, O.; Brudvig, G. W.; Crabtree, R. H., Highly Active and Robust Cp* Iridium Complexes for Catalytic Water Oxidation. *J. Am. Chem. Soc.* **2009,** *131* (25), 8730-8731.
11. Blakemore, J. D.; Schley, N. D.; Balcells, D.; Hull, J. F.; Olack, G. W.; Incarvito, C. D.; Eisenstein, O.; Brudvig, G. W.; Crabtree, R. H., Half-Sandwich Iridium Complexes for Homogeneous Water-Oxidation Catalysis. *J. Am. Chem. Soc.* **2010,** *132* (45), 16017-16029.
12. Naruta, Y.; Sasayama, M.-a.; Sasaki, T., Oxygen Evolution by Oxidation of Water with Manganese Porphyrin Dimers. *Angew. Chem. Int. Ed.* **1994,** *33* (18), 1839-1841.
13. Limburg, J.; Vrettos, J. S.; Liable-Sands, L. M.; Rheingold, A. L.; Crabtree, R. H.; Brudvig, G. W., A Functional Model for O-O Bond Formation by the O_2-Evolving Complex in Photosystem II. *Science* **1999,** *283* (5407), 1524-7.
14. Ellis, W. C.; McDaniel, N. D.; Bernhard, S.; Collins, T. J., Fast Water Oxidation Using Iron. *J. Am. Chem. Soc.* **2010,** *132* (32), 10990-10991.
15. Fillol, J. L.; Codolà, Z.; Garcia-Bosch, I.; Gómez, L.; Pla, J. J.; Costas, M., Efficient Water Oxidation Catalysts Based on Readily Available Iron Coordination Complexes. *Nat. Chem.* **2011,** *3* (10), 807-813.
16. Dogutan, D. K.; McGuire, R.; Nocera, D. G., Electocatalytic Water Oxidation by Cobalt(III) Hangman β-Octafluoro Corroles. *J. Am. Chem. Soc.* **2011,** *133* (24), 9178-9180.
17. Wasylenko, D. J.; Ganesamoorthy, C.; Borau-Garcia, J.; Berlinguette, C. P., Electrochemical Evidence for Catalytic Water Oxidation Mediated by a High-Valent Cobalt Complex. *Chem. Commun.* **2011,** *47* (14), 4249-4251.
18. Zhang, M.; Zhang, M.-T.; Hou, C.; Ke, Z.-F.; Lu, T.-B., Homogeneous Electrocatalytic Water Oxidation at Neutral pH by a Robust Macrocyclic Nickel(II) Complex. *Angew. Chem. Int. Ed.* **2014,** *53* (48), 13042-13048.
19. Han, Y.; Wu, Y.; Lai, W.; Cao, R., Electrocatalytic Water Oxidation by a Water-Soluble Nickel Porphyrin Complex at Neutral pH with Low Overpotential. *Inorg. Chem.* **2015,** *54* (11), 5604-5613.
20. Barnett, S. M.; Goldberg, K. I.; Mayer, J. M., A Soluble Copper-Bipyridine Water-Oxidation Electrocatalyst. *Nat. Chem.* **2012,** *4* (6), 498-502.
21. Zhang, M. T.; Chen, Z.; Kang, P.; Meyer, T. J., Electrocatalytic Water Oxidation with a Copper(II) Polypeptide Complex. *J. Am. Chem. Soc.* **2013,** *135* (6), 2048-51.

22. Lewis, E. A.; Tolman, W. B., Reactivity of Dioxygen−Copper Systems. *Chem. Rev.* **2004,** *104* (2), 1047-1076.
23. Fu, L.-Z.; Fang, T.; Zhou, L.-L.; Zhan, S.-Z., A Mononuclear Copper Electrocatalyst for Both Water Reduction and Oxidation. *RSC Adv.* **2014,** *4* (96), 53674-53680.
24. Garrido-Barros, P.; Funes-Ardoiz, I.; Drouet, S.; Benet-Buchholz, J.; Maseras, F.; Llobet, A., Redox Non-Innocent Ligand Controls Water Oxidation Overpotential in a New Family of Mononuclear Cu-Based Efficient Catalysts. *J. Am. Chem. Soc.* **2015,** *137* (21), 6758-6761.
25. Liu, X.; Zheng, H.; Sun, Z.; Han, A.; Du, P., Earth-Abundant Copper-Based Bifunctional Electrocatalyst for Both Catalytic Hydrogen Production and Water Oxidation. *ACS Catal.* **2015,** *5* (3), 1530-1538.
26. Lu, C.; Du, J.; Su, X.-J.; Zhang, M.-T.; Xu, X.; Meyer, T. J.; Chen, Z., Cu(II) Aliphatic Diamine Complexes for Both Heterogeneous and Homogeneous Water Oxidation Catalysis in Basic and Neutral Solutions. *ACS Catal.* **2016,** *6* (1), 77-83.
27. Su, X. J.; Gao, M.; Jiao, L.; Liao, R. Z.; Siegbahn, P. E.; Cheng, J. P.; Zhang, M. T., Electrocatalytic Water Oxidation by a Dinuclear Copper Complex in a Neutral Aqueous Solution. *Angew Chem Int Ed Engl* **2015,** *54* (16), 4909-14.
28. Xiang, R. J.; Wang, H. Y.; Xin, Z. J.; Li, C. B.; Lu, Y. X.; Gao, X. W.; Sun, H. M.; Cao, R., A Water-Soluble Copper-Polypyridine Complex as a Homogeneous Catalyst for Both Photo-Induced and Electrocatalytic O_2 Evolution. *Chem. Eur. J* **2016,** *22* (5), 1602-7.
29. Yu, F.; Li, F.; Hu, J.; Bai, L.; Zhu, Y.; Sun, L., Electrocatalytic Water Oxidation by a Macrocyclic Cu(Ii) Complex in Neutral Phosphate Buffer. *Chem Commun (Camb)* **2016,** *52* (68), 10377-80.
30. Yu, W. B.; He, Q. Y.; Ma, X. F.; Shi, H. T.; Wei, X., A New Copper Species Based on an Azo-Compound Utilized as a Homogeneous Catalyst for Water Oxidation. *Dalton Trans.* **2015,** *44* (1), 351-8.
31. Zhang, T.; Wang, C.; Liu, S.; Wang, J. L.; Lin, W., A Biomimetic Copper Water Oxidation Catalyst with Low Overpotential. *J. Am. Chem. Soc.* **2014,** *136* (1), 273-81.
32. Coggins, M. K.; Zhang, M. T.; Chen, Z.; Song, N.; Meyer, T. J., Single-Site Copper(II) Water Oxidation Electrocatalysis: Rate Enhancements with HPO_4^{2-} as a Proton Acceptor at pH 8. *Angew. Chem. Int. Ed.* **2014,** *53* (45), 12226-30.
33. Shopov, D. Y.; Rudshteyn, B.; Campos, J.; Batista, V. S.; Crabtree, R. H.; Brudvig, G. W., Stable Iridium(IV) Complexes of an Oxidation-Resistant Pyridine-Alkoxide Ligand: Highly Divergent Redox Properties Depending on the Isomeric Form Adopted. *J. Am. Chem. Soc.* **2015,** *137* (22), 7243-7250.
34. Sinha, S. B.; Shopov, D. Y.; Sharninghausen, L. S.; Vinyard, D. J.; Mercado, B. Q.; Brudvig, G. W.; Crabtree, R. H., A Stable Coordination Complex of Rh(IV) in an N,O-Donor Environment. *J. Am. Chem. Soc.* **2015,** *137* (50), 15692-15695.
35. Michaelos, T. K.; Lant, H. M. C.; Sharninghausen, L. S.; Craig, S. M.; Menges, F. S.; Mercado, B. Q.; Brudvig, G. W.; Crabtree, R. H., Catalytic Oxygen Evolution from Manganese Complexes with an Oxidation-Resistant N,N,O-Donor Ligand. *ChemPlusChem* **2016,** *81* (10), 1129-1132.
36. Michaelos, T. K.; Shopov, D. Y.; Sinha, S. B.; Sharninghausen, L. S.; Fisher, K. J.; Lant, H. M. C.; Crabtree, R. H.; Brudvig, G. W., A Pyridine Alkoxide Chelate Ligand That Promotes Both Unusually High Oxidation States and Water-Oxidation Catalysis. *Acc. Chem. Res.* **2017,** *50* (4), 952-959.
37. Thomsen, J. M.; Huang, D. L.; Crabtree, R. H.; Brudvig, G. W., Iridium-Based Complexes for Water Oxidation. *Dalton Trans.* **2015,** *44* (28), 12452-12472.
38. Lee, S. M.; Ryu, S. K.; Jung, C. H.; Won, H. J.; Oh, W. Z., The Effects of Picolinic Acid and pH on the Adsorption of Cu(II) by Activated Carbon Fibers. *Carbon* **2002,** *40* (3), 329-334.
39. Bard, A. J.; Faulkner, L. R., *Electrochemical Methods: Fundamentals and Applications*. 2nd ed.; Wiley: Hoboken, NJ, 2000.
40. Wong, Y.-L.; Yang, Q.; Zhou, Z.-Y.; Kay Lee, H.; Mak, T. C. W.; Ng, D. K. P., Synthesis, Structure and Oxo-Transfer Properties of Dioxotungsten(VI) Complexes with Pyridine-Based No- and NS-Bidentate Ligands. *New J. Chem.* **2001,** *25* (2), 353-357.
41. MSC, R. *Crystalclear*, The Woodlands, TX, 2005, 2005.
42. Diffraction, R. O. *Crysalispro*, The Woodlands, TX, 2015.

43. Sheldrick, G. M., A Short History of Shelx. *Acta Cryst.* **2008,** *64*, 112-122.
44. Antonioli, B.; Bray, D. J.; Clegg, J. K.; Jolliffe, K. A.; Gloe, K.; Gloe, K.; Lindoy, L. F., Proton and Anion Control of Framework Complexity in Copper(II) Complex Structures Derived from 2-(Hydroxymethyl)Pyridine. *Polyhedron* **2007,** *26* (3), 673-678.
45. Jeon, I.-R.; Ababei, R.; Lecren, L.; Li, Y.-G.; Wernsdorfer, W.; Roubeau, O.; Mathoniere, C.; Clerac, R., Two-Dimensional Assembly of $[Mn(III)_2\ Mn(II)_2]$ Single-Molecule Magnets and $[Cu(pic)_2]$ Linking Units (Hpic = Picolinic Acid). *Dalton Trans.* **2010,** *39* (20), 4744-4746.

3 Chapter 3. The water-nucleophilic attack mechanism for the $Cu(pyalk)_2$ water-oxidation electrocatalyst

This work is adapted from Rudshteyn, B.; Fisher, K. J.; Lant, H. M. C.; Yang, K. R.; Mercado, B. Q.; Brudvig, G. W.; Crabtree, R. H.; Batista, V. S. *ACS Catal.* **2018,** *8* (9), 7952-7960. BR performed all calculations. KJF performed KIE experiments and analyzed electrochemical data. HMCL synthesized bipydialk ligand and KJF and HMCL made Cu(bipydialk) and performed electrochemical experiments. BR and KJF wrote the manuscript. Reprinted with minor modifications with permission from the American Chemical Society, 2018.

3.1 Introduction

In the development of solar fuels devices, efficient and robust water-oxidation catalysts are required,[1-3] as discussed in the previous chapters. Compared to heterogeneous catalysts, molecular catalysts have the distinct advantage of tunability through their ligand framework, and as such modification of the ligand scaffold can be used to modulate catalytic parameters such as rate or selectivity, for example. In order to most efficiently tune molecular catalysts, the active form of the catalyst must be known and the mechanism by which the catalyst operates should be understood. Systematic investigation of catalytic mechanism, however, is often challenging, as intermediates in the catalytic cycle are often short-lived and reactive, making them challenging to observe even spectroscopically.[4-6] One notable example of a water-oxidation catalyst whose active form is still unknown is the iridium-based “blue solution” discussed in Chapter 1.[7] Due to the presence of many non-interconverting isomers in the blue solution, the exact structure of the active catalyst has yet to be determined directly through experiment.

One approach to studying the mechanisms of water-oxidation catalysts is through experimental-theoretical collaborations. Theory can give insight into the identitiy of the active catalytic species, plausible intermediates, and mechanistic pathways. Experimental results can support or rule out these possibilities. For example, through collaborative theoretical and experimental efforts, the solution structures of the blue solution catalysts have been determined, and these proposed structures are consistent with EXAFS data.[8]

Recent efforts in the water-oxidation community have focused on developing WOCs which incorporate Earth-abundant metal centers, including manganese[9-11] and copper.[12-13] However, the underlying reaction mechanisms for many of these catalysts has yet to be established. In fact, little

is known about the mechanism of electrocatalytic water oxidation by many copper complexes despite the first molecular copper water-oxidation electrocatalyst being reported in 2012.[12] In this chapter, we focus on elucidating the mechanism of water-oxidation electrocatalysis by $Cu(pyalk)_2$ (**1**), which is a robust and active electrocatalyst under basic conditions, as discussed in the previous chapter. Earlier, we found that that the catalyst has a TOF of 0.7 s^{-1}, at pH = 12.5, and observed that the catalyst remains active for over 30 turnovers with minimal degradation.[13] However, neither the active form of the catalyst nor the catalytic mechanism were resolved in our initial study. In this chapter, we find that only the *cis* isomer, **2** (**Figure 3.1**), is active for water-oxidation catalysis.

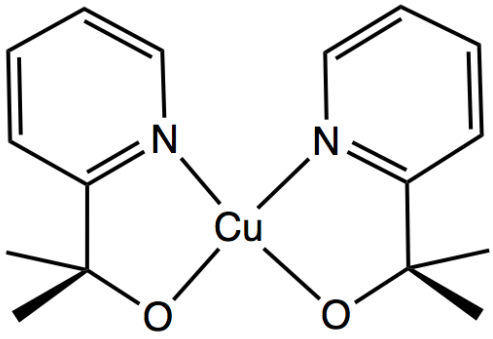

Figure 3.1. The structure of the proposed active water-oxidation electrocatalyst: *cis* $Cu^{II}(pyalk)_2$, **(2)**.

We also examine plausible mechanisms for water-oxidation catalysis by **2**. Three commonly proposed water-oxidation mechanisms for transition metal catalysts include the water-nucleophilic attack (WNA) on metal-oxo or metal-oxyl-radical species,[14-15] direct coupling of two M=O or two radical M—O• groups,[16] and redox isomerization.[17] Here, we explore whether any of these mechanisms could apply to water-oxidation electrocatalysis by $Cu(pyalk)_2$.

A recent study of dimeric copper WOCs suggested that a dinuclear water-nucleophilic attack or a redox-isomerization pathway may play a major role in some copper-based electrocatalytic water oxidation.[17] Many copper WOCs, however, have been shown to have first-order kinetics in catalyst concentration over a wide concentration range, suggesting that a mononuclear pathway may be viable.[12] Such a pathway could likely occur through a Cu(III)-oxyl radical intermediate, rather than a Cu(IV)-oxo intermediate, consistent with the “oxo wall” concept

(no tetragonal terminal oxo species have been isolated for any transition metal from group 9 onwards).[18] Such oxyl radical species have been suggested[19] but never observed experimentally.

In this chapter, we propose a plausible water-oxidation mechanism based on water-nucleophilic attack for the tautomeric *cis* form **2** that is consistent with density functional theory calculations and experimental measurements of turnover frequency, H/D kinetic isotope effects, foot-of-the-wave analysis, and synthesis of related derivatives. The catalytic process has the following interesting aspects: (a) the pyalk alkoxide group is a non-innocent ligand that activates the water nucleophile by acting as a base, facilitating water deprotonation; (b) the *cis* isomer, **2**, is the active form of the catalyst despite the *trans* form being the more stable crystallized form; and (c) an uncommon Cu(III)-oxyl radical intermediate is involved. The resulting mechanism accounts for the multiple oxidation state changes that are required for water oxidation, offering fundamental insights valuable for development of Earth-abundant water-oxidation catalysts.

3.2 Computational validation of model chemistry (in collaboration with Ben Rudshteyn)

Table 3.1 shows that the minimum energy structure obtained at the DFT ωB97X-D/(def2-SVP,6-31+G(d,p)) level in the gas-phase reproduces the crystal structure of **1**. **Figure 3.2** shows that the same level of theory reproduces the experimental UV-Visible absorption features in water, using either isomer, suggesting the presence of both isomers in water.

Table 3.1. Average theoretical (Theor.) bond lengths, bond angles, and dihedrals of **1** (without hydrogen-bonding waters) in the gas phase as compared to experimental values (Expt). *intra* indicates a bond angle defined within 1 pyalk ligand whereas *inter* indicates a bond angle defined spanning 2 pyalk ligands.

	Cu-N	**Cu-O**	**N-O-Cu (*intra*)**	**N-O-Cu (*inter*)**	**N-C-C-O**
Theor.	1.99 Å	1.89 Å	83.7°	96.3°	0°
Expt.	1.972(2) Å	1.883(1) Å	84.04(5)°	95.96°	-6.528°

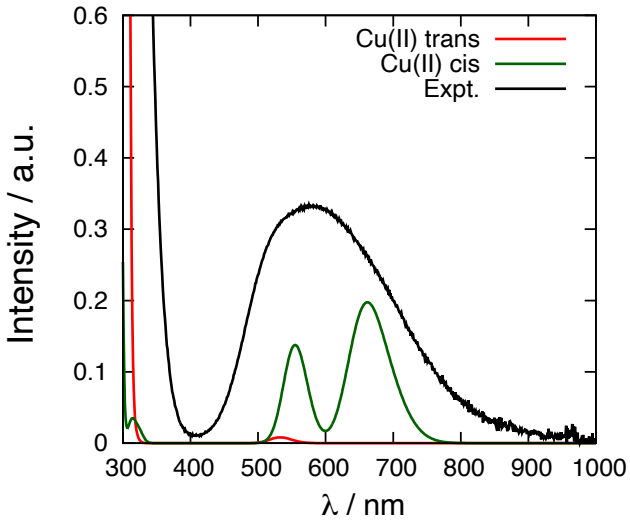

Figure 3.2. Computed UV-Vis spectra for *trans* (**1**) and *cis* (**2**) as compared to the experimental spectrum of a 2 mM sample in water.

3.3 Water-nucleophilic attack mechanism

Scheme 3.1 shows the mechanism appropriate for basic solutions predicted by DFT calculations, which includes bulk solvation from the dielectric continuum model as well as direct solvation by two hydrogen-bonded waters to the pyalk oxygen atoms.

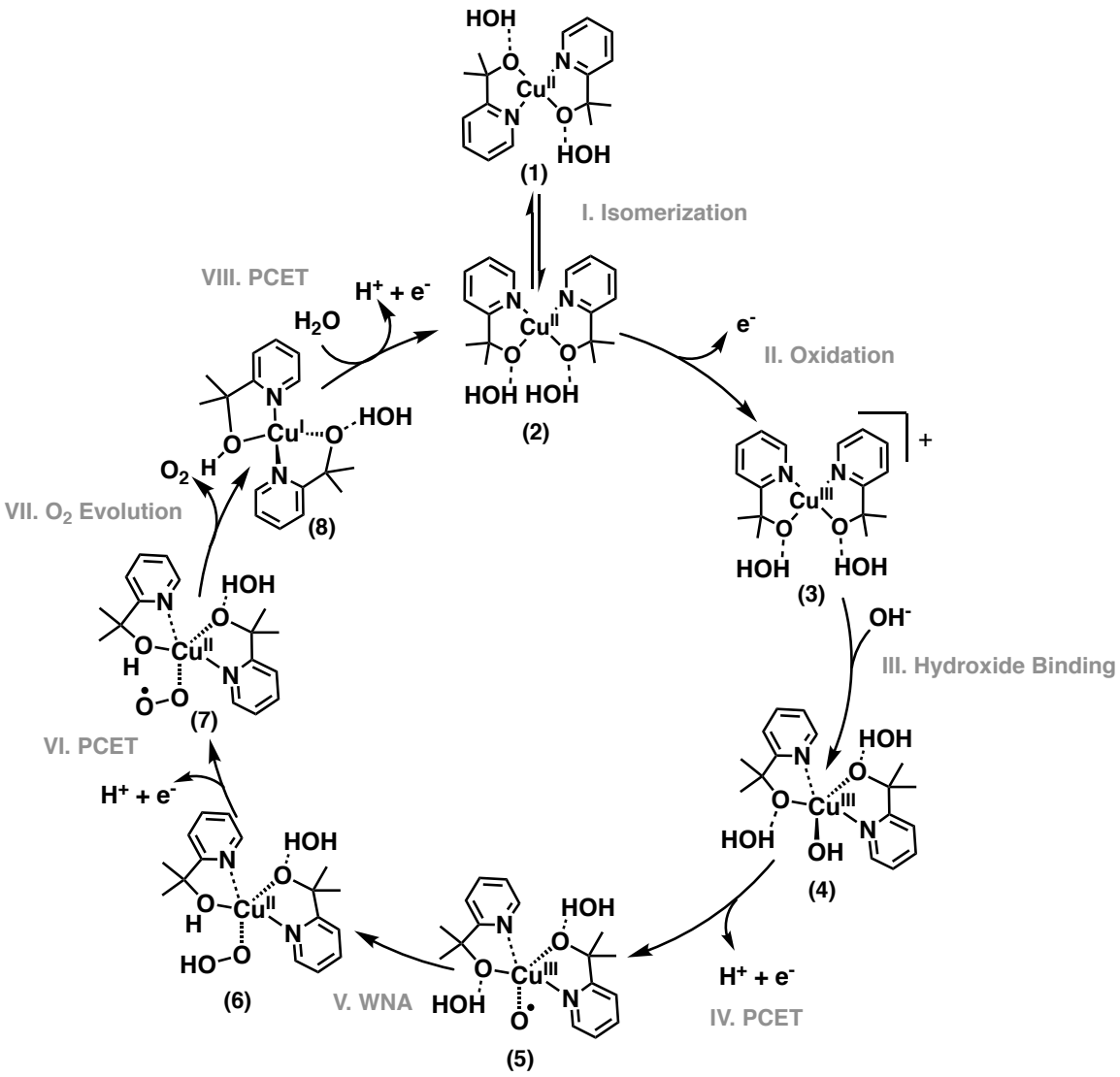

Scheme 3.1. Calculated mechanism of water oxidation catalyzed by Cu(pyalk)$_2$ **(1)**.

Step I (**Scheme 3.1**) involves the conversion of *trans* Cu(pyalk)$_2$ (**1**) into the *cis* form (**2**), which involves a ΔG of about 1.7 kcal/mol. While this difference suggests that there is more of the *trans* isomer in solution, there is still a catalytically relevant amount of *cis* isomer available. The conformational changes induced by the **1** → **2** conversion are shown in **Figure 3.3**.

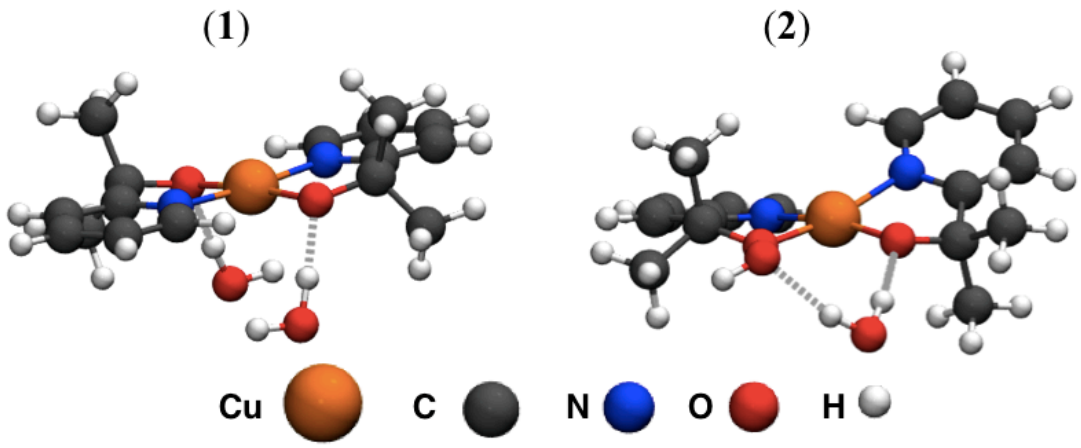

Figure 3.3. DFT optimized structures of **1** and **2**. The color code is indicated at the bottom of the figure. Hydrogen bonds are indicated by dashed lines.

Step II (**Scheme 3.1**) involves oxidation of **2** from Cu(II) to Cu(III), which includes a first-coordination sphere bond shortening of ~0.11 Å. The experimental potential for this quasireversible conversion is estimated to be 1.3 V vs. NHE.[20] The calculated reversible potentials for oxidation of the *cis* and *trans* forms are 1.9 V and 1.6 V vs. NHE, respectively. The calculated values for both isomers differ systematically from experiment, likely due to the lack of reversibility. Intermediate **3** is illustrated in **Figure 3.4**.

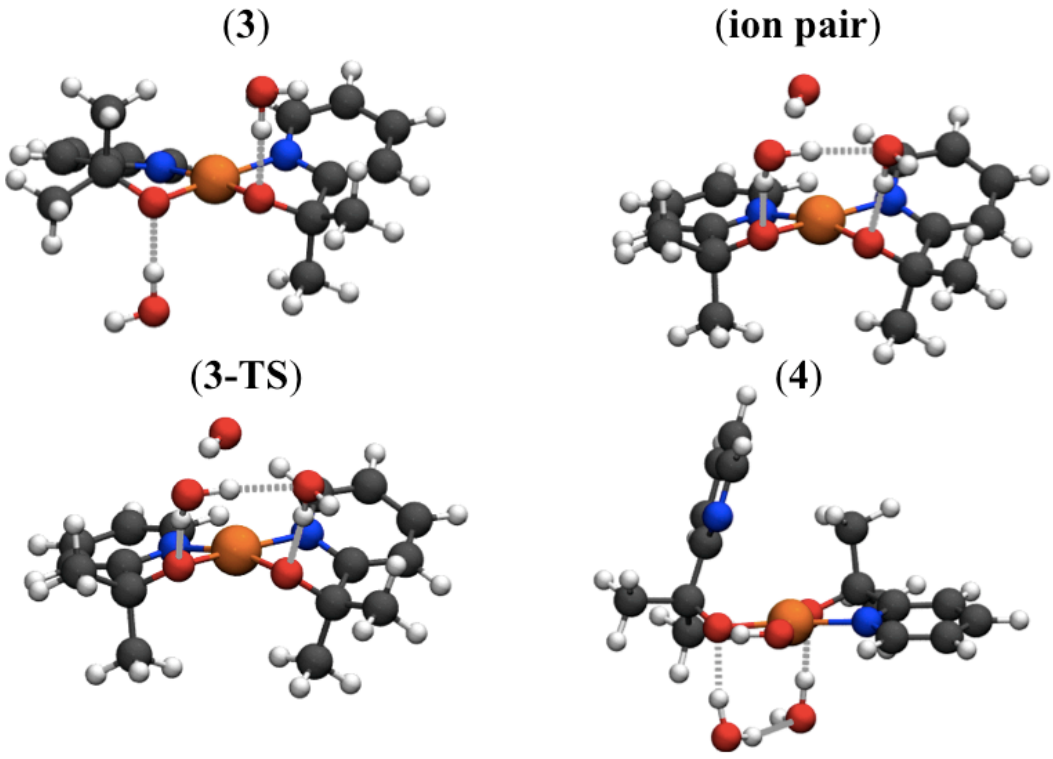

Figure 3.4. DFT optimized structures of intermediates **3** and **4** as well as the ion pair and transition states.

Step III (**Scheme 3.1**) involves binding of hydroxide to form a cationic five-coordinate Cu^{III} species, **4 (Figure 3.4**), since water deprotonates upon binding to the Cu^{III} species **3**. The free energy for this reaction was computed in two parts, including formation of the ion pair and the actual nucleophilic attack via **3-TS**, as shown in **Figure 3.4**. The free energy change necessary to form the ion pair is ΔG = 5.0 kcal/mol, presumably dominated by the entropic term, though this energy may be overestimated as ion pairs often form spontaneously in solution. From the ion pair, the free energy change for attachment to Cu is ΔG = -15.8 kcal/mol, leading to an overall free energy change ΔG = -10.8 kcal/mol. The barrier for the nucleophilic attack is 1.0 kcal/mol. Therefore, the barrier for the overall step is $\Delta G^{\ddagger}_{total} = \Delta G_{ion\ pair} + \Delta G^{\ddagger}$ = 5.0 + 1.0 kcal/mol = 6.0 kcal/mol.

Step IV (**Scheme 3.1**) of the cycle involves formation of the oxyl radical, **5**, likely through a proton-coupled electron transfer (PCET) step. The oxidation transforms the hydroxyl group to an oxyl radical, rather than forming a high-energy Cu^{IV} species, for which we could not even identify a stable structure, as expected from the “oxo wall” principle discussed previously. The oxyl-radical

intermediate has the structure shown in **Figure 3.5** and a spin density of 0.998 on the oxyl oxygen atom while copper has essentially zero spin density (**Table 3.3**). The presence of this second oxidation step cannot be ruled out experimentally as estimating the area under the CV trace is complicated by the fact that the substrate (OH^-) is part of the solvent. Mechanisms with only one oxidation were theoretically found not to yield intermediates with sufficient oxidizing power to oxidize water.

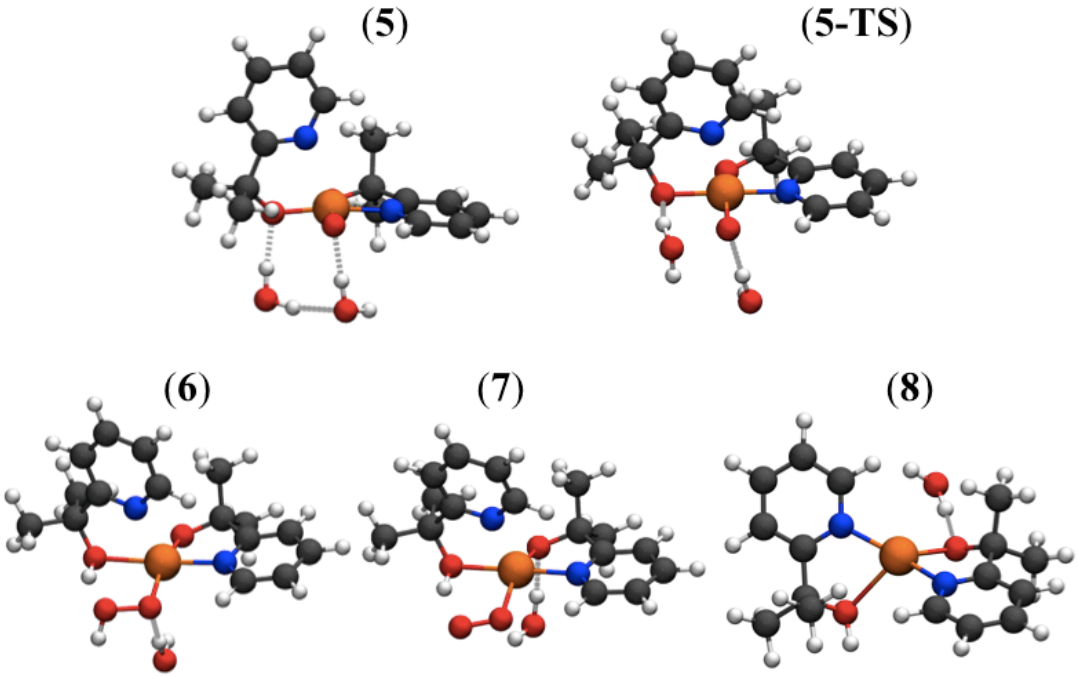

Figure 3.5. DFT optimized structures of intermediate **5**-**8** as well as transition state **5-TS**.

Step V (**Scheme 3.1**) is the nucleophilic attack of water on the oxyl radical with a synchronous proton transfer to the nearby alkoxide oxygen of the pyalk ligand (**Figure 3.5**). The transition state for that process, **5-TS**, and the resulting peroxy intermediate **6** are illustrated in **Figure 3.5**, while the mechanism is illustrated in **Scheme 3.2**. The net free energy change is ΔG = -20.4 kcal/mol, and the activation free energy $\Delta G^{\ddagger}$ is 19.3 kcal/mol. To compare to the experimental TOF = 0.7 s^{-1},[20] we used the Eyring equation of transition state theory (**Equation 3.1)**, which predicts a barrier of 17.6 kcal/mol.

$$k = \frac{k_b T}{h} \exp\left(\frac{-\Delta G^{\ddagger}}{RT}\right) \qquad \text{(Equation 3.1)}$$

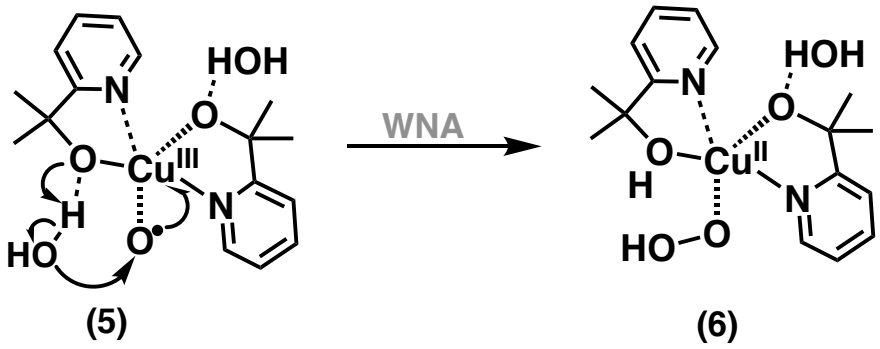

(5) (6)

Scheme 3.2. Water-nucleophilic attack (WNA) mechanism onto the oxyl radical of (**5**) to form (**6**) upon proton transfer to the pyalk ligand (as shown in Scheme 3.1).

Step VI (**Scheme 3.1**) involves another PCET oxidation of the terminal hydroxyl group, forming a triplet diradical with one spin shared by the two oxygens of the peroxyl group (**7** as shown in **Figure 3.5**), aligned parallel to the spin of Cu(II). The potential for this PCET is only 0.2 V vs. NHE, making it easily accessible under experimental electrochemical conditions.

Step VII (**Scheme 3.1**) involves triplet oxygen evolution through the mechanism illustrated in **Scheme 3.2**, with a modest Δ*G* = 4.0 kcal/mol, forming a tetrahedral Cu(I) with one of the pyalk ligands protonated.

Step VIII (**Scheme 3.1**) completes the cycle with another PCET that regenerates the Cu(II) complex in the *cis* form, **2**, as illustrated in **Scheme 3.3**. The subsequent oxidation is quite facile, with a potential of -0.4 V vs. NHE. **Figure 3.6** shows the potential surface for the entire mechanism under the conditions of zero bias potential and an operating potential of 2.0 V vs. NHE.

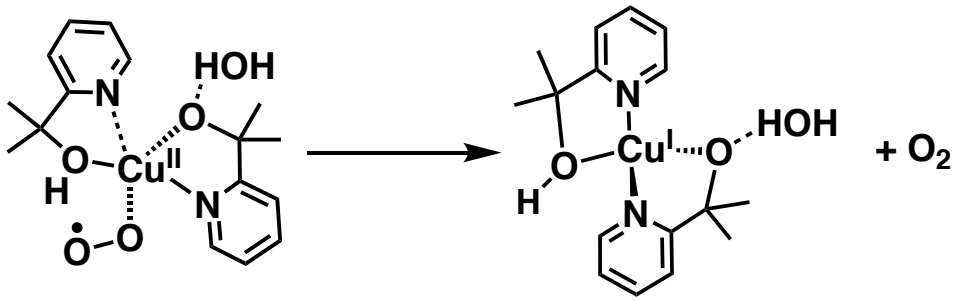

(7) (8)

Scheme 3.3. Mechanism of O_2 evolution by (**7**) to form (**8**) according to the reaction mechanism of Scheme 3.1. Spin alignment is indicated for the terminal oxyl and Cu center.

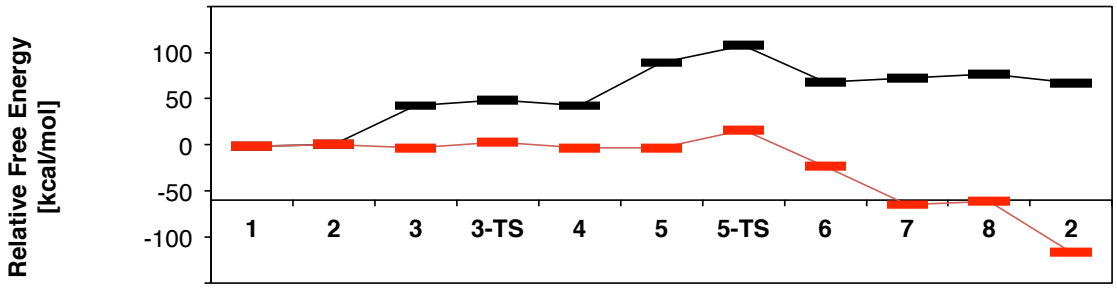

Figure 3.6. Potential energy surface for the water-oxidation reaction catalyzed by (**2**) under NHE (black, E = 0 V vs. NHE) and operating condition defined as E = 2.0 V vs. NHE (red).

An equivalent mechanism was found with the B3LYP functional (shown in **Figure 3.15** and **Figure 3.16**) with the transition state **5-TS** becoming just a proton transfer from the water to pyalk. Then two additional structures, **A**, a minimum, and **A-TS**, a transition state, for the O–O bond formation (highest point on the surface) were found. The mechanism still involves a water-nucleophilic attack though a predicted barrier of 16.2 kcal/mol (TOF = 8.03 s^{-1}).

3.4 Experimental corroboration

The mechanism described in **Scheme 3.1** suggests that a pyridine-Cu bond is lengthened and detaches from the Cu center in intermediates **4**–**7**, opening up a binding site for substrate water. Therefore, a complex with a similar ligand but without the possibility of pyridine flexibility should, in principle, be unable to bind water and therefore unable to perform water-oxidation catalysis. To test this hypothesis, complex **9**, Cu(bipydialk) (**Figure 3.7.A-B**), was synthesized.[10] Like $Cu(pyalk)_2$, **9** has two alkoxo and two pyridyl groups, and the ligand shape enforces the *cis*

geometry required for catalysis. The rigid, tetradentate ligand scaffold, however, does not allow for dissociation of either pyridine and would have difficulty supporting the tetrahedral Cu(I) intermediate **8**. Under the electrocatalytic conditions used for water oxidation by $Cu(pyalk)_2$, we found that **9** was found not competent for water-oxidation catalysis, as shown in **Figure 3.8**, thus supporting the catalytic mechanism of **Scheme 3.1**.

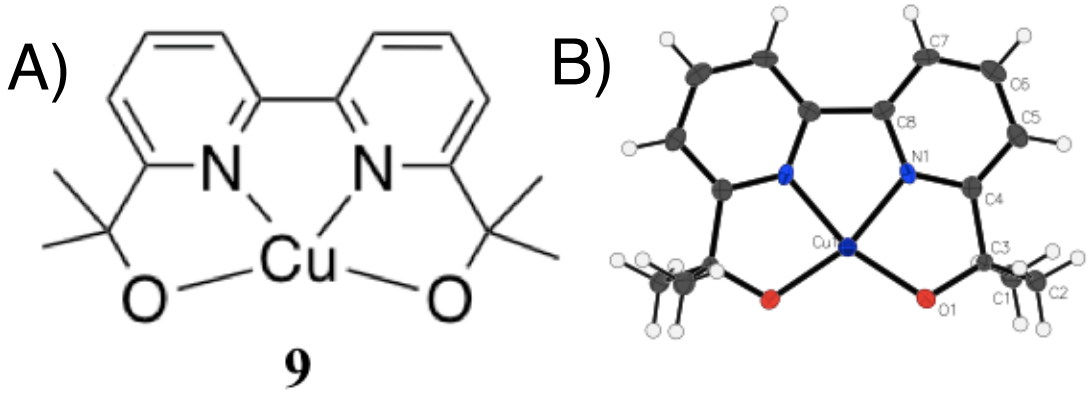

Figure 3.7. Structure of complex **9** Cu^{II}(bipydialk) (A) and X-ray crystallographic model (B).Thermal ellipsoids are shown at the 50% probability level.

Figure 3.9 shows the voltammogram analysis providing mechanistic information on the chemical step following electron transfer, k_1.[21] The foot-of-the-wave analysis (**Figure 3.13**) estimates a rate of about 10^6 s^{-1} while the barrier for the hydroxide nucleophilic attack was estimated to be 5.9 kcal/mol (2.8×10^8 s^{-1}) with the ωB97X-D functional and 9.6 kcal/mol (5.6×10^5 s^{-1}) with B3LYP, so the experimental estimation is within the range of values predicted by DFT when combined with transition state theory.

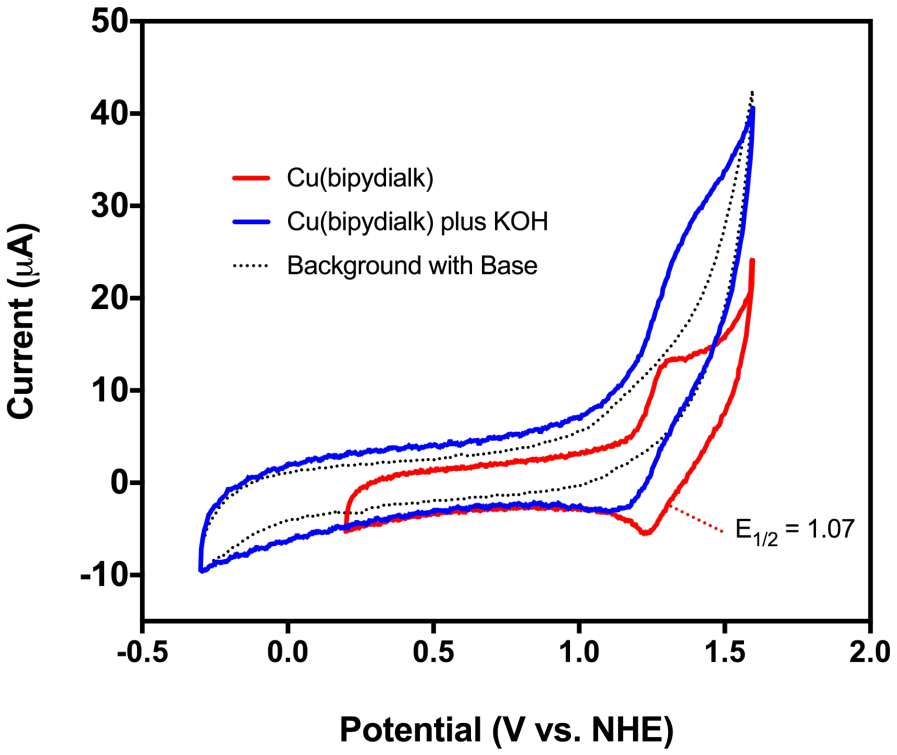

Figure 3.8. CV of **9** with and without KOH. Under basic conditions, no enhancement of current above background levels is observed.

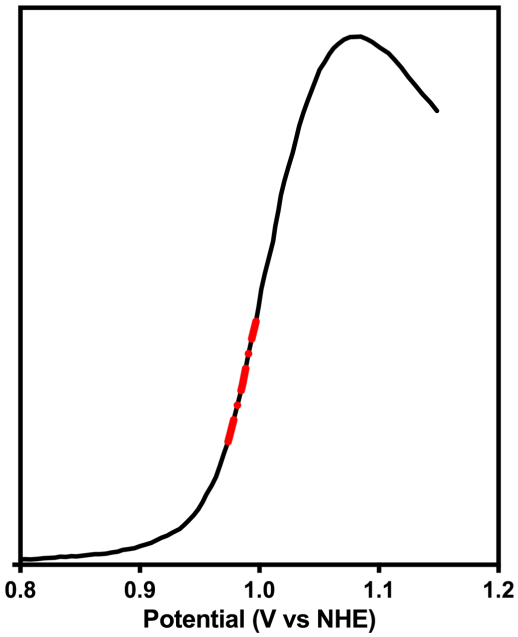

Figure 3.9. Linear sweep voltammogram of 2 mM **1** in 0.1 M KNO_3 adjusted to pH 13 with 0.1 M KOH (black). The region used for foot-of-the-wave calculations is shown in red. Inset: Linear fit of foot-of-the-wave data.

The H/D kinetic isotope effect (KIE) was measured by cyclic voltammetry of **1** in 0.01 M NaOH and 0.01 M NaOD solution (**Figure 3.10**), respectively, with both solutions with 0.1 M KNO_3 as electrolyte. The H/D KIE was obtained by taking the square of the ratio of the catalytic current under both conditions, as follows in **Equation 3.2**.

$$KIE = \frac{k_{H_2O}}{k_{D_2O}} = \left(\frac{i_{H_2O}}{i_{D_2O}} \right)^2 = \left(\frac{nFA[C]\sqrt{Dk_{H_2O}}}{nFA[C]\sqrt{Dk_{D_2O}}} \right)^2 \qquad \textbf{(Equation 3.2)}$$

In **Equation 3.2,** i is the catalytic current, n is the number of electrons in the catalytic process (4 for water oxidation), F = Faraday's constant, A = surface area of the electrode, [C] = catalyst concentration, D = diffusion coefficient of the catalyst, and k = pseudo-first order rate constant. The resulting experimental H/D KIE was found to be 3.4, consistent with proton involvement in the rate-determining step, and consistent with the proposed mechanism. The KIE for water oxidation by $Cu(pyalk)_2$ is similar to those found for several other mononuclear copper water-oxidation catalysts but is in stark contrast with those of reported for dinuclear catalysts, which are proposed to operate through a bimolecular rather than mononuclear mechanism (**Table 3.2**).

Table 3.2 Literature values for H/D kinetic isotope effects (KIE) for molecular copper water-oxidation catalysts.

Compound	Nuclearity of Cu	KIE	Ref.
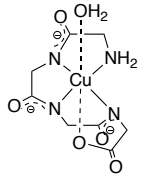	Mononuclear	2.0	22
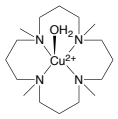	Mononuclear	2.1	23
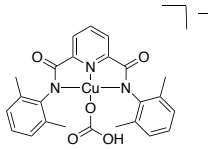	Mononuclear	1.81	24
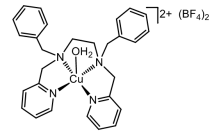	Mononuclear	2.0	25
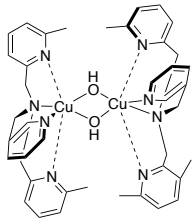	Dinuclear	20	17
Cu^{2+}	Mononuclear	1.01	26

For comparison with experiment, we computed the KIE with exchangeable polar hydrogen atoms swapped with deuterium atoms. We focused on the rate-determining step **5** → **5-TS** since chemical steps do not immediately precede it. The resulting KIE was evaluated as in our previous studies,[15] using transition state theory, as shown in **Equation 3.3**.[27-28]

$$KIE = \frac{k_{H_2O}}{k_{D_2O}} = \left(\frac{e^{-(-G_{R(1)}+G_{TS(1)})/RT}}{e^{-(-G_{R(2)}+G_{TS(2)})/RT}} \right) = e^{-(G_{R(2)}+G_{TS(1)}-G_{R(1)}-G_{TS(2)})/RT} \quad \textbf{(Equation 3.3)}$$

Using this method, calculated a KIE of 3.7, which is in excellent agreement with the experimental value of 3.4, further supporting the proposed mechanism. We also computed the KIE of hydroxide binding to Cu(III), the first chemical step of our proposed mechanism. This step only exhibits a KIE of 1.1, confirming that hydroxide binding is not the rate-limiting step.

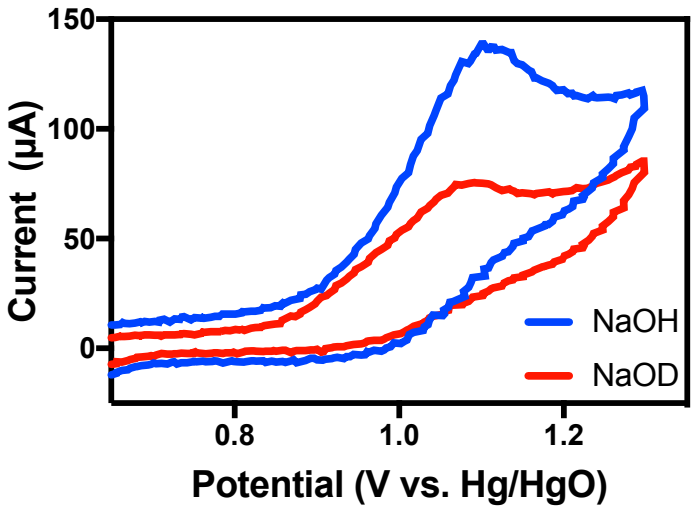

Figure 3.10. Cyclic voltammograms of 0.5 mM **1** with [NaOH] = [NaOD] = 0.01 M. CVs were taken with boron-doped diamond working electrode, Pt wire counter-electrode, and Hg/HgO reference electrode at a scan rate of 100 mV/s.

3.5 Conclusions and outlook

We have shown that Cu(pyalk)$_2$ catalyzes water oxidation through a water-nucleophilic attack onto an oxyl radical species, which is formed upon PCET oxidation of a catalyst-bound hydroxide. Remarkably, the pyalk ligand has the ability to remain bound even with a labile pyridine group that opens a coordination site for substrate binding, enabling robust functionality of a labile first-row transition metal catalyst. The mechanism proposed in this chapter shows good agreement between experiment and theory. First, the measured KIE of 3.4 compares well with the calculated KIE of 3.7. Next, the experimental free energy barrier of 17.6 kcal/mol (computed from measured turnover frequency) is in good agreement with the theoretical value of 19.3 kcal/mol. Finally, the rate of the first chemical step determined by foot-of-the-wave analysis of the voltammogram of **2** is

within the range of values determined by DFT. Synthesis and electrochemical analysis of an analogue of **2** with a rigid ligand scaffold suggests that ligand flexibility is required for electrocatalysis, consistent with the proposed mechanism. The resulting insights are particularly valuable for ligand design and future development of even more efficient water-oxidation catalysts based on Earth-abundant transition metal complexes. Further work to corroborate the proposed mechanism may involve immobilization of catalysts on electrode surfaces and measurements of other catalytic and electrochemical parameters, including $^{16}O/^{18}O$ kinetic isotope effects under electrocatalytic conditions.

3.6 Experimental Details

3.6.1 General

All chemicals were purchased from Sigma Aldrich or TCI America and used as received. Solvents used in air-free conditions were dried over activated alumina using a Grubbs-type solvent purification system. Solutions of n-butyl lithium were titrated against diphenylacetic acid before use.

3.6.2 Physical Methods

^{1}H NMR: NMR spectra were recorded on an Agilent DD2 400 MHz spectrometer and chemical shifts were referenced to solvent residual peaks.

UV-Visible Spectroscopy: Absorption spectra were collected using a Cary 50 spectrophotometer.

High Resolution Mass Spectrometry (HR-MS) of Cu(bipydialk)$_2$ (9): High-resolution mass spectrometry was performed at the Keck Biotechnology Resource Laboratory using a Bruker 9.4 Tesla Apex-Qe Hybrid Qe-Fourier Transform Ion Cyclotron Resonance (FT-ICR) mass spectrometer consisting of an Apollo II electrospray ionization source.

FTIR: FTIR spectra were recorded on a Thermo Scientific Nicolet 6700 spectrometer outfitted with a Smart Orbit diamond ATR cell.

Electrochemical measurements: Electrochemical measurements were performed on a Pine AFCBP1 bipotentiostat using a standard three-electrode configuration with 0.1 M KNO_3 electrolyte. A boron-doped diamond working electrode and a platinum counter-electrode were used. Ag/AgCl (sat. KCl) was used as a reference electrode. To convert potentials to NHE, 0.199 V was added to measured potentials.

3.6.3 Synthesis and characterization

Synthesis of 2,2'-([2,2'-bipyridine]-6,6'-diyl)bis(propan-2-ol) (bipydialk).

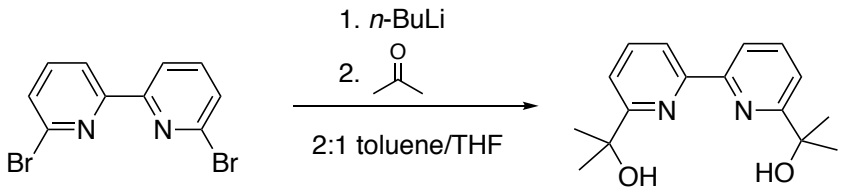

Scheme 3.4. Synthetic route for the preparation of the bipydialk ligand.

Under an atmosphere of N_2, 6,6'-dibromo-2,2'-bipyridine (0.318 mmol, 100 mg) was partially solvated in 6 mL toluene. 2 mL of THF was then added to the stirring slurry to solvate the remaining starting material, which was found to be insoluble in most of the pure solvents appropriate for lithium halogen exchange reactions. The solution was cooled to -78° C in a dry ice/acetone bath and nBuLi (2.5 eq, 0.56 mL of 1.42 M solution) was added dropwise, yielding a dark red solution. After 15 minutes, extra dry acetone (30 eq, 0.7 mL) was added dropwise, giving a dark green solution. The reaction was brought to -20° C with a salt/ice bath and allowed to stir for 3 hours. The reaction was quenched with 2 mL H_2O, and then extracted with saturated NH_4Cl (3 x 3 mL) and hexanes (3 x 3 mL). Organics were combined, dried over Na_2SO_4, and concentration *in vacuo* to give a yellow oil. Unreacted starting material, which likely results from its low solubility in the reaction solvent, was found to precipitate cleanly from this oil with the addition of DCM and could be collected via vacuum filtration. The filtrate was concentrated to give a yellow oil that was purified via flash column chromatography on silica pre-treated with Et_3N (eluent: gradient from pure hexanes to 4:1 hexanes/EtOAc, all with 1% Et_3N). The desired product was collected as a yellow oil, but can be recrystallized by dissolution in minimal acetone and precipitation with pentane to yield a white powder. Isolated Yield: 28%. ^{1}H NMR (400 MHz, $CDCl_3$, 25°C, TMS): δ = 1.60 (s, 12H) 5.26 (s, 2H), 7.41 (d, 2H), 7.87 (t, 2H), 8.34 (d, 2H) ppm; IR (solid): v = 431.8, 533.2, 584.3,613.1, 640.4, 738.3, 755.6, 808.2, 867.6, 920.2, 957.8, 991.8, 1078.2, 1100.4, 1123.2, 1155.2, 1276.2, 1348.4, 1388.4, 1435.9, 1459.3, 1572.0, 2928.5, 2970.7, 3079.0, 3387.2 cm^{-1}

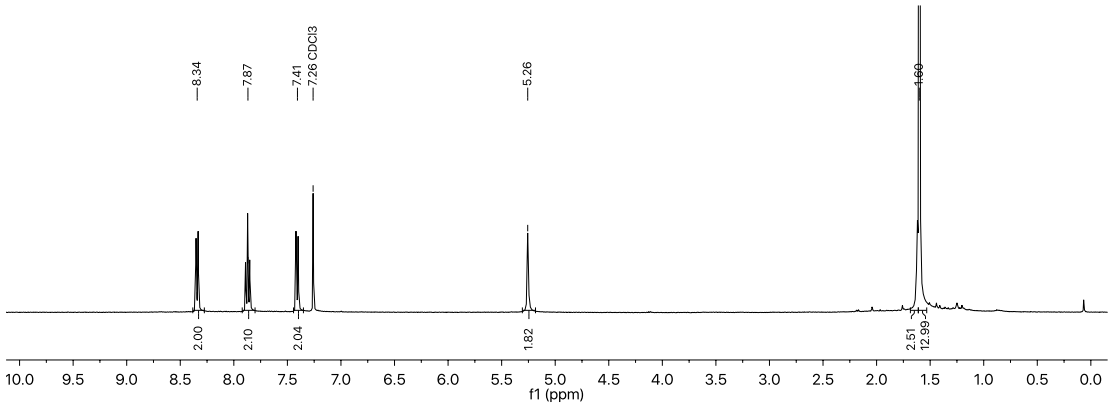

Figure 3.11. ^{1}H NMR spectrum of 2,2'-([2,2'-bipyridine]-6,6'-diyl)bis(propan-2-ol).

Synthesis of Cu(bipydialk)$_2$ (9).

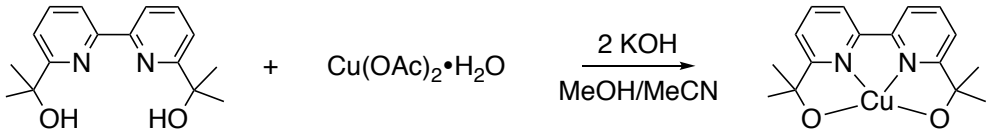

Scheme 3.5. Synthetic route for the preparation of **9**.

To a stirred light blue solution of $Cu(OAc)_2 \cdot H_2O$ (0.0699 mmol, 14.0 mg in 5 mL of MeOH/MeCN 1:10) was added bipydialkH_2 (0.073 mmol, 20 mg in MeCN) dropwise. A color change to royal blue was observed, and the solution was allowed to react for 20 minutes. A solution of KOH in MeOH was added dropwise (1.4 mL of a 0.1 M solution or 2 eq. The reaction mixture was then extracted into DCM, leaving behind a green precipitate shown to be $Cu(OAc)_2$. The resulting dark blue organic layer was dried over Na_2SO_4 and concentrated *in vacuo* to give a dark blue powder. Crystals suitable for diffraction were prepared via layering of pentane onto a solution of powder in DCM. IR (solid): v= 436.5, 485.6, 532.6, 556.8, 573.7, 601.1, 632.1, 666.4, 697.7, 726.4, 753.3, 807.5, 860.9, 961.9, 1025, 1077.4, 1086.6, 1103, 1122.5, 1155.9, 1194.2, 1209, 1283.5, 1352.2, 1374.7, 1419, 1430.1, 1456.7, 1472.1, 1559, 2340.4, 2360.5, 2920.7, 2967.4, 3079.4, 3382.6 cm^{-1}. Isolated Yield: 67%.

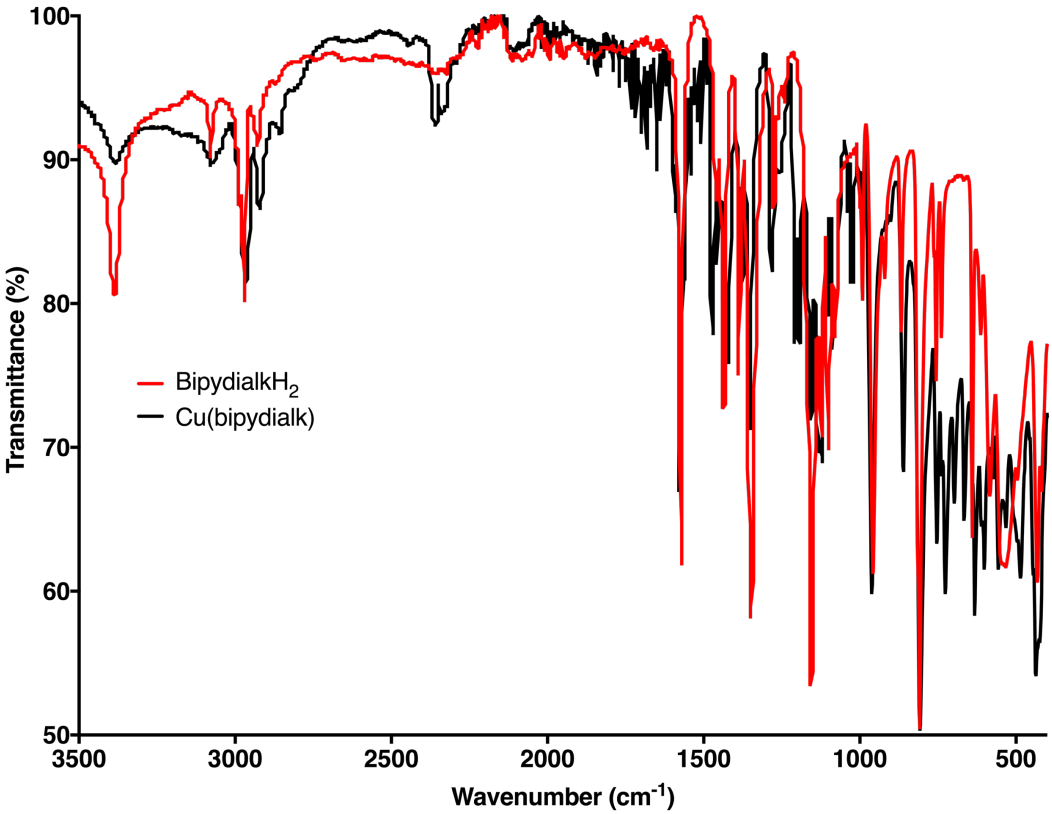

Figure 3.12. FTIR spectra of bipydialkH_2 and Cu(bipydialk).

3.7 Supplementary Figures and Discussion

3.7.1 Supplementary Figures

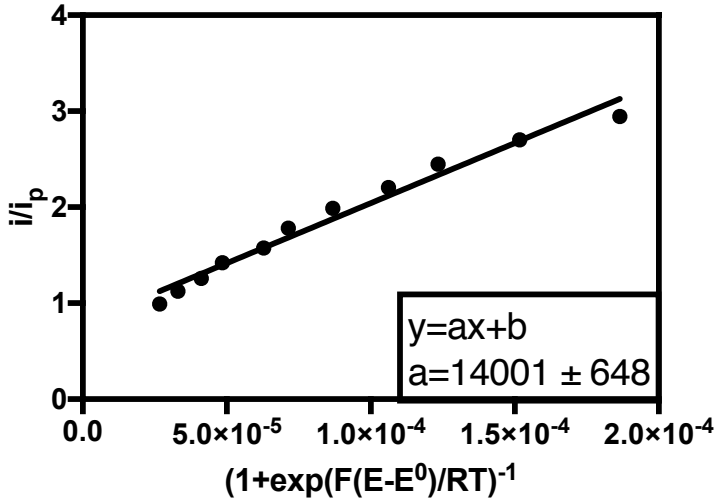

Figure 3.13. Linear regression of foot-of-the-wave data used to determine k_1.

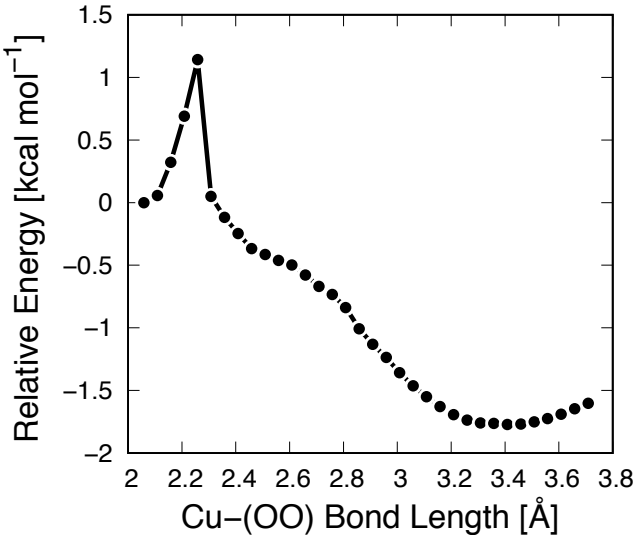

Figure 3.14. Relaxed energy scan for triplet oxygen evolution from **7**.

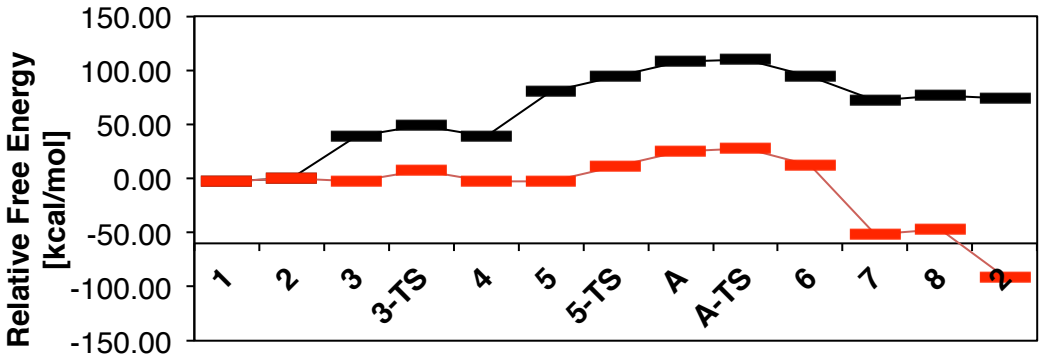

Figure 3.15. Potential energy surface for the water-oxidation reaction catalyzed by (**2**) under NHE (black, E = 0 V vs. NHE) and operating condition defined as (red, E = 1.8 V vs. NHE) as computed with B3LYP.

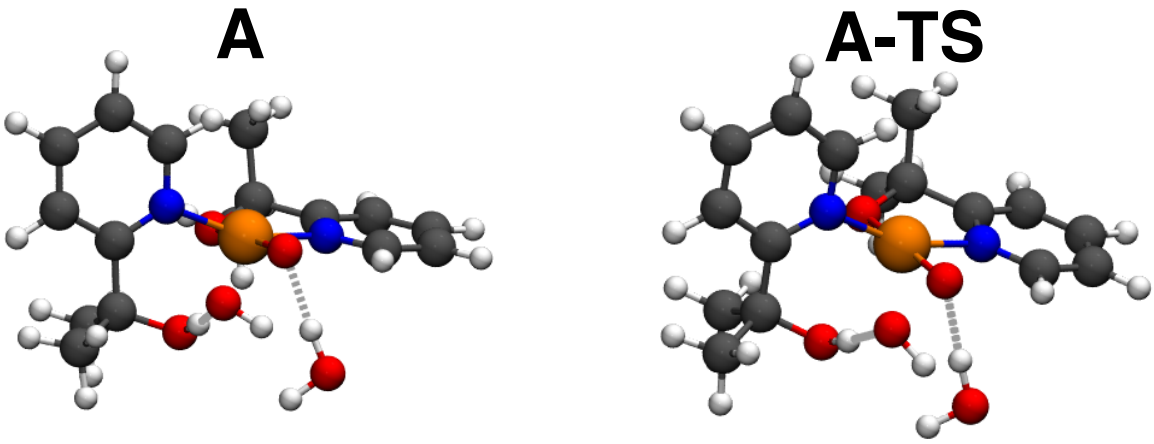

Figure 3.16. Structures of the additional intermediate (A) and transition state (A-TS) after the proton transfer. The numbering shown here is the same as in the ωB97X-D mechanism in the main text.

3.7.2 Spin Contamination Check

Unrestricted DFT can suffer from spin contamination problems where the $\langle S^2 \rangle$ value deviates significantly from $S(S+1)$. To check for such issues, these values were collected in **Table 3.3**. Since they do not deviate greatly (within 5%) from (½)(½+1) = 0.750 for a doublet or (1)(1+1) = 2.000 for a triplet, no spin contamination corrections were required.

Table 3.3. $\langle S^2 \rangle$ values for all doublet minima as well as Mulliken spin densities for the Cu center and the oxyl radical oxygen O1 or the nucleophilic water oxygen O2, when applicable.

Minimum	**1**	**2**	**5**	**6**	**7**
$\langle S^2 \rangle$	0.753	0.753	0.775	0.752	2.009
Cu spin	0.657	0.647	0.004	0.653	0.702
O1	-	-	0.998	0.079	0.538
O2	-	-	-	0.001	0.547

3.7.3 Concentration Correction

The thermal corrections (at room temperature (*T*) i.e. 298 K) provided by the rigid rotor (rotational entropy), harmonic oscillator (vibrational entropy), and free particle (translational entropy) are for molecules in their standard state e.g. pressure (*P*) of 1 atm (concentration (*C*) of $C = P/(RT) = 24.46^{-1}$ M),[29] where *R* is the usual gas constant. However, we would like to compute free energies for molecules at a concentration of 1 M (except for water which should be around 55.6 M). Therefore, the following procedure is used to correct the free energies for the following generic chemical reaction, where the stoichiometry change is $c + d - a - b$:

$$aA(aq) + bB(aq) \rightarrow cC(aq) + dD(aq) \qquad \textbf{(Equation 3.4)}$$

First, for non-water molecules, the following expression is utilized where the new free energy change is $\Delta G'$ and the free energy change for $P = 1$ atm is $\Delta G°$:

$$\Delta G' - \Delta G^0 = RT \ln \frac{\frac{[D]^d[C]^c}{[B]^b[A]^a}}{\frac{[D]^d[C]^c}{[B]^b[A]^a}} = RT \ln \frac{\frac{[1]^d[1]^c}{[1]^b[1]^c}}{\frac{[\frac{1}{24.46}]^d[\frac{1}{24.46}]^c}{[\frac{1}{24.46}]^b[\frac{1}{24.46}]^c}} = RT \ln \frac{1^{d+c-b-a}}{[\frac{1}{24.46}]^{d+c-b-a}} \qquad \textbf{(Equation 3.5)}$$

Therefore, for a hydroxide nucleophilic attack ($c + d - a - b = -1$), the correction is

$$\Delta G' - \Delta G^0 = RT \ln \frac{1^{-1}}{[\frac{1}{24.46}]^{-1}} = RT \ln \frac{1}{[\frac{1}{24.46}]} = -1.89 kcal/mol \qquad \textbf{(Equation 3.6)}$$

On the other hand, for a water nucleophilic attack ($c + d - a - b = -1$), the correction is

$$\Delta G' - \Delta G^0 = RT \ln \frac{55.6^{-1}}{[\frac{1}{24.46}]^{-1}} = RT \ln \frac{1}{55.6 * 24.46} = -4.27 kcal / mol \qquad \textbf{(Equation 3.7)}$$

3.7.4 Crystallographic Experimental Details

Low-temperature diffraction data (ω-scans) were collected on a Rigaku R-AXIS RAPID diffractometer coupled to an R-AXIS RAPID imaging plate detector with Mo Kα radiation (λ = 0.71073 Å) for the structure of **9**. The diffraction images were processed and scaled using the Rigaku CrystalClear software (CrystalClear and CrystalStructure; Rigaku/MSC: The Woodlands, TX, 2005). The structure was solved with SHELXT and was refined against F^2 on all data by full-matrix least squares with SHELXL (Sheldrick, G. M. Acta Cryst. 2008, A64, 112–122). All non-hydrogen atoms were refined anisotropically. Hydrogen atoms were included in the model at geometrically calculated positions and refined using a riding model. The isotropic displacement parameters of all hydrogen atoms were fixed to 1.2 times the U value of the atoms to which they are linked (1.5 times for methyl groups). The full numbering scheme of compound spider-17021 can be found in the full details of the X-ray structure determination (CIF), which is included as Supporting Information. CCDC number 1827954 (**9**) contains the supplementary crystallographic data for this paper.

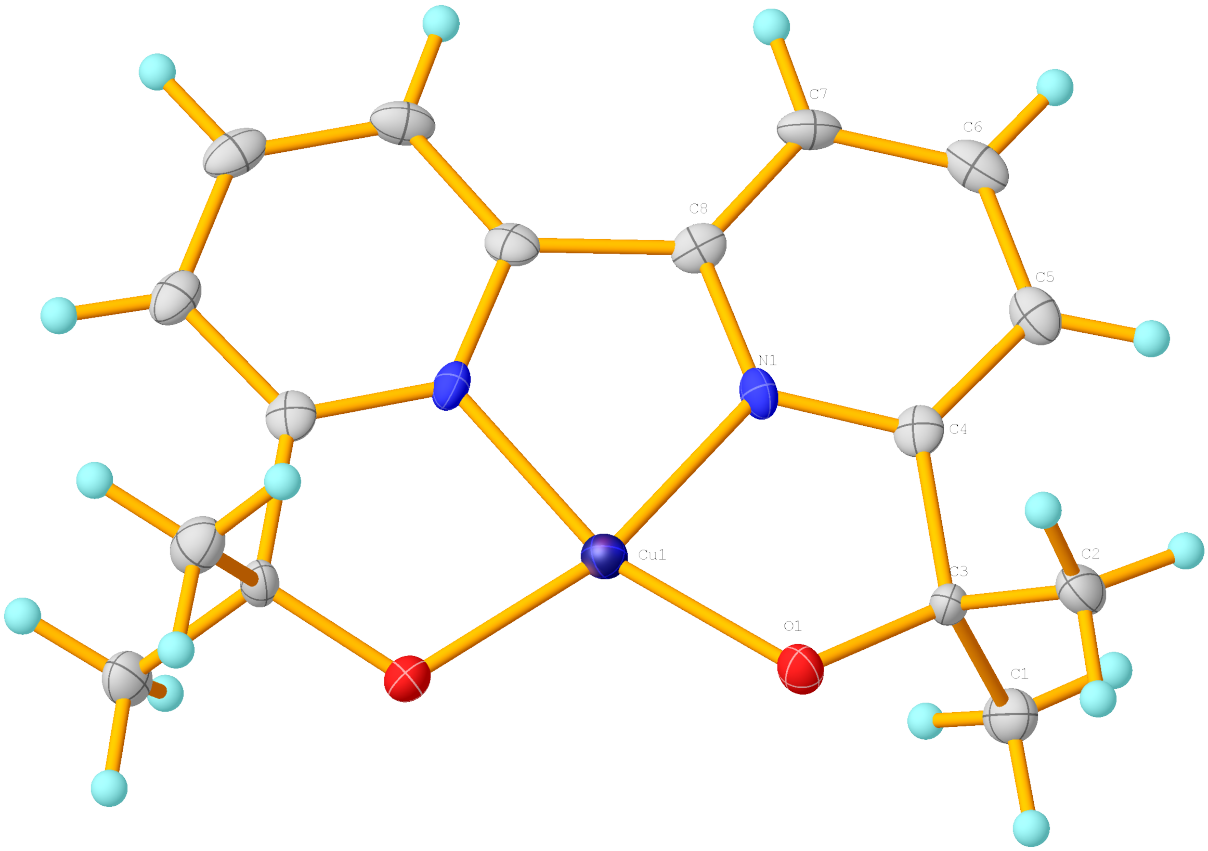

Figure 3.17. Thermal ellipsoid diagram for **9** with complete numbering scheme. Thermal ellipsoids are displayed at the 50% probability level. The hydrogen atoms are shown as circles for clarity. The model is on a special position; only the asymmetric unit is labeled.

Table 3.4. Crystal data and structure refinement for **9**.

Identification code	spider-17021	
Empirical formula	C16 H18 Cu N2 O2	
Formula weight	333.86	
Temperature	93(2) K	
Wavelength	0.71073 Å	
Crystal system	Orthorhombic	
Space group	Fdd2	
Unit cell dimensions	a = 17.1965(12) Å	α = 90°.
	b = 20.8788(15) Å	β = 90°.
	c = 8.0662(6) Å	γ = 90°.
Volume	2896.1(4) $Å^3$	
Z	8	
Density (calculated)	1.531 Mg/m^3	
Absorption coefficient	1.514 mm^{-1}	
F(000)	1384	
Crystal size	0.200 x 0.200 x 0.200 mm^3	
Crystal color and habit	Blue Prism	
Diffractometer	Rigaku R-AXIS RAPID imaging plate	
Theta range for data collection	2.955 to 25.020°.	
Index ranges	-19<=h<=19, -24<=k<=24, -9<=l<=9	
Reflections collected	6742	
Independent reflections	1259 [R(int) = 0.0986]	
Observed reflections (I > 2sigma(I))	1086	
Completeness to theta = 25.020°	98.5 %	
Absorption correction	Semi-empirical from equivalents	
Max. and min. transmission	1.000 and 0.777	
Solution method	SHELXT-2014/5 (Sheldrick, 2014)	

Refinement method	SHELXL-2014/7 (Sheldrick, 2014)
Data / restraints / parameters	1259 / 1 / 98
Goodness-of-fit on F^2	1.074
Final R indices [I>2sigma(I)]	R1 = 0.0370, wR2 = 0.0738
R indices (all data)	R1 = 0.0526, wR2 = 0.0789
Absolute structure parameter	0.02(2)
Largest diff. peak and hole	0.441 and -0.331 e.$Å^{-3}$

3.8 References

1. Blakemore, J. D.; Crabtree, R. H.; Brudvig, G. W., Molecular Catalysts for Water Oxidation. *Chem. Rev.* **2015,** *115* (23), 12974-13005.
2. Craig, M. J.; Coulter, G.; Dolan, E.; Soriano-López, J.; Mates-Torres, E.; Schmitt, W.; García-Melchor, M., Universal Scaling Relations for the Rational Design of Molecular Water Oxidation Catalysts with Near-Zero Overpotential. *Nat. Chem.* **2019,** *10* (1), 4993.
3. Song, J.; Wei, C.; Huang, Z.-F.; Liu, C.; Zeng, L.; Wang, X.; Xu, Z. J., A Review on Fundamentals for Designing Oxygen Evolution Electrocatalysts. *Chem. Soc. Rev.* **2020,** *49* (7), 2196-2214.
4. Lee, K. J.; Elgrishi, N.; Kandemir, B.; Dempsey, J. L., Electrochemical and Spectroscopic Methods for Evaluating Molecular Electrocatalysts. *Nat. Rev. Chem.* **2017,** *1* (5).
5. Neri, G.; Walsh, J. J.; Teobaldi, G.; Donaldson, P. M.; Cowan, A. J., Detection of Catalytic Intermediates at an Electrode Surface During Carbon Dioxide Reduction by an Earth-Abundant Catalyst. *Nat. Catal.* **2018,** *1* (12), 952-959.
6. Foster, A. J.; Lobo, R. F., Identifying Reaction Intermediates and Catalytic Active Sites through in Situ Characterization Techniques. *Chem. Soc. Rev.* **2010,** *39* (12), 4783-93.
7. Thomsen, J. M.; Huang, D. L.; Crabtree, R. H.; Brudvig, G. W., Iridium-Based Complexes for Water Oxidation. *Dalton Trans.* **2015,** *44* (28), 12452-12472.
8. Yang, K. R.; Matula, A. J.; Kwon, G.; Hong, J.; Sheehan, S. W.; Thomsen, J. M.; Brudvig, G. W.; Crabtree, R. H.; Tiede, D. M.; Chen, L. X.; Batista, V. S., Solution Structures of Highly Active Molecular Ir Water-Oxidation Catalysts from Density Functional Theory Combined with High-Energy X-Ray Scattering and EXAFS Spectroscopy. *J. Am. Chem. Soc.* **2016,** *138* (17), 5511-5514.
9. Lant, H. M. C.; Michaelos, T. K.; Sharninghausen, L. S.; Mercado, B. Q.; Crabtree, R. H.; Brudvig, G. W., N,N,O Pincer Ligand with a Deprotonatable Site That Promotes Redox-Leveling, High Mn Oxidation States, and a Mn_2O_2 Dimer Competent for Catalytic Oxygen Evolution. *Eur. J. Inorg. Chem.* **2019,** *2019* (15), 2115-2123.
10. Michaelos, T. K.; Lant, H.; Sharninghausen, L. S.; Craig, S. M.; Menges, F. S.; Mercado, B. Q.; Brudvig, G. W.; Crabtree, R. H., Catalytic Oxygen Evolution from Manganese Complexes with an Oxidation-Resistant N, N, O-Donor Ligand. *ChemPlusChem* **2016,** *81* (10), 1129-1132.
11. Limburg, J.; Vrettos, J. S.; Liable-Sands, L. M.; Rheingold, A. L.; Crabtree, R. H.; Brudvig, G. W., A Functional Model for O-O Bond Formation by the O_2-Evolving Complex in Photosystem II. *Science* **1999,** *283* (5407), 1524-7.
12. Barnett, S. M.; Goldberg, K. I.; Mayer, J. M., A Soluble Copper-Bipyridine Water-Oxidation Electrocatalyst. *Nat. Chem.* **2012,** *4* (6), 498-502.
13. Fisher, K. J.; Materna, K. L.; Mercado, B. Q.; Crabtree, R. H.; Brudvig, G. W., Electrocatalytic Water Oxidation by a Copper(II) Complex of an Oxidation-Resistant Ligand. *ACS Catal.* **2017,** *7*, 3384-3387.
14. Hughes, T. F.; Friesner, R. A., Systematic Investigation of the Catalytic Cycle of a Single Site Ruthenium Oxygen Evolving Complex Using Density Functional Theory. *J. Phys. Chem. B* **2011,** *115* (29), 9280-9289.
15. Khan, S.; Yang, K. R.; Ertem, M. Z.; Batista, V. S.; Brudvig, G. W., Mechanism of Manganese-Catalyzed Oxygen Evolution from Experimental and Theoretical Analyses of ^{18}O Kinetic Isotope Effects. *ACS Catal.* **2015,** *5* (12), 7104-7113.
16. Francàs, L.; Sala, X.; Benet-Buchholz, J.; Escriche, L.; Llobet, A., A Ru-Hbpp-Based Water-Oxidation Catalyst Anchored on Rutile TiO_2. *ChemSusChem* **2009,** *2* (4), 321-329.
17. Koepke, S. J.; Light, K. M.; VanNatta, P. E.; Wiley, K. M.; Kieber-Emmons, M. T., Electrocatalytic Water Oxidation by a Homogeneous Copper Catalyst Disfavors Single-Site Mechanisms. *J. Am. Chem. Soc.* **2017**.
18. Winkler, J. R.; Gray, H. B., Electronic Structures of Oxo-Metal Ions. In *Molecular Electronic Structures of Transition Metal Complexes I*, Springer: 2011; pp 17-28.
19. Zhang, M.-T.; Chen, Z.; Kang, P.; Meyer, T. J., Electrocatalytic Water Oxidation with a Copper (II) Polypeptide Complex. *J. Am. Chem. Soc.* **2013,** *135* (6), 2048-2051.

20. Fisher, K. J.; Materna, K. L.; Mercado, B. Q.; Crabtree, R. H.; Brudvig, G. W., Electrocatalytic Water Oxidation by a Copper (II) Complex of an Oxidation-Resistant Ligand. *ACS Catal.* **2017,** *7* (5), 3384-3387.
21. Matheu, R.; Neudeck, S.; Meyer, F.; Sala, X.; Llobet, A., Foot of the Wave Analysis for Mechanistic Elucidation and Benchmarking Applications in Molecular Water Oxidation Catalysis. *ChemSusChem* **2016,** *9* (23), 3361-3369.
22. Coggins, M. K.; Zhang, M. T.; Chen, Z.; Song, N.; Meyer, T. J., Single-Site Copper(II) Water Oxidation Electrocatalysis: Rate Enhancements with HPO_4^{2-} as a Proton Acceptor at pH 8. *Angew. Chem. Int. Ed.* **2014,** *53* (45), 12226-30.
23. Yu, F.; Li, F.; Hu, J.; Bai, L.; Zhu, Y.; Sun, L., Electrocatalytic Water Oxidation by a Macrocyclic Cu(II) Complex in Neutral Phosphate Buffer. *Chem. Commun.* **2016,** *52* (68), 10377-10380.
24. Chen, F.; Wang, N.; Lei, H.; Guo, D.; Liu, H.; Zhang, Z.; Zhang, W.; Lai, W.; Cao, R., Electrocatalytic Water Oxidation by a Water-Soluble Copper(II) Complex with a Copper-Bound Carbonate Group Acting as a Potential Proton Shuttle. *Inorg. Chem.* **2017,** *56* (21), 13368-13375.
25. Shen, J.; Wang, M.; Zhang, P.; Jiang, J.; Sun, L., Electrocatalytic Water Oxidation by Copper (II) Complexes Containing a Tetra-or Pentadentate Amine-Pyridine Ligand. *Chem. Commun.* **2017,** *53* (31), 4374-4377.
26. Huang, H. H.; Wang, J. W.; Sahoo, P.; Zhong, D. C.; Lu, T. B., Electrocatalytic Water Oxidation by Cu(II) Ions in a Neutral Borate Buffer Solution. *Chem. Commun.* **2017,** *53* (67), 9324-9327.
27. Bigeleisen, J.; Mayer, M. G., Calculation of Equilibrium Constants for Isotopic Exchange Reactions. *J. Chem. Phys.* **1947,** *15* (5), 261-267.
28. Bigeleisen, J.; Wolfsberg, M., Theoretical and Experimental Aspects of Isotope Effects in Chemical Kinetics. *Adv. Chem. Phys.* **1958,** *1*, 15-76.
29. Cramer, C. J., *Essentials of Computational Chemistry: Theories and Models*. John Wiley & Sons: 2013.

Part Two. Study of proton-coupled electron transfer by high-valent metal complexes.

4 Chapter 4. Concerted Proton-Electron Transfer Oxidation of Phenols and Hydrocarbons by a High-Valent Nickel Complex

This work is adapted from Fisher, K. J.; Feuer, M. L.; Lant, H. M. C.; Mercado, B. Q.; Crabtree, R. H.; Brudvig, G. W. *Chemical Science* **2020,** *11* (6), 1683-1690. KJF performed all kinetics experiments, analyzed date, and wrote the manuscript. MLF contributed to synthesis of $Ni(pyalk)_2^+$. HMCL performed EPR experiments and helped with modeling. BQM prepared crystal structures. Originally published by the Royal Society of Chemistry, 2020.

4.1 Introduction

Reactions in which protons and electrons move in a single, concerted step (concerted proton-electron transfer, or CPET) play a significant role in many organic, inorganic, and bioinorganic catalytic systems, as discussed in Chapter 1. CPET at high-valent metal centers has been proposed or observed in the catalytic mechanisms ranging from enzymatic reactions[1-2] to water-oxidation catalysis[3-4] to organic synthesis.[5-6] In many of these systems, the proton and electron are transferred to a high-valent metal-oxo species; however, another strategy involves the transfer of the proton to the ligand scaffold instead. This approach is also relevant to some bioinorganic systems. For instance, in nickel superoxide dismutase (NiSOD), a CPET step is proposed to occur at a highly oxidized nickel(III) intermediate in which a coordinated thiol or amide moiety acts as a proton donor.[7-9]

Understanding the CPET reactivity of high-valent metal centers may give some insight into their reactivity in catalytic systems. In particular, understanding CPET steps in systems in which the proton is transferred to the ligand may provide insight into catalytic systems that do not or cannot go through metal-oxo intermediates, such as copper- or nickel-containing water-oxidation catalysts or NiSOD.

As discussed in previous chapters, we have found that the strongly donating pyalk ligand can stabilize metal centers in high oxidation states, including species as highly oxidized as Ir(V).[10] In addition, the pyalk alkoxide has been suggested to act as a proton shuttle in catalytic water oxidation, as proposed in the catalytic water oxidation cycle for $Cu(pyalk)_2$ in Chapter 3.[11-12] We therefore reasoned that a high-valent metal compound stabilized by the pyalk ligand was a good

candidate for fast CPET. In this chapter, we describe the preparation of a stable Ni(III) species capable of reacting with a variety of O-H and C-H bonds via CPET.

4.2 Synthesis and characterization of Ni(pyalk) and [Ni(pyalk)]$^+$

We first prepared **1**, a new square-planar nickel(II) complex with two pyalk ligands arranged in a *trans* orientation (**Figure 4.1A**), which was characterized by X-ray crystallography, ^{1}H NMR spectroscopy, and cyclic voltammetry (CV). The CV of **1** shows a reversible redox feature at 0.15 V vs. Fc/Fc$^+$, suggesting that oxidation generates a stable Ni(III) species (**Figure 4.1B**).

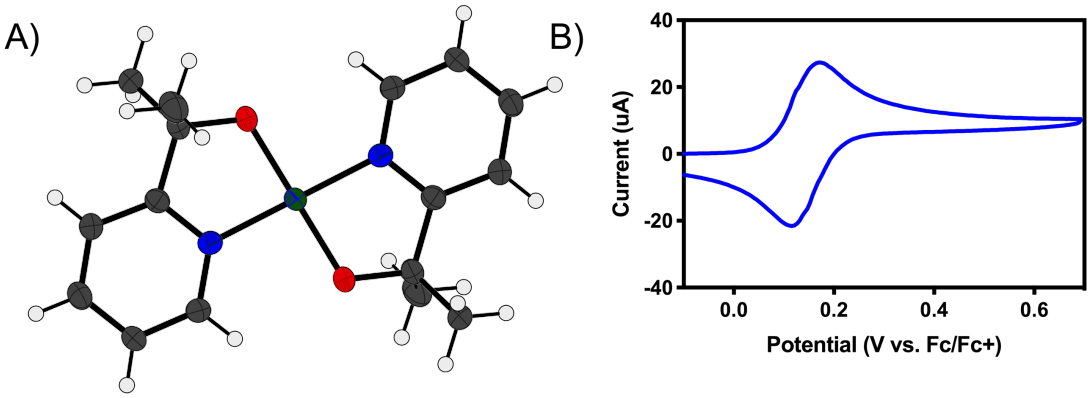

Figure 4.1. A) X-ray crystal structure of Ni(pyalk)$_2$ (**1**). Atoms are shown at the 50% probability level. (**1**). B) Cyclic voltammogram of **1** in MeCN. The reversible wave at 0.15 V vs. Fc/Fc$^+$ is assigned as a Ni(II/III) couple.

In CH_2Cl_2, **1** was treated with [NO][BF_4] or [NO][PF_6] (E^0 = 0.6 V vs. Fc/Fc$^+$) to generate the oxidized species (**Scheme 4.1**). Upon addition of oxidant, the solution immediately changed from light green to deep blue. UV-visible spectroscopy indicated the presence of two intense features in the absorption spectrum (λ_{max} = 340 nm and 610 nm, **Figure 4.11**). Such intense absorption features in the visible and NIR regions are consistent with the data from other Ni(III) compounds,[13] which led us to suspect that the Ni center had been oxidized. In addition, ^{1}H NMR of **2** gave a broad paramagnetic spectrum, in contrast to the diamagnetic spectrum of **1** (**Figure 4.13**). Measurement of the solution magnetic susceptibility by the Evans method[14] at room temperature gave a μ_{eff} of 1.87 for **2**, consistent with the presence of one unpaired electron, as expected for a square-planar Ni(III) compound.

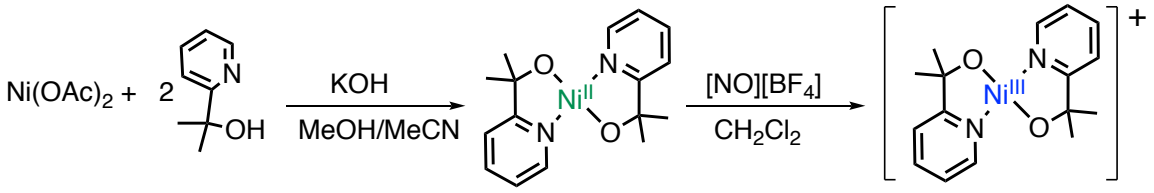

Scheme 4.1. Synthetic route for preparation of $Ni^{II}(pyalk)_2$ (**1**) and $Ni^{III}(pyalk)_2^+$ (**2**).

Electron paramagnetic resonance (EPR) spectroscopy showed the presence of a single S = ½ species (**Figure 4.2A**). A ligand centered oxidation would be expected to show an isotropic signal near g = 2.0. However, the observed rhombic spectrum had g values of g_x = 2.077, g_y = 2.091, g_z = 2.274. These g values, as well as g_{ave} = 2.145, are consistent with a low-spin square-planar d^7 Ni(III) complex.[15]

As demonstrated for a variety of iridium complexes,[16-19] X-ray photoelectron spectroscopy (XPS) provides another method for identifying a metal-centered oxidation. For metal-centered redox events with no change to the ligand set, the Ni 2p binding energy is expected to increase with oxidation state. Between **1** and **2**, the Ni 2p binding energy increases by 1.4 eV, consistent with a metal-centered oxidation from Ni(II) to Ni(III) (**Figure 4.2B**).

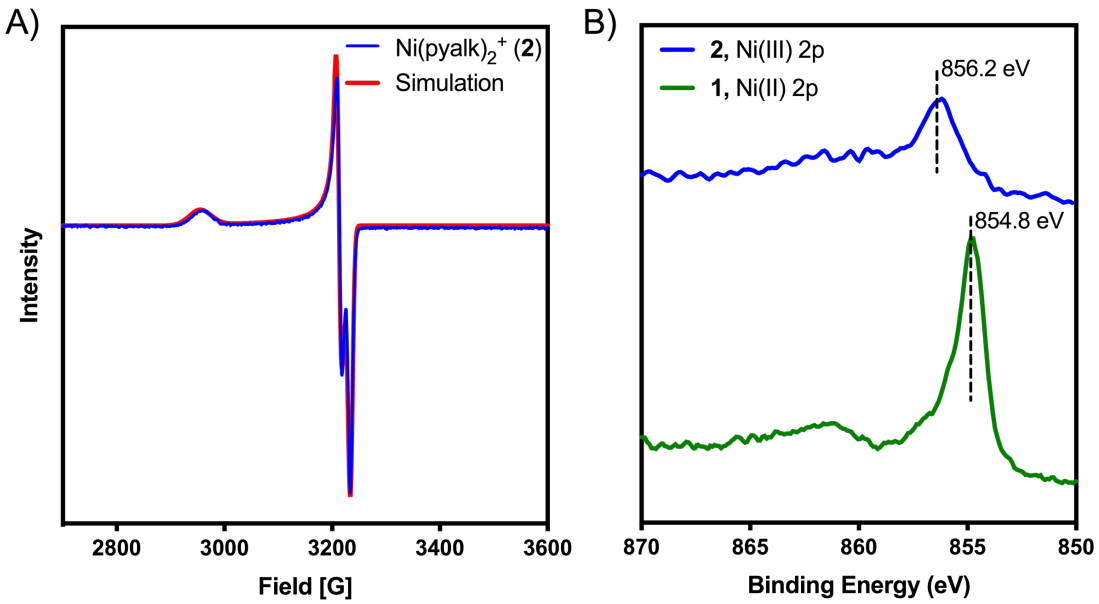

Figure 4.2. A) experimental (blue) and simulated (red) EPR spectrum of **2** taken in CH_2Cl_2/toluene at 77 K. B) XPS spectrum of **2** (top) and **1** (bottom). The ~1 eV shift is consistent with a one-electron oxidation of the nickel center.

High-resolution electrospray ionization (ESI) mass spectrometry confirmed the molecular formula of **2**. A solution of **2** in CH_2Cl_2 gave a peak at m/z = 330.09 with the expected isotopic pattern for nickel (**Figure 4.12A**). A mass spectrum of the parent compound, **1**, was also taken, which showed a peak at m/z = 331.09 (**Figure 4.12B**), corresponding to [**1** + H^+]. Despite having the same elemental formula, **1** is uncharged, and thus is observed as the positively charged protonated species, whereas **2** bears a positive charge already, and thus is observed without any associated ions. This result confirms that **2** is the one-electron oxidation product of **1**. The ESI mass spectrum of **2** does show a small signal at m/z = 331.09, which may indicate that some reduction of **2** occurs during the mass spectral analysis or over time in CH_2Cl_2.

Despite our best efforts, we were unable to obtain a crystal structure of **2**. While attempting to use pyridine as a co-solvent for crystallization, however, the solution changed from deep blue to bright orange (λ_{max} = 420 nm, **Figure 4.11**), suggesting the formation of a new Ni(III) compound. Crystals of this new complex, **3**, were successfully grown from CH_2Cl_2/pentanes (**Figure 4.3A**). **3** proved to be an octahedral complex, with two equatorial pyalk ligands and two axial pyridines. **3** contains a PF_6^- counteranion, and a comparison of Ni-O bond lengths (**Table 4.4**) indicate that the alkoxide arms of the pyalk ligand on **3** remain deprotonated, suggesting that **3** remains in the Ni(III) oxidation state. The EPR spectrum of **3** (**Figure 4.3B**) exhibits an axial signal with g_x = 2.202, g_y = 2.163, and g_z = 2.030. A five-line hyperfine pattern is observed on the g_z turning point, indicating coupling of the unpaired electron to the pyridyl nitrogens.[20] We found that the pyridine ligands do not remain bound in solution unless excess pyridine is present; when crystals of **3** were dissolved in CH_2Cl_2, **3** immediately reverted to **2**, as observed by UV-Visible spectroscopy (**Figure 4.11**). Upon addition of excess pyridine, the absorbance spectrum of **3** was re-established.

Remarkably, **2** and **3** are stable at room temperature, both as solids and in solution; this is rare for Ni(III) compounds, which tend to be stable only between -80 °C and -20 °C.[13, 21-22]

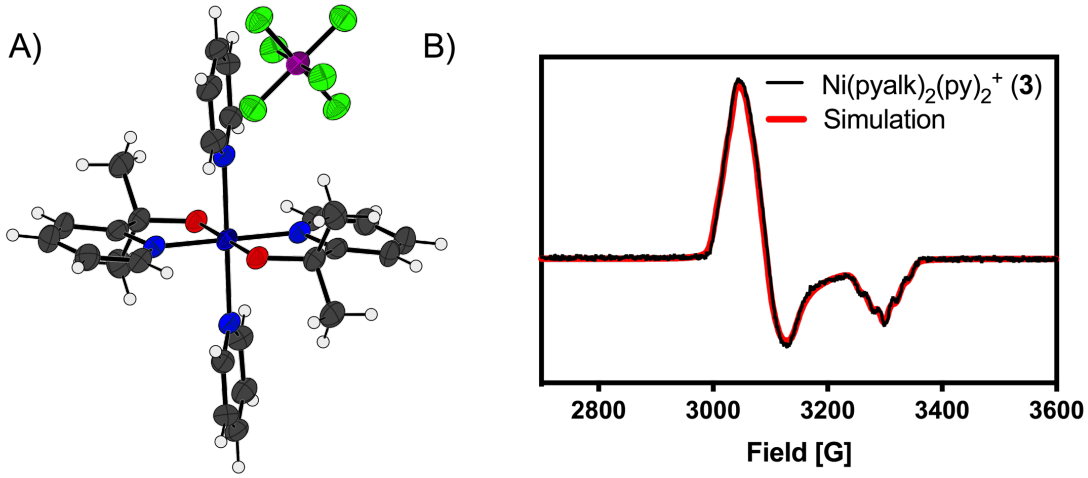

Figure 4.3. A) X-ray crystal structure of **3**. Atoms are shown at the 50% probability level. A non-coordinated pyridine has been omitted for clarity. B) experimental (black) and simulated (red) EPR spectrum of **3** in CH_2Cl_2/pyridine at 193 K.

4.3 Oxidation of phenols

With the oxidation state of **2** established, we sought to test its oxidative reactivity. We had shown in previous studies that the pyalk ligand could be reversibly protonated while coordinated to first row transition metals;[23] therefore, we hypothesized that **2** could undergo proton-coupled electron transfer (PCET) through the reaction proposed in **Scheme 4.2**.

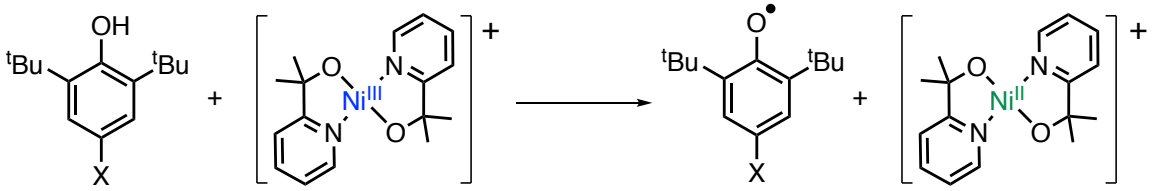

Scheme 4.2. Proposed PCET pathway for oxidation of phenols by **2**.

To test **2** for PCET reactivity, **2** was treated with 100 equivalents of 2,4,6-tri-tert-butylphenol (TTBP), a common substrate for PCET reactions due to the stability of the phenoxyl radical formed upon the loss of proton and electron. When the colorless solution of TTBP was added to the deep blue solution of **2** in CH_2Cl_2, a color change was immediately observed. The appearance of the characteristic peaks at 383 nm and 400 nm in the UV-Visible absorbance spectrum of this solution (**Figure 4.4**) indicated that the tri-tert-butylphenoxyl radical had been formed, causing the observed color change,[24] and the disappearance of the features at 340 nm and 610 nm indicated that **2** had

been consumed. In a similar reaction between **2** and 2,6-di-tert-butyl-phenol (DTBP), the radical coupling product 3,3',5,5'-tetra-*tert*-butyl-[1,1'-bi(cyclohexylidene)]-2,2',5,5'-tetraene-4,4'-dione was detected by gas chromatography-mass spectrometry (GC-MS, **Figure 4.14**). These results suggested that **2** was undergoing PCET.

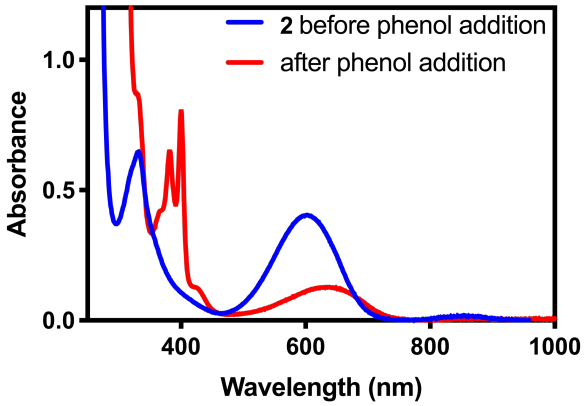

Figure 4.4. UV-visible spectrum of **2** before (blue) and after (red) addition of excess tri-tert-butylphenol. The red trace is consistent with the published UV-visible spectrum of the tri-tert-butylphenoxyl radical.[24]

For reactions of highly oxidized metal species with phenols, several types of PCET reactions are possible: proton transfer followed by electron transfer (PT-ET), electron transfer followed by proton transfer (ET-PT), and concerted proton-electron transfer (CPET)/hydrogen atom transfer (HAT) mechanisms have all been observed for transition metal systems.[25-27] Analysis of kinetic measurements can be used to differentiate between these mechanisms. Therefore, the kinetics of the reaction of **2** with a series of *para*-substituted 2,6-di-t-butylphenols (4-X-2,6-DTBP) was studied by stopped-flow UV-Visible spectrophotometry in order to further investigate the mechanism of oxidation by **2**. For these reactions, excess substrate was used to ensure pseudo-first order conditions (10-100 equivalents 4-X-2,6-DTBP). Representative UV-visible spectra as a function of time are displayed in **Figure 4.5** and representative time traces can be found in **Figure 4.15** and **Figure 4.16**. Reactions with all substrates under these conditions fit well to a single exponential decay at a single wavelength (λ = 610 nm), for which global analysis gave k_{obs} values. Plots of k_{obs} vs. initial substrate concentration displayed a linear dependence (**Figure 4.17**-**Figure 4.23**), allowing us to determine the second-order rate constant (k_2) for each substrate

(**Table 4.3**).

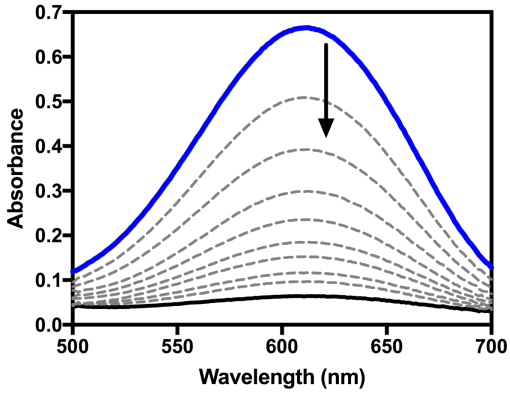

Figure 4.5. Representative UV-visible spectra as a function of time for the reaction of **2** with 4-X-2,6-DTBP in CH_2Cl_2. The dashed curves show one out of every 100 intermediate traces.

Measured k_2 values were plotted against the Hammett parameter σ_p^+ (**Figure 4.6.A**). The σ_p^+ constant was chosen rather than σ_p because σ_p^+ is suggested to more accurately represent the electronic structure of the transition state for CPET from phenols,[28] and a strong negative correlation between σ_p^+ and reaction rate is well known for this class of reactions.[29] Hammett analysis showed that k_2 decreases with the electron-withdrawing capabilities of the *para*-substituent of the substrate (ρ = -2.19). This result is inconsistent with a rate-limiting proton transfer followed by electron transfer (PT-ET) mechanism, which would show a positive linear correlation in the Hammett plot.[30] The observed strong negative association is, however, consistent with the formation of the electron deficient phenoxyl radical intermediate.[31-32] These results suggest a CPET mechanism for the reaction of 4-X-2,6-DTBP substrates with **2**. Similarly, the plot of log(k_2) vs. O-H bond dissociation enthalpy (BDE_{O-H}) of the phenol substrates also demonstrated a strong linear correlation (**Figure 4.6.B**).[33] In contrast, the plots of k_2 vs. substrate pK_a or $E_{1/2}$ showed a much poorer correlation (**Figure 4.24**). This linear dependence between log(k_2) and BDE_{O-H} also suggests a CPET mechanism and is consistent with similar plots constructed for other metal-based oxidants.[21, 34-35] It should be noted that this mechanism could also be described as hydrogen atom transfer (HAT) and is frequently referred to as such in the literature.[36]

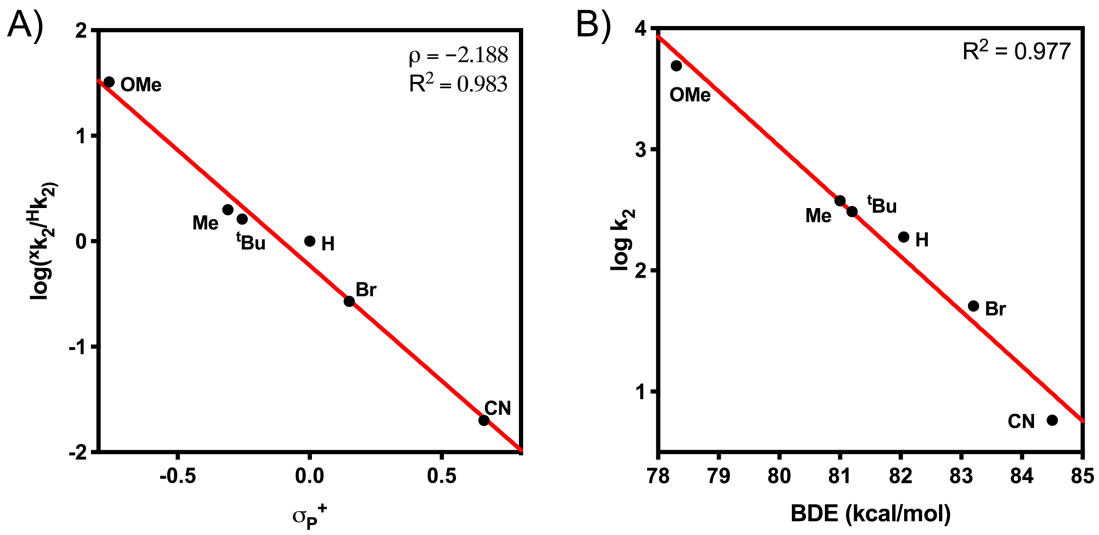

Figure 4.6. A) Hammett plot for the reaction of **2** with 4-X-2,6-DTBP substrates. B) Plot of log(k_2) vs. BDE of 4-X-2,6-DTBP substrates.

H/D kinetic isotope effects (k_2(H)/k_2(D), KIE) can help differentiate between the previously discussed mechanisms. When the phenolic proton of 2,6-DTBP was replaced with a deuterium atom, the measured k_2 value decreased dramatically, and a KIE of ~4 was calculated (**Figure 4.7**). A primary KIE of this magnitude implies that the cleavage of an O-H bond occurs in the rate-determining step, ruling out pathways involving rate-limiting electron transfer. This value for the KIE is also in good agreement with KIEs reported for the reaction of other metal-based oxidants with 2,6-DTBP that react via CPET.[22, 31]

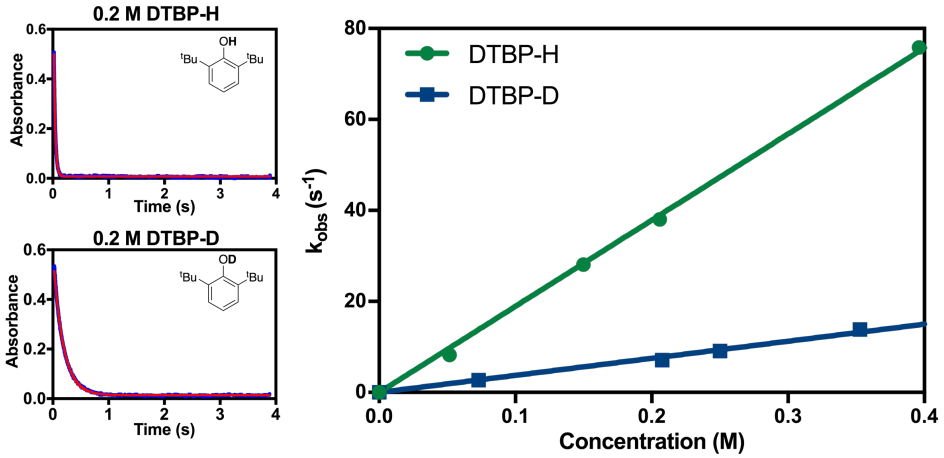

Figure 4.7. Representative time trace of the absorbance at λ = 610 nm for the reaction of **2** with 2-6-DTBP-H (top left) and 2,6-DTBP-D (bottom left), and plot of k_{obs} vs. concentration for 2,6-DTBP-H and 2,6-DTBP-D substrates (right).

It should be noted that pK_a and BDE values used in our analysis were measured in dimethyl sulfoxide (DMSO) rather than CH_2Cl_2, due to the lack of an absolute pK_a scale in CH_2Cl_2.[37] The general linear trend, however, is expected to remain the same regardless of solvent, as relative bond dissociation enthalpies and bond dissociation free energies (BDFEs) do not change significantly with solvent. To test this assumption, the BDFEs in CH_2Cl_2 of several phenol substrates were estimated by converting from DMSO values using Abraham's empirical model.[38-40] Calculating BDFEs in this manner relies on a number of assumptions, which are discussed in more detail in the supporting information (**Section 4.8.4**), so the BDFE values should be treated as estimates. Even so, we still see a strong linear correlation between $\log(k_2)$ and $BDFE_{CH2Cl2}$ (**Figure 4.25**). In a similar fashion, we also used Ingold's kinetic solvent effect relationship to calculate the expected rate constants in DMSO,[41] which we then plotted against known BDFEs and BDEs measured in DMSO (**Figure 4.26**). Once again, we saw a strong linear correlation, further supporting our conclusion that **2** reacts with phenols through a CPET mechanism.

4.4 Oxidation of hydrocarbons

To further probe its CPET reactivity, **2** was treated with a number of hydrocarbon substrates. Initial reactions of **2** with 1,4-cyclohexadiene and 9,10-dihydroanthracene produced the expected products of benzene and anthracene, as determined by gas chromatography and ^{1}H-NMR (**Figure 4.27A**). To determine the extent of reactivity of **2** with hydrocarbons, **2** was treated with a number of substrates having a range of C-H bond strengths.

As with phenols, the reactions were monitored by stopped-flow UV-visible spectroscopy, or by UV-visible spectroscopy for slowly reacting substrates. All reactions were carried out under pseudo-first order conditions (10-100 equivalents of substrate). Reactions with all substrates under these conditions gave a good fit to a single exponential decay at a single wavelength (λ = 610 nm, representative examples can be found in **Figure 4.28**), except for reactions with THF, and global analysis was used to find k_{obs} values. For reactions with THF, the method of initial rates was used to find k_{obs} values. Plots of k_{obs} vs. substrate concentration gave good linear fits for all substrates, and the slopes of these fits were used to extract k_2 values for each substrate (**Figure 4.29** – **Figure**

4.35). When appropriate, the data were statistically corrected to account for the number of hydrogen atoms susceptible to oxidation. For kinetic analysis of multi-proton/multi-electron reactions, such as the oxidation of 9,10-dihydroanthracene to anthracene (**Figure 4.27B**), the first CPET step was considered to be the rate-determining step, since the resulting radical species generally have significantly lower BDEs than the parent compounds.[38, 42-43]

2 was found to react with hydrocarbons with C-H bond strengths that ranged from 77-92 kcal/mol. For substrates with low C-H bond strengths, **2** reacted at appreciable rates – log k_2 values of 0.89 and 0.74 were found for reactions of **2** with 1,4-cyclohexadiene and 9,10-dihydroanthracene (DHA), respectively. A plot of log(k_2) vs. C-H BDE showed a strong linear correlation (**Figure 4.8**). In contrast, plots of log(k_2) vs. substrate $E_{1/2}$ or pK_a showed a very poor correlation (**Figure 4.36**). This result strongly suggests a CPET mechanism for hydrocarbon oxidation as well.

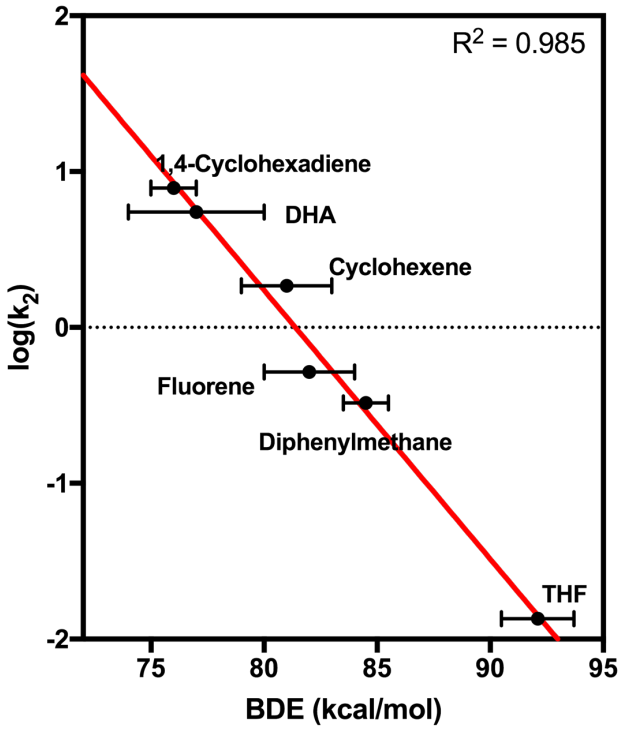

Figure 4.8. Plot of log(k_2) vs. bond dissociation enthalpy (BDE) for the reaction of **2** with hydrocarbon substrates.

To further investigate the mechanism of PCET by **2**, dihydroanthracene-d_4 was prepared, and an H/D kinetic isotope effect was measured. A large H/D KIE of ~11 was observed, indicating

the involvement of a proton in the rate-determining step (**Figure 4.37**). This result, in combination with the linear correlation between log(k_2) and C-H bond strength, further supports our assignment of a CPET mechanism.

4.5 Thermodynamic analysis

We sought to identify the nickel-containing products of the reaction of **2** with phenol and hydrocarbon substrates. Based on our results suggesting that a CPET mechanism was at play, we suspected that the nickel center was being reduced and that the pyalk ligand was accepting a proton and transforming the alkoxide ligand to an alcohol, resulting in the formation $[Ni(pyalk)(pyalkH)]^+$. ^1H NMR of reaction products of **2** with 2,6-DTBP, however, showed only the presence of the fully deprotonated **1** in solution. A blue precipitate was also identified. This precipitate was dissolved in water and extracted into CH_2Cl_2 using $NaBAr^F$ (BAr^F = $[B[3,5\text{-}(CF_3)_2C_6H_3]_4]^-$). ^1H NMR analysis of the resulting product indicated the presence of $[Ni(pyalkH)_2][2(BAr^F)]$ (**4**) (**Figure 4.9A**, **Figure 4.38**). This result suggests that, once the nickel metal center has been reduced, the pyalkH proton is labile enough to rearrange. Attempts to crystallize **4** were unsuccessful; however, when treating $Ni(OAc)_2$ with the pyalkH ligand, $Ni(pyalkH)_2(OAc)_2$ (**5**) was crystallized, demonstrating the binding of the pyalkH ligand to a nickel center (**Figure 4.9.B**).

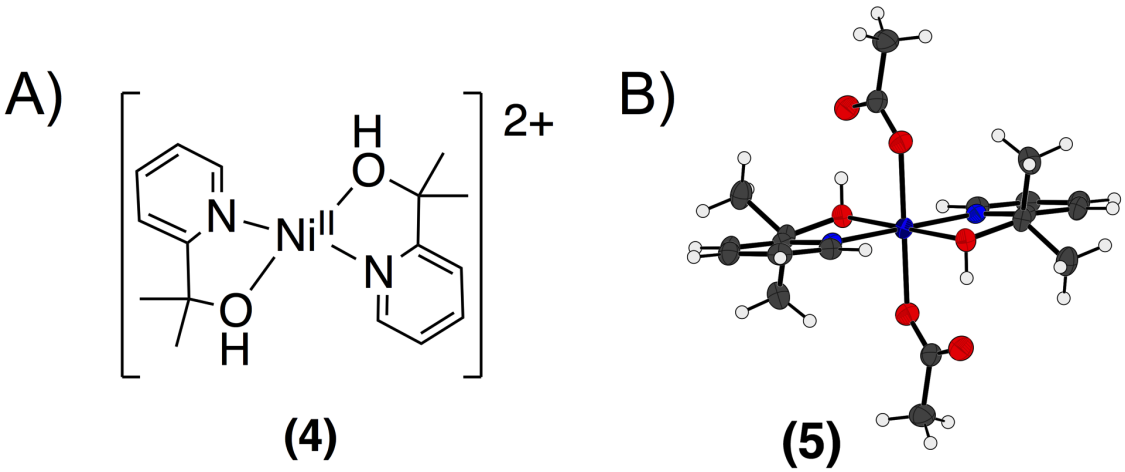

Figure 4.9. A) Structure of $[Ni(pyalkH)_2]^{2+}$ (**4**). B) X-ray crystal structure of $Ni(pyalkH)_2(OAc)_2$ (**5**).

With the reaction products more fully understood, we constructed the square scheme in **Scheme 4.3** to determine the thermodynamics of the reaction. The pK_a for the first deprotonation of the pyalk ligand of **4** (pK_{a1},**Figure 4.39**) was estimated spectroscopically to be ~25 in MeCN using data from the deprotonation of **4** to **1**. Using this value, along with the $E^0_{1/2}$ value of 0.15 V vs. Fc/Fc^+ in MeCN, we were able to determine a BDFE for the bound pyalk O-H bond of ~91 kcal/mol in MeCN using the square scheme shown in **Scheme 4.3** and **Equation 4.1**:[38]

$$BDFE = 1.37pK_a + 23.06E^0 + C_{G,sol} \qquad \textbf{(Equation 4.1)}$$

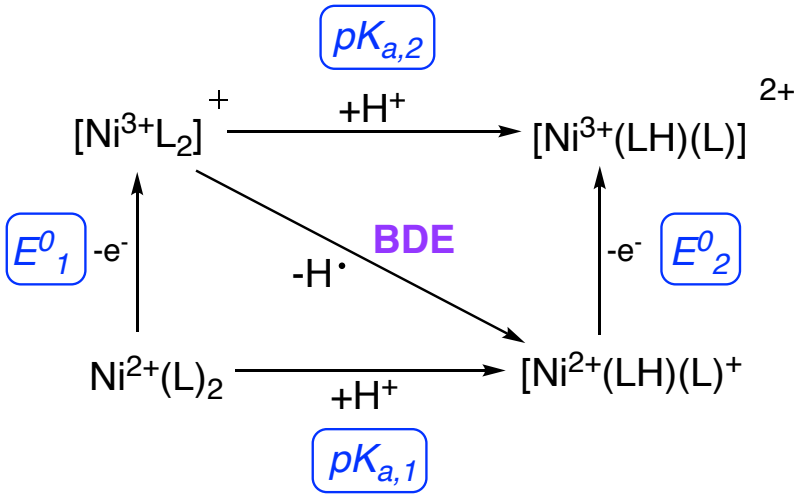

$$2\,[Ni(pyalk)(pyalkH)]^+ \longrightarrow Ni(pyalk)_2 + [Ni(pyalkH)_2]^{2+}$$

Scheme 4.3. Thermochemical square scheme for stepwise vs. concerted proton and electron transfer to the complexes described in this work (L=pyalk, LH = pyalkH). The lower equation shows the proposed proton exchange, explaining the observed products of reactions of **2** with substrates.

It is generally considered more appropriate to use BDFEs to describe the thermodynamics of PCET by transition metal complexes due to non-negligible entropic contributions.[38] However, many reported high-valent metal-oxo or metal-hydroxo oxidants report only the BDE of the O-H bond formed upon the reaction with substrate. Therefore, in order to facilitate a comparison between **2** and reported high-valent CPET/HAT reagents, the BDE of the pyalk O-H bond was also calculated. The BDE of the pyalk O-H bond for the CPET product of **2** was calculated using same thermochemical parameters described above and **Equation 4.2**:

$$BDE = 1.37pK_a + 23.06E^0 + C_{H,sol} \qquad \textbf{(Equation. 4.2)}$$

For **2**, a BDE of ~94 kcal/mol in MeCN was calculated, using a value of 59.4 kcal/mol for C_H in MeCN.[38] This BDE can be compared with the value of 105 kcal/mol for ^{t}BuO-H,[44] taken as a model compound for free pyalkH, suggesting a modest O-H bond weakening on binding.

By cyclic voltammetry, **4** also showed a quasi-reversible redox feature in MeCN at $E^0_{1/2}$ = 0.58 V vs. Fc/Fc^+ (**Figure 4.10**). Using the BDFE calculated from Equation 1 and the square-scheme relationship, we can estimate the value for pK_{a2} to be ~18, 7 pK_a units below the calculated $pK_{a,1}$ of 25.

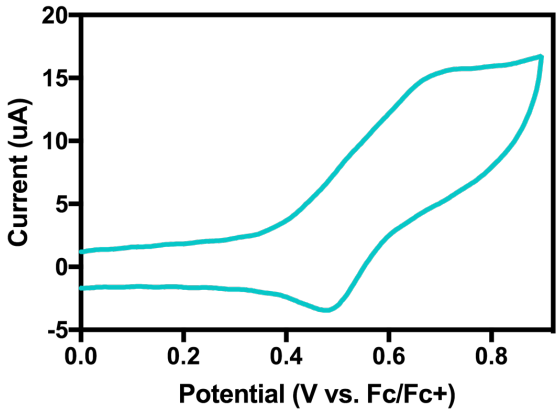

Figure 4.10. Cyclic voltammogram of **4** in MeCN.The quasi-reversible couple at E^0 = 0.58 V vs. Fc/Fc^+ is assigned as a Ni(II/III) couple.

Table 4.1. Thermodynamic and kinetic parameters of high-valent metal compounds capable of performing CPET with hydrocarbon substrates

Compound	E^0_1 (V vs. Fc/Fc^+)	BDE (kcal/mol)	log(k_2) DHA[a,b]	log(k_2) TTBP[a,b]	Ref
$[Ni^{III}(pyalk)_2]^+$ (2)	0.15	94	0.74	2.48	This work
$Ni^{III}(^{Me}pyN_2)(ONO_2)$[f]	0.43	-	0.91		21
$Ni^{III}(^{Me}pyN_2)(Cl)$[f]	0.56	-	-	0.394[d]	22
$[(MeAN)Cu^{III}(\mu\text{-}O_2)Ni^{III}(^{Me}Nacnac)]^+$ [g]	-	-	-	-0.82	45
$[Mn^{III}(H_3buea)(O)]^{2-}$ [h]	-2.0	77	-0.53	-	25
$[Mn^{IV}(H_3buea)(O)]^-$ [h]	-1.0	89	-1.59	-	25
$[Fe^{III}(PY5)(OCH_3)]^{2+}$ [i]	0.73	84	-2.25	-0.22[e]	46
$Cu^{III}(^{iPr}pyN_2)(OH)$[j]	-0.074	90	2.27	-	34
$Ru^{IV}(bpy)_2(py)(O)$	0.48[c]	84	2.09	-	35, 47-48

[a] k_2 = second-order rate constant for reaction with the designated substrate, measured at 25 °C unless otherwise noted; [b] DHA = 9,10-dihydroanthracene, TTBP = tri-tert-butylphenol (4-tBu-2,6-DTPB) [c] vs. SCE; [d] measured at -40 °C; [e] measured at -50 °C; [f] $^{Me}pyN_2$ = N, N′-(2,6-dimethylphenyl)-2,6-pyridinedicarboxamide; [g] MeAN = N,N,N′,N′,N′-pentamethyl-dipropylenetriamine and ^{Me}Nacnac = $[HC(CMeNC_6H_3(^iPr)_2)_2]$); [h] H_3buea = tris[(*N*′-*tert*-butylureaylato)-*N*-ethylene]amine; [i] PY5 = 2,6-bis(bis(2-pyridyl)methoxymethane)pyridine; [j] $^{iPr}pyN_2$ = N, N′-bis(2,6-diisopropylphenyl)-2,6-pyridinedicarboxamide.

The reactivity of **2** with 2,6-DTBP and DHA compares favorably with other reported high-valent metal-oxo and metal-hydroxo complexes capable of CPET or HAT (**Table 4.1**). **2** reacts with DHA at a faster rate than several manganese- and iron-oxo complexes. **2** also compares extremely well with high-valent metal alkoxide and carboxylate compounds, including the only other reported Ni(III) systems, which tend to react with C-H bonds at slower rates than their metal-oxo counterparts. We hypothesize that the particularly strong BDE of the O-H bond formed and the strong oxidizing power of **2** contribute to its high reactivity toward O-H and C-H bonds. This result demonstrates that fast CPET can be achieved in high-valent metal systems without the formation a metal-oxo or metal-hydroxo intermediate, a result relevant to several proposed water-oxidation mechanisms in artificial photosynthetic systems of cobalt,[49] copper,[11] and nickel.[50] This result also demonstrates that high-valent metal-alkoxide systems are capable of attacking strong C-H and O-H bonds, which is particularly relevant to water-oxidation catalysis. The pyalk ligand thus proves particularly useful for catalytic oxidations of this type.

4.6 Conclusions and outlook

We have synthesized and characterized a Ni(III)-alkoxide compound capable of reacting with strong C-H and O-H bonds at appreciable rates. A strong correlation between the second-order rate constant, k_2, and substrate bond dissociation enthalpy indicates a CPET mechanism. Large H/D kinetic isotope effects also support this assignment, while Hammett analysis and poor correlation between $\log(k_2)$ and substrate pK_a and $E_{1/2}$ disfavor stepwise mechanisms. We attribute the fast reactivity of **2** to the strong O-H BDE of the pyalk/pyalkH supporting ligand and the high oxidizing power of the complex. This result demonstrates that fast PCET can occur in high-valent metal oxidants without a metal-oxo unit, which may be relevant to certain nickel-containing enzymes or water-oxidation catalysts of cobalt, copper, or nickel. This report also provides the first full thermodynamic analysis of CPET by a high-valent nickel complex. The value of pyalk as a ligand for catalytic oxidations is further supported.

4.7 Experimental Details

4.7.1 General

Reagents were purchased from Sigma-Aldrich or Alfa Aesar and used as received unless otherwise specified. $[NO][BF_4]$ and $[NO][PF_6]$ were purified by sublimation under vacuum before use and stored at -25 °C in a glove box after purification. All solvents were purified prior to use by passing over a column of activated alumina and stored over molecular sieves. Experiments were performed under dinitrogen atmosphere in a glove box or using standard Schlenk technique, unless otherwise noted. pyalkH[51], 2,6-di-tert-butylphenol-d_1,[52] dihydroanthracene-d_4[46] were prepared according to literature procedures.

4.7.2 Physical Methods

^{1}H NMR: ^{1}H NMR spectra were recorded on an Agilent DD2 400 MHz spectrometer and ^{1}H chemical shifts were referenced to residual solvent. The solution magnetic susceptibility was determined using the Evans method in $CDCl_3$.[14]

UV-Visible Spectroscopy: Absorption spectra were collected using a Cary 50 spectrophotometer.

High Resolution Mass Spectrometry (HR-MS) of Ni(pyalk)$_2$ (1): The mass spectral data were obtained from a Thermo Scientific (Waltham, MA) LTQ Orbitrap ELITE mass spectrometer. The sample was directly infused into the mass spectrometer via a micro pump. Data were acquired and analyzed with Xcalibur (v2.1). Resolution was set at 120000, and with a mass range (m/z) generally from 150 to 1000. Exact masses were obtained for the entire broadband spectrum.

HR-MS of [Ni(pyalk)$_2$]$^+$ (2): HR-MS was performed with a Thermo Scientific Orbitrap Velos Pro Mass Spectrometer. HR-MS data were recorded in cation mode with a resolution (FWHM) of at least 30,000 at 400 m/z and averaged over at least 100 spectra. The spray needle was held at 3.5 kV with an injection rate of 10 µL/min, source temperature 44 °C, capillary temperature 225 °C and sheath gas flow rate 8 a.u. Instrument parameters were held constant for all MS experiments.

Gas Chromatography-Mass Spectrometry (GC-MS): GC-MS data were taken on an Agilent 6890N/5973 spectrometer.

EPR: EPR spectra were measured on a Bruker EXELSYS E500 spectrometer utilizing a super-high Q resonator and a liquid nitrogen finger dewar at 77 K. Instrument parameters included microwave frequency: 9.374 GHz; microwave power: 0.00206 mW; modulation frequency: 100 kHz; modulation amplitude: 5.00 G; conversion time 5.12 ms; time constant: 1.28 ms. Samples were prepared at 1 mM in a 1:1 CH_2Cl_2/toluene mixture. Simulations were performed using Matlab and the Easyspin package.[53]

X-ray Photoelectron Spectroscopy: The XPS spectra were collected using a monochromatic 1486.7 eV Al Kα X-ray source on PHI VersaProbe II X-ray Photoelectron Spectrometer with a 0.47 eV system resolution. The energy scale was calibrated using Cu 2p3/2 (932.67eV) and Au 4f7/2 (84.00 eV) peaks on a clean copper plate and a clean gold foil. The samples were prepared by drop casting a solution of **2** in CH_2Cl_2 onto a Si wafer. The reported shifts were referenced using the Si 2p peak (99.3 eV) from the Si wafer.

Electrochemical measurements: Electrochemical measurements were performed on a Pine AFCBP1 bipotentiostat using a standard three-electrode configuration. A boron-doped diamond working electrode and a platinum counter-electrode were used. A silver wire was used as a pseudo-reference electrode, and the potential was referenced using a ferrocene internal standard. Spectra were taking in dry MeCN with 0.1 M tetrabutylammonium hexafluorophosphate used as electrolyte.

Kinetics: Reactions were monitored by stopped-flow (except for the reaction of **2** with THF). All stopped flow experiments were performed at room temperature using an On-line Instruments Systems, Inc. (Olis) U.S.A. Stopped-Flow paired with an Olis RSM 1000 Rapid Scanning Spectrophotometer. In a typical experiment, a 2 mM stock solution of $Ni^{3+}(pyalk)_2$ in CH_2Cl_2 was prepared under dinitrogen atmosphere in a glove box, along with solutions of phenol or hydrocarbon substrates at various concentrations. Solutions were transferred to gas-tight stopped flow syringes with Luer Lock tips. Before a run, the stopped-flow mixing lines were flushed with dry CH_2Cl_2 and then washed with $Ni^{3+}(pyalk)_2$ or substrate. During the run, equal volumes of $Ni^{3+}(pyalk)_2$ and substrate were mixed, and 500-4000 UV-visible spectra were taken over the

course of the reaction. Observed rate constants were determined using global analysis fitting with the SPECFIT/32 software.

The reaction of **2** with THF was monitored by UV-visible spectroscopy on an Agilent 845x UV-visible spectrophotometer. In a typical experiment, **2** was added to a sealable quartz cuvette equipped with a septum top in an N_2-filled glove box. The cuvette was sealed and removed from the glovebox. Dry THF was injected into the cuvette by syringe, shaken briefly to dissolve the solid **2**, and then the first UV-visible spectrum was taken. Observed rate constants were determined using a method of initial rates.

pK_a determination of 1: Titrations to determine the pK_a of **1** were monitored by UV-visible spectroscopy. As **4** appears to be sensitive to excess acid, the pK_a of **1** was determined by the titration of **4** with DBU to generate **1**. The pK_a was determined from a plot of [DBU] vs. [**1**][DBU-H^+]/[**4**]. Concentrations of **1**, **4**, DBU, and DBU-H^+ were determined by mass balance as described in reference 54.[54] The titration was performed 3 times, and the final pK_a was found by averaging the pK_a values found in each titration.

4.7.3 Synthesis and characterization

Synthesis of Ni(pyalk)$_2$ (1). 0.60 g (2.5 mmol) $NiCl_2 \bullet 6H_2O$ was dissolved in 20 mL MeOH and 40 mL MeCN. 0.70 g of pyalkH (5.1 mmol, 2.1 eq) was added and stirred for several minutes, during which time the color of the solution changed from teal to dark blue. This mixture was allowed to stir for an hour, at which time 1.0 mL (10 mmol, 4 eq) of a 0.1 M solution of KOH in MeOH was added, which caused the solution to turn yellow-green. This solution was allowed to stir for an hour. The solution was then taken to dryness by rotary evaporation, and the solid was redissolved in 5 mL CH_2Cl_2. 25 mL MeCN was added to this solution, and the CH_2Cl_2 was removed by rotary evaporation, resulting in the precipitation of a light green solid from the remaining MeCN. Crystals suitable for X-ray diffraction were grown from diffusion of pentanes into a solution of **1**. ^{1}H NMR ($CDCl_3$, 400 MHz): δ_H 8.03 (2H, d), 7.63 (2H, t), 7.07 (2H, t), 6.92 (2H, d), 1.54 (12 H, s) ppm. UV-visible λ_{max}, nm (ε M^{-1} cm^{-1}): 365 (150), 620 (75). Elemental analysis calculated for $NiC_{16}H_{20}N_2O_2$: C, 58.05; H, 6.09; N, 8.46. Found: C, 57.96; H, 6.14; N, 8.29. Yield: 0.65 g, 78%.

Synthesis of $[Ni(pyalk)_2]^+$ (2). To a 20 mL vial equipped with stir bar, 0.40 g (1.2 mmol) $Ni(pyalk)_2$ was added and dissolved in 10 mL dry CH_2Cl_2. Excess $[NO][BF_4]$ was added. Within seconds, the light green solution turned dark blue. This solution was allowed to stir for 5 minutes. The solution was then filtered in order to remove any unreacted $[NO][BF_4]$. The resulting solution was then triturated with 50 mL pentanes, resulting in the precipitation of a dark blue solid. The solid was filtered under vacuum and washed with pentanes. UV-visible λ_{max}, nm (ε, M^{-1} cm^{-1}): 340 (990), 610 (1025). Evans method μ_{eff}: 1.87 μ_b. EPR (9.4 GW, 77K): Yield: 0.36 g, 75%.

$[Ni(pyalk)_2(py)_2]^+$ (3). 0.05 g **2** was dissolved in 2 mL CH_2Cl_2. To this solution, 0.5 mL pyridine was added. The solution immediately turned a bright yellow color. Crystals were obtained by vapor diffusion with pentanes at 0 °C. UV-visible λ_{max}, nm (ε, M^{-1} cm^{-1}): 415 (1100). EPR (9.4 GW, 77 K): $g_x = 2.202$, $g_y = 2.163$, $g_z = 2.030$. Yield: 0.04 g, 70%.

Synthesis of $[Ni(pyalkH)_2][2(Bar^F)]$ (4). In a reaction of **2** with dihydroanthracene (see below), a blue precipitate was identified. This precipitate was collected by vacuum filtration, dissolved in water and excess $NaBAr^F$ was added. This resulting product was then extracted into CH_2Cl_2 and triturated with pentanes, resulting in the formation of a blue solid.

$[Ni(pyalkH)_2][2(Bar^F)]$ (4) alternate synthesis. 0.1 g (0.3 mmol) $Ni(BF_4)_2 \bullet 6H_2O$ was dissolved in 10 mL H_2O. 0.081 g of pyalkH (0.6 mmol, 2.1 eq) was added and stirred for several minutes. This solution was transferred to a separatory funnel, and excess $NaBAr^F$ and CH_2Cl_2 were added. The resulting product was extracted into CH_2Cl_2 and washed 3 times with water. The organic layer was dried over $MgSO_4$ and brought to dryness by rotary evaporation. The resulting solid was redissolved in CH_2Cl_2, filtered, and layered with pentanes, resulting in a light blue powder. ^1H NMR ($CDCl_3$, 400 MHz): δ_H 8.53 (2H, d), 8.11 (t, 2H), 7.71 (s, 16H), 7.63 (d, 2H), 7.55 (s, 10H), 1.53 (s, 12H). Elemental analysis calculated for $NiC_{88}H_{56}B_2F_{48}N_3O_3$: C, 48.14; H, 2.57; N, 1.91. Found: C, 47.94; H, 2.56, N, 2.02 Yield: 0.31 g, 46%.

Synthesis of $Ni(pyalkH)_2(OAc)_2$ (5). 0.10 g (0.56 mmol) $NiOAc_2 \bullet 4H_2O$ was dissolved in 10 mL MeOH and 20 mL MeCN. 0.170 g of pyalkH (1.25 mmol, 2.2 eq) was added and stirred for several minutes, during which time the color of the solution changed from teal to bright blue. The solution was brought to dryness by rotary evaporation and redissolved in CH_2Cl_2. This solution was layered with pentanes and stored at -20 °C, affording blue crystals after several days. Elemental analysis calculated for $NiC_{20}H_{28}N_2O_6$: C, 53.25; H, 6.26; N, 6.21. Found: C, 52.34; H, 6.30, N, 5.96. Yield: 0.18 g, 85%.

*Reaction of **2** with 9,10 dihydroanthracene*: To a 20 mL vial equipped with stir bar in an N_2-filled glove box, 0.01 g (0.024 mmol) **2** was added. **2** was dissolved in 10 mL dry CH_2Cl_2, and to this solution 0.0095 g (2.2 eq) 9,10-dihydroanthracene was added. The solution was stirred for 4 hr, during which time the color changed from dark blue to light green and slightly cloudy. The solution was removed from the glove box and run over a plug of alumina to remove the reduced nickel species. The resulting solution was then brought to dryness by rotary evaporation and redissolved in $CDCl_3$ for ^1H NMR analysis.

4.8 Supplementary Figures and Discussion

4.8.1 Characterization of **1**-**3**

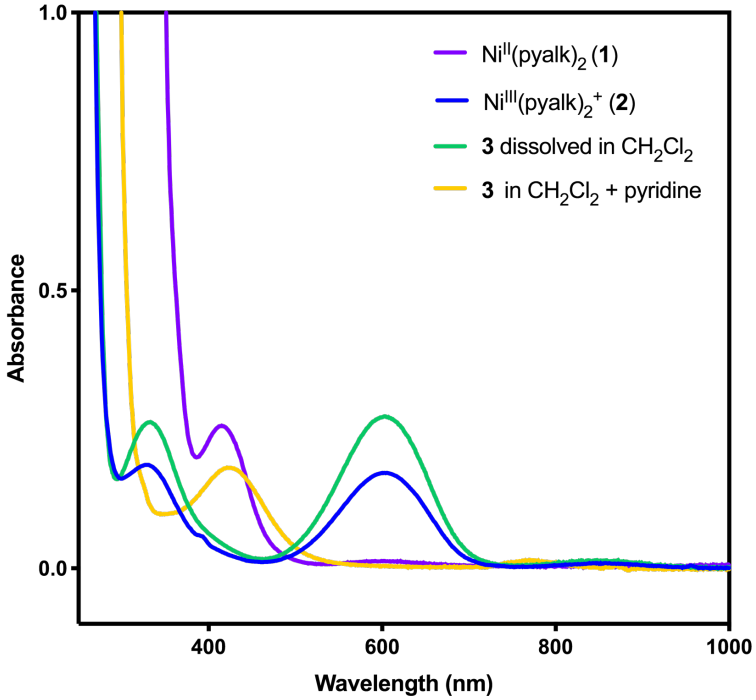

Figure 4.11. UV-visible spectrum of **3** in the absence (blue) and presence of excess pyridine (yellow). When pure crystals of **3** are dissolved in CH_2Cl_2, the UV-visible spectrum is identical to that of **2**, indicating that the pyridine ligands do not remain bound. When excess pyridine is added to this solution, the UV-visible spectrum of **3** is re-obtained. The spectrum of **1** has been included for comparison.

A)

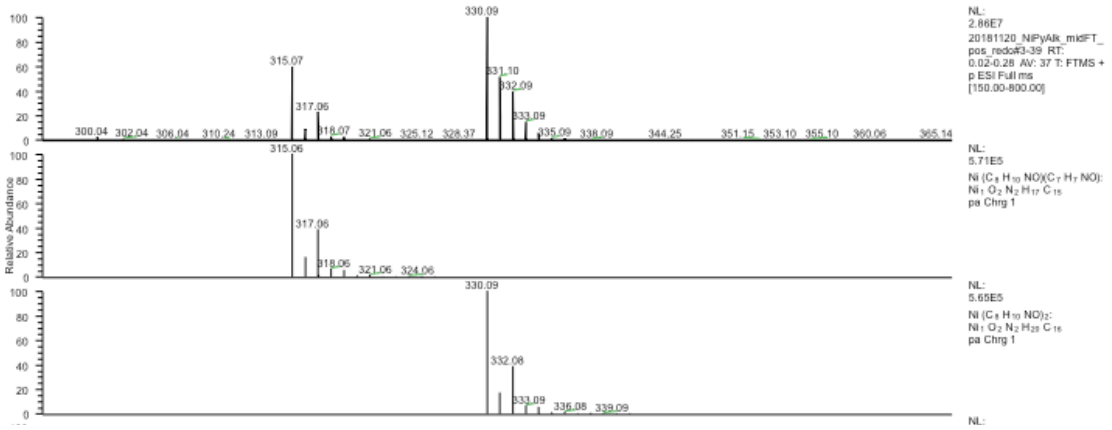

B)

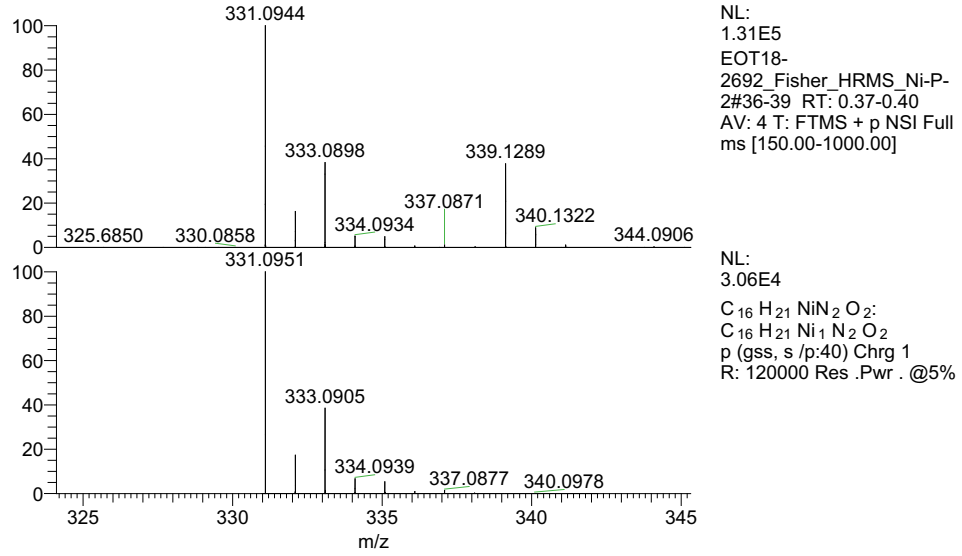

Figure 4.12. A) Actual (top) and theoretical (middle and bottom) HRMS spectra of $[Ni(pyalk)_2]^+$ (**2**) in positive mode. B) Actual (top) and theoretical (bottom) HRMS spectrum of $Ni(pyalk)_2$ (**1**) in positive mode.

A)

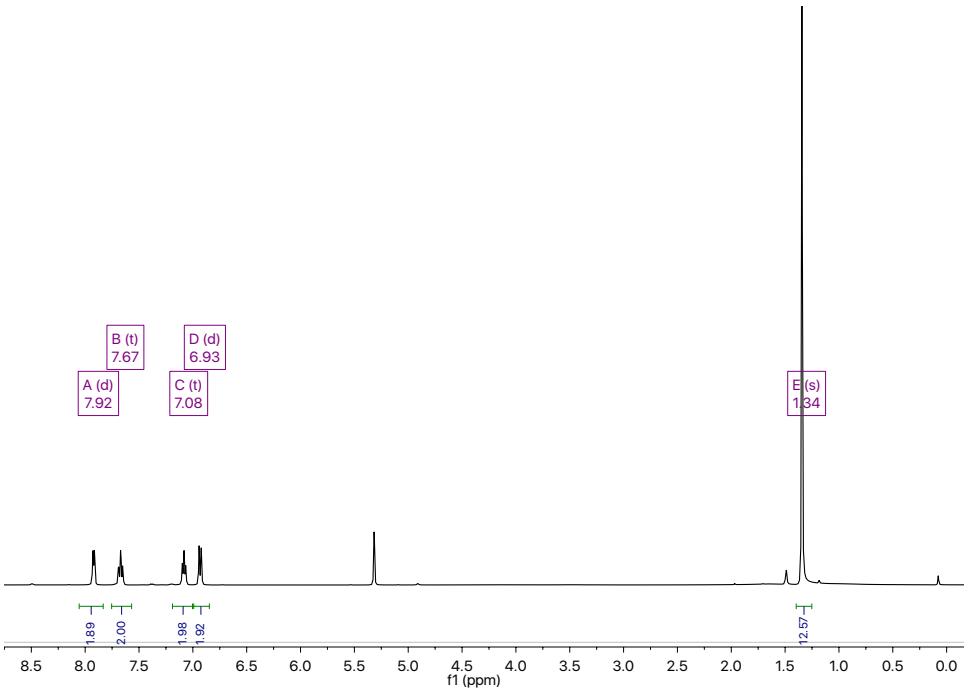

B)

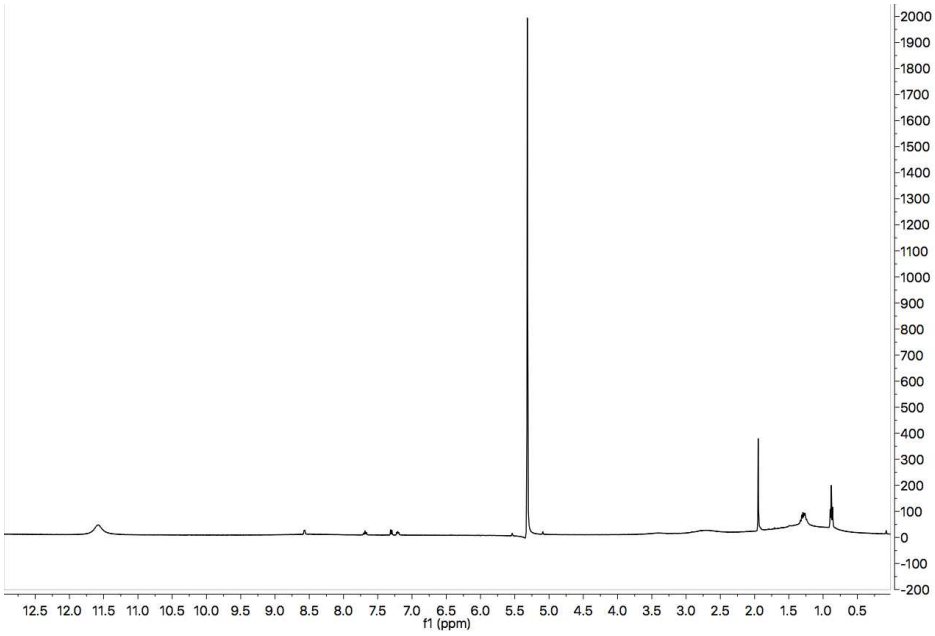

Figure 4.13. A) ^{1}H NMR spectrum of a 5mM solution of Ni(pyalk)$_2$ (**1**) in CD_2Cl_2. B) ^{1}H NMR spectrum of Ni(pyalk)$_2^+$ (**1**) in CD_2Cl_2.

4.8.2 Kinetic measurements for the reaction of **2** with phenol and hydrocarbon substrates

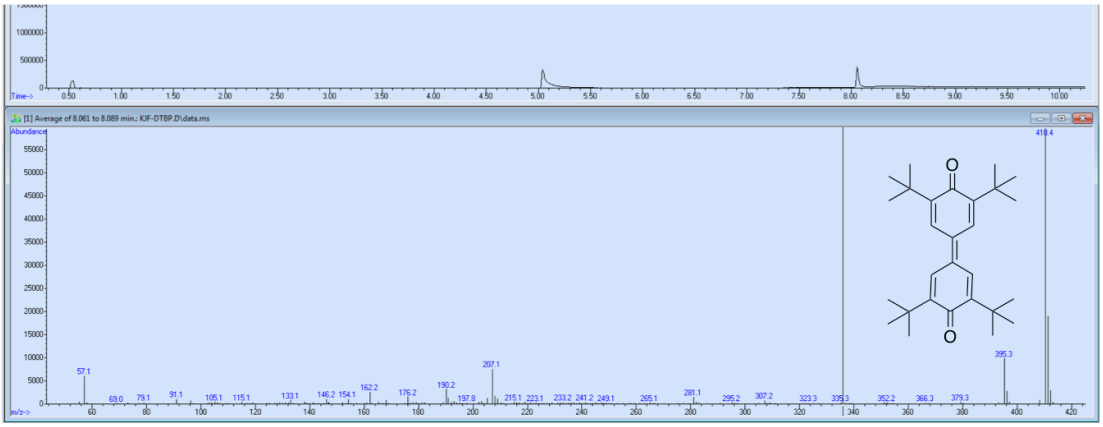

Figure 4.14. GC-MS spectrum of the products of the reaction between **2** and 2,6-DTBP.

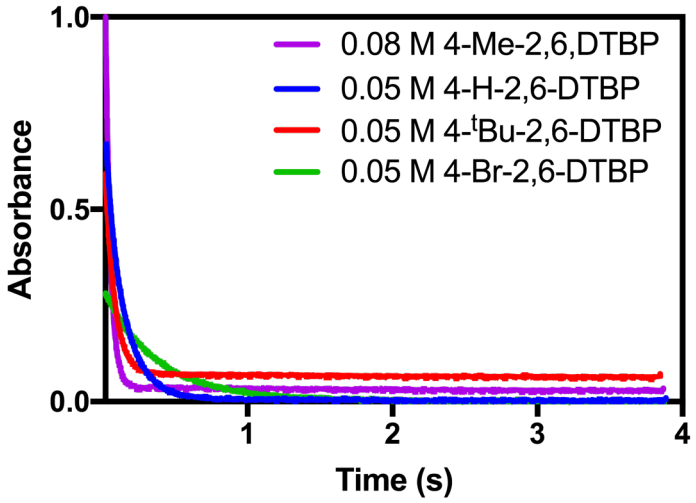

Figure 4.15. Representative traces of the absorbance at λ = 610 nm as a function of time for four of the phenol substrates under pseudo-first order conditions.

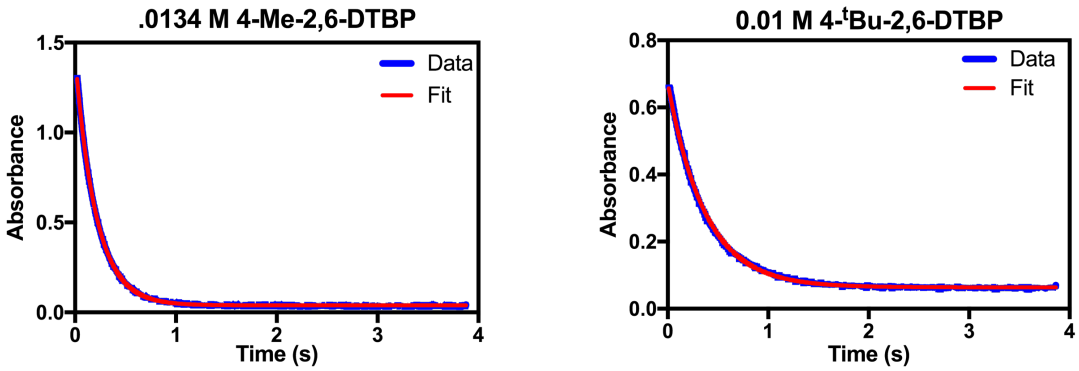

Figure 4.16. Representative fits of the absorbance at λ = 610 nm of two of these phenol substrates: 4-Me-2,6-DTBP (left) and 4-^{t}Bu-2,6-DTBP (right).

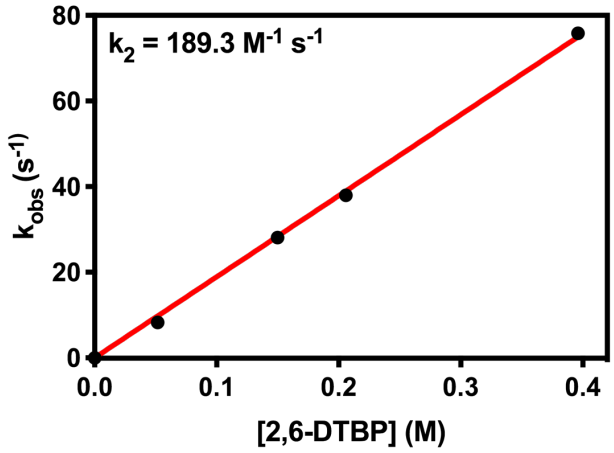

Figure 4.17. Plot of k_{obs} vs. concentration the pseudo-first order reaction of **2** with 2,6-di-tert-butylphenol in CH_2Cl_2 at 25 °C.

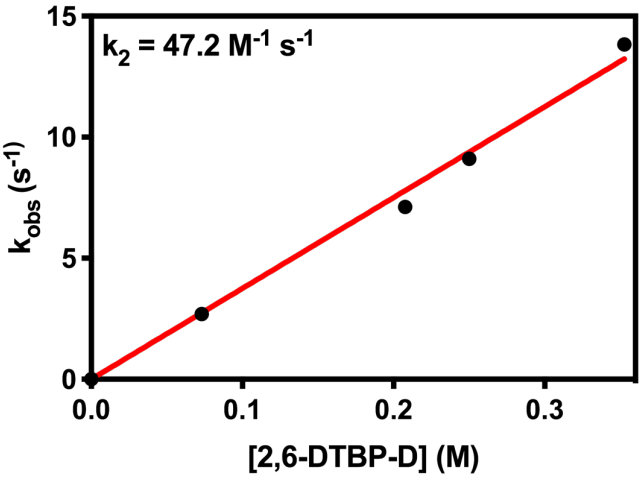

Figure 4.18. Plot of k_{obs} vs. concentration for the pseudo-first order reaction of **2** with 2,6-di-tert-butylphenol-D in CH_2Cl_2 at 25 °C.

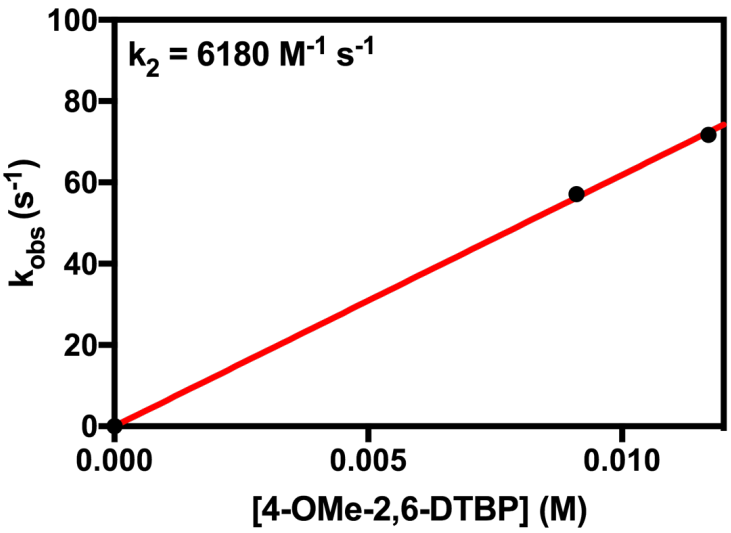

Figure 4.19. Plot of k_{obs} vs. concentration for the pseudo-first order reaction of **2** with 4-OMe-2,6-di-tert-butyl-phenol in CH_2Cl_2 at 25 °C.

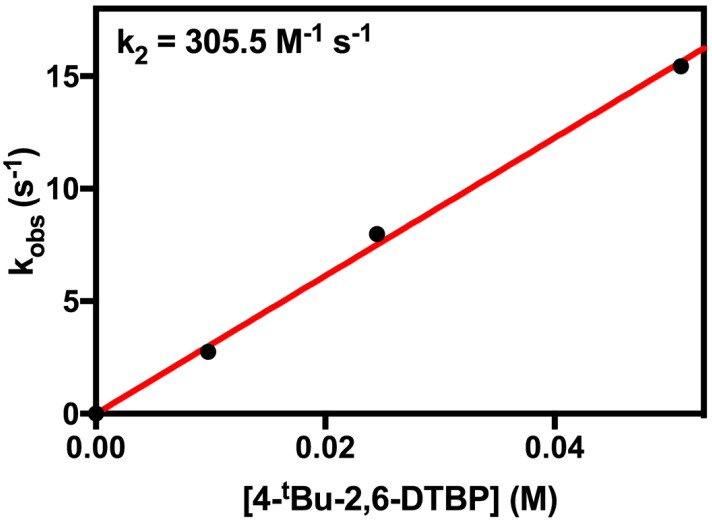

Figure 4.20. Plot of k_{obs} vs. concentration for the pseudo-first order reaction of **2** with 2,4,6-tri-tert-butylphenol in CH_2Cl_2 at 25 °C.

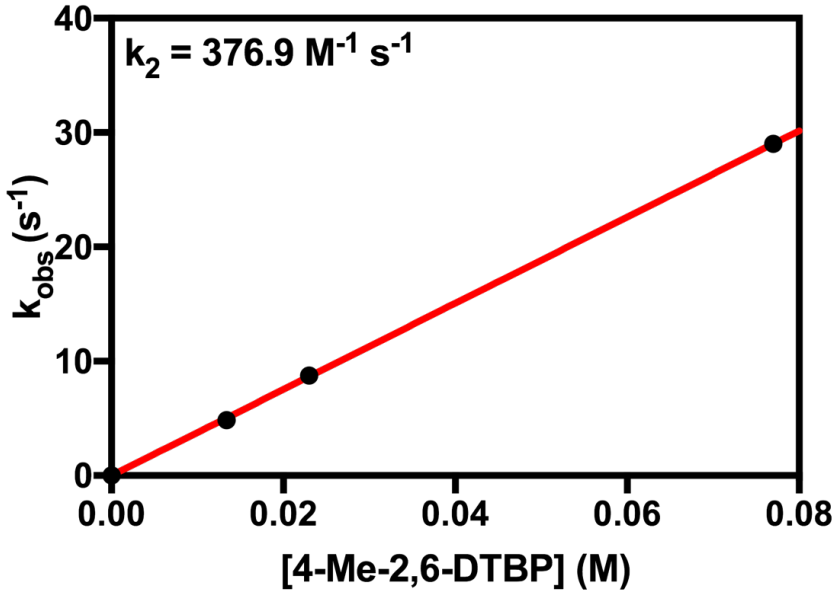

Figure 4.21. Plot of k_{obs} vs. concentration for the pseudo-first order reaction of **2** with 4-methyl-2,6-di-tert-butylphenol in CH_2Cl_2 at 25 °C.

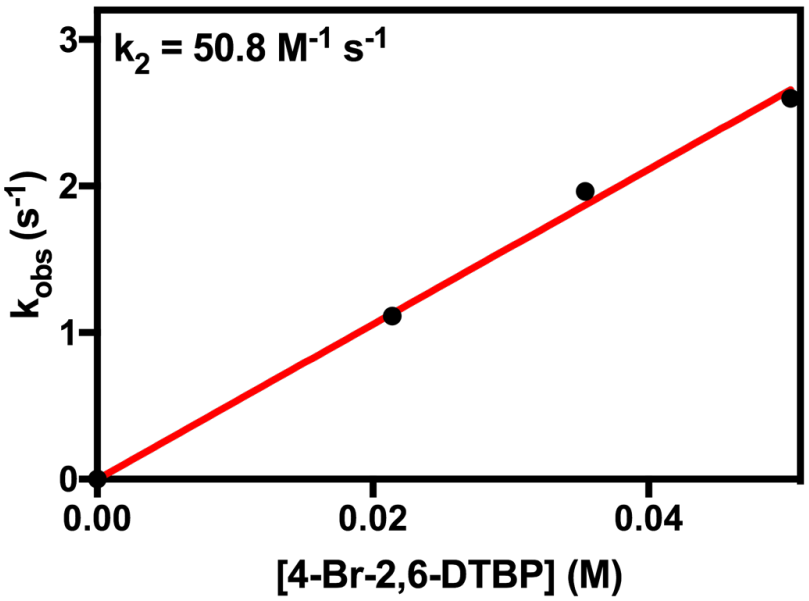

Figure 4.22. Plot of k_{obs} vs. concentration for the pseudo-first order reaction of **2** with 4-Br-2,6-di-tert-butylphenol in CH_2Cl_2 at 25 °C.

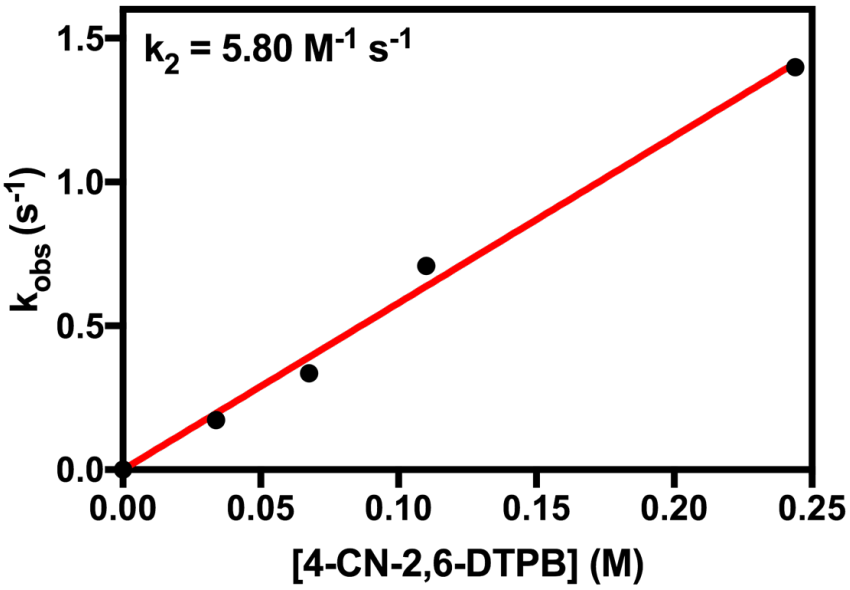

Figure 4.23. Plot of k_{obs} vs. concentration for the pseudo-first order reaction of **2** with 4-CN-2,6-di-tert-butylphenol in CH_2Cl_2 at 25 °C.

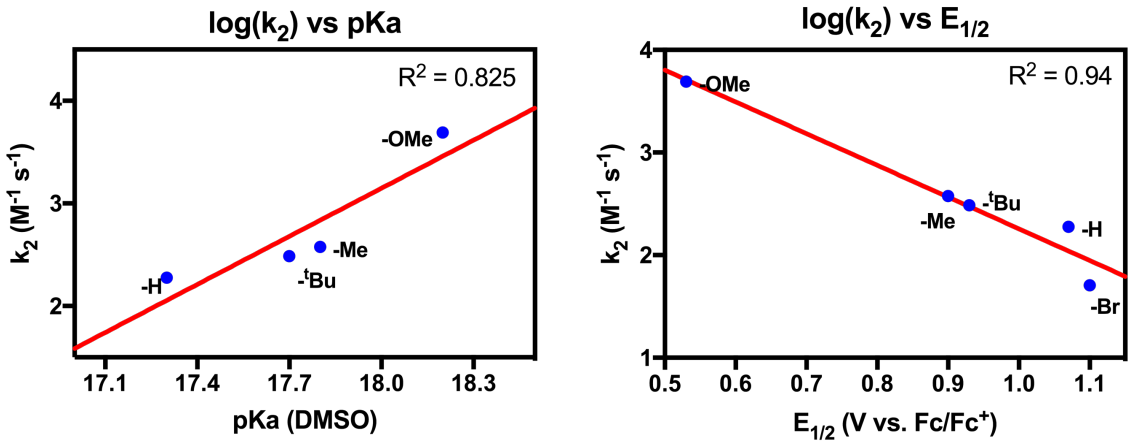

Figure 4.24. Plots of log(k_2) vs. substrate pK_a (left) and log(k_2) vs. substrate redox potential (right). The linear fits of these graphs are poorer than the linear fit of log(k_2) vs. substrate BDE shown in **Figure 4.8**.

Table 4.2. Summary of kinetic and thermodynamic parameters used for analysis of the reaction of **2** with substituted phenols

-X	$E^{\circ}_{1/2}$ (V vs Fc/Fc^{+})[45, 55]	pK_a[a] (DMSO)[56]	BDE (kcal/mol)[56-57]	k_2 (M^{-1} s^{-1} in CH_2Cl_2)
-OMe	0.53	18.2	78.3	6183
-Me	0.90	17.7	81.0	376.9
-^{t}Bu	0.93	17.8	81.2	305.5
-H	1.07	17.3	82.0	189.3
-Br	1.10	-	83.2	50.8
-CN	-	-	84.3	5.80

[a] All BDEs reported as measured in DMSO. When multiple BDE values were available, values determined using pK_a and E^0 data were chosen for the sake of consistency.

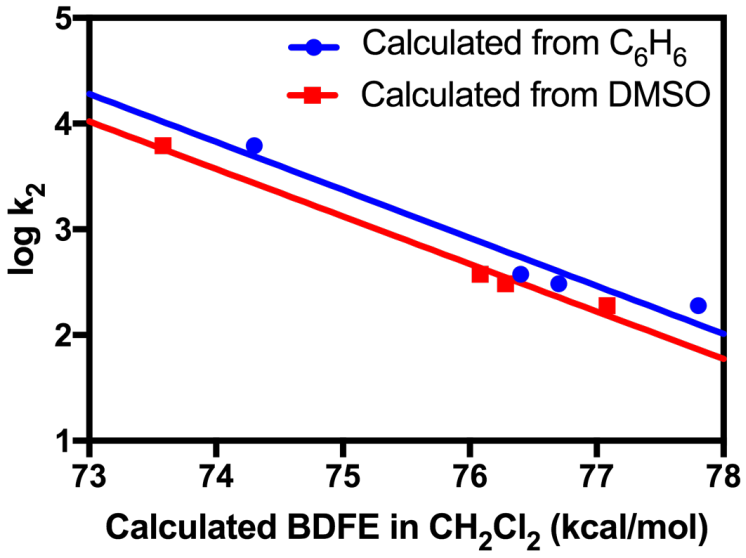

Figure 4.25. Plot of log(k_2) vs. substrate BDFE in CH_2Cl_2. BDFEs in CH_2Cl_2 were calculated from both BDFEs in DMSO and BDFEs in C_6H_6[38] and were found to be within 0.9 kcal/mol. For a more detailed discussion on calculating BDFEs in CH_2Cl_2, see **Section 4.8.4.**

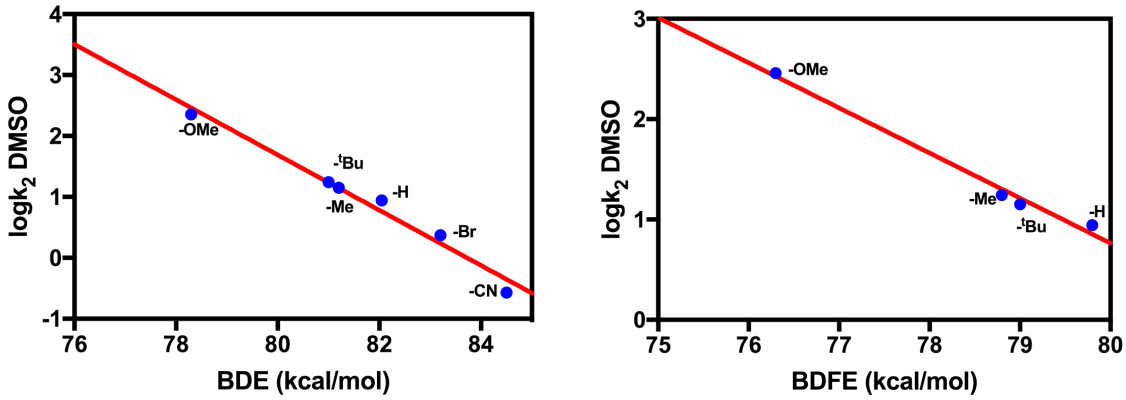

Figure 4.26. Left: Plot of $\log(k_2)_{DMSO}$ vs. substrate BDE. Right: Plot of $\log(k_2)_{DMSO}$ vs. substrate BDFE. BDFE's were calculated from the pK_a and E^0 data given in equation 2. For a more detailed discussion on calculating $k_{2,DMSO}$ see **Section 4.8.4.**

A)

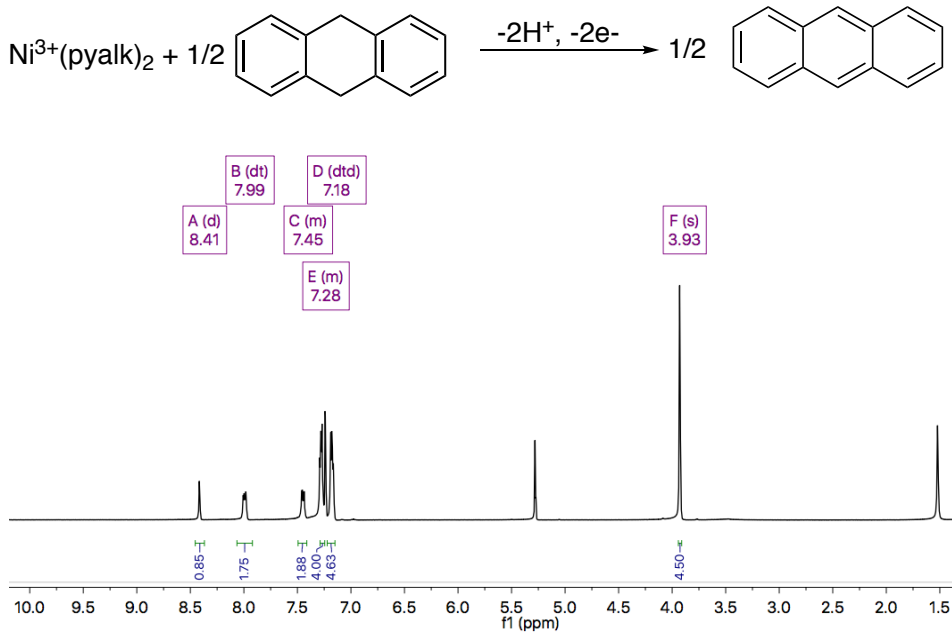

B)

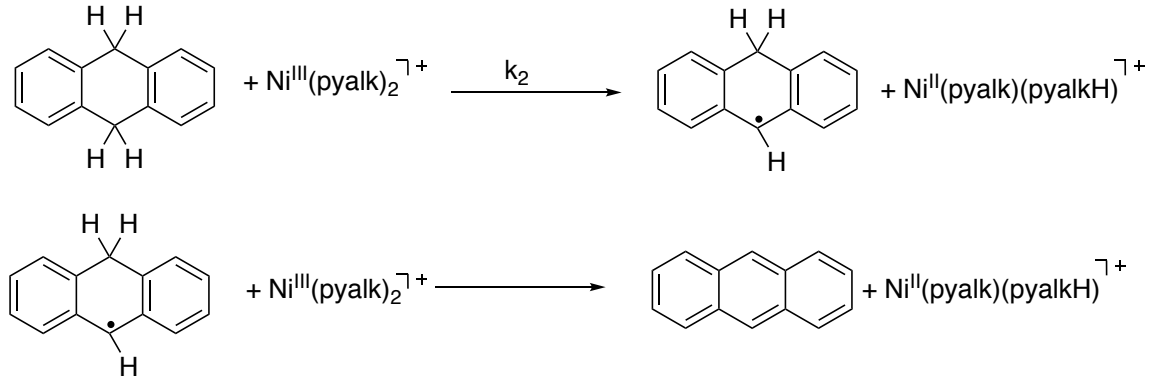

Figure 4.27. (A)^{1}H NMR spectrum of the reaction of a 1 mM solution of dihydroanthracene with a 1 mM solution of **2**. Based on integration, the yield of anthracene is ~50%. (B) Proposed mechanism for the 2 H^{+}/2 e^{-} oxidation of 9,10-dihydroanthracene to anthracene by 2 equivalents of **2**.

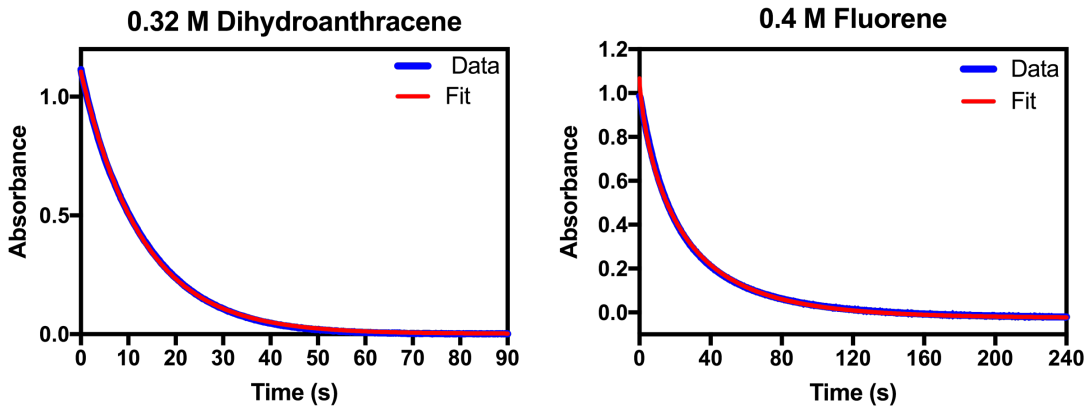

Figure 4.28. Representative fits of the absorbance at λ = 610 nm as a function of time for two hydrocarbon substrates: dihydroanthracene (left) and fluorene (right).

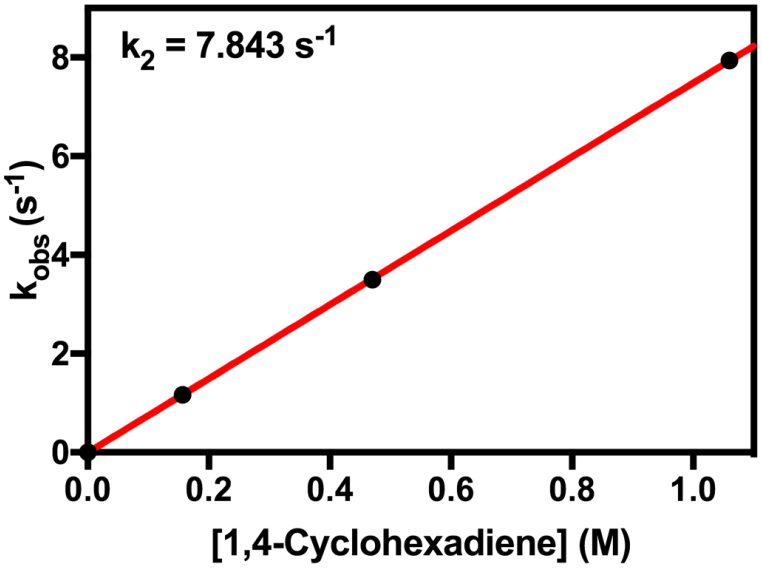

Figure 4.29. Plot of k_{obs} vs. concentration for the reaction of **2** with 1,4-cyclohexadiene in CH_2Cl_2 at 25 °C.

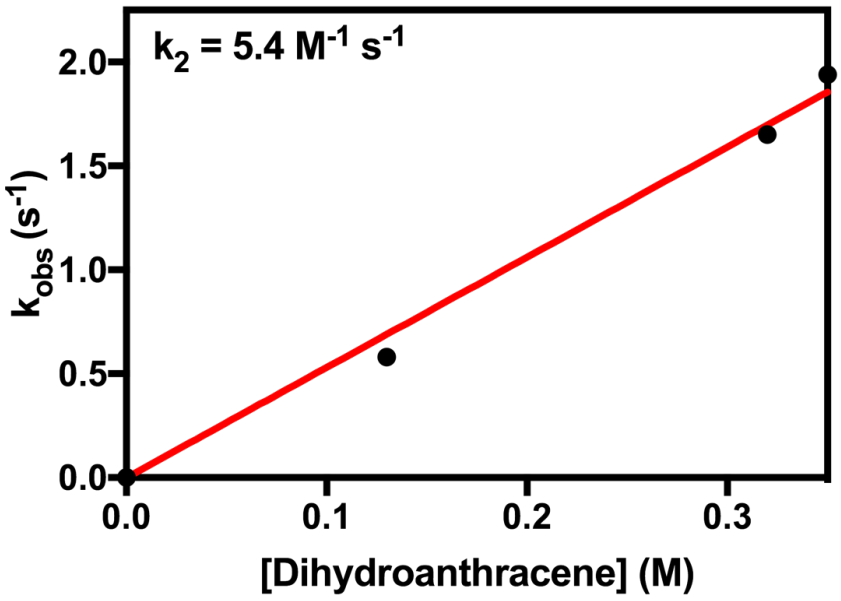

Figure 4.30. Plot of k_{obs} vs. concentration for the reaction of **2** with dihydroanthracene in CH_2Cl_2 at 25 °C.

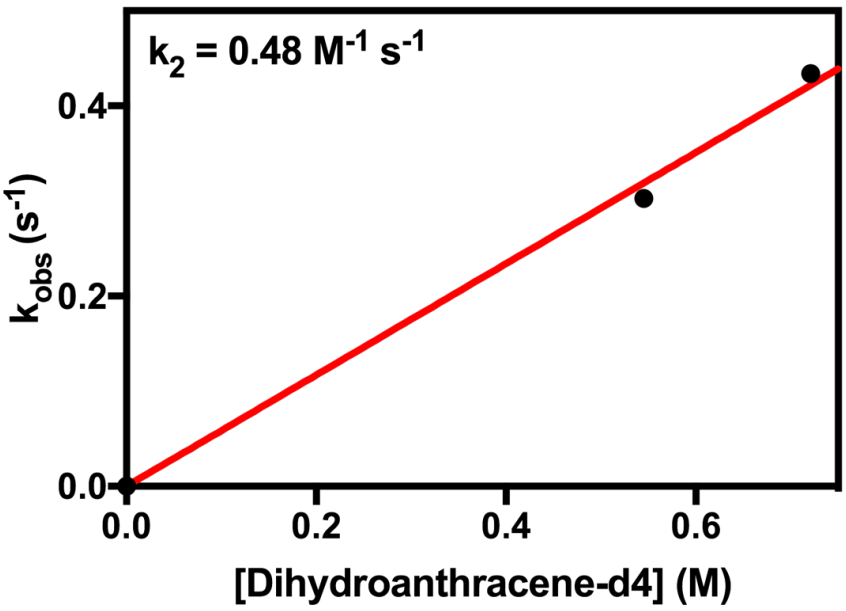

Figure 4.31. Plot of k_{obs} vs. concentration for the reaction of **2** with dihydroanthracene-d_4 in CH_2Cl_2 at 25 °C.

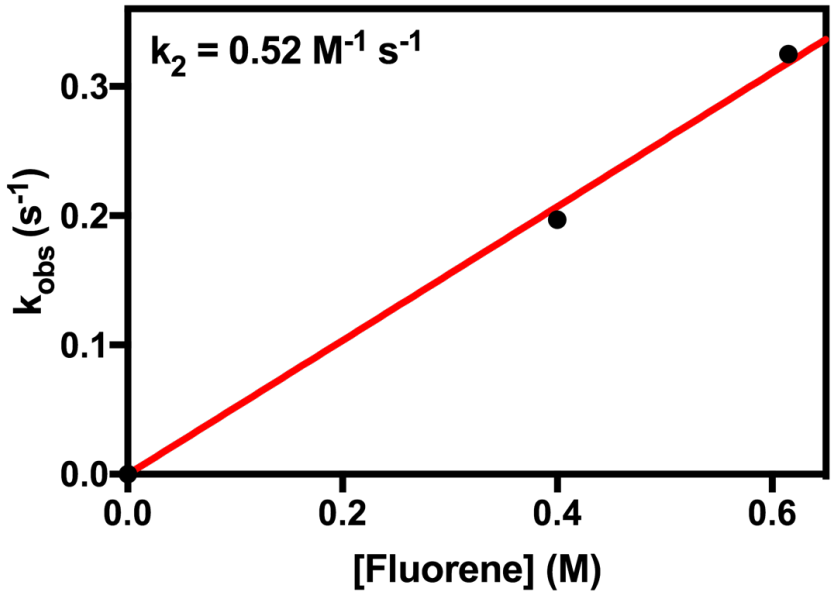

Figure 4.32. Plot of k_{obs} vs. concentration for the reaction of **2** with fluorene in CH_2Cl_2 at 25 °C.

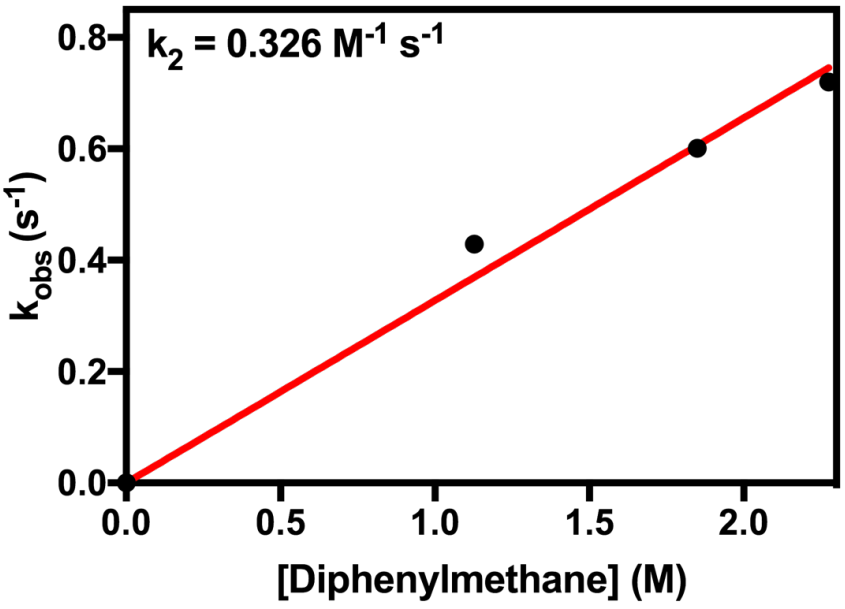

Figure 4.33. Plot of k_{obs} vs. concentration for the reaction of **2** with diphenylmethane in CH_2Cl_2 at 25 °C.

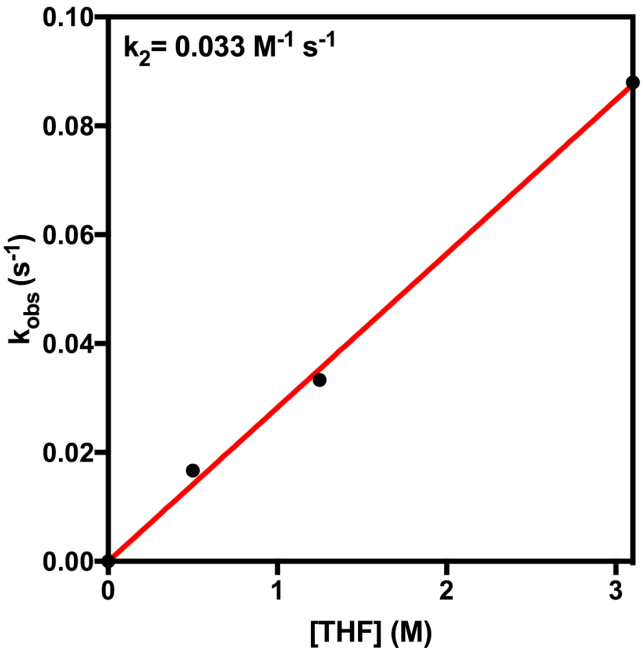

Figure 4.34. Plot of k_{obs} vs. concentration for the reaction of **2** with tetrahydrofuran (THF) in CH_2Cl_2 at 25 °C.

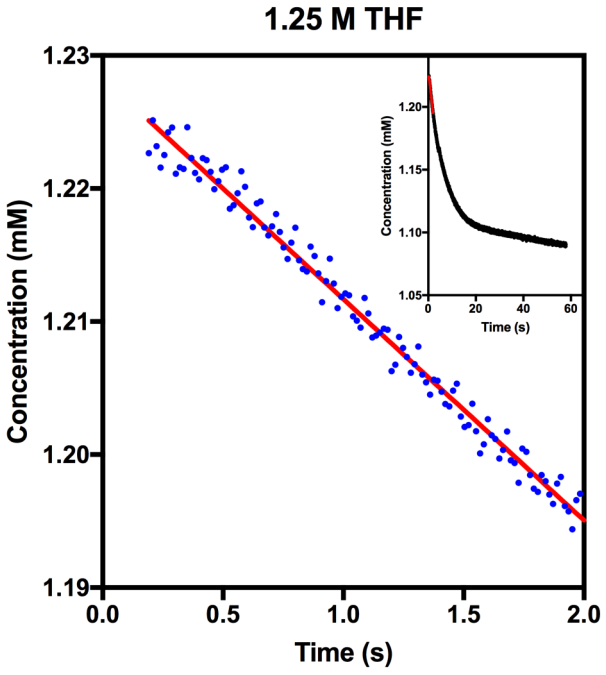

Figure 4.35. Representative fitting of pseudo-first order reaction between **2** and THF by method of initial rates.

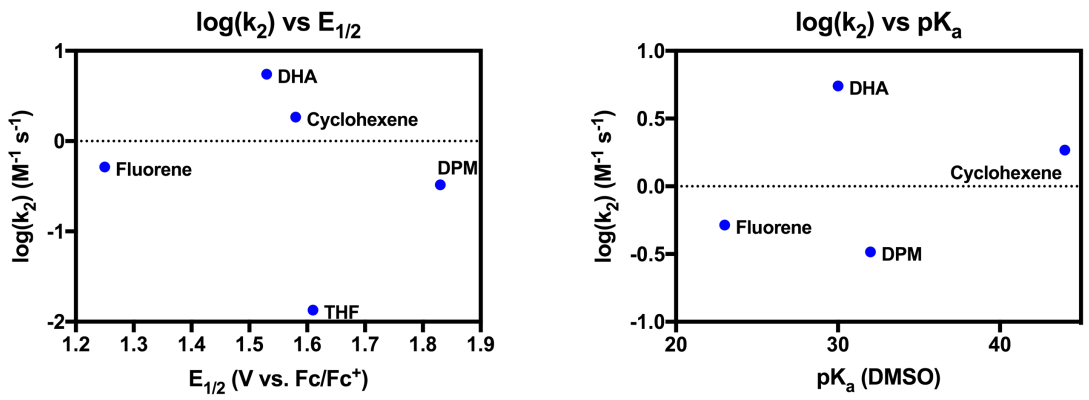

Figure 4.36. Plots of log(k_2) vs. substrate redox potential (left) and log(k_2) vs. substrate pK_a (right).The linear fits of these graphs are poorer than the linear fit of log(k_2) vs. substrate BDE shown in **Figure 4.8**. Plot of log(k_2) vs. bond dissociation enthalpy (BDE) for the reaction of **2** with hydrocarbon substrates.

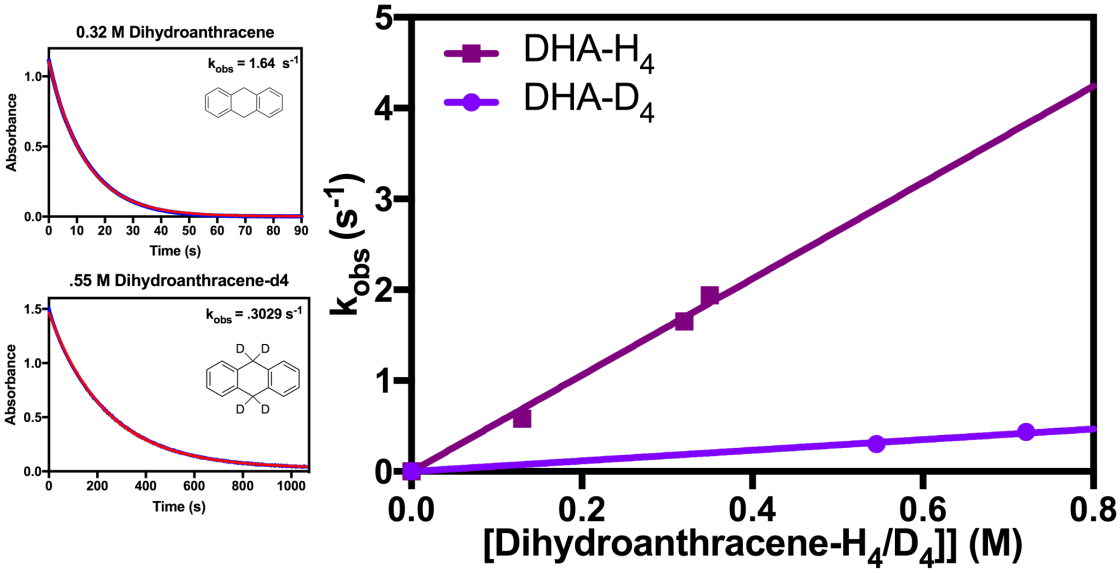

Figure 4.37. *Left*: representative time trace of the absorbance at λ = 610 nm for the reaction of **2** with dihydroanthracene (DHA) (top) and DHA-d_4 (bottom). *Right*: Plot of k_{obs} vs. concentration for the reaction of **2** with DHA and DHA-d_4.

Table 4.3. Summary of thermodynamic and kinetic parameters in our analysis of the reaction of **2** with hydrocarbon substrates.

Substrate	$E°_{1/2}$ (V vs Ag/Ag^+ in MeCN)[58]	pK_a (DMSO)[59]	BDE[a] (kcal/mol)[35, 38, 60]	k_2 (M^{-1} s^{-1} in CH_2Cl_2)
1,4-cyclohexadiene	-	-	76 ± 1	7.48
9,10-dihydroanthracene	1.53	30	78 ± 3	5.4
Cyclohexene	1.58	44	81 ± 2	1.94
Fluorene	1.25	23	82 ± 2	0.52
Diphenylmethane	1.83	32	84.3 ± 1	0.33
THF	1.61	-	92 ± 1	0.033

[a]All BDEs reported as measured in DMSO. When multiple BDE values were available, values determined using pK_a and E^0 data were chosen for the sake of consistency.

4.8.3 Characterization of **4**

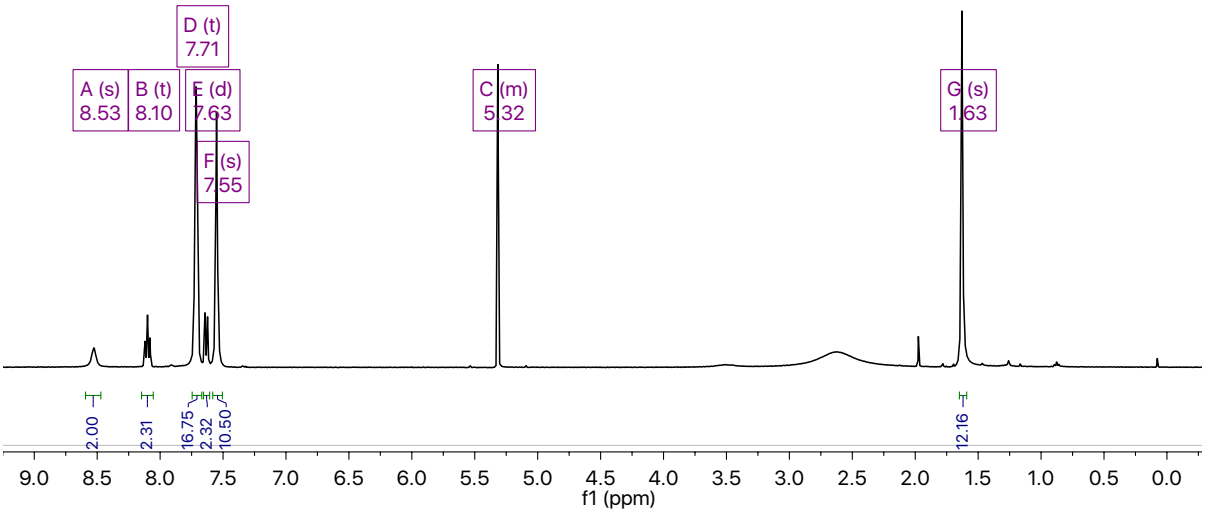

Figure 4.38. ^1H NMR spectrum of **4**, $[(Ni)(pyalkH)_2][2(BAr^F)]$ in CD_2Cl_2.

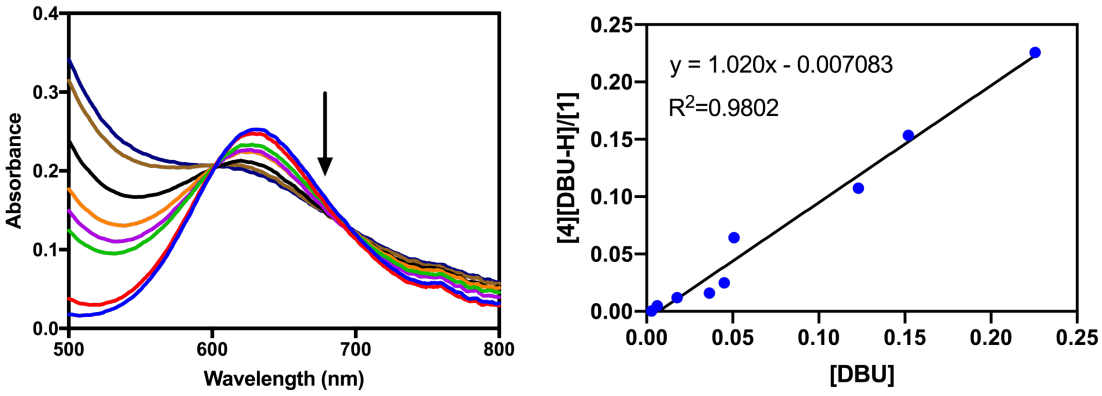

Figure 4.39. Representative UV-visible spectra of a titration of **4** with DBU (left) and linearized titration plot for the conversion of **4** to **1** (right).

Table 4.4. Comparison of bond lengths between nickel in various oxidation states and the pyalk oxygen for several compounds discussed in this report.

Compound	Oxidation state of Ni	Ni-O_{pyalk} bond length (Å)
$Ni(pyalk)_2$ (1)	2+	1.8365(15)
$[Ni(pyalk)_2(py)_2]^+$ (3)	3+	1.840(2)
$Ni(pyalkH)_2(OAc)_2$ (4)	2+	2.076(18)

4.8.4 Discussion of Bond Dissociation Enthalpies/Bond Dissociation Free Energies and Solvent Effects

The interconversion of bond dissociation free energies between solvents for a species XH can be accomplished by converting a BDFE measured in a given solvent to the gas phase and then estimating the free energy of solvation of H• and the difference solvation free energy between X• and XH.[39, 41]

$$BDFE_{solv} = BFDE_g + \Delta G^o(H\bullet) + \Delta G^o(X\bullet) - \Delta G^o(XH). \quad \textbf{(Equation 4.3)}$$

The free energy of solvation of H• is assumed to be the same as the free energy of solvation of H_2 at STP.[41] The difference in free energy of solvation between X• and XH can be estimated as the energy of the XH-solvent hydrogen bond in aprotic solvents. This value can be found using the empirical equation[40]:

$$\Delta G^0_{solv} = -10.02\alpha_2^H\beta_2^H - 1.492 \quad \textbf{(Equation 4.4)}$$

where α_2^H is a hydrogen-bonding acidity parameter unique to each substrate and β_2^H is a hydrogen-bonding basicity parameter unique to each solvent.

This calculation is made for both solvents (in our case, DMSO and CH_2Cl_2), using the parameters found in **Table 4.5**, resulting in the following equations:

$$BDFE_{CH2Cl2} = BFDE_g + \Delta G^o_{solv}(H_2)_{CH2Cl2} - (-10.02\alpha_2^H(0.05) - 1.492) \quad \textbf{(Equation 4.5)}$$

$$BDFE_{DMSO} = BFDE_g + \Delta G^o_{solv}(H_2)_{DMSO} - (-10.02\alpha_2^H(0.78) - 1.492) \quad \textbf{(Equation 4.6)}$$

These equations can then be subtracted from one other and rearranged to provide the following relationship for 4-X-2,6-DTBP, $\alpha_2^H = 0.22$ for all 4-X-2,6-DTBP substrates:[41]

$$BDFE_{CH2Cl2} = BDFE_{DMSO} - [\Delta G^o_{solv}(H_2)_{DMSO} - (-10.02\alpha_2^H(0.78) - 1.492)] + [\Delta G^o_{solv}(H_2)_{CH2Cl2} - (-10.02\alpha_2^H(0.05) - 1.492)] \quad \textbf{(Equation 4.7)}$$

To ensure that this procedure resulted in reliable BDFE's, the same process was repeated with C_6H_6 instead of DMSO as one of the solvents. The $BDFE_{CH2Cl2}$ values found using C_6H_6 BDFE values were within 0.9 kcal/mol of those found using the DMSO values. Plots of $\log(k_2)$ vs. $BDFE_{CH2Cl2}$ can be found in **Figure 4.25**.

Table 4.5. Solvent parameters used in this analysis.

Solvent	β_2^H [20]	$\Delta G^o(H_2)$ [61]
CH_2Cl_2	0.05	4.5[1]
DMSO	0.78	5.61
C_6H_6	0.14	4.80

[1]Estimated to be the same as $\Delta G^o_{solv}(H_2)$ in 1,2-dichloroethane as the value in CH_2Cl_2 has not been reported.

The interconversion of k_2 values between different solvents can be found in a similar fashion. The empirical equation relating reaction rates across different solvents can be found in the following equation, where k^{solv} is the rate constant in a hydrogen-bonding solvent and k^0 is the rate constant in a non-hydrogen bonding alkane solvent:[41]

$$\log(k^{solv}) = k^0 - 8.3\alpha_2^H\beta_2^H \quad \textbf{(Equation 4.8)}$$

As above, α_2^H is a hydrogen-bonding acidity parameter unique to each substrate and β_2^H is a hydrogen-bonding basicity parameter unique to each solvent. To convert $k_{2,CH2Cl2}$ to $k_{2,DMSO,}$ we plugged in the appropriate β_2^H parameters to the equation above to obtain:

$$\log(k^{DMSO}) = k^0 - 8.3\alpha_2^H(0.78) \quad \textbf{(Equation 4.9)}$$

$$\log(k^{CH2Cl2}) = k^0 - 8.3\alpha_2^H(0.05) \quad \textbf{(Equation 4.10)}$$

Subtracting these two equations from one another and rearranging provides the following relationship:

$$\log(k^{DMSO}) = \log(k^{CH2Cl2}) - 6.06\alpha_2^H \quad \textbf{(Equation 4.11)}$$

$\alpha_2^H = 0.22$ for all 4-X-2,6-DTBP substrates. Plots of $\log(k^{DMSO})$ vs. BDFE and $\log(k^{DMSO})$ vs. BDE can be found in **Figure 4.26**.

The analyses described above could not be performed for experiments involving the oxidation of hydrocarbons, as α_2^H values are not available for most of those substrates.

4.8.5 Crystallographic Experimental Details

Low-temperature diffraction data (ω-scans) were collected on a Rigaku R-AXIS RAPID diffractometer coupled to an R-AXIS RAPID imaging plate detector with Mo Kα radiation (λ = 0.71073 Å) for the structure of **1**; similar data were collected on a Rigaku MicroMax-007HF diffractometer coupled to a Saturn994+ CCD detector with Cu Kα (λ = 1.54178 Å) for the structures of **3** and **4**. The diffraction images of **1** were processed and scaled using the Rigaku CrystalClear software (CrystalClear and CrystalStructure; Rigaku/MSC: The Woodlands, TX, 2005). The diffraction images of **3** and **4** were processed and scaled using Rigaku Oxford Diffraction software (CrysAlisPro; Rigaku OD: The Woodlands, TX, 2015). All structures were solved with SHELXT and were refined against F^2 on all data by full-matrix least squares with SHELXL (Sheldrick, G. M. Acta Cryst. 2008, A64, 112–122). All non-hydrogen atoms were refined anisotropically. Unless stated otherwise, hydrogen atoms were included in the model at geometrically calculated positions and refined using a riding model. The isotropic displacement parameters of all hydrogen atoms were fixed to 1.2 times the U value of the atoms to which they are linked (1.5 times for methyl groups).

CCDC numbers 1954011 (**1**), 1954012 (**3**), and 1954013 (**5**) contains the supplementary crystallographic data for this paper. These data can be obtained free of charge from The Cambridge Crystallographic Data Center via www.ccdc.cam.ac.uk/data_request/cif.

Crystallographic Information for **1**

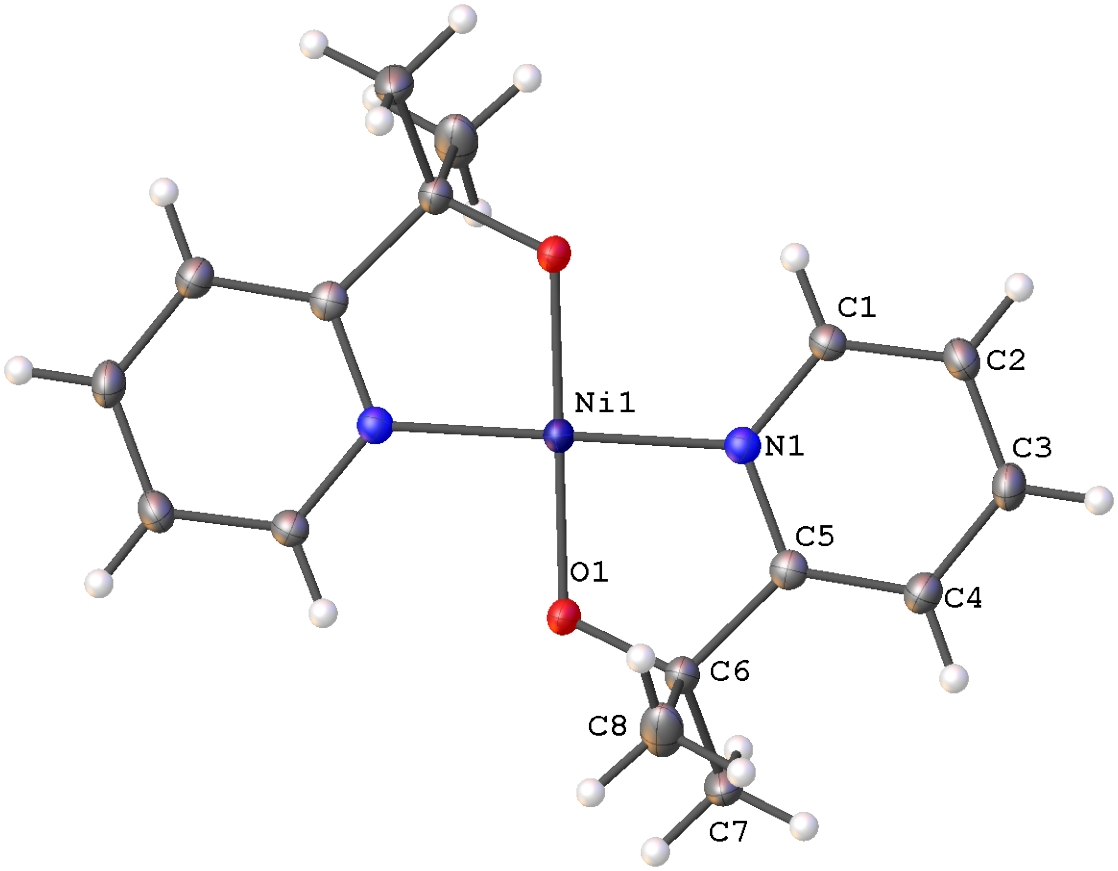

Figure 4.40. Thermal ellipsoid diagram for **1** with complete numbering scheme. Thermal ellipsoids are displayed at the probability level. The hydrogen atoms are shown as circles for clarity. The model is on a special position; only the asymmetric unit is labeled.

Table 4.6. Crystal data and structure refinement for **1**.

Identification code	007a-17123	
Empirical formula	C16 H20 N2 Ni O2	
Formula weight	331.05	
Temperature	93(2) K	
Wavelength	1.54184 Å	
Crystal system	Monoclinic	
Space group	$P2_1/n$	
Unit cell dimensions	a = 14.557(3) Å	α = 90°.
	b = 10.2366(5) Å	β = 141.27(4)°.
	c = 8.2137(14) Å	γ = 90°.
Volume	765.8(4) $Å^3$	
Z	2	
Density (calculated)	1.436 Mg/m^3	
Absorption coefficient	1.871 mm^{-1}	
F(000)	348	
Crystal size	0.200 x 0.200 x 0.200 mm^3	
Crystal color and habit	Green Plate	
Diffractometer	Rigaku Saturn 944+ CCD	
Theta range for data collection	5.698 to 66.757°.	
Index ranges	-17<=h<=17, -12<=k<=12, -9<=l<=9	
Reflections collected	21932	
Independent reflections	1361 [R(int) = 0.0690]	
Observed reflections (I > 2sigma(I))	1234	
Completeness to theta = 66.757°	99.9 %	
Absorption correction	Semi-empirical from equivalents	
Max. and min. transmission	1.00000 and 0.75022	
Solution method	SHELXT-2014/5 (Sheldrick, 2014)	
Refinement method	SHELXL-2014/7 (Sheldrick, 2014)	
Data / restraints / parameters	1361 / 0 / 99	
Goodness-of-fit on F^2	1.048	
Final R indices [I>2sigma(I)]	R1 = 0.0281, wR2 = 0.0708	
R indices (all data)	R1 = 0.0318, wR2 = 0.0733	
Largest diff. peak and hole	0.284 and -0.224 $e.Å^{-3}$	

Crystallographic Information for **3**

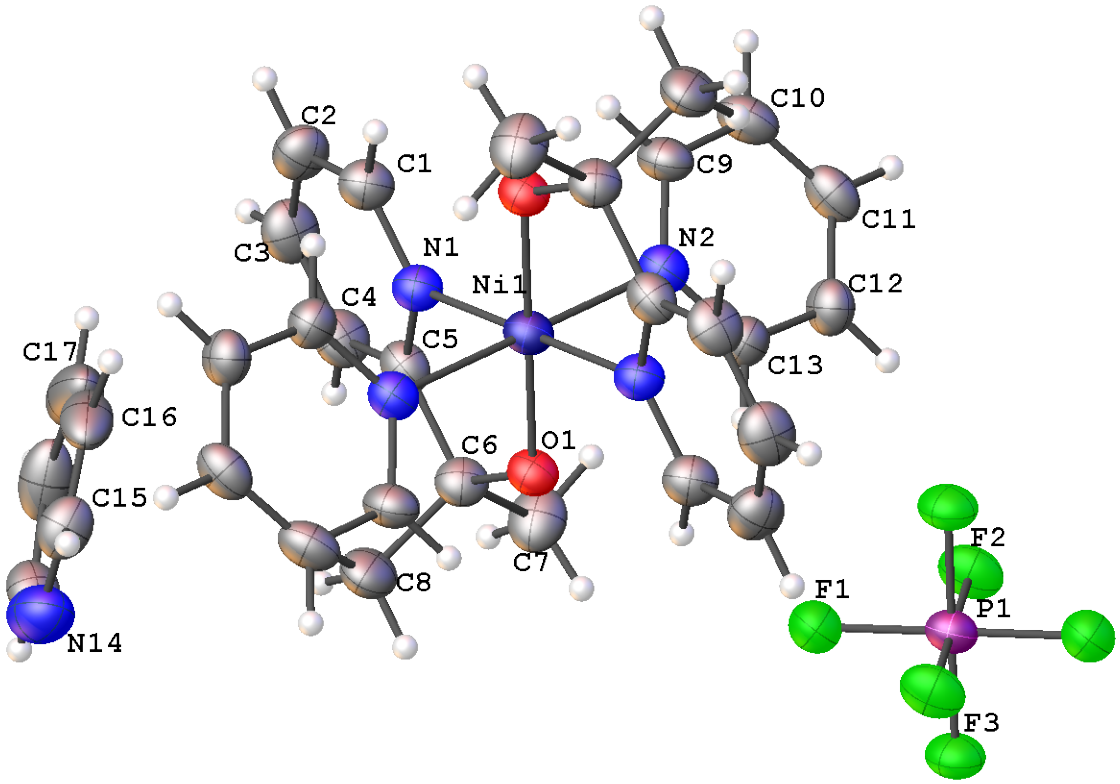

Figure 4.41. Thermal ellipsoid diagram for **3** with complete numbering scheme. Thermal ellipsoids are displayed at the 50% probability level. The hydrogen atoms are shown as circles for clarity. The model is on a crystallographic special position; only the asymmetric unit is labeled.

Table 4.7. Crystal data and structure refinement for **3**.

Identification code	007a-18050	
Empirical formula	C31 H35 F6 N5 Ni O2 P	
Formula weight	713.32	
Temperature	93(2) K	
Wavelength	1.54184 Å	
Crystal system	Monoclinic	
Space group	I2/a	
Unit cell dimensions	a = 22.4997(12) Å	α = 90°.
	b = 8.4913(3) Å	β = 111.646(5)°.
	c = 17.7726(7) Å	γ = 90°.
Volume	3156.0(3) $Å^3$	
Z	4	
Density (calculated)	1.501 Mg/m^3	
Absorption coefficient	2.017 mm^{-1}	
F(000)	1476	
Crystal size	0.100 x 0.100 x 0.050 mm^3	
Crystal color and habit	Yellow Plate	
Diffractometer	Rigaku Saturn 944+ CCD	
Theta range for data collection	4.228 to 66.893°.	
Index ranges	-26<=h<=26, -9<=k<=9, -21<=l<=21	
Reflections collected	54705	
Independent reflections	2801 [R(int) = 0.0908]	
Observed reflections (I > 2sigma(I))	2231	
Completeness to theta = 66.893°	99.4 %	
Absorption correction	Semi-empirical from equivalents	
Max. and min. transmission	1.00000 and 0.71733	
Solution method	SHELXT-2014/5 (Sheldrick, 2014)	
Refinement method	SHELXL-2014/7 (Sheldrick, 2014)	
Data / restraints / parameters	2801 / 0 / 214	
Goodness-of-fit on F^2	1.071	
Final R indices [I>2sigma(I)]	R1 = 0.0526, wR2 = 0.1320	
R indices (all data)	R1 = 0.0692, wR2 = 0.1434	
Largest diff. peak and hole	0.487 and -0.512 $e.Å^{-3}$	

Crystallographic information for **5**:

The proton on O1 was found in the difference map and freely refined.

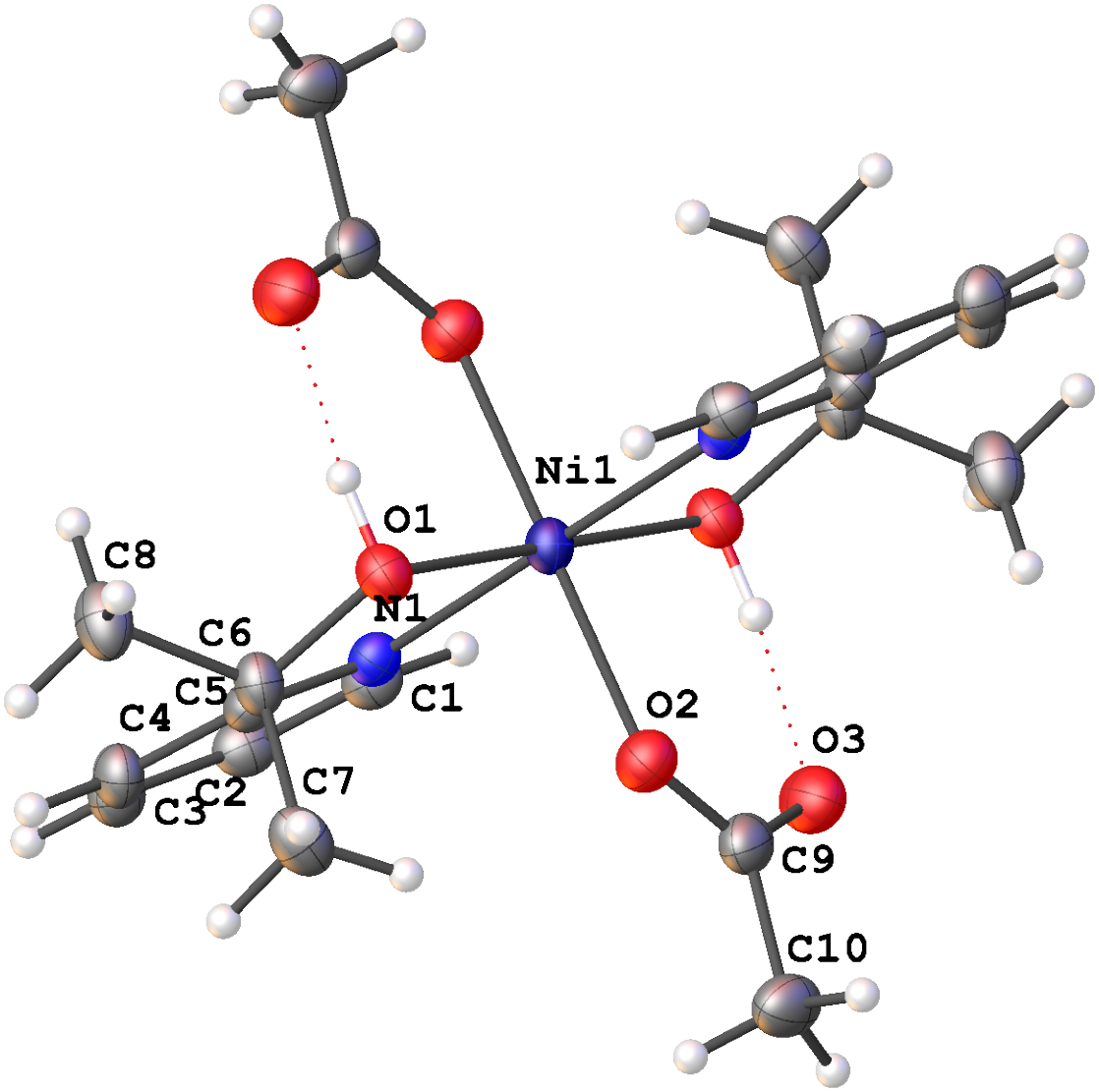

Figure 4.42. Thermal ellipsoid diagram for **5** with complete numbering scheme. Thermal ellipsoids are displayed at the 50% probability level. The hydrogen atoms are shown as circles for clarity. The model is on a crystallographic special position; only the asymmetric unit is labeled.

Table 4.8. Crystal data and structure refinement for **5**.

Identification code	spider-16039	
Empirical formula	C20 H28 N2 Ni O6	
Formula weight	451.15	
Temperature	93(2) K	
Wavelength	0.71075 Å	
Crystal system	Monoclinic	
Space group	$P2_1/n$	
Unit cell dimensions	a = 8.3939(4) Å	α = 90°.
	b = 14.9329(8) Å	β = 108.791(8)°.
	c = 8.7611(6) Å	γ = 90°.
Volume	1039.63(11) $Å^3$	
Z	2	
Density (calculated)	1.441 Mg/m^3	
Absorption coefficient	0.972 mm^{-1}	
F(000)	476	
Crystal size	0.200 x 0.200 x 0.050 mm^3	
Crystal color and habit	green plate	
Diffractometer		
Theta range for data collection	3.226 to 25.008°.	
Index ranges	-9<=h<=9, -17<=k<=17, -10<=l<=10	
Reflections collected	20757	
Independent reflections	1829 [R(int) = 0.0888]	
Observed reflections (I > 2sigma(I))	1536	
Completeness to theta = 25.008°	99.8 %	
Absorption correction	Semi-empirical from equivalents	
Max. and min. transmission	1.000 and 0.778	
Solution method	?	
Refinement method	SHELXL-2014/7 (Sheldrick, 2014)	
Data / restraints / parameters	1829 / 0 / 140	
Goodness-of-fit on F^2	1.046	
Final R indices [I>2sigma(I)]	R1 = 0.0418, wR2 = 0.0800	
R indices (all data)	R1 = 0.0538, wR2 = 0.0846	
Largest diff. peak and hole	0.303 and -0.335 $e.Å^{-3}$	

4.9 References

1. Meunier, B.; de Visser, S. P.; Shaik, S., Mechanism of Oxidation Reactions Catalyzed by Cytochrome P450 Enzymes. *Chem. Rev.* **2004,** *104* (9), 3947-3980.
2. Ortiz de Montellano, P. R.; De Voss, J. J., Oxidizing Species in the Mechanism of Cytochrome P450. *Nat. Prod. Rep.* **2002,** *19* (4), 477-493.
3. Weinberg, D. R.; Gagliardi, C. J.; Hull, J. F.; Murphy, C. F.; Kent, C. A.; Westlake, B. C.; Paul, A.; Ess, D. H.; McCafferty, D. G.; Meyer, T. J., Proton-Coupled Electron Transfer. *Chem. Rev.* **2012,** *112* (7), 4016-4093.
4. Zhang, Y.; Zhang, H.; Ji, H.; Ma, W.; Chen, C.; Zhao, J., Pivotal Role and Regulation of Proton Transfer in Water Oxidation on Hematite Photoanodes. *J. Am. Chem. Soc.* **2016,** *138* (8), 2705-2711.
5. Miller, D. C.; Tarantino, K. T.; Knowles, R. R., Proton-Coupled Electron Transfer in Organic Synthesis: Fundamentals, Applications, and Opportunities. *Top. Curr. Chem.* **2016,** *374* (3), 30.
6. Crossley, S. W. M.; Obradors, C.; Martinez, R. M.; Shenvi, R. A., Mn-, Fe-, and Co-Catalyzed Radical Hydrofunctionalizations of Olefins. *Chem. Rev.* **2016,** *116* (15), 8912-9000.
7. Barondeau, D. P.; Kassmann, C. J.; Bruns, C. K.; Tainer, J. A.; Getzoff, E. D., Nickel Superoxide Dismutase Structure and Mechanism. *Biochemistry* **2004,** *43* (25), 8038-8047.
8. Shearer, J., Use of a Metallopeptide-Based Mimic Provides Evidence for a Proton-Coupled Electron-Transfer Mechanism for Superoxide Reduction by Nickel-Containing Superoxide Dismutase. *Angew. Chem. Int. Ed.* **2013,** *52* (9), 2569-2572.
9. Shearer, J., Insight into the Structure and Mechanism of Nickel-Containing Superoxide Dismutase Derived from Peptide-Based Mimics. *Acc. Chem. Res.* **2014,** *47* (8), 2332-2341.
10. Michaelos, T. K.; Shopov, D. Y.; Sinha, S. B.; Sharninghausen, L. S.; Fisher, K. J.; Lant, H. M. C.; Crabtree, R. H.; Brudvig, G. W., A Pyridine Alkoxide Chelate Ligand That Promotes Both Unusually High Oxidation States and Water-Oxidation Catalysis. *Acc. Chem. Res.* **2017,** *50* (4), 952-959.
11. Rudshteyn, B.; Fisher, K. J.; Lant, H. M. C.; Yang, K. R.; Mercado, B. Q.; Brudvig, G. W.; Crabtree, R. H.; Batista, V. S., Water-Nucleophilic Attack Mechanism for the $Cu^{II}(pyalk)_2$ Water-Oxidation Catalyst. *ACS Catal.* **2018,** *8* (9), 7952-7960.
12. Chen, F.; Wang, N.; Lei, H.; Guo, D.; Liu, H.; Zhang, Z.; Zhang, W.; Lai, W.; Cao, R., Electrocatalytic Water Oxidation by a Water-Soluble Copper(II) Complex with a Copper-Bound Carbonate Group Acting as a Potential Proton Shuttle. *Inorg. Chem.* **2017,** *56* (21), 13368-13375.
13. Pirovano, P.; Farquhar, E. R.; Swart, M.; Fitzpatrick, A. J.; Morgan, G. G.; McDonald, A. R., Characterization and Reactivity of a Terminal Nickel(III)–Oxygen Adduct. *Chem. Eur. J.* **2015,** *21* (9), 3785-3790.
14. Evans, D. F.; Jakubovic, D. A., Water-Soluble Hexadentate Schiff-Base Ligands as Sequestrating Agents for Iron(III) and Gallium(III). *J. Chem. Soc., Dalton Trans.* **1988,** (12), 2927-2933.
15. Lancaster, J. R., *The Bioinorganic Chemistry of Nickel*. VCH Publishers: 1988.
16. Shopov, D. Y.; Sharninghausen, L. S.; Sinha, S. B.; Mercado, B. Q.; Balcells, D.; Brudvig, G. W.; Crabtree, R. H., A Dinuclear Iridium(V,V) Oxo-Bridged Complex Characterized Using a Bulk Electrolysis Technique for Crystallizing Highly Oxidizing Compounds. *Inorg. Chem.* **2018,** *57* (9), 5684-5691.
17. Sharninghausen, L. S.; Sinha, S. B.; Shopov, D. Y.; Choi, B.; Mercado, B. Q.; Roy, X.; Balcells, D.; Brudvig, G. W.; Crabtree, R. H., High Oxidation State Iridium Mono-μ-Oxo Dimers Related to Water Oxidation Catalysis. *J. Am. Chem. Soc.* **2016,** *138* (49), 15917-15926.
18. Sinha, S. B.; Shopov, D. Y.; Sharninghausen, L. S.; Stein, C. J.; Mercado, B. Q.; Balcells, D.; Pedersen, T. B.; Reiher, M.; Brudvig, G. W.; Crabtree, R. H., Redox Activity of Oxo-Bridged Iridium Dimers in an N,O-Donor Environment: Characterization of Remarkably Stable Ir(IV,V) Complexes. *J. Am. Chem. Soc.* **2017,** *139* (28), 9672-9683.
19. Sharninghausen, L. S.; Sinha, S. B.; Shopov, D. Y.; Mercado, B. Q.; Balcells, D.; Brudvig, G. W.; Crabtree, R. H., Synthesis and Characterization of Iridium(V) Coordination Complexes with an N,O-Donor Organic Ligand. *Angew. Chem.* **2017,** *129* (42), 13227-13231.

20. De Castro, B.; Freire, C., EPR and Electrochemical Study of Nickel(III) Complexes of Bis(3,5-Dichlorosalicylaldehyde) o-Phenylenediimine. Evidence for Adduct Formation with Pyridines. *Inorg. Chem.* **1990,** *29* (25), 5113-5119.
21. Pirovano, P.; Farquhar, E. R.; Swart, M.; McDonald, A. R., Tuning the Reactivity of Terminal Nickel(III)–Oxygen Adducts for C–H Bond Activation. *J. Am. Chem. Soc.* **2016,** *138* (43), 14362-14370.
22. Mondal, P.; Pirovano, P.; Das, A.; Farquhar, E. R.; McDonald, A. R., Hydrogen Atom Transfer by a High-Valent Nickel-Chloride Complex. *J. Am. Chem. Soc.* **2018,** *140* (5), 1834-1841.
23. Fisher, K. J.; Materna, K. L.; Mercado, B. Q.; Crabtree, R. H.; Brudvig, G. W., Electrocatalytic Water Oxidation by a Copper(II) Complex of an Oxidation-Resistant Ligand. *ACS Catal.* **2017,** *7* (5), 3384-3387.
24. Manner, V. W.; Markle, T. F.; Freudenthal, J. H.; Roth, J. P.; Mayer, J. M., The First Crystal Structure of a Monomeric Phenoxyl Radical: 2,4,6-Tri-Tert-Butylphenoxyl Radical. *Chem. Commun.* **2008,** (2), 256-258.
25. Parsell, T. H.; Yang, M.-Y.; Borovik, A. S., C−H Bond Cleavage with Reductants: Re-Investigating the Reactivity of Monomeric $Mn^{III/IV}$−Oxo Complexes and the Role of Oxo Ligand Basicity. *J. Am. Chem. Soc.* **2009,** *131* (8), 2762-2763.
26. Gupta, R.; Borovik, A. S., Monomeric $Mn^{III/II}$ and $Fe^{III/II}$ Complexes with Terminal Hydroxo and Oxo Ligands: Probing Reactivity Via O−H Bond Dissociation Energies. *J. Am. Chem. Soc.* **2003,** *125* (43), 13234-13242.
27. Chiavarino, B.; Cipollini, R.; Crestoni, M. E.; Fornarini, S.; Lanucara, F.; Lapi, A., Probing the Compound I-Like Reactivity of a Bare High-Valent Oxo Iron Porphyrin Complex: The Oxidation of Tertiary Amines. *J. Am. Chem. Soc.* **2008,** *130* (10), 3208-3217.
28. Yoshida, T.; Hirozumi, K.; Harada, M.; Hitaoka, S.; Chuman, H., Density Functional Theory Study of Hydrogen Atom Abstraction from a Series of Para-Substituted Phenols: Why Is the Hammett Σp+ Constant Able to Represent Radical Reaction Rates? *J. Org. Chem.* **2011,** *76* (11), 4564-4570.
29. Pratt, D. A.; DiLabio, G. A.; Mulder, P.; Ingold, K. U., Bond Strengths of Toluenes, Anilines, and Phenols: To Hammett or Not. *Acc. Chem. Res.* **2004,** *37* (5), 334-340.
30. Dhar, D.; Yee, G. M.; Markle, T. F.; Mayer, J. M.; Tolman, W. B., Reactivity of the Copper(III)-Hydroxide Unit with Phenols. *Chem. Sci.* **2017,** *8* (2), 1075-1085.
31. Lansky, D. E.; Goldberg, D. P., Hydrogen Atom Abstraction by a High-Valent Manganese(V)−Oxo Corrolazine. *Inorg. Chem.* **2006,** *45* (13), 5119-5125.
32. Mulder, P.; Saastad, O. W.; Griller, D., Oxygen-Hydrogen Bond Dissociation Energies in Para-Substituted Phenols. *J. Am. Chem. Soc.* **1988,** *110* (12), 4090-4092.
33. While the thermodynamics of this reaction are perhaps more accurately captured by the use of bond dissociation free energies (BDFEs), we chose to use BDEs in this analysis because of limited BDFE data for these compounds. A plot of log(k2) vs. BDFE is provided in the supplementary information for substrates with reported BDFEs.
34. Dhar, D.; Tolman, W. B., Hydrogen Atom Abstraction from Hydrocarbons by a Copper(III)-Hydroxide Complex. *J. Am. Chem. Soc.* **2015,** *137* (3), 1322-1329.
35. Bryant, J. R.; Mayer, J. M., Oxidation of C−H Bonds by $[(bpy)_2(py)Ru^{IV}O]^{2+}$ Occurs by Hydrogen Atom Abstraction. *J. Am. Chem. Soc.* **2003,** *125* (34), 10351-10361.
36. Darcy, J. W.; Koronkiewicz, B.; Parada, G. A.; Mayer, J. M., A Continuum of Proton-Coupled Electron Transfer Reactivity. *Acc. Chem. Res.* **2018,** *51* (10), 2391-2399.
37. Kütt, A.; Selberg, S.; Kaljurand, I.; Tshepelevitsh, S.; Heering, A.; Darnell, A.; Kaupmees, K.; Piirsalu, M.; Leito, I., pKa Values in Organic Chemistry – Making Maximum Use of the Available Data. *Tetrahedron Lett.* **2018,** *59* (42), 3738-3748.
38. Warren, J. J.; Tronic, T. A.; Mayer, J. M., Thermochemistry of Proton-Coupled Electron Transfer Reagents and Its Implications. *Chem. Rev.* **2010,** *110* (12), 6961-7001.
39. Porter, T. R.; Mayer, J. M., Radical Reactivity of the Fe(III)/(II) Tetramesitylporphyrin Couple: Hydrogen Atom Transfer, Oxyl Radical Dissociation, and Catalytic Disproportionation of a Hydroxylamine. *Chem. Sci.* **2014,** *5* (1), 372-380.
40. Abraham, M. H.; Grellier, P. L.; Prior, D. V.; Taft, R. W.; Morris, J. J.; Taylor, P. J.; Laurence, C.; Berthelot, M.; Doherty, R. M.; et al., A General Treatment of Hydrogen Bond Complexation Constants in Tetrachloromethane. *J. Am. Chem. Soc.* **1988,** *110* (25), 8534-8536.

41. Warren, J. J.; Mayer, J. M., Predicting Organic Hydrogen Atom Transfer Rate Constants Using the Marcus Cross Relation. *Proc. Natl. Acad. Sci. U. S. A.* **2010,** *107* (12), 5282.
42. Gao, Y.; DeYonker, N. J.; Garrett, E. C.; Wilson, A. K.; Cundari, T. R.; Marshall, P., Enthalpy of Formation of the Cyclohexadienyl Radical and the C−H Bond Enthalpy of 1,4-Cyclohexadiene: An Experimental and Computational Re-Evaluation. *J. Phys. Chem. A* **2009,** *113* (25), 6955-6963.
43. Johansson, A. J.; Blomberg, M. R. A.; Siegbahn, P. E. M., Quantum Chemical Modeling of the Oxidation of Dihydroanthracene by the Biomimetic Nonheme Iron Catalyst $[(TMC)Fe^{IV}(O)]^{2+}$. *J. Phys. Chem. C* **2007,** *111* (33), 12397-12406.
44. Finn, M.; Friedline, R.; Suleman, N. K.; Wohl, C. J.; Tanko, J. M., Chemistry of the T-Butoxyl Radical: Evidence That Most Hydrogen Abstractions from Carbon Are Entropy-Controlled. *J. Am. Chem. Soc.* **2004,** *126* (24), 7578-7584.
45. Kundu, S.; Miceli, E.; Farquhar, E. R.; Ray, K., Mechanism of Phenol Oxidation by Heterodinuclear Ni Cu Bis(μ-Oxo) Complexes Involving Nucleophilic Oxo Groups. *Dalton Trans.* **2014,** *43* (11), 4264-4267.
46. Goldsmith, C. R.; Jonas, R. T.; Stack, T. D. P., C−H Bond Activation by a Ferric Methoxide Complex: Modeling the Rate-Determining Step in the Mechanism of Lipoxygenase. *J. Am. Chem. Soc.* **2002,** *124* (1), 83-96.
47. Moyer, B. A.; Meyer, T. J., Properties of the Oxo/Aqua System $(bpy)_2(py)RuO^{2+}/(bpy)_2(py)Ru(OH_2)^{2+}$. *Inorg. Chem.* **1981,** *20* (2), 436-444.
48. Lebeau, E. L.; Binstead, R. A.; Meyer, T. J., Mechanistic Implications of Proton Transfer Coupled to Electron Transfer. *J. Am. Chem. Soc.* **2001,** *123* (43), 10535-10544.
49. Das, D.; Pattanayak, S.; Singh, K. K.; Garai, B.; Sen Gupta, S., Electrocatalytic Water Oxidation by a Molecular Cobalt Complex through a High Valent Cobalt Oxo Intermediate. *Chem. Commun.* **2016,** *52* (79), 11787-11790.
50. Zhang, M.; Zhang, M.-T.; Hou, C.; Ke, Z.-F.; Lu, T.-B., Homogeneous Electrocatalytic Water Oxidation at Neutral pH by a Robust Macrocyclic Nickel(II) Complex. *Angew. Chem. Int. Ed.* **2014,** *53* (48), 13042-13048.
51. Wong, Y.-L.; Yang, Q.; Zhou, Z.-Y.; Kay Lee, H.; Mak, T. C. W.; Ng, D. K. P., Synthesis, Structure and Oxo-Transfer Properties of Dioxotungsten(VI) Complexes with Pyridine-Based No- and NS-Bidentate Ligands. *New J. Chem.* **2001,** *25* (2), 353-357.
52. Kurahashi, T.; Kikuchi, A.; Shiro, Y.; Hada, M.; Fujii, H., Unique Properties and Reactivity of High-Valent Manganese−Oxo Versus Manganese−Hydroxo in the Salen Platform. *Inorg. Chem.* **2010,** *49* (14), 6664-6672.
53. Stoll, S.; Schweiger, A., Easyspin, a Comprehensive Software Package for Spectral Simulation and Analysis in EPR. *J. Magn. Reson.* **2006,** *178* (1), 42-55.
54. Saouma, C. T.; Kaminsky, W.; Mayer, J. M., Protonation and Concerted Proton–Electron Transfer Reactivity of a Bis-Benzimidazolate Ligated [2Fe–2S] Model for Rieske Clusters. *J. Am. Chem. Soc.* **2012,** *134* (17), 7293-7296.
55. Lee, J. Y.; Peterson, R. L.; Ohkubo, K.; Garcia-Bosch, I.; Himes, R. A.; Woertink, J.; Moore, C. D.; Solomon, E. I.; Fukuzumi, S.; Karlin, K. D., Mechanistic Insights into the Oxidation of Substituted Phenols Via Hydrogen Atom Abstraction by a Cupric–Superoxo Complex. *J. Am. Chem. Soc.* **2014,** *136* (28), 9925-9937.
56. Bordwell, F. G.; Zhang, X.-M., Acidities and Homolytic Bond Dissociation Enthalpies of 4-Substituted-2,6-Di-Tert-Butylphenols. *J. Phys. Org. Chem.* **1995,** *8* (8), 529-535.
57. Kundu, S.; Chernev, P.; Engelmann, X.; Chung, C. S.; Dau, H.; Bill, E.; England, J.; Nam, W.; Ray, K., A Cobalt(II) Iminoiodane Complex and Its Scandium Adduct: Mechanistic Promiscuity in Hydrogen Atom Abstraction Reactions. *Dalton Trans.* **2016,** *45* (37), 14538-14543.
58. Blum, Z.; Cedheim, L.; Eberson, L., Studies on Anodic Substitution Reactions. XI. The Anodic Acetoxylation of Triptycene and Fluorene and Its Implications for the Side-Chain Substitution Mechanism. *Acta Chem. Scand.* **1977,** *31b*, 662-666.
59. Bordwell, F. G., Equilibrium Acidities in Dimethyl Sulfoxide Solution. *Acc. Chem. Res.* **1988,** *21* (12), 456-463.
60. Laarhoven, L. J. J.; Mulder, P., α-C−H Bond Strengths in Tetralin and Thf: Application of Competition Experiments in Photoacoustic Calorimetry. *J. Phys. Chem. B* **1997,** *101* (1), 73-77.

61. *Solubility Data Series: Hydrogen and Deuterium*. Pergamon Press Inc: Elmsford, New York, 1981; Vol. 5/6.

5 Chapter 5. Concerted proton-electron transfer by a high-valent copper(III) complex and comparisons with an isostructural nickel(III) complex

5.1 Introduction

Oxidative transformations mediated by copper have been the topic of considerable study to solve problems in both organic and inorganic chemistry. Copper an attractive choice for designing catalysts or stoichiometric oxidants for oxidative transformations due to its low cost, versatile range of oxidation states, and well-studied biomimetic reactivity with molecular oxygen. Copper in the 3+ oxidation state is a proposed intermediate in several of these transformations,[1-2] but Cu(III) species are rarely isolated due to their reactive nature. Understanding the electronics of these species and probing their reactivity may provide further insight into the role of Cu(III) in oxidative transformations.

A common step in oxidative transformations, proton-coupled electron transfer (PCET) is proposed in catalytic alcohol oxidation by Cu/TEMPO[3-5] and sp^3-fluorination by a copper(III) compound.[6] Furthermore, PCET is hypothesized to play a role in several mechanisms of catalytic water oxidation by copper compounds, including our own previously reported $Cu(pyalk)_2$ (**1**).[7] It is therefore important to understand not only the thermodynamics of PCET, but also the mechanism and degree of coupling between the proton and electron in these systems. PCET can occur through the stepwise pathways of proton transfer followed by electron transfer (PT-ET) or electron transfer followed by proton transfer (ET-PT). Alternatively, the proton and electron can be transferred simultaneously in a process known as concerted proton-electron transfer (CPET), also known as hydrogen atom transfer (HAT). Reactions that occur through concerted mechanisms generally avoid the formation of the high-energy intermediates generated by stepwise mechanisms. Recently, computational and experimental evidence has suggested that CPET can occur through "asynchronous" pathways, in which proton and electron transfer are neither entirely separated nor entirely concerted.[8-10] In an asynchronous pathway, the transition state displays more proton transfer- or electron transfer-like character than that of a purely concerted transition. It has also been proposed that asynchronous pathways may have lower activation energies than synchronous

ones. With mechanism having such a strong effect on reaction energetics, the mechanism by which PCET occurs is relevant for understanding oxidative reactivity by high-valent metal species.

A number of Cu(III) species have been explored for their PCET reactivity, particularly with phenols and hydrocarbons.[11-14] Several of these studies have examined how variations of the ligand backbone affect rates of PCET[15] and the mechanism through which the proton and electron are transferred.[10, 12] Fewer studies, however, have examined the effects of systematically altering the metal center in isostructural compounds.[13] This approach may be advantageous in some circumstances, as altering the metal center in such compounds can have relatively large effects on reduction potential, which modulates bond dissociation enthalpy (BDE) and bond dissociation free energy (BDFE). As BD(F)E has been found to play a major role in PCET reactivity of high-valent metal compounds, we hypothesized that we could tune the rate of PCET by square planar high-valent metal-pyalk compounds by modifying the identity of the metal center. As we had previously observed fast CPET with hydrocarbons and phenols by the high-valent Ni(III) compound, $Ni(pyalk)_2^+$ (**Scheme 5.1**),[16] as discussed in Chapter 4, we hypothesized that by changing the metal center from nickel to copper, we might achieve even faster rates of PCET.

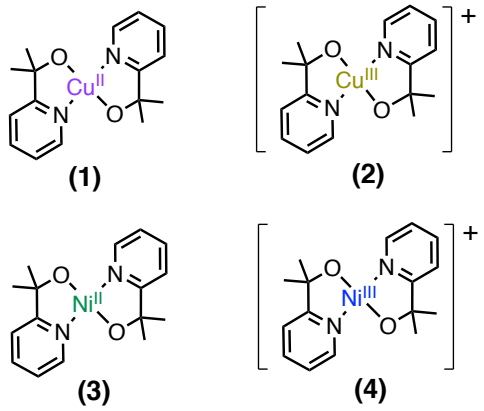

Scheme 5.1. Metal pyalk compounds discussed in this work in their reduced and oxidized states. **2** is reported in this work, while **1**, **3**, and **4** were reported by us in previous publications.[7, 16]

In this work, we identify a Cu(III) species supported by the pyalk ligand, related to the water-oxidation electrocatalyst (**1**), that is capable of PCET with phenol and hydrocarbon substrates. Like $Ni(pyalk)_2^+$ (**4**), it reacts through a concerted mechanism, with reduction of the metal center and protonation of the ligand oxygen. $Cu(pyalk)_2^+$ (**2**) was found to react 4-5 times

more quickly than its nickel counterpart, and the BDE of the relevant O-H bond formed was ~4 kcal/mol larger than for the nickel species. We examine the role of asynchronicity in CPET by both $Ni(pyalk)_2^+$ and $Cu(pyalk)_2^+$ and find that the nickel species undergoes more asynchronous concerted-proton electron transfer than the copper species. To the best of our knowledge, this work is the first result to demonstrate a change in synchronicity of PCET by changing the metal center of a molecule. Furthermore, this work may help explain previously published results demonstrating similar rates of PCET reactivity between high-valent copper and nickel compounds.[13]

5.2 Characterization of $Cu(pyalk)_2^+$ (**2**)

Based on our previous work with $Ni(pyalk)_2^+$ and the presentation of a reversible Cu(II/III) couple in the cyclic voltammogram of $Cu(pyalk)_2$ (**1**), we reasoned that it would be feasible to prepare the Cu(III) species $Cu(pyalk)_2^+$ (**2**). Using tris(4-bromophenyl)ammoniumyl hexachloroantimonate or 1,1'-diacetylferrocenium tetrafluoroborate as oxidants in CH_2Cl_2 proved successful (**Scheme 5.2**). Upon addition of oxidant, the light purple solution of $Cu(pyalk)_2$ immediately turned bright yellow, and corresponding UV-Visible data showed the appearance of an intense absorption feature at 420 nm (ε = 1100 M^{-1} cm^{-1}, **Figure 5.6**), which was attributed to the oxidized compound **2**. High-resolution electrospray ionization mass spectrometry data confirmed the molecular formula of **2**. The mass spectrum of **2** gave an *m/z* = 335.08, consistent with the expected elemental formula for the one-electron oxidized species (**Figure 5.7**).

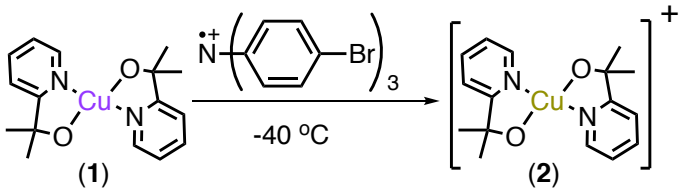

Scheme 5.2. Preparation of **2** by oxidation of **1** with tris(4-bromophenyl)ammoniumyl hexachloroantimonate at -40 °C in CH_2Cl_2.

2 proved to be thermally unstable at room temperature in CH_2Cl_2, as evidenced by the re-appearance of the characteristic peak at 735 nm of tris(4-bromophenyl)ammoniumyl

hexachloroantimonate in the UV-Visible spectrum after 5 minutes (**Figure 5.8**). At -40 °C, however, **2** was produced in quantitative yield and was stable in solution for over an hour (**Figure 5.9**).

One important concern in identifying highly oxidized species is oxidation of the ligand rather than the metal center. As demonstrated for a variety of iridium and nickel compounds, X-ray photoelectron spectroscopy (XPS) can be a useful tool for demonstrating oxidation of the metal center.[17-18] For a one-electron metal centered oxidation with no change in ligand set, a ~1 eV shift in the metal $2p_{3/2}$ binding energy is expected. Between $Cu(pyalk)_2$ and $Cu(pyalk)_2^+$ a 1.07 eV increase in binding energy was indeed observed for the Cu $2p_{3/2}$ peak (**Figure 5.1**), supporting the assignment of **2** as a Cu(III) species.

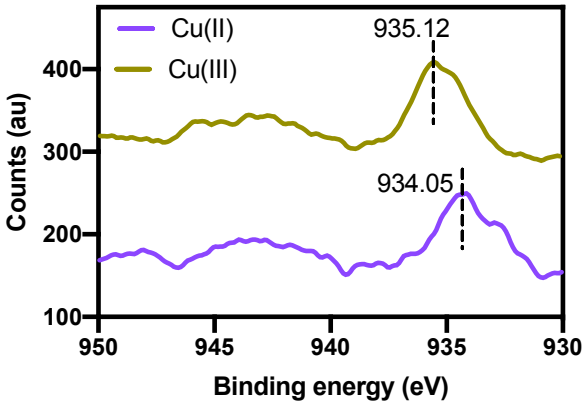

Figure 5.1. XPS spectrum of **1** (purple) and **2** (brown). The 1.07 eV increase in binding energy is attributed to oxidation of the copper metal center in **2**.

2 was also characterized by X-ray crystallography (**Figure 5.2**). Crystals were obtained from a 1:1 mixture of CH_2Cl_2 and fluorobenzene layered with pentanes at -20 °C under air- and water-free conditions. The X-ray crystal structure of **2** shows copper coordinated in a square planar environment with the pyalk ligand alkoxides mutually *trans*. An $SbCl_6$ counteranion is also present in the structure.

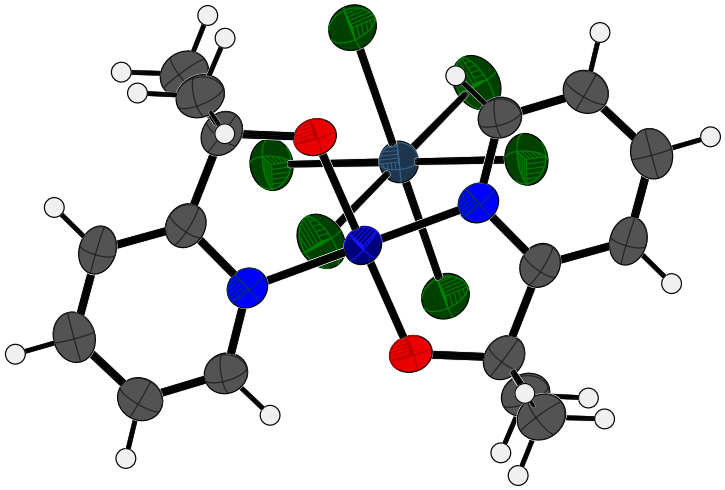

Figure 5.2. X-ray crystal structure of **2**. Atoms are displayed at the 50% probability level.

Compared to **1**, the Cu-O bond distances in **2** are shortened symmetrically by ~0.07 Å (**Table 5.1**). This value is similar to the Cu-O bond shortening observed by others from EXAFS and resonance Raman measurements between Cu(II) and Cu(III) species.[13, 19] Further comparison of the Cu-O bond lengths in **2** and the Cu-O bond lengths in $Cu(pyalkH)_2^{2+}$ (**$1H_2$**) confirms that the pyalk ligand of **2** is not protonated—in the square planar **$1H_2$**, Cu-OH bond lengths are ~1.96 Å, significantly longer than those observed in **1** or **2**.

Table 5.1. Relevant bond lengths and angles from the X-ray crystal structures of **1**, **$1H_2$**, and **2**.

	$Cu(pyalk)_2^+$ (2)	**$Cu(pyalk)_2$ (1)**	**$Cu(pyalkH)_2^{2+}$ ($1H_2$)**
Cu-O (Å)	1.814(4)	1.8806(13)	1.9589(16)
Cu-N (Å)	1.869(5)	1.9714(4)	1.965(2)
O-C (Å)	1.424(7)	1.402(2)	1.449(3)
∠O-Cu-N (°)	86.19(2)	83.97(6)	81.41(8)

The Cu-N distances between **1** and **2** are also symmetrically shortened by ~0.1 Å. No other bond lengths appear to be shortened between **1** and **2**. Furthermore, no contraction of the C-N and C-O bond lengths are observed in **2** compared to **1**. This contraction of only the copper coordination sphere and no other bonds further supports assignment that **2** is a Cu(III) species rather than a Cu(II) species with a ligand-centered radical.

Coordination compounds of copper(III), particularly those without metal-carbon bonds, are relatively rare but are not completely unknown. When prepared, the oxidation states of these compounds are generally characterized by X-ray absorption spectroscopy (XAS) or extended X-ray absorption fine structure (EXAFS). Cu(III) coordination compounds characterized by X-ray crystallography remain particularly rare. Of the published structures of non-organometallic copper in the 3+ oxidation state, almost all utilize anionic tetradentate scaffolds to enforce square planar geometry and prevent ligand loss in solution.[20-25] This strategy has led to several well-characterized crystal structures of copper(III) compounds; however, these compounds and their copper(II) counterparts are often poor targets for oxidative catalysis due to their rigid structures. Additionally, these ligands can be so electron rich that they over-stabilize the compounds, inhibiting reactivity.[26] **2**, on the other hand, features two bidentate ligands, allowing for some ligand flexibility, and **1** has been shown to act as a water-oxidation electrocatalyst under basic conditions, with **2**, in its *cis* orientation, as a plausible first intermediate in the catalytic cycle.[7, 27]

In summary, we have prepared and characterized a highly oxidized, formally Cu(III) species that has been characterized by a variety of methods, including X-ray crystallography. **2** is one of a very small number of monomeric Cu(III) compounds characterized crystallographically. To the best of our knowledge, this structure is the first non-organometallic copper(III) compound without a tetradentate ligand scaffold to be characterized crystallographically.

5.3 CPET Reactivity of **2**

With a more complete understanding of the electronic structure of **2**, we turned to examining its activity for PCET. Having recently observed such activity with the related high-valent nickel complex $Ni(pyalk)_2^+$, we suspected that $Cu(pyalk)_2^+$ should react similarly. 2,6-di-tert-butylphenol was chosen as a model substrate, as it is commonly used to assay CPET reactivity with high-valent metal substrates. It was expected that the Cu(III) center of **2** would be reduced, with the pyalk ligand accepting a proton, analogous to the reactivity of $Ni(pyalk)_2^+$. A proposed scheme for the reaction of **2** with 2,6-di-tert-butylphenol is shown below in **Scheme 5.3**.

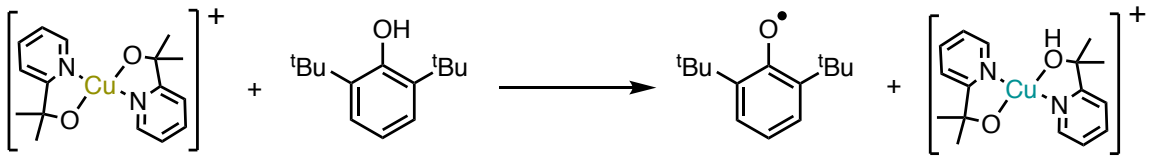

Scheme 5.3. Proposed PCET pathway for oxidation of phenols by $Cu(pyalk)_2^+$.

Reactions of **2** with all PCET substrates were monitored with UV-Visible spectroscopy at -40 °C, and all reactions were performed under pseudo-first order conditions (10-100 equivalents of substrate). All reactions were fit to a single exponential decay at a single wavelength (λ = 430 nm) to produce k_{obs} values. Plots of k_{obs} vs. substrate concentration gave linear fits for all substrates. The slopes of these fits were used to determine vaues for the second-order rate constant, k, each substrate.

When 2,6-di-tert-butylphenol was added to a solution of **2** in CH_2Cl_2 at -40 °C, the absorbance at λ = 430 nm was observed to quickly decay (**Figure 5.3A-B**). Based on plots of k_{obs} vs. phenol concentration, a second-order rate constant, k, of 12.78 M^{-1} s^{-1} was determined (**Figure 5.3C**). Based on the relatively low bond dissociation enthalpies of di-tert-butylphenol substrates and the formation of small amounts of phenol dimers upon oxidation that absorb at the same wavelength as **2**,[28] other phenol substrates were not tested for PCET reactivity.

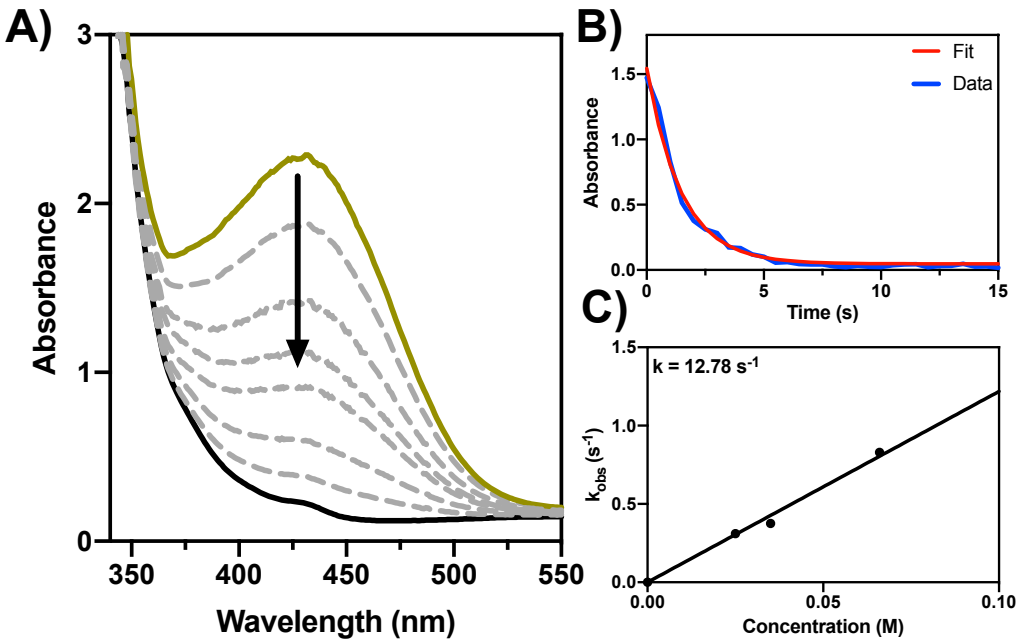

Figure 5.3. A) Representative UV-Visible spectra as a function of time for the reaction of **2** with 2,6-di-tert-butylphenol. B) Typical plot of absorbance at 430 nm vs. time for the reaction of **2** with 2,6-di-tert-butylphenol. The red line is the computed fit to a first-order decay. C) Plot of k_{obs} vs. substrate concentration for the reaction of **2** with 2,6-di-tert-butylphenol. The slope of the line of best fit (black line) corresponds to the second-order rate constant, k.

To further probe PCET reactivity, **2** was treated with hydrocarbon substrates, which have a wide range of bond dissociation enthalpies (BDE). To demonstrate this reactivity, **2** was first reacted with 9,10-dihydroanthracene (DHA). ^{1}H NMR analysis of the product of this reaction showed the expected product of anthracene in 94% yield (**Figure 5.12**). Next, to determine the extent of the PCET reactivity of **2**, a number of hydrocarbons with varying bond strengths were tested.

As expected, **2** reacted with hydrocarbon substrates over a wide range of bond dissociation enthalpies, from 77-92 kcal/mol (**Figure 5.13** - **Figure 5.22**). Much as in the nickel case, we observed a strong linear correlation between log(k) and the substrate BDE (**Figure 5.4**). Such a linear correlation is strongly suggestive of a CPET mechanism.

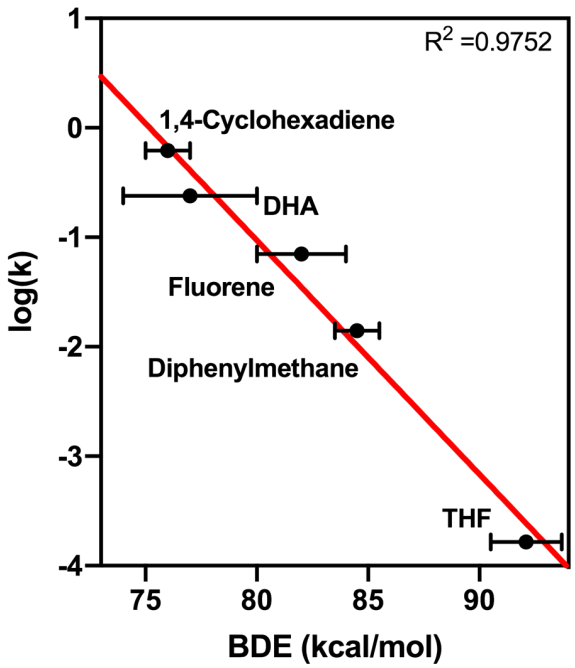

Figure 5.4. Plot of log(k) vs. hydrocarbon substrate bond dissociation enthalpy. This linear correlation is suggestive of a CPET mechanism.

To further investigate the mechanism of PCET, we probed for the presence of an H/D kinetic isotope effect for the reaction of **2** with 9,10-dihydroanthracene and 9,10-dihydroanthracene-d_4. If the reaction were to proceed through rate-limiting electron transfer followed by proton transfer (ET-PT) or pre-equilibrium proton transfer followed by rate-limiting electron transfer, no kinetic isotope effect or a very small equilibrium isotope effect would be observed. For the reaction of **2** with 9,10-dihydroanthracene and 9,10-dihydroanthracene-d_4, a kinetic isotope effect of 8.6 was observed (**Figure 5.25**). This result is inconsistent with a rate-limiting ET mechanism, but is quite consistent with other high-valent oxidants that undergo CPET, including our previously reported nickel system. Plots of log(k) vs. substrate pK_a or $E_{1/2}$ also yielded very poor correlations, further disfavoring stepwise mechanisms (**Figure 5.23**, **Figure 5.24**).

5.4 Thermodynamic Analysis

Based on the UV-Visible spectrum of the reaction products, it was clear that the copper center of **2** was reduced during CPET. We suspected that protonation was occurring at the pyalk

ligand. However, the mono-protonated product, Cu(pyalk)(pyalkH)$^+$ (**1H**) was never isolated. Instead, UV-Visible spectroscopy and X-ray crystallography results indicated the presence of a mixture of Cu(pyalk)$_2$ and [Cu(pyalkH)$_2$Cl]$^+$ (**1** and **1H$_2$Cl**) as the reaction products (**Figure 5.26**). These results suggest that, in the Cu(II) state, the pyalkH proton is labile enough to rearrange, resulting in an equilibrium that favors the fully deprotonated and fully protonated products. The chloride found in the protonated species was presumably abstracted from either the solvent (DCM) or the $SbCl_6$ anion. This result is analogous to what was observed for the CPET reaction of Ni(pyalk)$_2^+$.

With a more thorough understanding of the products of the reaction, we constructed a "square scheme" (**Figure 5.5**) to further understand the thermodynamics of the CPET reaction.

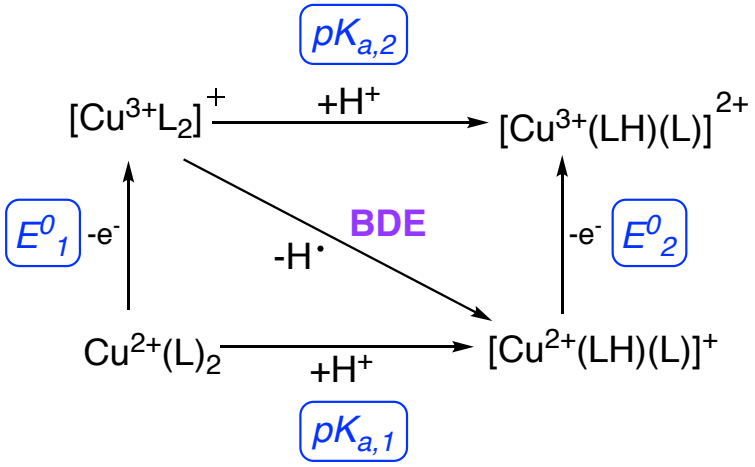

Figure 5.5. Thermochemical square scheme for stepwise vs. CPET for the copper compounds described in this work (L = pyalk).

The $E_{1/2}$ of **1** in MeCN was measured to be 0.45 V vs. Fc/Fc$^+$ by cyclic voltammetry (**Figure 5.27**). The pK_a of **1** was determined by UV-Visible spectroscopy from the titration of **1** with acid. The presence of isosbestic points in the UV-Visible spectrum indicate a clean first protonation event in MeCN. Based on these results, we estimate the pK_a for the first protonation of **1** to be ~21 (**Figure 5.28**, **Figure 5.29**), slightly more acidic than the reported pK_a of ~25 for the analogous Ni(pyalk)$_2$, which is consistent with the higher $E_{1/2}$ of Cu(pyalk)$_2$ compared to Ni(pyalk)$_2$. Using these values, we were able to determine the BDE and BDFE for the O-H bond of the bound pyalk ligand, the bond formed during the CPET reaction (**Equation 5.1** and **Equation 5.2**). The BDE of the O-H

bond formed in this reaction was found to be a substantial ~98 ± 2 kcal/mol, and the BDFE was found to be ~94 kcal/mol based on **Equations 5.1** and **5.2** below. For MeCN, C_G = 54.9 kcal/mol and C_H = 59.4 kcal/mol.[29]

$$BDFE = 1.37pK_a + 23.06E^o + C_{G,sol} \quad \textbf{(Equation 5.1)}$$

$$BDE = 1.37pK_a + 23.06E^o + C_{H,sol} \quad \textbf{(Equation 5.2)}$$

Upon the addition of one equivalent of acid in MeCN, the $E_{1/2}$ of **1** was found to shift to more oxidizing potentials (**Figure 5.27**), with $E_{1/2}$ = ~0.7 V vs. Fc/Fc^+. Using the BDE equation and square scheme shown in **Figure 5.5**, we were able to calculate a pK_a for **2H** of 17, 4 pK_a units lower than that of **1**.

Table 5.2. Thermodynamic and kinetic parameters of high-valent metal compounds capable of performing CPET with hydrocarbon substrates.

Compound	E^0_1 (V vs. Fc/Fc^+)	BDE (kcal/mol)	log(k) DHA[a,b]	Ref
$[Cu^{III}(pyalk)_2]^+$ (2)	0.45	98	1.06[c]	This work
$[Ni^{III}(pyalk)_2]^+$ (4)	0.15	94	0.74	[16]
$Cu^{III}(^{iPr}pyN_2)(OAc)$[d]	0.17	-	0.39	[13]
$Ni^{III}(^{Me}pyN_2)(ONO_2)$[e]	0.43	-	0.91	[30]
$[Fe^{III}(PY5)(OCH_3)]^{2+}$ [f]	0.73	84	-2.25	[31]
$Cu^{III}(^{iPr}pyN_2)(OH)$[d]	-0.074	90	2.27	[11]
$Ru^{IV}(bpy)_2(py)(O)$[g]	0.48[h]	84	2.09	[32-34]

[a] k = second-order rate constant for reaction with the designated substrate, measured at 25 °C unless otherwise noted; [b] DHA = 9,10-dihydroanthracene; [c] as this value could not be determined experimentally due to temperature instability at 25 °C, it was estimated based on activation parameters; [d] $^{iPr}pyN_2$ = N, N′-bis(2,6-diisopropylphenyl)-2,6-pyridinedicarboxamide; [e] $^{Me}pyN_2$ = N,N′-(2,6-dimethylphenyl)-2,6-pyridinedicarboxamide; [f] PY5 = 2,6-bis(bis(2-pyridyl)methoxymethane)pyridine; [g] bpy = 2,2'-bipyridine; py = pyridine; [h] vs. SCE.

While these bond strength values appear to be fairly high compared to other reported high-valent metals for CPET, they are not particularly surprising: as has been noted for other high-valent CPET systems, BD(F)E is affected most by the $E_{1/2}$ of the complex, and **2** has a relatively high $E_{1/2}$ compared to other reported systems (**Table 5.2**). Possibly as a result of its high BD(F)E, the rate of reaction of **2** with dihydroanthracene at 25 °C (estimated based on activation energy parameters) compares quite well to the reported rates of other high-valent metal CPET systems.

5.5 Comparison to $Ni(pyalk)_2^+$ (**4**)

To better compare the CPET reactivity of **2** with our previously reported Ni(III) compound $Ni(pyalk)_2^+$ (**4**), the rate constant, k, was measured at -40 °C for the reaction of **4** with substrates

2,6-di-tert-butylphenol and 9,10-dihydroanthracene in CH_2Cl_2. For these substrates, k was found to be 4-5 times smaller for **4** than **2** (**Table 5.2**). This result is consistent with other reports of rate differences between analogous high-valent copper and nickel compounds that undergo CPET reactivity.[13]

Next, the rates of the reaction of **2** and **4** with 9,10-dihydroanthracene were measured at a variety of temperatures in order to determine apparent activation energy parameters via the construction of Eyring plots. **2** was found to have a $\Delta H^{\ddagger}$ of 5.7 kcal/mol and a $\Delta S^{\ddagger}$ of -35 cal/mol. **4** was found to have $\Delta H^{\ddagger}$ of 4.8 kcal/mol and $\Delta S^{\ddagger}$ of -40 cal/mol. Both have relatively negative $\Delta S^{\ddagger}$ values, indicating a well-ordered transition state, and their $\Delta H^{\ddagger}$ values are quite similar, indicating little difference in activation enthalpies. The same activation energy parameters were determined for the reaction of **2** and **4** with 2,6-di-tert-butylphenol, which gave similar results (**Figure 5.47** and **Figure 5.52**).

Table 5.3. Comparison of rate constant (k) values, activation energy parameters, and bond strengths for **2** and **4**

	$Cu(pyalk)_2^+$	**$Ni(pyalk)_2^+$**
2,6-di-tert-butylphenol rate constant k (M^{-1} s^{-1})[a]	12.78	2.56
9,10-dihydroanthracene (DHA) rate constant k (M^{-1} s^{-1})[a]	0.25	0.055
$\Delta H^{\ddagger}_{DHA}$ (kcal/mol)	5.7 ± 0.4	4.8 ± 0.1
$\Delta S^{\ddagger}_{DHA}$(cal/mol T)	-35 ± 2	-40 ± 1
BDE (kcal/mol)	98	94

[a]measured at -40 °C in CH_2Cl_2

While the relatively small difference in CPET rates between Ni(III) and Cu(III) species has been previously reported, it was still puzzling to us why complexes with a relatively large difference in BDEs should react with CPET substrates at such similar rates. To examine the potential cause of this phenomenon, we investigated the asynchronicity factor for the reactions of both **2** and **4** with CPET substrates. “Asynchronicity” in a CPET mechanism refers to the transition state for the reaction having more PT-like character in the transition state (referred to as “basic asynchronous”) or more ET-like character (referred to as “oxidatively asynchronous”). Given the large disparity

between the strongly basic pK_a of **4** and its rather mild $E_{1/2}$, we hypothesized that the reaction of **4** with CPET substrates might proceed along a more asynchronous pathway than that of **2**. To that end, we calculated the "asynchronicity factor" (η) for each molecule based on the following equation (**Equation 5.3**):[8]

$$\eta = 2^{-1/2}(\Delta E^{\circ\prime} - \frac{RT}{F}\ln(10) \times \Delta pK_{a,red}) \qquad \textbf{(Equation 5.3)}$$

where ΔE°' is the difference between reduction potential of the *protonated* metal complex (E^{o}_2 in **Figure 5.5**) and substrate, and $\Delta pK_{a,red}$ is the difference in pK_a values between the non-protonated metal complex ($pK_{a,1}$ in **Figure 5.5**) and the substrate.

Based on the data presented in **Table 5.3**, an asynchronicity factor of -286 mV was calculated for the reaction of **4** with 2,6-di-tert-butylphenol, while a factor of -592 mV was calculated for **2** with the same substrate, indicating a more asynchronous mechanism in the nickel case. Work from Srnec and coworkers suggest that asynchronicity in CPET may affect the driving force for the reaction: higher degrees of asynchronicity lead to lower $\Delta G^{\ddagger}$ values.[8] Therefore, these results suggest while **2** has a higher BD(F)E than **4** and therefore should react with CPET substrates much more rapidly, **2** has a higher degree of asynchronicity in its reaction mechanism, so **2** reacts faster than would be expected based on BD(F)E alone.

5.6 Conclusions

We have isolated and characterized a copper(III) species, $[Cu(pyalk)_2]^+$. This compound was characterized by X-ray crystallography and X-ray photoelectron spectroscopy, which confirmed oxidation of the metal center. **2** proves to be a rare example of a copper(III) species characterized crystallographically.

2 was shown to undergo fast proton-coupled electron transfer with a variety of hydrocarbon and phenol substrates with BDEs ranging from 77-92 kcal/mol. Analysis of the kinetics of the reaction of **2** with hydrocarbon substrates suggests that **2** reacts through a concerted proton-electron transfer pathway. **2** proves to be one of the few first-row transition metal complexes to undergo PCET. Thermodynamic analysis using the $E_{1/2}$ of **2** and ligand pK_a result in a BDE of ~98 kcal/mol for the pyalk O-H bond formed during PCET, which may explain its fast reactivity.

2 was further compared to its nickel(III) analogue. A comparison of rates showed that **2** reacted only 4-5 more quickly than **4** with the same substrate, despite having a higher BDE by ~4 kcal/mol. Analysis of activation energy barriers did not show significant differences between the two complexes. The asynchronicity factor for the reaction of both complexes with 9,10-dihydroanthracene and 2,6-di-tert-butylphenol was calculated. The results suggested that **4** may undergo more oxidatively asynchronous CPET compared to **2**, which may result in a lower barrier than would be expected for a purely concerted process.

The observation that high-valent copper and nickel compounds react at similar rates for CPET reactions has been previously noted, but the reasons for such reactivity could not be explained due to lack of pK_a data. This work demonstrates that modulation of the metal center may result in difference in the asynchronicity of CPET between different complexes, further modulating their reactivity.

5.7 Experimental Procedures

5.7.1 General

General Considerations: Reagents were purchased from Sigma-Aldrich or Alfa Aesar and used as received unless otherwise specified. Experiments were performed in an N_2-filled M Braun glove box or using standard Schlenk technique unless otherwise specified. $Cu(pyalk)_2$, $Ni(pyalk)_2^+$, 1,1'-diacetylferrocenium tetrafluoroborate, and dihydroanthracene-d_4 were prepared according to literature procedures.[7, 16, 31, 35]

5.7.2 Physical Methods

UV-Visible Spectroscopy: Absorption spectra were collected using a Cary 50 spectrophotometer.

^{1}H NMR: ^{1}H NMR spectra were recorded on an Agilent DD2 400 MHz spectrometer and ^{1}H chemical shifts were referenced to residual solvent.

Mass spectrometry: High resolution mass spectrometry was done on a QExactive Orbitrap FT-MS.

X-ray Photoelectron Spectroscopy: The XPS spectra were collected using a monochromatic 1486.7 eV Al KαXray source on PHI VersaProbe II X-ray Photoelectron Spectrometer with a 0.47 eV system resolution. The energy scale has been calibrated using Cu $2p_{3/2}$ (932.67eV) and Au $4f_{7/2}$ (84.00 eV) peaks on a clean copper plate and a clean gold foil. The samples were prepared by drop casting a concentrated solution of $Cu(pyalk)_2$ or $Cu(pyalk)_2^+$ in dry CH_2Cl_2 onto a Si wafer. The reported shifts were referenced using the Si 2p peak (99.3 eV) from the Si wafer.

Electrochemical measurements: Electrochemical measurements were performed on a Pine AFCBP1 bipotentiostat using a standard three-electrode configuration. A boron-doped diamond working electrode and a platinum counter-electrode were used. A silver wire was used as a pseudo-

reference, and the potential was referenced using a ferrocene internal standard. Spectra were taking in dry MeCN with 0.1 M tetrabutylammonium hexafluorophosphate used as electrolyte.

Kinetics for CPET reactions with 2: UV-Visible kinetics data were collected on an Agilent 8453 diode array spectrophotometer. Temperature was controlled using a Unisoku CoolSpeK cryostat. In a typical experiment, 2 mL of a 0.5 mM solution of $Cu(pyalk)_2$ was added to a sealable quartz cuvette equipped with a stir bar and septum in an N_2-filled glove box. A 2 mM solution of tris(4-bromophenyl)ammoniumyl hexachloroantimonate in CH_2Cl_2 was also prepared, and 0.5 mL of this solution was loaded into a syringe. Finally, a solution of hydrocarbon substrate in CH_2Cl_2 was prepared at the desired concentration, and 0.5 mL of this solution was loaded into a syringe. The cuvette and syringes were removed from the glove box, and the cuvette cooled to -40 °C in the cryostat (*ca* 5 minutes). The tris(4-bromophenyl)ammoniumyl hexachloroantimonate solution was then injected via syringe, and the first UV-Visible spectra were taken. Once the absorbance at 420 nm had stabilized for 2-3 minutes, the substrate solution was injected via syringe. Spectra were generally taken every 0.5 seconds for the first six minutes, with subsequent traces recorded after a 5% delay time if applicable. The solution volume at the end of each experiment was 3.0 mL; this value was used to calculate substrate concentration for plots of observed rate vs. substrate concentration.

Kinetics for reaction of 4 with 2,6-di-tert-butylphenol: UV-Visible kinetics data were collected on an Agilent 8453 diode array spectrophotometer. Temperature was controlled using a Unisoku CoolSpeK cryostat. In a typical experiment, 2 mL of a 0.5 mM solution of $Ni(pyalk)_2^+$ was added to a sealable quartz cuvette equipped with a stir bar and septum in an N_2-filled glove box. A solution of the substrate at the desired concentration in CH_2Cl_2 was prepared and loaded into a syringe. The cuvette and syringes were removed from the glove box, and the cuvette cooled to -40 °C in the cryostat (*ca* 5 minutes). The first UV-Visible spectrum was taken, and then the substrate was quickly injected via syringe. Spectra were taken every 0.5 seconds for the first six minutes, with subsequent traces recorded after a 5% delay time if applicable. The solution volume at the end of

each experiment was 3.0 mL; this value was used to calculate substrate concentration for plots of observed rate vs. substrate concentration.

Kinetics for reaction of 4 with 9,10-dihydroanthracene (DHA): Variable-temperature stopped-flow measurements for the reaction between **4** and 9,10-dihydroanthracene were performed using a TgK Scientific HI-TECH SCIENTIFIC CryoStopped-Flow (SF-61DX2) apparatus equipped with a diode array detector. In a typical experiment, a solution of **4** in CH_2Cl_2 was prepared under N_2 atmosphere in a glove box and loaded into a syringe. A separate syringe of 9,10-dihydroanthracene in CH_2Cl_2 was also prepared under the same conditions. The stopped-flow apparatus was allowed to cool to the desired temperature for 5 minutes, and then equal volumes of the solutions were mixed. Observed rate constants from all stopped-flow analyses were derived using SPECFIT/32 software.

pKa measurement of 1: Titrations to determine the pK_a of **1** were monitored by UV-Visible spectroscopy on a Cary 50 spectrophotometer. The pK_a of **1** was determined by addition of 1 M acetic acid to generate **1H**. The pK_a was determined from a plot of [pyalkH][OAc^-]/[**1**] vs. acetic acid concentration as described in reference [36]. The titration was performed 3 times, and the final pK_a was found by averaging the pK_a found in each titration.

5.7.3 Synthetic Procedures:

Synthesis of $Cu(pyalk)_2^+$ (2), In a Schlenk flask under inert atmosphere, 0.01 g (30 μmol) of $Cu(pyalk)_2$ was dissolved in dry CH_2Cl_2. The flask was cooled to -20 °C in an ice-salt bath. In separate flask, 0.027 g (33 μmol, 1.1 eq) of tris(4-bromophenyl)ammoniumyl hexachloroantimonate ("magic blue") was dissolved in enough CH_2Cl_2 to completely dissolve the powder (approx. 10 mL). This solution was also cooled to -40 °C, and then the Magic Blue solution was transferred to the $Cu(pyalk)_2$ solution via syringe. The resulting yellow solution was triturated with 20 mL pentanes to afford a yellow powder. The supernatant was removed the product dried under vacuum. Yield: 0.016 g (80%). HRMS: 335.08 (M^+)

Crystals were grown from a 1:1 mixture of CH_2Cl_2 and fluorobenzene layered with pentanes stored at -20 °C in the glove box. UV-Visible λ_{max}, nm (ε, M^{-1} cm^{-1}): 420 (1100)

Preparation of $Cu(pyalkH)_2^{2+}$ ($1H_2$): In a round-bottom flask equipped with stir bar, 0.10 g (0.29 mmol) $Cu(BF_4)_2 \bullet 6H_2O$ was dissolved in a 1:1 mixture of CH_3OH/CH_3CN. To this solution, 0.085 g (0.61 mmol, 2.1 eq) pyalkH was added, causing an immediate color change to dark blue. This solution was allowed to stir under air atmosphere for one hour, and then was dried via rotary evaporation. The resulting blue solid was redissolved in CH_3CN and placed in the freezer. Dark blue crystals were obtained after 24 hours. Yield: 0.091 g (62%)

Stoichiometric conversion of 9,10-dihydroanthracene to anthracene: In a Schlenk flask under inert atmosphere, 0.05 g (0.15 mmol) of $Cu(pyalk)_2$ was dissolved in dry CH_2Cl_2. The flask was cooled to -78 °C in a dry ice/acetone bath. In separate flask, 0.13 g (0.16 mmol, 1.1 eq) of tris(4-bromophenyl)ammoniumyl hexachloroantimonate ("magic blue") was dissolved in enough CH_2Cl_2 to completely dissolve the powder (approx. 15 mL). This solution was also cooled to -78 °C, and then the magic blue solution was transferred to the $Cu(pyalk)_2$ solution via syringe. In a separate 20 mL flask, 0.027 g 9,10-dihydroanthracene (0.15 mmol, 1 eq) was dissolved in 5 mL of dry CH_2Cl_2 and cooled to -78 °C, then transferred to the $Cu(pyalk)_2^+$ solution via syringe. This reaction mixture was stirred overnight at -78 °C, during which time the solution changed from bright yellow to light blue. The solution was then opened to atmosphere and run over a plug of silica to remove the reduced copper species. The resulting clear solution was then brought to dryness by rotary evaporation and redissolved in $CDCl_3$ for ^1H NMR analysis.

Isolation of copper-containing products from reaction of 2 with 9,10-dihydroanthracene: A 1 mM solution of $Cu(pyalk)_2^+$ in CH_2Cl_2 was prepared at -78 °C under inert atmosphere. A 0.1 M solution of 9,10-dihydroanthracene in CH_2Cl_2 was prepared separately at the same temperature. The dihydroanthracene solution was then added to the solution of $Cu(pyalk)_2^+$ via syringe. The reaction was allowed to proceed to completion over the course of several hours. The solution was then

concentrated *in vacuo*, layered with pentanes, and stored in the freezer. After 24 hours, blue-green (**1H$_2$Cl**) and purple (**1**) crystals were observed.

5.8 Supplementary Figures

5.8.1 Characterization data

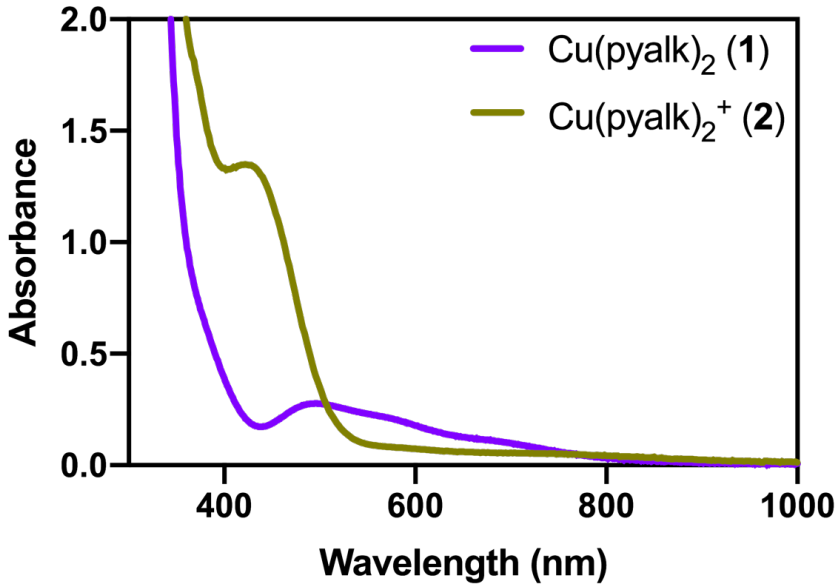

Figure 5.6. UV-Visible spectrum of **1** and **2** in CH_2Cl_2.

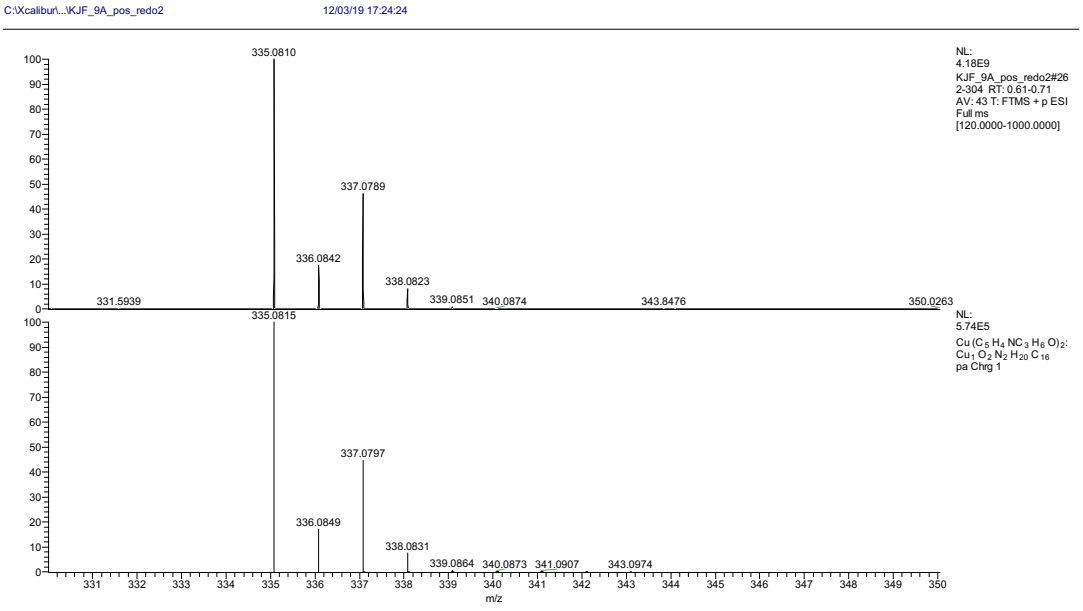

Figure 5.7. High resolution mass spectrum of **2** (top) and calculated spectrum (bottom).

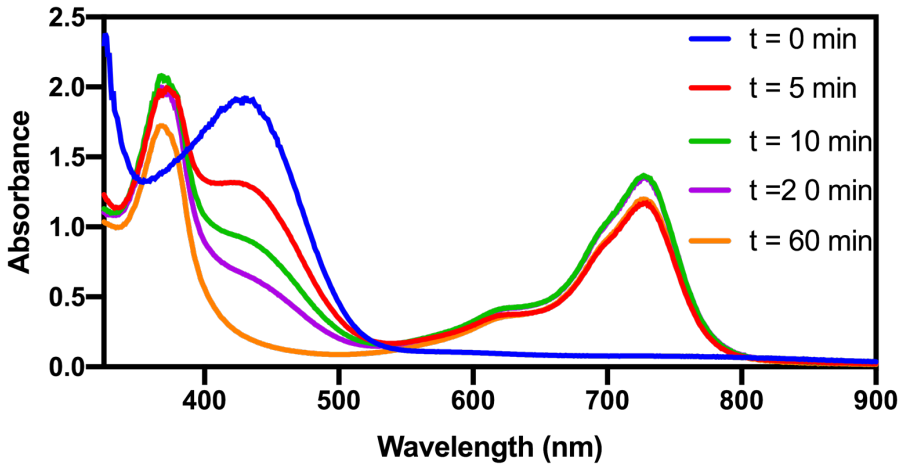

Figure 5.8. UV-Visible spectra of the reaction of **1** with tris(4-bromophenyl)ammoniumyl hexachloroantimonate to form **2** at 25 °C in CH_2Cl_2 over several minutes, demonstrating the instability of **2** with time at this temperature.

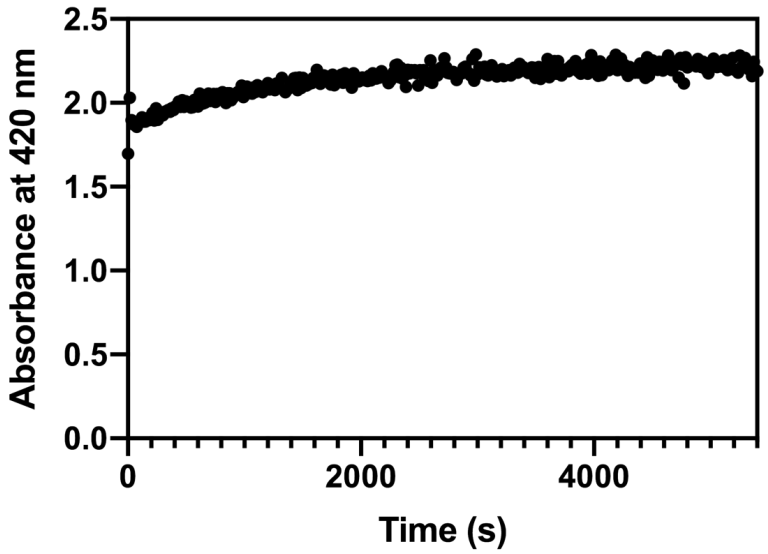

Figure 5.9. Plot of the absorbance at 420 nm vs. time for the reaction of **1** with tris(4-bromophenyl)ammoniumyl hexachloroantimonate to form **2** at -40 °C in CH_2Cl_2 over the course of 1.5 hours. One trace was taken every 30 seconds. At this temperature, no decay of **2** is observed over this time period, which was the maximum timeframe used for reactions with hydrocarbon substrate.

5.8.2 PCET Oxidation by **2**

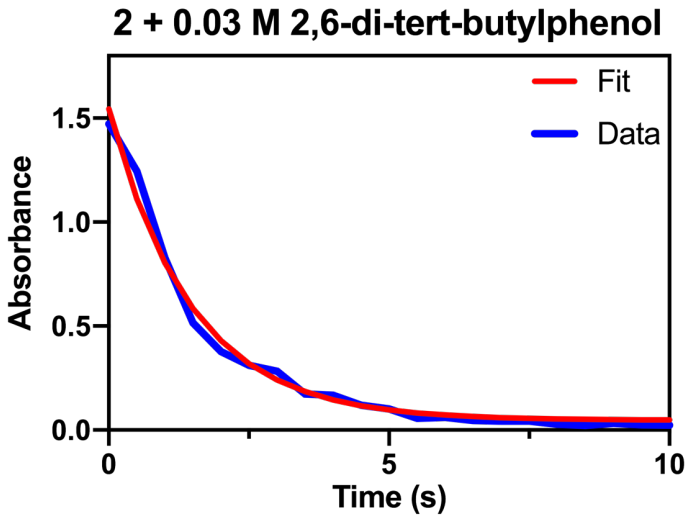

Figure 5.10. Representative fit of absorbance at λ = 430 nm vs. time for the reaction of **2** with 2,6-di-tert-butylphenol at -40 °C.

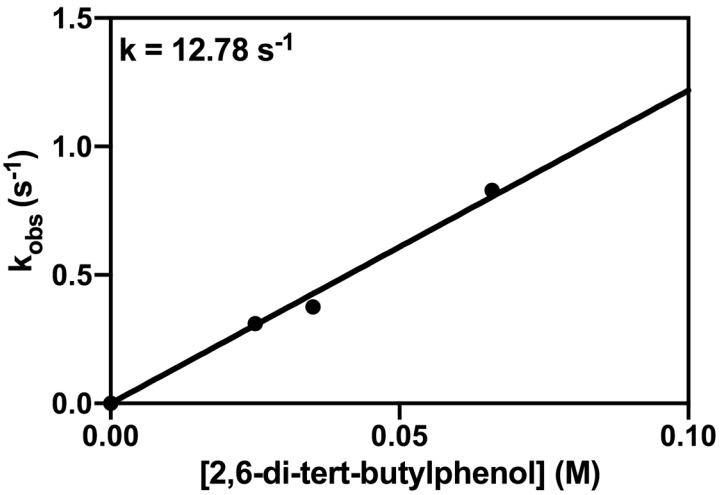

Figure 5.11. Plot of k_{obs} vs. concentration for the reaction of **2** with 2,6-di-tert-butylphenol at -40 °C.

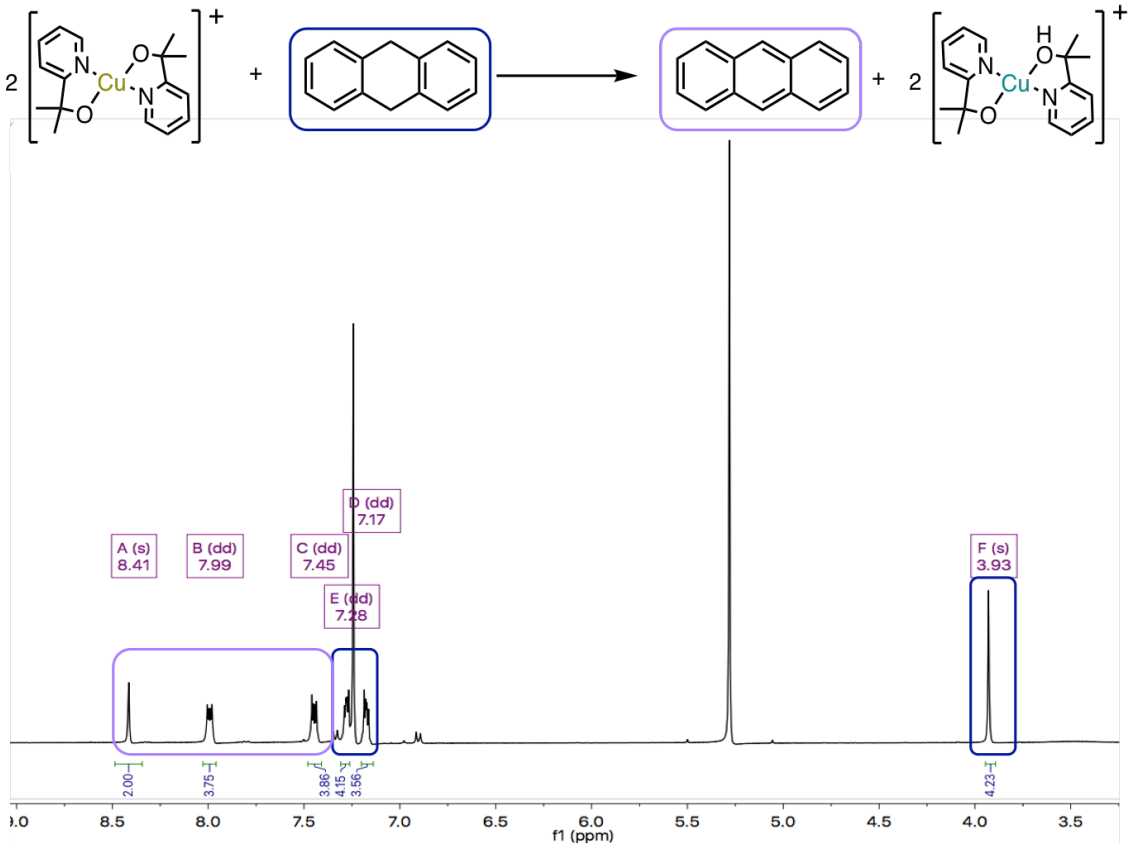

Figure 5.12. ^{1}H NMR spectrum of reaction of **2** with 2 equivalents 9,10-dihydroanthracene at -78 °C. Based on integration, the yield of anthracene was determined to be 94%.

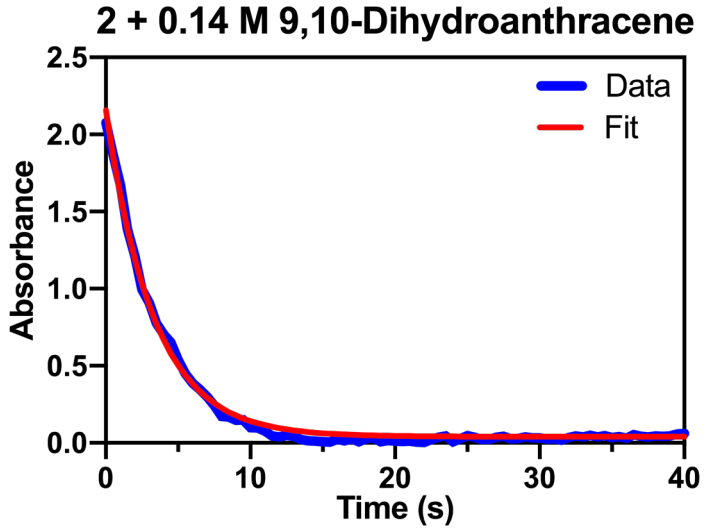

Figure 5.13. Representative fit of absorbance at λ = 430 nm vs. time for the reaction of **2** with 9,10-dihydroanthracene at -40 °C.

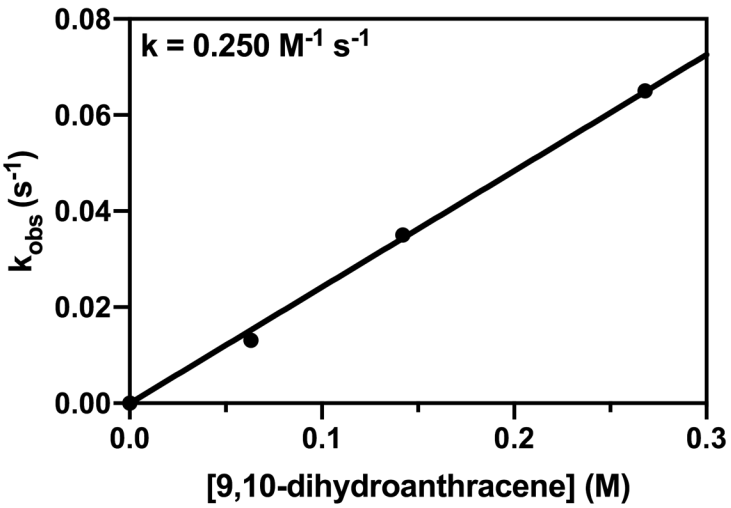

Figure 5.14. Plot of k_{obs} vs. concentration for the reaction of **2** with 9,10-dihydroanthracene at -40 °C.

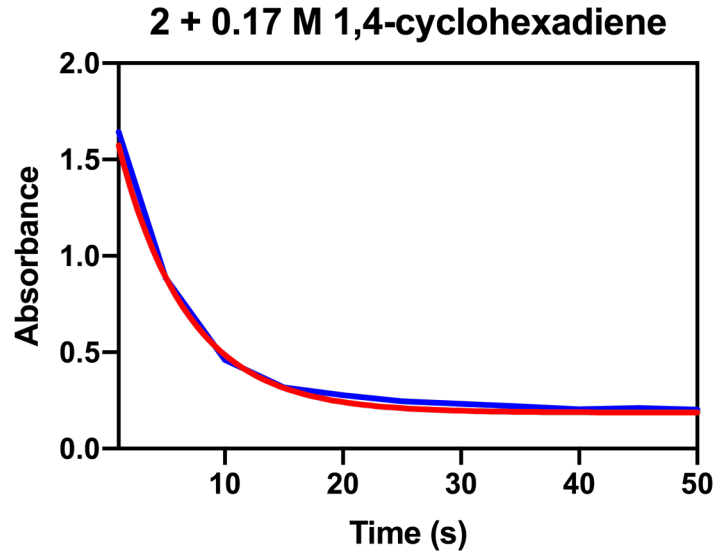

Figure 5.15. Representative fit of absorbance at λ = 430 nm vs. time for the reaction of **2** with 1,4-cyclohexadiene at -40 °C.

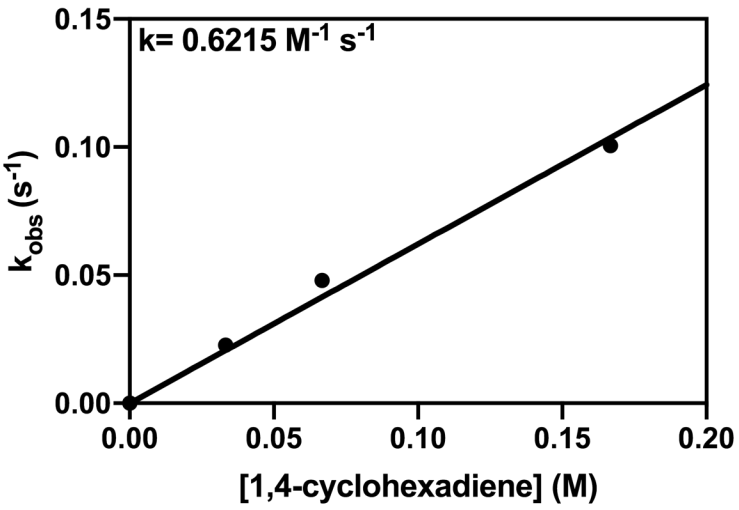

Figure 5.16. Plot of k_{obs} vs. concentration for the reaction of **2** with 1,4-cyclohexadiene.

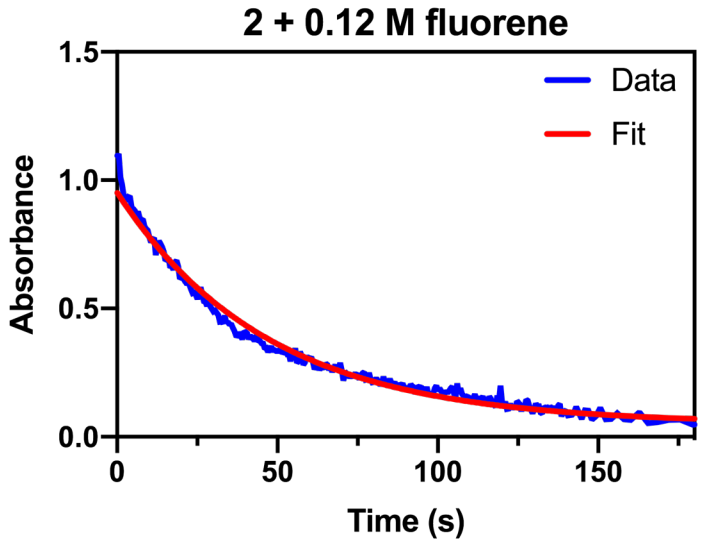

Figure 5.17. Representative fit of absorbance at λ = 430 nm vs. time for the reaction of **2** with fluorene at -40 °C.

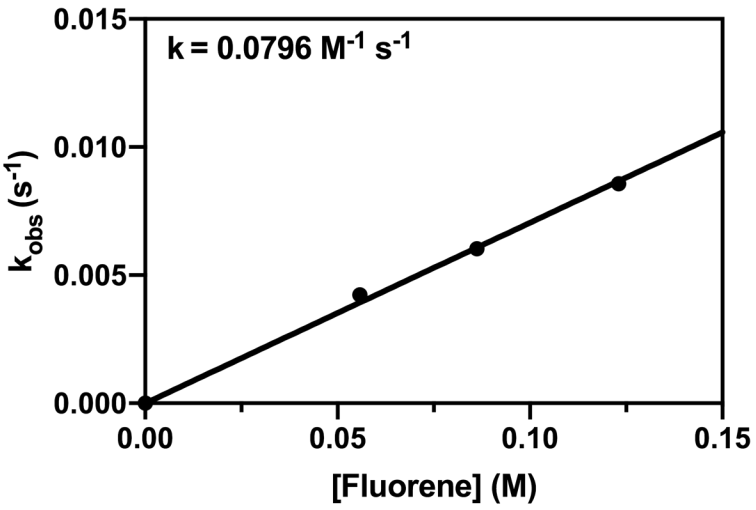

Figure 5.18. Plot of k_{obs} vs. concentration for the reaction of **2** with fluorene at -40 °C.

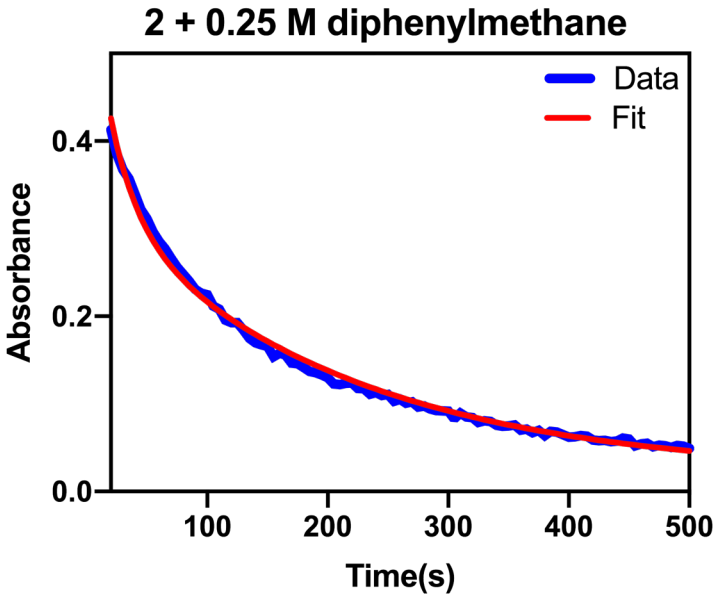

Figure 5.19. Representative fit of absorbance at λ = 430 nm vs. time for the reaction of **2** with diphenylmethane at -40 °C.

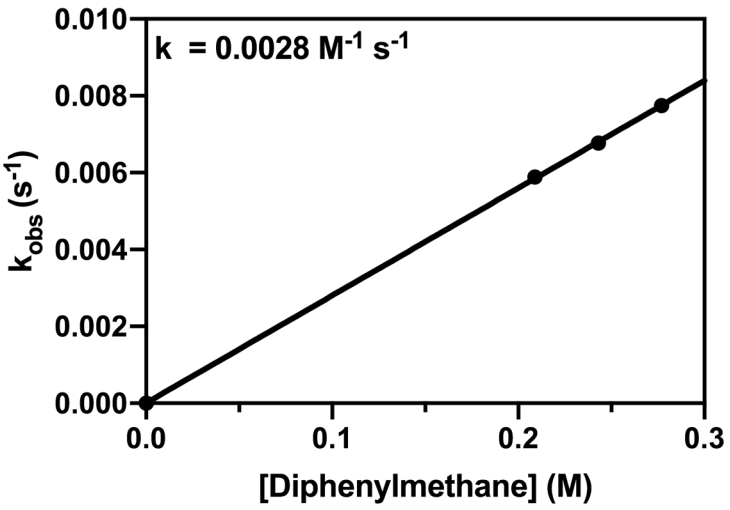

Figure 5.20. Plot of k_{obs} vs. concentration for the reaction of **2** with diphenylmethane at -40 °C.

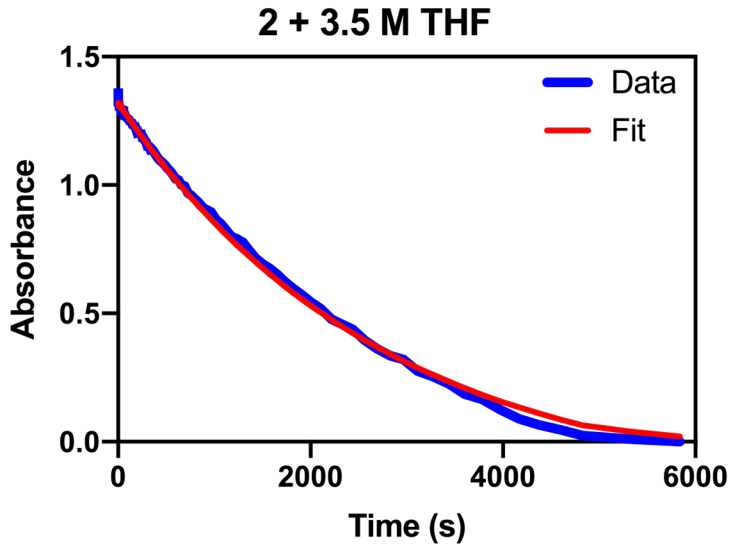

Figure 5.21. Representative fit of absorbance at λ = 430 nm vs. time for the reaction of **2** with tetrahydrofuran (THF) at -40 °C.

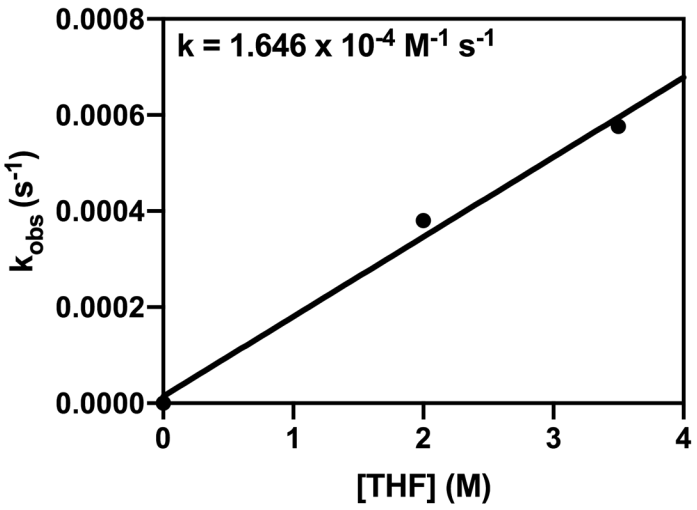

Figure 5.22. Plot of k_{obs} vs. concentration for the reaction of **2** with tetrahydrofuran (THF) at -40 °C.

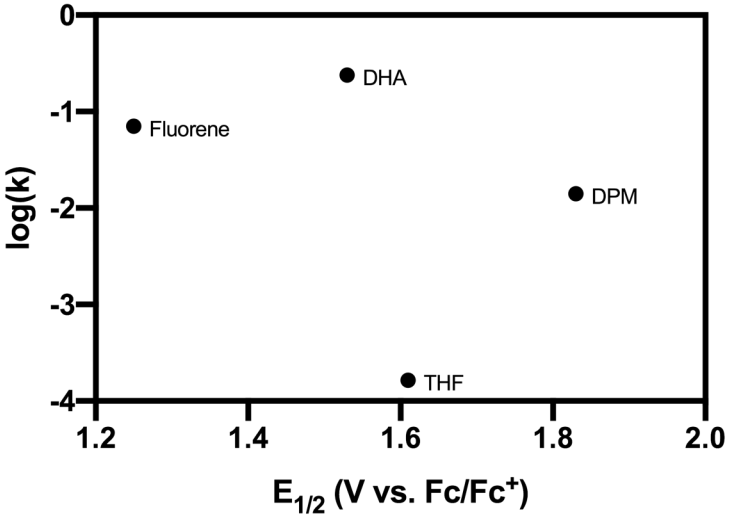

Figure 5.23. Plot of log(k) vs. $E_{1/2}$ data for the reaction of **2** hydrocarbon substrates. For 1,4-cyclohexadiene, no $E_{1/2}$ value was available.

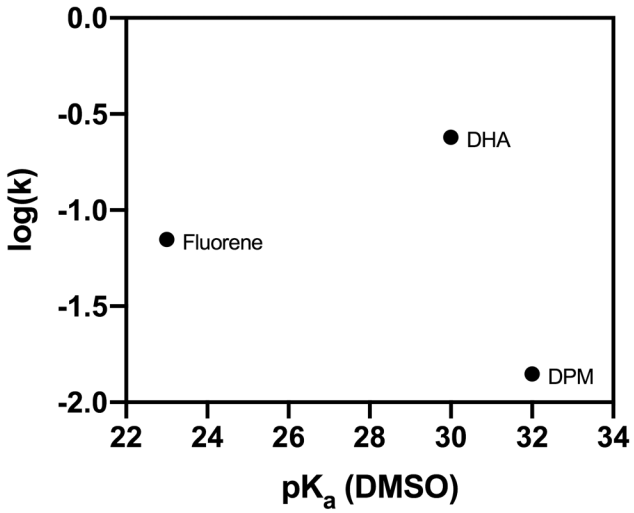

Figure 5.24. Plot of log(k) vs. pK_a for the reaction of **2** with hydrocarbon substrates. For 1,4-cyclohexadiene and THF, no pK_a values were available.

Table 5.4. Summary of thermodynamic and kinetic parameters in our analysis of the reaction of **2** with hydrocarbon substrates at -40 °C.

Substrate	**$E°_{1/2}$ (V vs Ag/Ag^+ in MeCN)[37]**	**pK_a (DMSO)[38]**	**BDE[a] (kcal/mol)[29, 34, 39]**	**k (M^{-1} s^{-1} in CH_2Cl_2)**
1,4-cyclohexadiene	-	-	76 ± 1	0.62
9,10-dihydroanthracene	1.53	30	78 ± 3	0.25
Fluorene	1.25	23	82 ± 2	0.0796
Diphenylmethane	1.83	32	84.3 ± 1	0.0028
THF	1.61	-	92 ± 1	0.000165

[a]All BDEs reported as measured in DMSO. When multiple BDE values were available, values determined using pK_a and E^0 data were chosen for the sake of consistency.

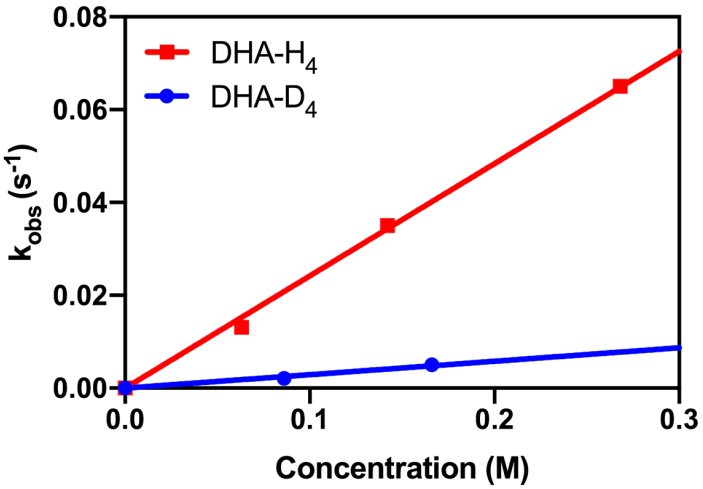

Figure 5.25. Plots of k_{obs} vs, concentration for the reaction of **2** with 9,10-dihydroanthracene (DHA-H_4) and deuterated 9,10-dihydroanthracene (DHA-D_4). The ratio of the slopes of both plots was used to determine the kinetic isotope of effect of 8.6.

5.8.3 Thermodynamics supporting data

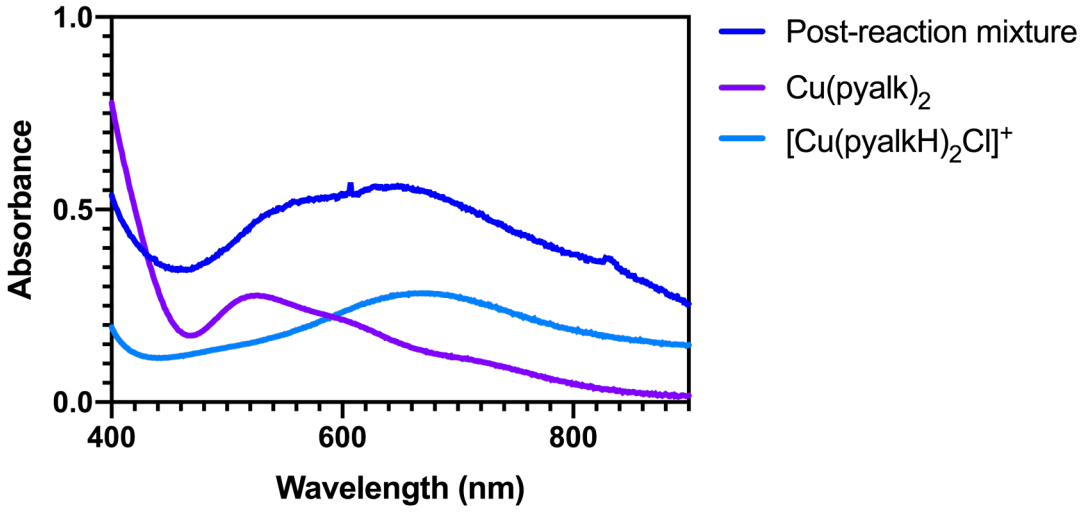

Figure 5.26. UV-Visible spectrum of copper-containing species after the reaction of **2** with 10 equivalents of 9,10-dihydroanthracene. The UV-Visible spectra of **1** and **1H₂Cl** are shown below for reference. The post-reaction mixture appears to have both species present in solution.

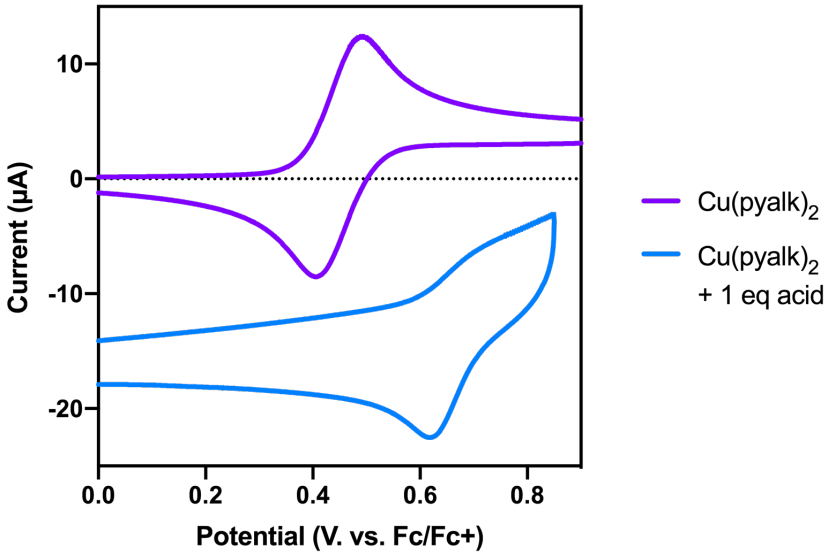

Figure 5.27. CVs of **1** and **1H** in acetonitrile. Scan rate: 100 mV s^{-1}

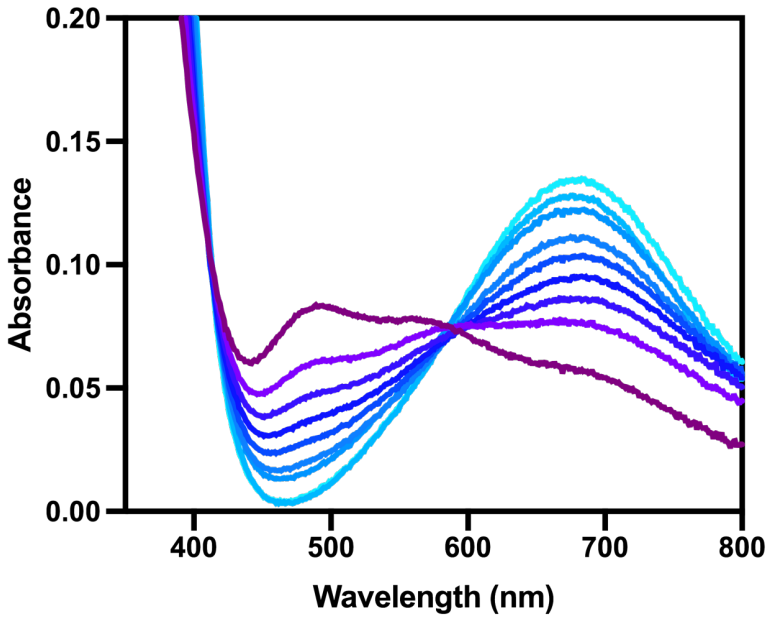

Figure 5.28. Representative UV-Visible titration of **1** with acetic acid.

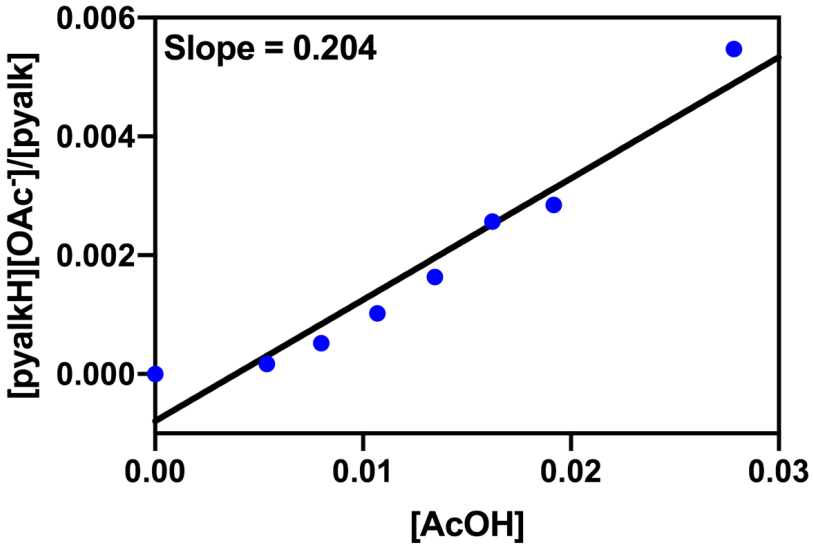

Figure 5.29. Linearized titration plot for the conversion of **1** to **1H**.

5.8.4 Variable Temperature Kinetic Data for Reactions of **2** and **4**

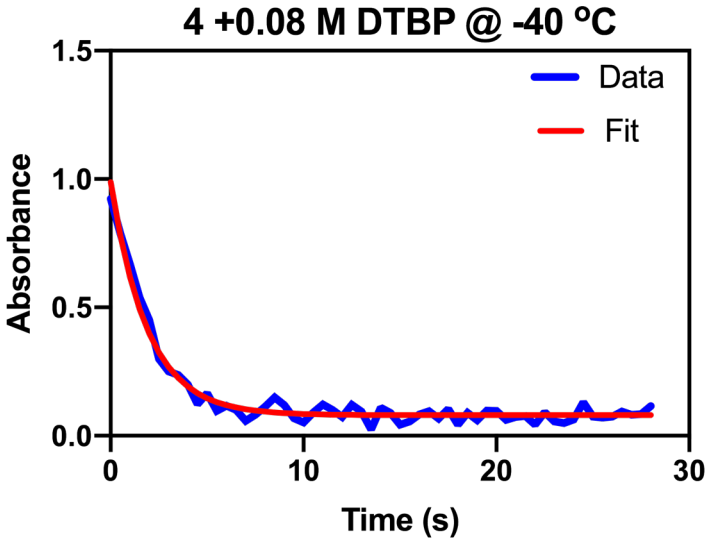

Figure 5.30. Representative fit of absorbance at λ = 610 nm vs. time for the reaction of **4** with 2,6-di-tert-butylphenol at -40 °C.

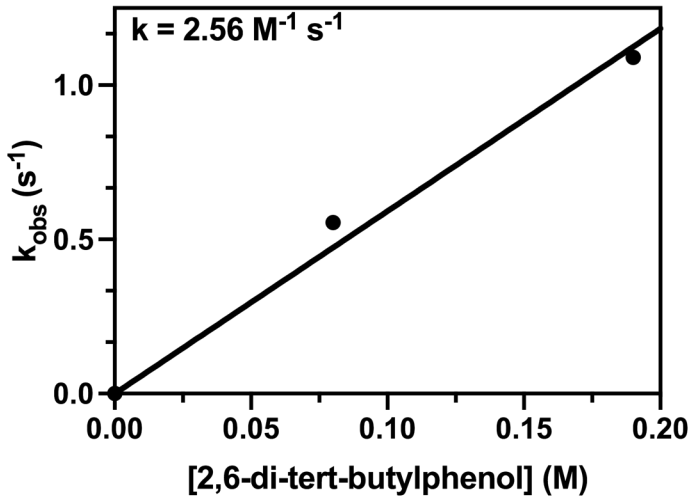

Figure 5.31. Plot of k_{obs} vs. concentration for the reaction of **4** with 2,6-di-tert-butylphenol at -40 °C.

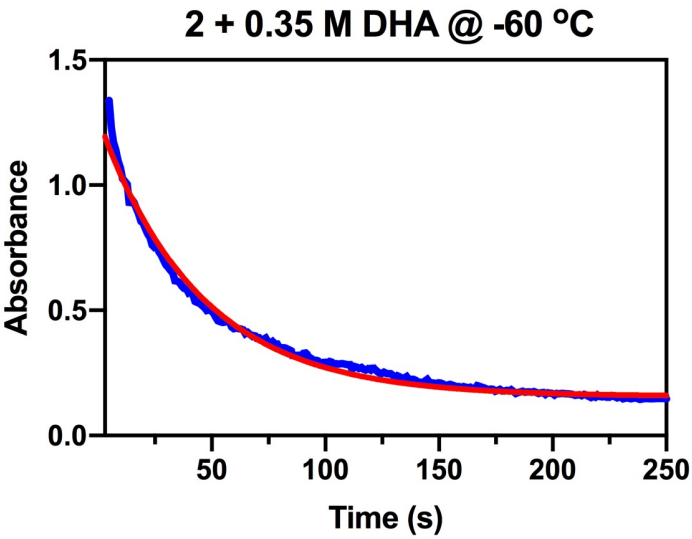

Figure 5.32. Representative fit of absorbance at λ = 430 nm vs. time for the reaction of **2** with 9,10-diyhdroanthracene at -60 °C.

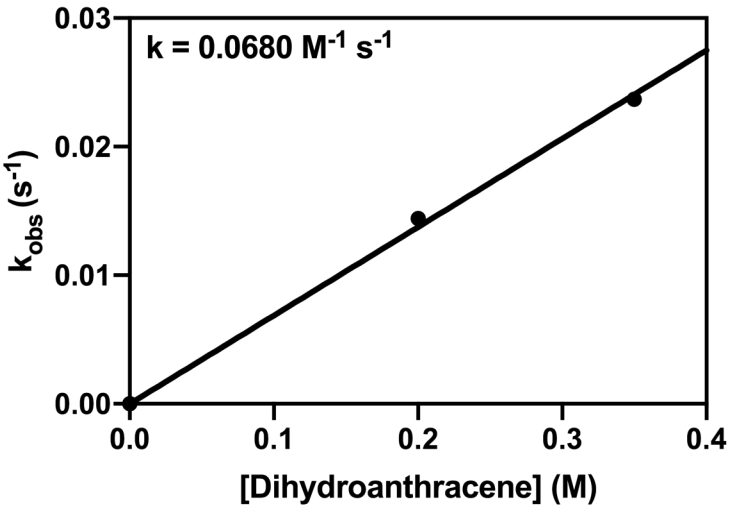

Figure 5.33. Plot of k_{obs} vs. concentration for the reaction of **2** with 9,10-dihydroanthracene at -60 °C.

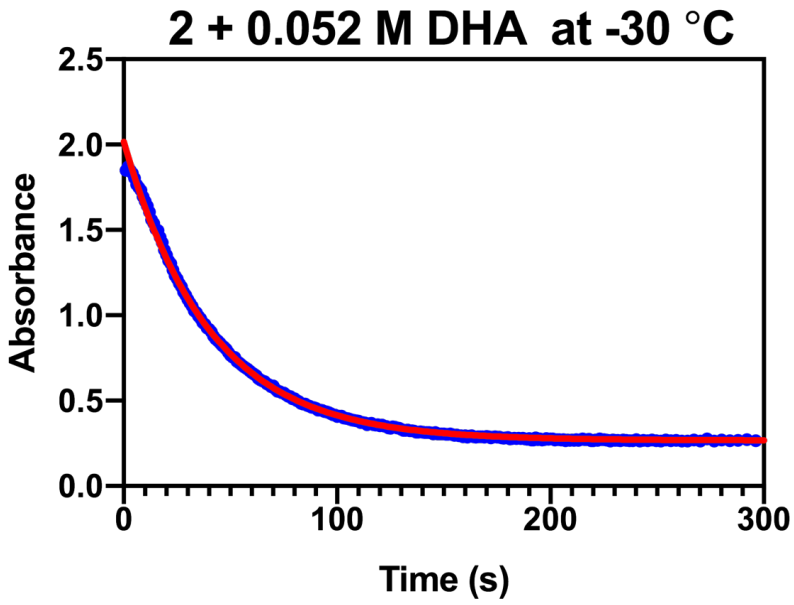

Figure 5.34. Representative fit of absorbance at λ = 430 nm vs. time for the reaction of **2** with 9,10-diyhdroanthracene at -30 °C.

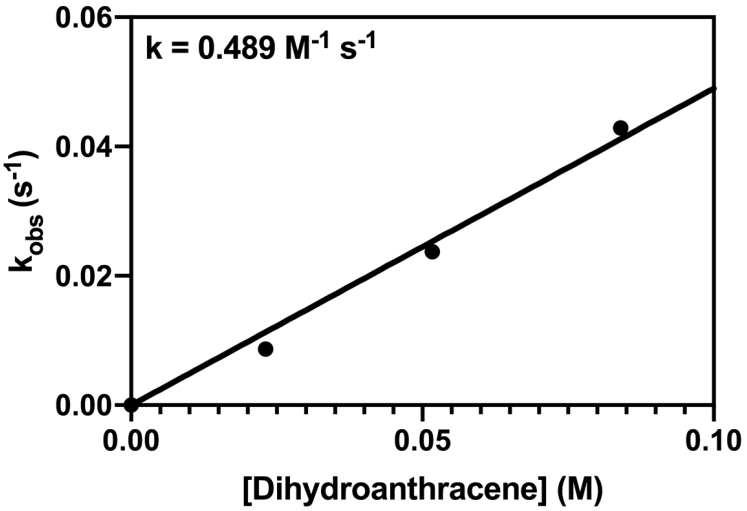

Figure 5.35. Plot of k_{obs} vs. concentration for the reaction of **2** with 9,10-dihydroanthracene at -30 °C.

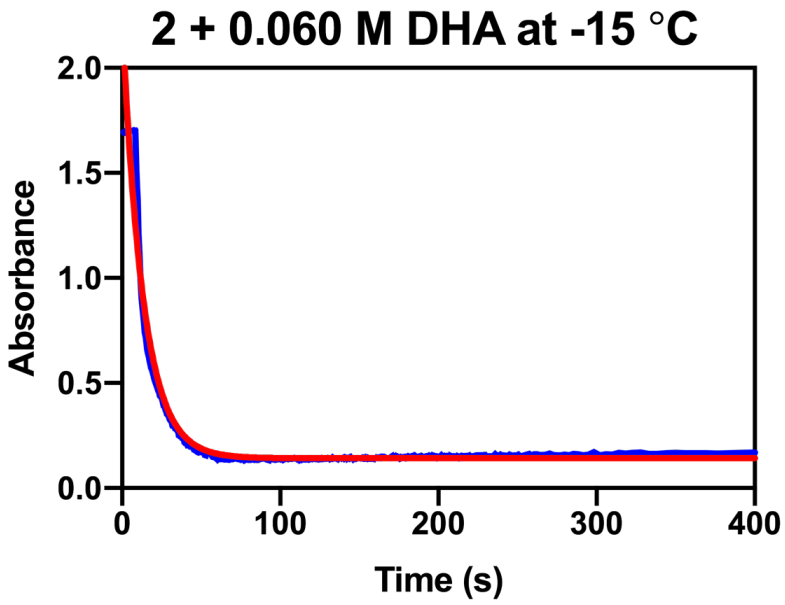

Figure 5.36. Representative fit of absorbance at λ = 430 nm vs. time for the reaction of **2** with 9,10-diyhdroanthracene at -15 °C.

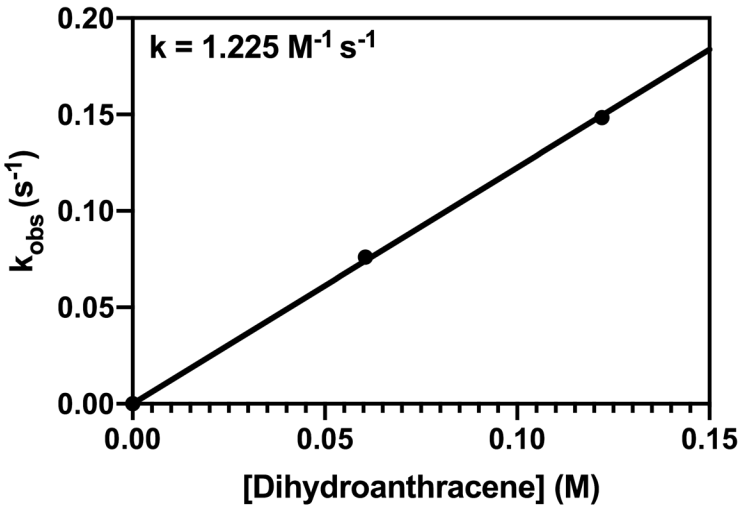

Figure 5.37. Plot of k_{obs} vs. concentration for the reaction of **2** with 9,10-dihydroanthracene at -15 °C.

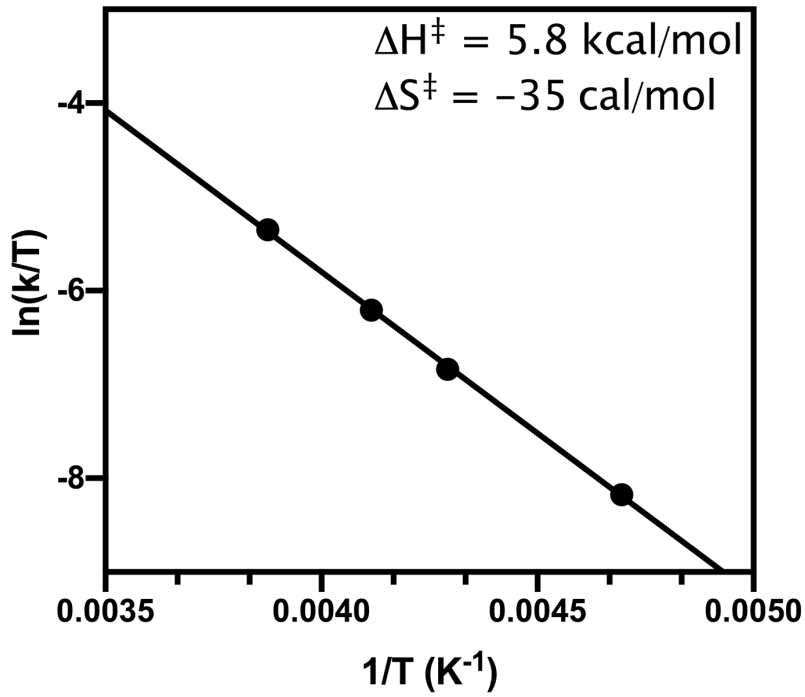

Figure 5.38. Plot of ln(k/T) vs. 1/T for the reaction of **2** with 9,10-dihydroanthracene. Activation enthalpy and entropy parameters were extracted from the slope and y-intercept of the fit.

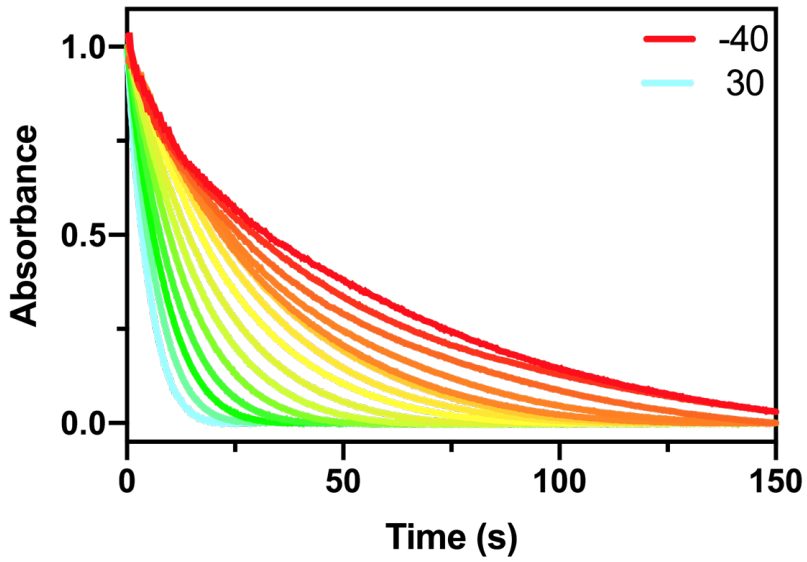

Figure 5.39. Representative fits of the decay of the absorbance at λ = 610 nm vs. time for the reaction of **4** with 9,10-diyhdroanthracene at various temperatures, beginning at -40 °C (red trace) and ending at 30 °C (light blue trace) in 5 °C increments.

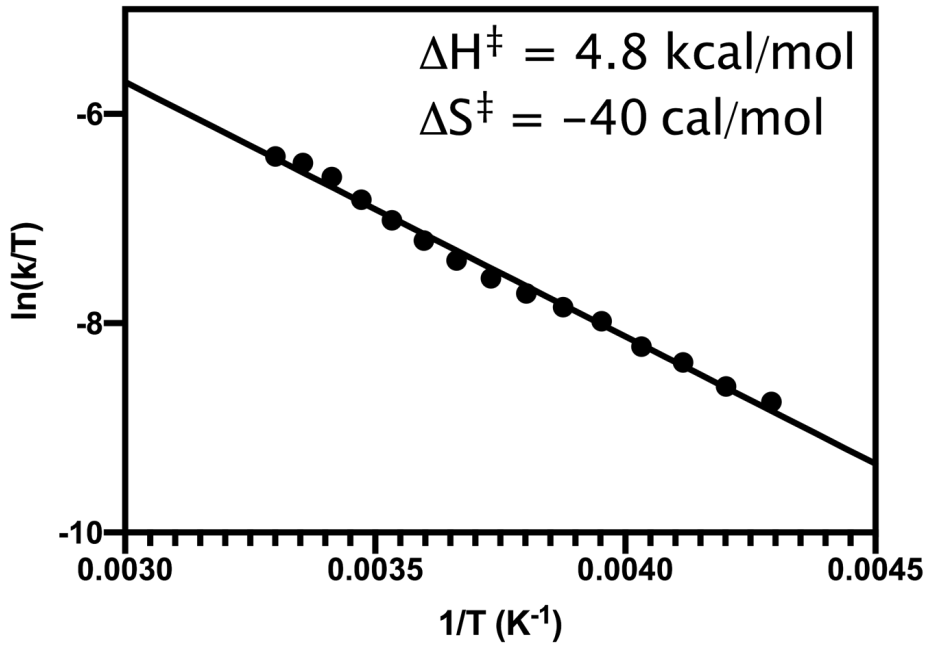

Figure 5.40. Plot of ln(k/T) vs. 1/T for the reaction of **4** with 9,10-dihydroanthracene. Activation enthalpy and entropy parameters were extracted from the slope and y-intercept of the fit.

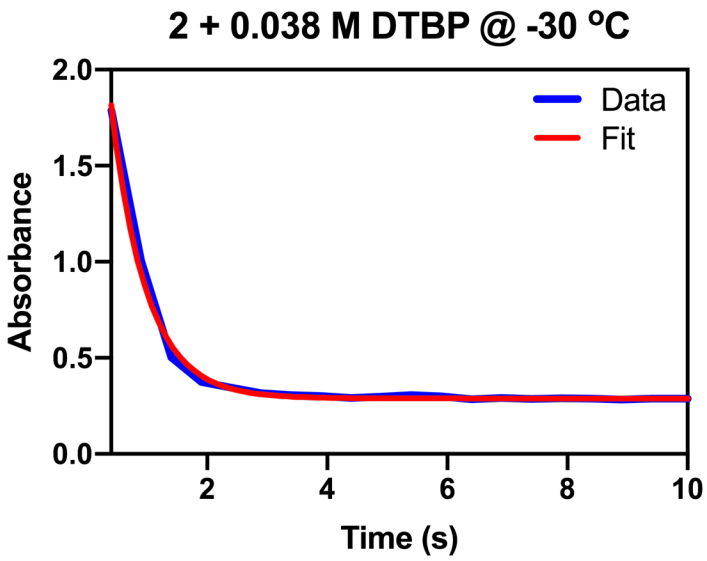

Figure 5.41. Representative fit of absorbance at λ = 430 nm vs. time for the reaction of **2** with 2,6-di-tert-butlyphenol at -30 °C.

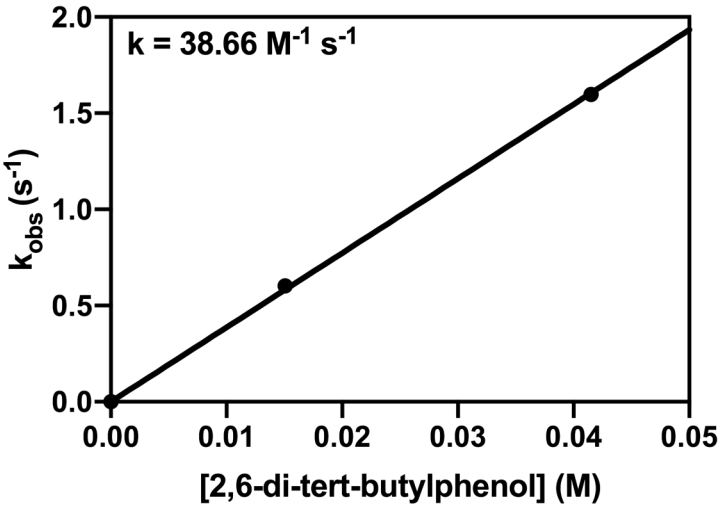

Figure 5.42. Plot of k_{obs} vs. concentration for the reaction of **2** with 2,6-di-tert-butlyphenol at -30 °C.

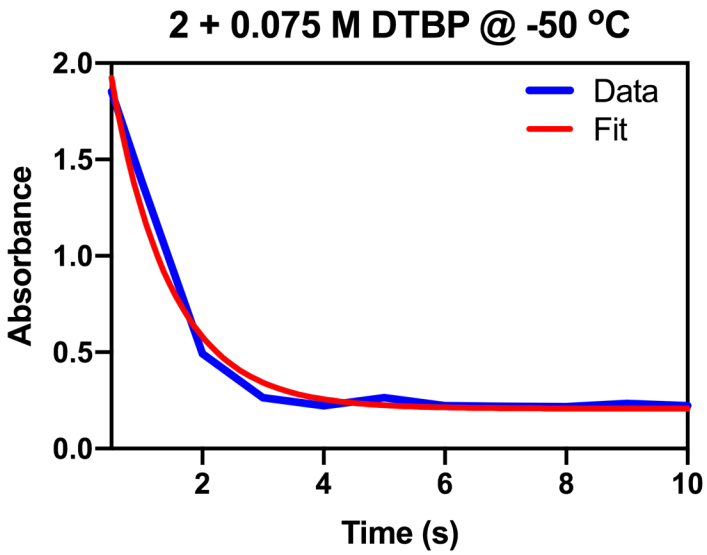

Figure 5.43. Representative fit of absorbance at λ = 430 nm vs. time for the reaction of **2** with 2,6-di-tert-butlyphenol at -50 °C.

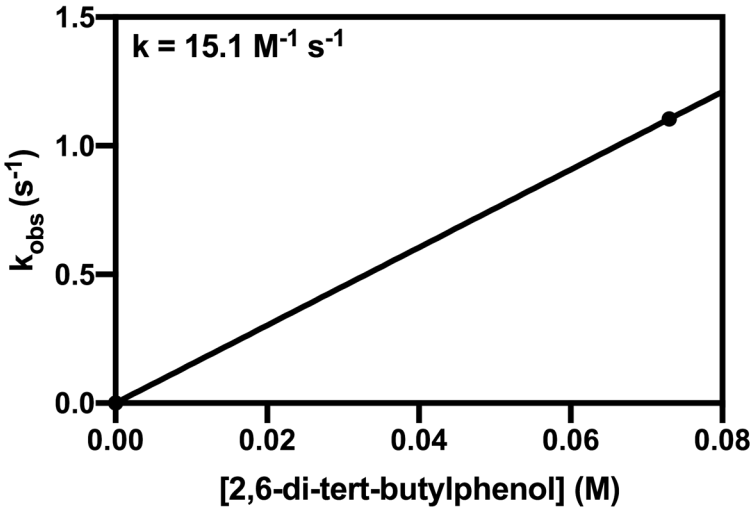

Figure 5.44. Plot of k_{obs} vs. concentration for the reaction of **2** with 2,6-di-tert-butlyphenol at -50 °C.

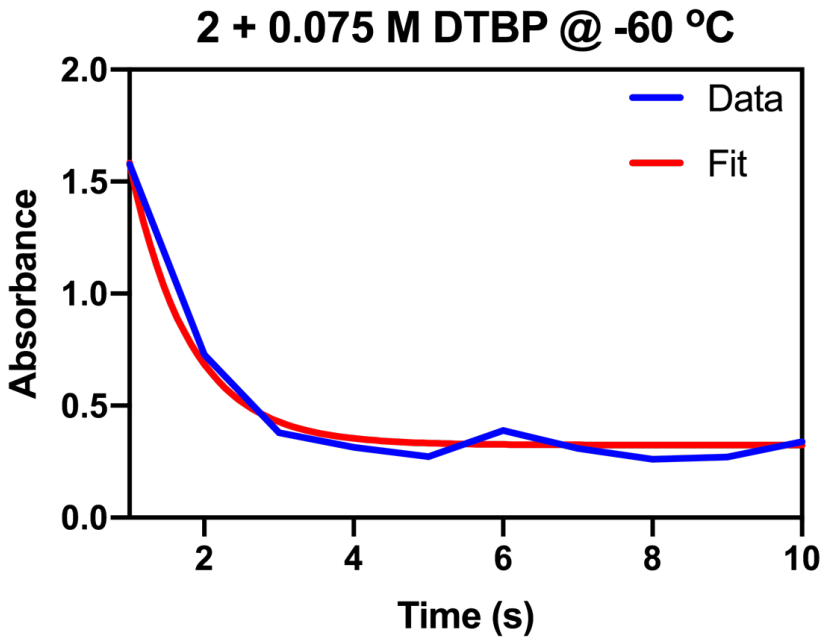

Figure 5.45. Representative fit of absorbance at λ = 430 nm vs. time for the reaction of **2** with 2,6-di-tert-butlyphenol at -60 °C.

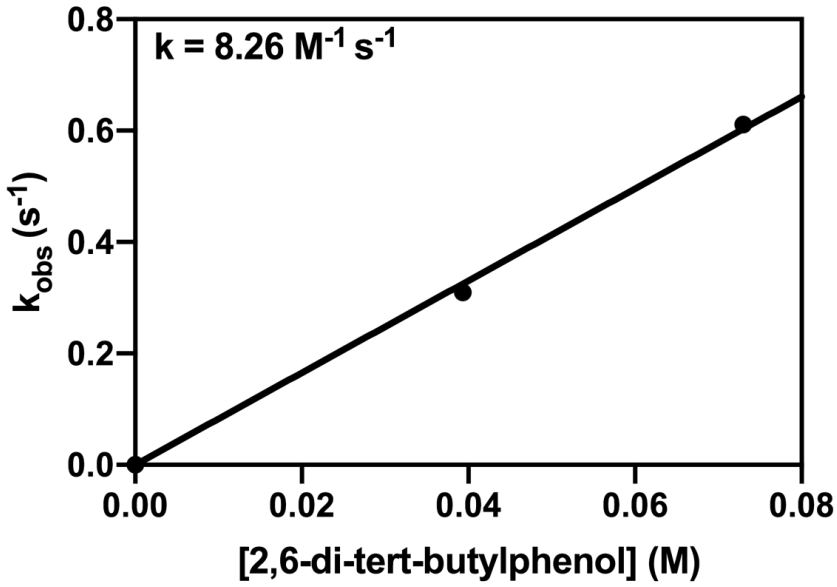

Figure 5.46. Plot of k_{obs} vs. concentration for the reaction of **2** with 2,6-di-tert-butlyphenol at -60 °C.

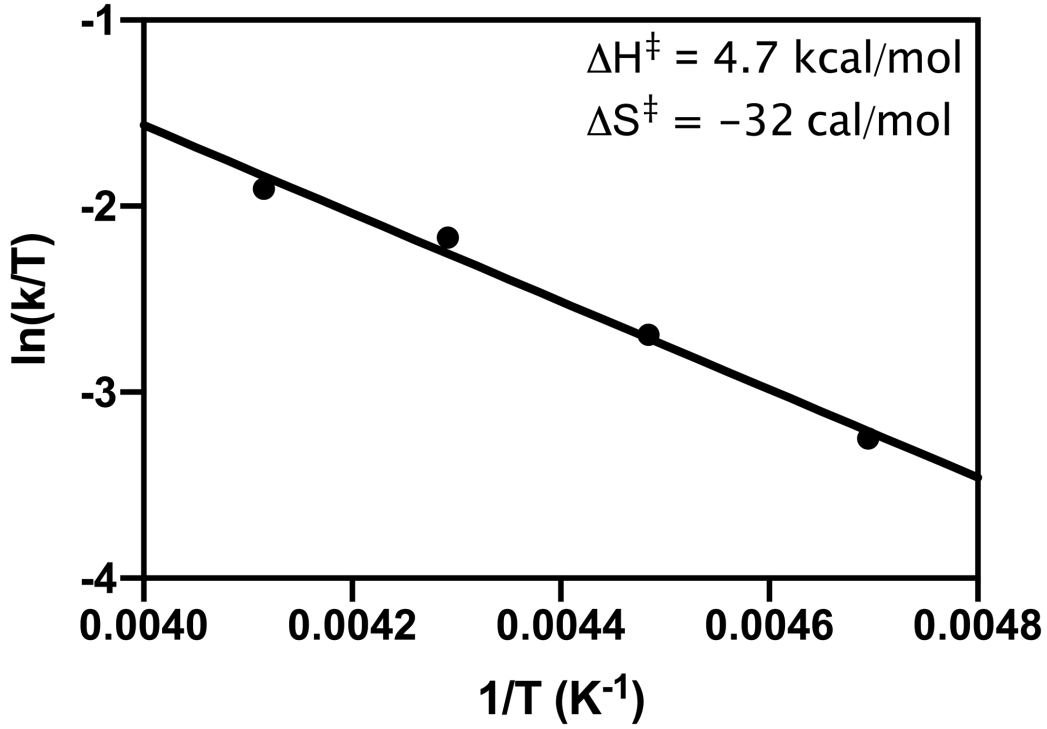

Figure 5.47. Plot of ln(k/T) vs. 1/T for the reaction of **2** with 2,6-di-tert-butylphenol. Activation enthalpy and entropy parameters were extracted from the slope and y-intercept of the fit.

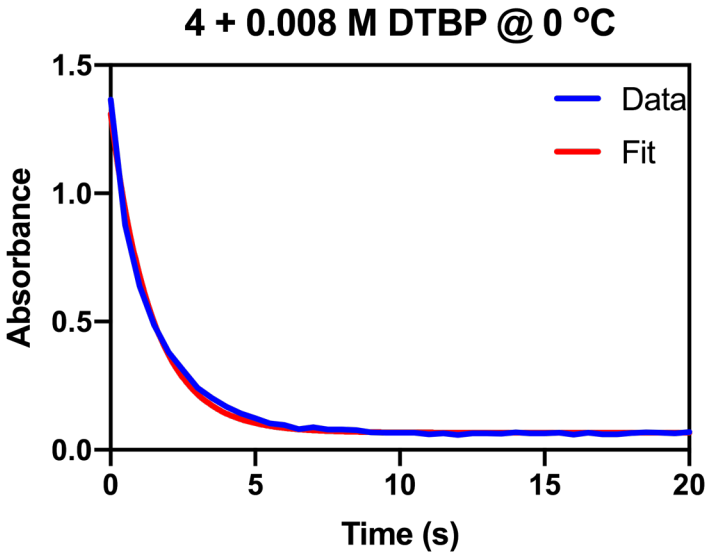

Figure 5.48. Representative fit of absorbance at λ = 430 nm vs. time for the reaction of **4** with 2,6-di-tert-butlyphenol at 0 °C.

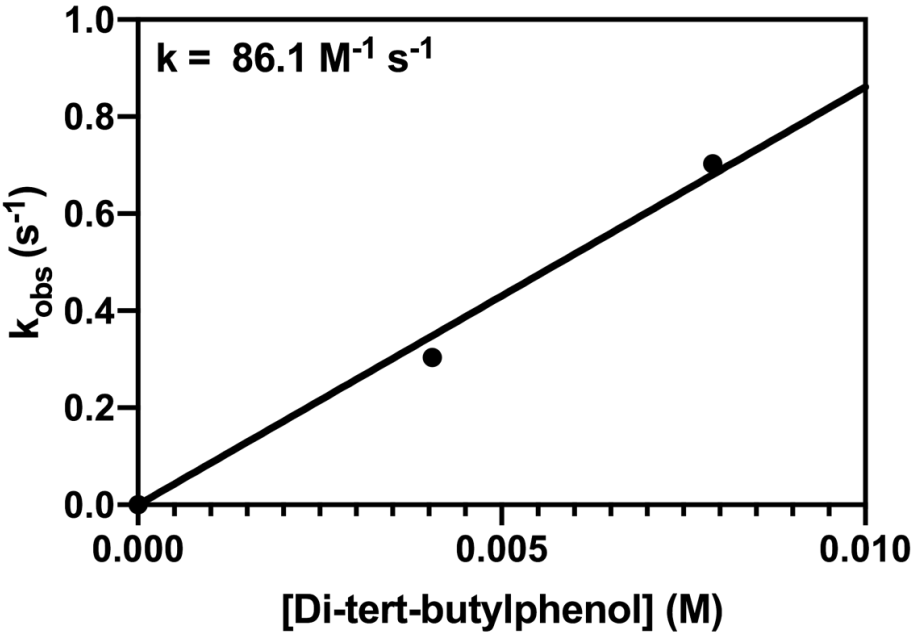

Figure 5.49. Plot of k_{obs} vs. concentration for the reaction of **4** with 2,6-di-tert-butlyphenol at 0 °C.

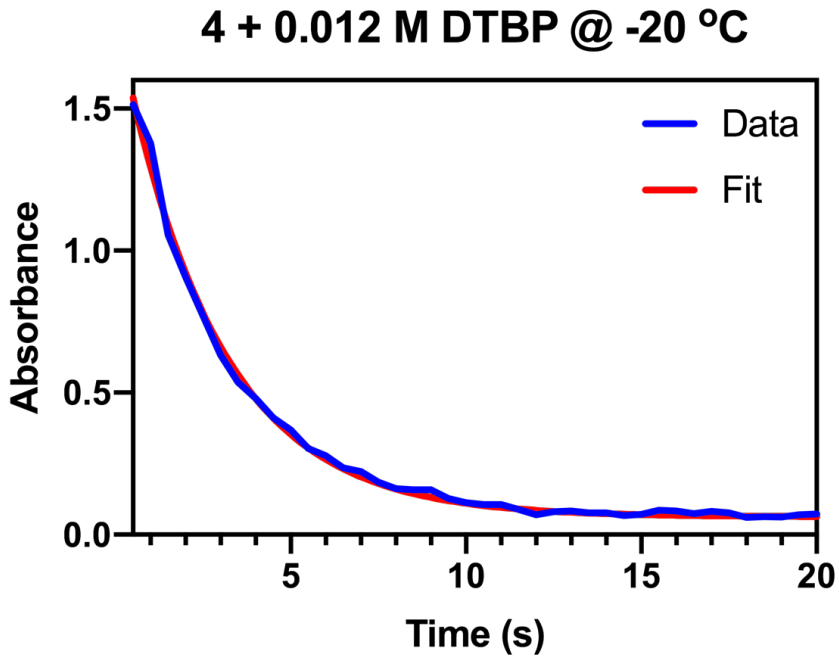

Figure 5.50. Representative fit of absorbance at λ = 430 nm vs. time for the reaction of **4** with 2,6-di-tert-butlyphenol at -20 °C.

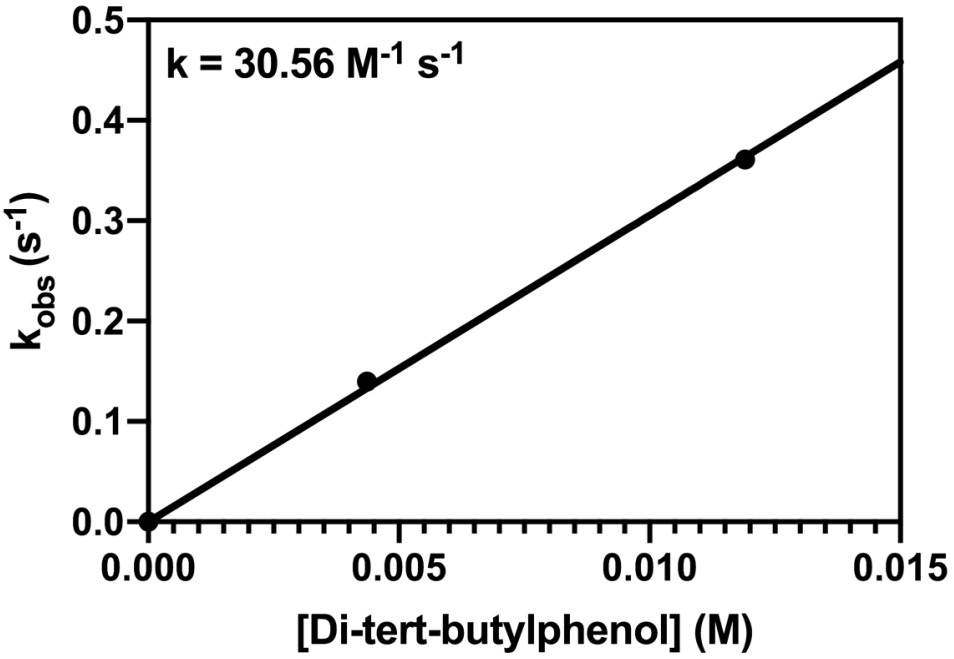

Figure 5.51. Plot of k_{obs} vs. concentration for the reaction of **4** with 2,6-di-tert-butlyphenol at -20 °C.

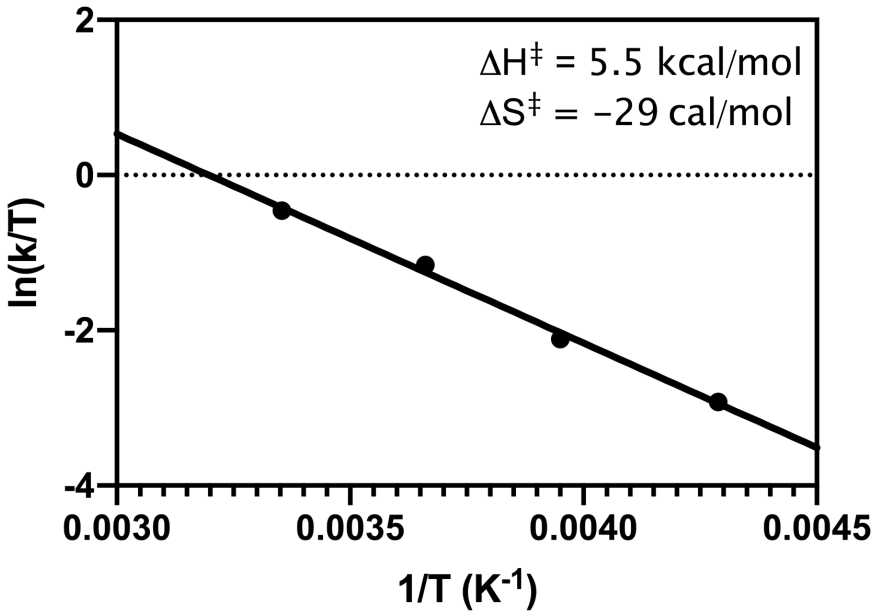

Figure 5.52. Plot of ln(k/T) vs. 1/T for the reaction of **4** with 2,6-di-tert-butylphenol. Activation enthalpy and entropy parameters were extracted from the slope and y-intercept of the fit. Kinetic data for the reaction at 25 °C was taken from reference 16.

Table 5.5. Data used for asynchronicity factor (η) calculations in **Equation 5.3**.

Species	$E^{o'}$	pK_a (MeCN)[a]
2,6-di-tert-butylphenol	1.08	17.3
$Cu(pyalk)_2^+$	0.8	20
$Ni(pyalk)_2^+$	0.55	24

[a]pK_a values in MeCN were converted from values in DMSO (found in reference [29]) using the empirical conversion for phenols found in reference 40.

5.8.5 Crystallographic Details

Experimental

Low-temperature diffraction data (ω-scans) were collected on a Rigaku MicroMax-007HF diffractometer coupled to a Saturn994+ CCD detector with Cu Kα (λ = 1.54178 Å) for the structure of 007a-19086. The diffraction images were processed and scaled using Rigaku Oxford Diffraction software (CrysAlisPro; Rigaku OD: The Woodlands, TX, 2015). The structure was solved with SHELXT and was refined against F^2 on all data by full-matrix least squares with SHELXL (Sheldrick, G. M. Acta Cryst. 2008, A64, 112–122). All non-hydrogen atoms were refined anisotropically. Hydrogen atoms were included in the model at geometrically calculated positions and refined using a riding model. The isotropic displacement parameters of all hydrogen atoms were fixed to 1.2 times the U value of the atoms to which they are linked (1.5 times for methyl groups).

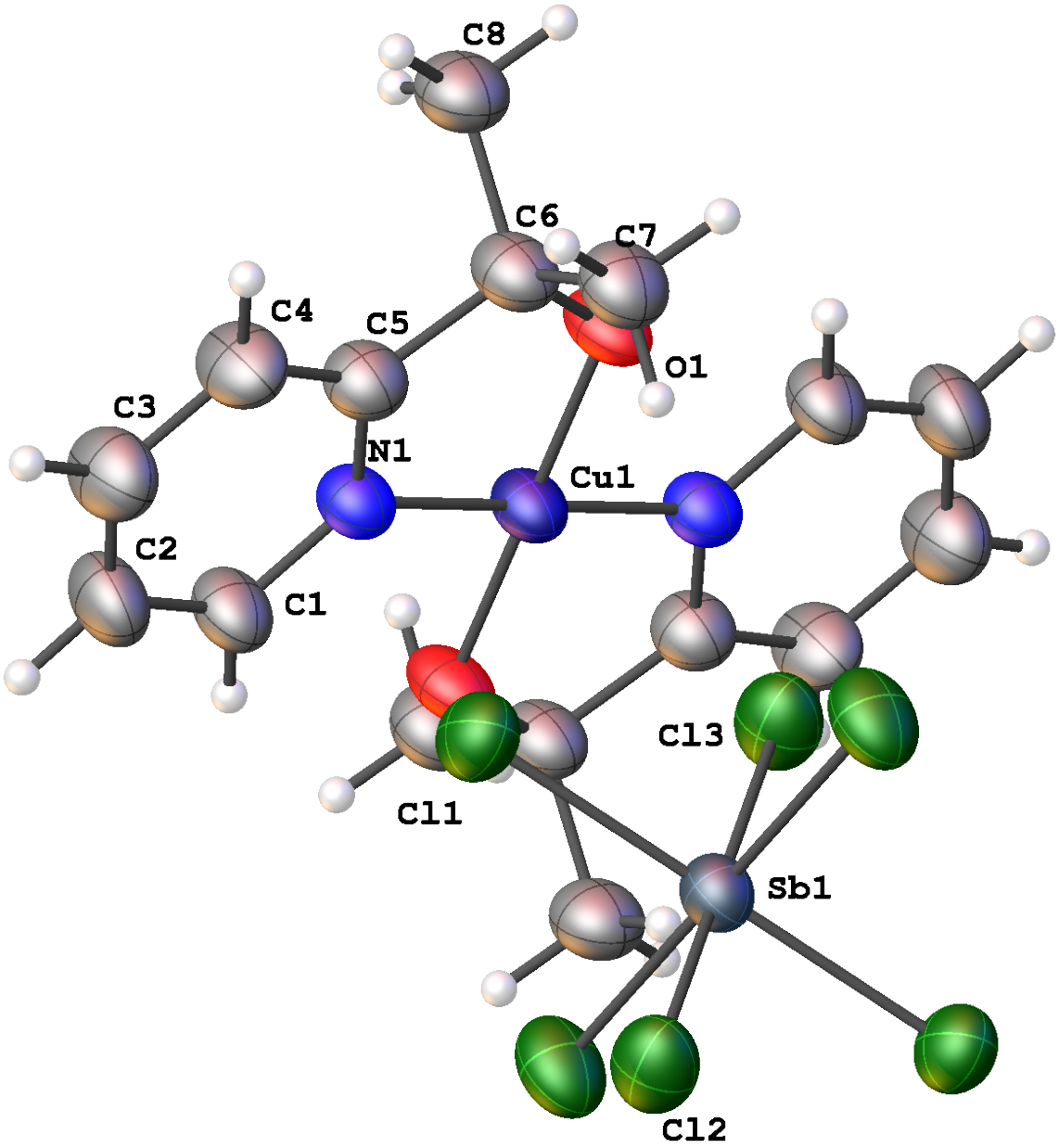

Figure 5.53. Thermal ellipsoid diagram for **2** with complete numbering scheme. Thermal ellipsoids are displayed at the 50% probability level. The hydrogen atoms are shown as circles for clarity. The model is on a special position; only the asymmetric unit is labeled.

Table 5.6. Crystal data and structure refinement for **2**.

Identification code	007a-19086	
Empirical formula	C16 H20 Cl6 Cu N2 O2 Sb	
Formula weight	670.33	
Temperature	93(2) K	
Wavelength	1.54184 Å	
Crystal system	Triclinic	
Space group	P-1	
Unit cell dimensions	a = 8.0212(4) Å	α = 109.349(6)°.
	b = 9.1161(6) Å	β = 95.043(5)°.
	c = 9.8940(7) Å	γ = 113.527(6)°.
Volume	605.26(7) $Å^3$	
Z	1	
Density (calculated)	1.839 Mg/m^3	
Absorption coefficient	16.161 mm^{-1}	
F(000)	328	
Crystal size	0.150 x 0.120 x 0.040 mm^3	
Crystal color and habit	Green Plate	
Diffractometer	Rigaku Saturn 944+ CCD	
Theta range for data collection	4.899 to 66.600°.	
Index ranges	-9<=h<=9, -9<=k<=10, -11<=l<=11	
Reflections collected	21716	
Independent reflections	2106 [R(int) = 0.1026]	
Observed reflections (I > 2sigma(I))	1935	
Completeness to theta = 66.600°	98.6 %	
Absorption correction	Semi-empirical from equivalents	
Max. and min. transmission	1.00000 and 0.32006	
Solution method	SHELXT-2014/5 (Sheldrick, 2014)	
Refinement method	SHELXL-2014/7 (Sheldrick, 2014)	
Data / restraints / parameters	2106 / 0 / 132	
Goodness-of-fit on F^2	1.076	
Final R indices [I>2sigma(I)]	R1 = 0.0451, wR2 = 0.1209	
R indices (all data)	R1 = 0.0478, wR2 = 0.1227	
Largest diff. peak and hole	1.188 and -1.045 $e.Å^{-3}$	

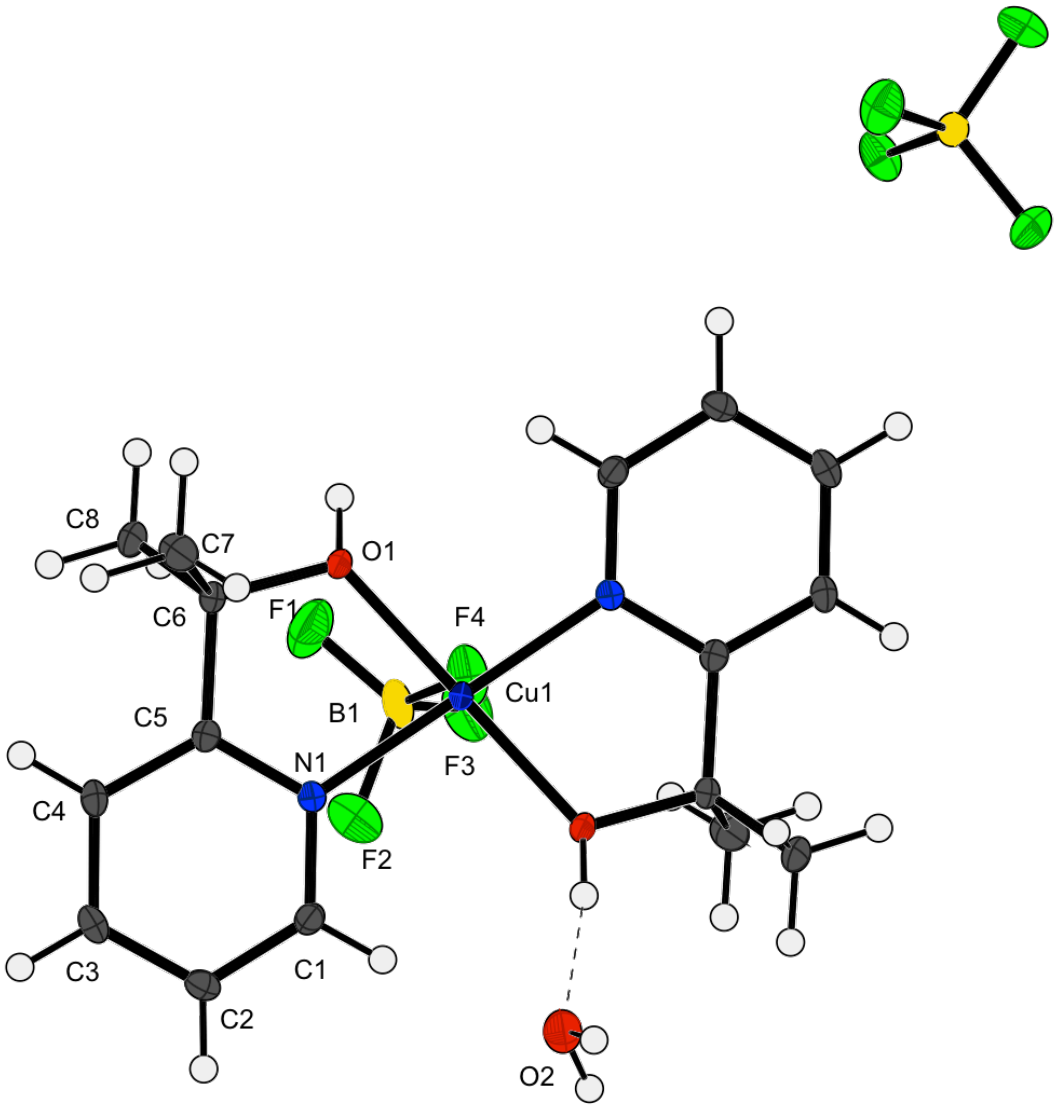

Figure 5.54. Thermal ellipsoid diagram for **1H₂** with complete numbering scheme. Thermal ellipsoids are displayed at the 50% probability level. The hydrogen atoms are shown as circles for clarity. The model is on a special position; only the asymmetric unit is labeled.

Table 5.7. Crystal data and structure refinement for **1H$_2$**.

Identification code	KJF-56-b	
Empirical formula	B2 C16 H24 Cu F8 N2 O3	
Formula weight	529.53	
Temperature	93(2) K	
Wavelength	0.71075 Å	
Crystal system	Triclinic	
Space group	P-1	
Unit cell dimensions	a = 7.9147(4) Å	α = 81.964(6)°.
	b = 9.6937(5) Å	β = 75.490(5)°.
	c = 15.1809(10)) Å	γ = 88.444(6)°.
Volume	1116.46(11) Å^3	
Z	2	
Density (calculated)	1.623 Mg/m^3	
Absorption coefficient	16.161 mm^{-1}	
F(000)	554	
Crystal color and habit	Blue Plate	
Diffractometer	Rigaku Saturn 944+ CCD	
Theta range for data collection	4.899 to 66.600°.	
Index ranges	-10<=h<=10, -12<=k<=12, -19<=l<=19	
Reflections collected	19640	
Independent reflections	5516 [R(int) = 0.0459]	
Observed reflections (I > 2sigma(I))	4102	
Completeness to theta = 66.600°	99.8%	
Absorption correction	Semi-empirical from equivalents	
Max. and min. transmission	1.00000 and 0.32006	
Solution method	SHELXT-2014/5 (Sheldrick, 2014)	
Refinement method	SHELXL-2014/7 (Sheldrick, 2014)	
Data / restraints / parameters	5516 / 0 / 318	
Goodness-of-fit on F^2	1.106	
Final R indices [I>2sigma(I)]	R1 = 0.0459, wR2 = 0.1106	
R indices (all data)	R1 = 0.0552, wR2 = 0.1155	
Largest diff. peak and hole	0.778 and -0.601 e.Å^{-3}	

5.9 References

1. Hickman, A. J.; Sanford, M. S., High-Valent Organometallic Copper and Palladium in Catalysis. *Nature* **2012,** *484* (7393), 177-185.
2. Keown, W.; Gary, J. B.; Stack, T. D., High-Valent Copper in Biomimetic and Biological Oxidations. *J. Biol. Inorg. Chem.* **2017,** *22* (2-3), 289-305.
3. McCann, S. D.; Stahl, S. S., Copper-Catalyzed Aerobic Oxidations of Organic Molecules: Pathways for Two-Electron Oxidation with a Four-Electron Oxidant and a One-Electron Redox-Active Catalyst. *Acc. Chem. Res.* **2015,** *48* (6), 1756-1766.
4. King, A. E.; Huffman, L. M.; Casitas, A.; Costas, M.; Ribas, X.; Stahl, S. S., Copper-Catalyzed Aerobic Oxidative Functionalization of an Arene C−H Bond: Evidence for an Aryl-Copper(III) Intermediate. *J. Am. Chem. Soc.* **2010,** *132* (34), 12068-12073.
5. Hoover, J. M.; Ryland, B. L.; Stahl, S. S., Copper/Tempo-Catalyzed Aerobic Alcohol Oxidation: Mechanistic Assessment of Different Catalyst Systems. *ACS Catal.* **2013,** *3* (11), 2599-2605.
6. Bower, J. K.; Cypcar, A. D.; Henriquez, B.; Stieber, S. C. E.; Zhang, S., C(sp^3)–H Fluorination with a Copper(II)/(III) Redox Couple. *J. Am. Chem. Soc.* **2020**.
7. Fisher, K. J.; Materna, K. L.; Mercado, B. Q.; Crabtree, R. H.; Brudvig, G. W., Electrocatalytic Water Oxidation by a Copper(II) Complex of an Oxidation-Resistant Ligand. *ACS Catal.* **2017,** *7*, 3384-3387.
8. Bim, D.; Maldonado-Dominguez, M.; Rulisek, L.; Srnec, M., Beyond the Classical Thermodynamic Contributions to Hydrogen Atom Abstraction Reactivity. *Proc. Natl. Acad. Sci.* **2018,** *115* (44), E10287-E10294.
9. Goetz, M. K.; Anderson, J. S., Experimental Evidence for pK_a-Driven Asynchronicity in C-H Activation by a Terminal Co(III)-Oxo Complex. *J. Am. Chem. Soc.* **2019,** *141* (9), 4051-4062.
10. Mandal, M.; Elwell, C. E.; Bouchey, C. J.; Zerk, T. J.; Tolman, W. B.; Cramer, C. J., Mechanisms for Hydrogen-Atom Abstraction by Mononuclear Copper(III) Cores: Hydrogen-Atom Transfer or Concerted Proton-Coupled Electron Transfer? *J. Am. Chem. Soc.* **2019,** *141* (43), 17236-17244.
11. Dhar, D.; Tolman, W. B., Hydrogen Atom Abstraction from Hydrocarbons by a Copper(III)-Hydroxide Complex. *J. Am. Chem. Soc.* **2015,** *137* (3), 1322-1329.
12. Bailey, W. D.; Dhar, D.; Cramblitt, A. C.; Tolman, W. B., Mechanistic Dichotomy in Proton-Coupled Electron-Transfer Reactions of Phenols with a Copper Superoxide Complex. *J. Am. Chem. Soc.* **2019,** *141* (13), 5470-5480.
13. Unjaroen, D.; Gericke, R.; Lovisari, M.; Nelis, D.; Mondal, P.; Pirovano, P.; Twamley, B.; Farquhar, E. R.; McDonald, A. R., High-Valent d^7 Ni^{III} Versus d^8 Cu^{III} Oxidants in PCET. *Inorg. Chem.* **2019,** *58* (24), 16838-16848.
14. Kundu, S.; Miceli, E.; Farquhar, E. R.; Ray, K., Mechanism of Phenol Oxidation by Heterodinuclear Ni Cu Bis(μ-Oxo) Complexes Involving Nucleophilic Oxo Groups. *Dalton Trans.* **2014,** *43* (11), 4264-4267.
15. Dhar, D.; Yee, G. M.; Spaeth, A. D.; Boyce, D. W.; Zhang, H.; Dereli, B.; Cramer, C. J.; Tolman, W. B., Perturbing the Copper(III)–Hydroxide Unit through Ligand Structural Variation. *J. Am. Chem. Soc.* **2016,** *138* (1), 356-368.
16. Fisher, K. J.; Feuer, M. L.; Lant, H. M. C.; Mercado, B. Q.; Crabtree, R. H.; Brudvig, G. W., Concerted Proton-Electron Transfer Oxidation of Phenols and Hydrocarbons by a High-Valent Nickel Complex. *Chem. Sci.* **2020,** *11* (6), 1683-1690.
17. Sharninghausen, L. S.; Sinha, S. B.; Shopov, D. Y.; Choi, B.; Mercado, B. Q.; Roy, X.; Balcells, D.; Brudvig, G. W.; Crabtree, R. H., High Oxidation State Iridium Mono-μ-Oxo Dimers Related to Water Oxidation Catalysis. *J. Am. Chem. Soc.* **2016**.
18. Shopov, D. Y.; Sharninghausen, L. S.; Sinha, S. B.; Mercado, B. Q.; Balcells, D.; Brudvig, G. W.; Crabtree, R. H., A Dinuclear Iridium(V,V) Oxo-Bridged Complex Characterized Using a Bulk Electrolysis Technique for Crystallizing Highly Oxidizing Compounds. *Inorg. Chem.* **2018,** *57* (9), 5684-5691.
19. Spaeth, A. D.; Gagnon, N. L.; Dhar, D.; Yee, G. M.; Tolman, W. B., Determination of the Cu(III)–OH Bond Distance by Resonance Raman Spectroscopy Using a Normalized Version of Badger's Rule. *J. Am. Chem. Soc.* **2017,** *139* (12), 4477-4485.

20. Oliver, K. J.; Waters, T. N., X-Ray Crystal Structure of a Stable Complex of Copper(III); the Use of Deprotonated Nitrogen Atoms as Donors. *J. Chem. Soc., Chem. Commun.* **1982,** (19), 1111-1112.
21. Anson, F. C.; Collins, T. J.; Richmond, T. G.; Santarsiero, B. D.; Toth, J. E.; Treco, B. G. R. T., Highly Stabilized Copper(III) Complexes. *J. Am. Chem. Soc.* **1987,** *109* (10), 2974-2979.
22. Akbar Ali, M.; Bernhardt, P. V.; Brax, M. A. H.; England, J.; Farlow, A. J.; Hanson, G. R.; Yeng, L. L.; Mirza, A. H.; Wieghardt, K., The Trivalent Copper Complex of a Conjugated Bis-Dithiocarbazate Schiff Base: Stabilization of Cu in Three Different Oxidation States. *Inorg. Chem.* **2013,** *52* (3), 1650-1657.
23. Hanss, J.; Krüger, H.-J., The First Stable Copper(III) Complex Containing Aliphatic Thiolates as Ligands: Structural and Spectroscopic Evidence for CuII and CuIII Ions in Complexes with Square-Planar CuN_2S_2 Coordination Environments. *Angew. Chem. Int. Ed.* **1996,** *35* (23-24), 2827-2830.
24. Hanss, J.; Beckmann, A.; Krüger, H.-J., Stabilization of Copper(III) Ions with Deprotonated Hydroxyiminoamide Ligands: Syntheses, Structures, and Electronic Properties of Copper(II) and Copper(III) Complexes. *Eur. J. Inorg. Chem.* **1999,** *1999* (1), 163-172.
25. Kochem, A.; Molloy, J. K.; Gellon, G.; Leconte, N.; Philouze, C.; Berthiol, F.; Jarjayes, O.; Thomas, F., A Structurally Characterized CuIII Complex Supported by a Bis(Anilido) Ligand and Its Oxidative Catalytic Activity. *Chem. Eur. J.* **2017,** *23* (56), 13929-13940.
26. Gherman, B. F.; Tolman, W. B.; Cramer, C. J., Characterization of the Structure and Reactivity of Monocopper–Oxygen Complexes Supported by β-Diketiminate and Anilido-Imine Ligands. *J. Comput. Chem.* **2006,** *27* (16), 1950-1961.
27. Rudshteyn, B.; Fisher, K. J.; Lant, H. M. C.; Yang, K. R.; Mercado, B. Q.; Brudvig, G. W.; Crabtree, R. H.; Batista, V. S., Water-Nucleophilic Attack Mechanism for the $Cu^{II}(pyalk)_2$ Water-Oxidation Catalyst. *ACS Catal.* **2018,** *8* (9), 7952-7960.
28. Wei, M.; Musie, G. T.; Busch, D. H.; Subramaniam, B., Autoxidation of 2,6-Di-Tert-Butylphenol with Cobalt Schiff Base Catalysts by Oxygen in CO_2-Expanded Liquids. *Green Chem.* **2004,** *6* (8), 387-393.
29. Warren, J. J.; Tronic, T. A.; Mayer, J. M., Thermochemistry of Proton-Coupled Electron Transfer Reagents and Its Implications. *Chem. Rev.* **2010,** *110* (12), 6961-7001.
30. Pirovano, P.; Farquhar, E. R.; Swart, M.; McDonald, A. R., Tuning the Reactivity of Terminal Nickel(III)–Oxygen Adducts for C–H Bond Activation. *J. Am. Chem. Soc.* **2016,** *138* (43), 14362-14370.
31. Goldsmith, C. R.; Jonas, R. T.; Stack, T. D. P., C−H Bond Activation by a Ferric Methoxide Complex: Modeling the Rate-Determining Step in the Mechanism of Lipoxygenase. *Journal of the American Chemical Society* **2002,** *124* (1), 83-96.
32. Moyer, B. A.; Meyer, T. J., Properties of the Oxo/Aqua System $(bpy)_2(py)RuO^{2+}/(bpy)_2(py)Ru(OH_2)^{2+}$. *Inorg. Chem.* **1981,** *20* (2), 436-444.
33. Lebeau, E. L.; Binstead, R. A.; Meyer, T. J., Mechanistic Implications of Proton Transfer Coupled to Electron Transfer. *J. Am. Chem. Soc.* **2001,** *123* (43), 10535-10544.
34. Bryant, J. R.; Mayer, J. M., Oxidation of C−H Bonds by $[(bpy)_2(py)Ru^{IV}O]^{2+}$ Occurs by Hydrogen Atom Abstraction. *J. Am. Chem. Soc.* **2003,** *125* (34), 10351-10361.
35. Connelly, N. G.; Geiger, W. E., Chemical Redox Agents for Organometallic Chemistry. *Chem. Rev.* **1996,** *96* (2), 877-910.
36. Saouma, C. T.; Kaminsky, W.; Mayer, J. M., Protonation and Concerted Proton-Electron Transfer Reactivity of a Bis-Benzimidazolate Ligated [2Fe-2S] Model for Rieske Clusters. *J. Am. Chem. Soc.* **2012,** *134* (17), 7293-6.
37. Blum, Z.; Cedheim, L.; Eberson, L., Studies on Anodic Substitution Reactions. XI. The Anodic Acetoxylation of Triptycene and Fluorene and Its Implications for the Side-Chain Substitution Mechanism. *Acta Chem. Scand.* **1977,** *31b*, 662-666.
38. Bordwell, F. G., Equilibrium Acidities in Dimethyl Sulfoxide Solution. *Acc. Chem. Res.* **1988,** *21* (12), 456-463.
39. Laarhoven, L. J. J.; Mulder, P., α-C−H Bond Strengths in Tetralin and Thf: Application of Competition Experiments in Photoacoustic Calorimetry. *J. Phys. Chem. B* **1997,** *101* (1), 73-77.

40. Rossini, E.; Bochevarov, A. D.; Knapp, E. W., Empirical Conversion of pK_a Values between Different Solvents and Interpretation of the Parameters: Application to Water, Acetonitrile, Dimethyl Sulfoxide, and Methanol. *ACS Omega* **2018,** *3* (2), 1653-1662.